DEVELOPMENT OF ANTIMICROBIAL METAL ALLOYS

By

DAISY LILY ADONIA RABBITT

A thesis submitted to the University of Birmingham for the degree of
DOCTOR OF PHILOSOPHY

School of Chemical Engineering
College of Engineering and Physical Sciences
University of Birmingham
April 2025

Abstract

With rising rates of orthopaedic implant infections and antimicrobial resistance, novel methods to combat these clinical challenges are greatly needed. This thesis focusses on producing an inherently antimicrobial material to offer a localised solution for infection prevention.

Ti-Cu alloys are investigated as potential candidates for biomedical alloys due to their evidenced antimicrobial efficacy. This thesis contributes knowledge to understanding what microstructural features drive the antimicrobial efficacy of Ti-Cu alloys and demonstrates that additive manufacturing may be used to amplify these effects.

Initially, arc melted specimen of Ti-11.5 (wt.%) Cu and Ti-33 (wt.%) Cu were manufactured and heat treated to examine the influence of microstructural refinement to fine tune antimicrobial efficacy. Larger (approximately 5 μm), rounded Ti_xCu precipitates had increased antimicrobial efficacy, compared to nanoscale and elongated precipitates, though no specimen showed efficacy towards *E. coli*.

Further investigations using powder metallurgy and additive manufacturing demonstrated that processing routes markedly affect microstructure and copper ion release, enhancing antimicrobial potency. Notably, AM-fabricated alloys with only 3 wt.% Cu exhibited significant antimicrobial efficacy against both *S. aureus* and *E. coli.* Improvements in their responses to native bone cells were also prominent, with cell viability of 78 % and 51 % after 7 days for Ti-3Cu and Ti-11.5Cu respectively. However, concerns around the long-term biocompatibility of Ti-11.5Cu due to the ion release mechanism must be considered.

Finally, to address concerns around the mechanical mismatches that may lead to aseptic loosening, the potential for developing a Ti-Mo-Cu alloy was explored. Using low laser energy densities and post-processing heat treatments, successful Mo diffusion was achieved. This led to fabrication of promising alloy systems with 100 % antimicrobial efficacy. These findings underscore the importance of compositional tuning and role of heat treatments in optimising both the mechanical integrity and biological functionality of titanium alloys for advanced biomedical applications.

Acknowledgements

First and foremost, I would like to express my sincere gratitude to my supervisors, Dr. Sophie Cox and Prof. Sandy Knowles, for their unwavering support, guidance, and encouragement throughout this project. Their insight and mentorship have been invaluable to both my research and my personal development.

Special thanks to Dr. Luke Carter and Dr. Victor Villapún. Luke, for his endless support, wisdom, and willingness to always lend an ear when things got tough; and Victor, for his help and guidance with all the biological work, and for enabling me to fully understand the processes that underpinned this project. I am also incredibly grateful to Dan Wilmot, whose efforts ensured the smooth running of the labs, his contributions cannot be overstated.

Further thanks to Paraic O'Kelly for completing the TEM work on my behalf, and to Christopher Stark for his work on the ICP-OES analysis.

This work was supported by the UKRI Future Leaders Fellowship [MR/T019174/1, MR/Y034155/1 and MR/T017783/1] and the Royal Academy of Engineering Research Fellowship [RF\201819\18\158]. I also gratefully acknowledge the funding from UoB alumnus, James Webber, which not only supported significant portions of my PhD research, but is also enabling me to continue this work for the next three months.

Finally, I would like to thank my family and friends for their constant belief in me and their unwavering support throughout this journey. To all of those at Edgbaston Hockey Club who have helped provide the best kind of sporting distractions. To my Mum and Grandma, for always being at the end of the phone and providing endless encouragement and support. And of course, to Jonny, thank you for being my rock during these past few years. I truly couldn't have done this without you.

ACKNOWLEDGEMENT OF CONTRIBUTING MATERIAL AND AUTHORS

Content within this thesis has been published in the following journal papers:

- D. Rabbitt, V. M. Villapún, L. N. Carter, K. Man, M. Lowther, P. O'Kelly, A. J. Knowles, A. Mottura, Y. T. Tang, L. Luerti, R. C. Reed, S. C. Cox, Rethinking Biomedical Titanium Alloy Design: A Review of Challenges from Biological and Manufacturing Perspectives. *Adv. Healthcare Mater.* 2025, 14, 2403129.
- D. Rabbitt, P. O'Kelly, V. M. Villapún, L. N. Carter, A. J. Knowles, S. C. Cox, Antimicrobial Titanium-Copper Alloys: The Role of Microstructure in Arc-melted Compositions. (In review)

As primary author, D Rabbitt produced all written work within this thesis.

The contributions from publication co-authors and co-workers to content in this thesis are as follows:

- P. O'Kelly: Completion of TEM analysis
- V. M. Villapún: Assistance with bacterial and mammalian cell culture and flow cytometry.
- C. Stark: Operation of inductively coupled plasma optical emission spectroscopy (ICP-OES)
- A. Nicum: Assistance with Ti-Mo study as part of her Final Year project.
- L. N. Carter, K. Man, M. Lowther, A. Mottura, Y. T. Tang, L. Luerti, R. C. Reed: Editorial guidance.
- A. J. Knowles and S. C. Cox: Editorial and supervisory guidance.

Table of Contents

Abstract ii

Acknowledgements iii

Table of Contents v

List of Figures xiv

List of Tables xxii

List of Abbreviations xxiv

1. Introduction 28

1.1. Objectives 31

1.2. Thesis Outline 32

2. Literature Review 34

2.1. Background to Metal Implants 34

2.1.1. Titanium Based Alloys: Current Materials and Developments 34

2.1.2. Clinical Challenges 39

2.1.3. Fundamentals of Bacterial Colonisation and Biofilm Formation 42

2.1.4. *Staphylococci* Infections 44

2.2. Current Strategies for Managing Implant Associated Infections 45

2.3. Antimicrobial Resistance 47

2.3.1. Antimicrobial metals 49

2.3.1.1. Mode of Action of Antimicrobial Metals 49

2.3.1.2. Physiological and Biochemical Responses to Metal Stress in Bacteria ... 53

2.3.1.3. Common Examples of Metallic Antimicrobial Elements 55

2.4. Ti-Cu Alloys 58

2.4.1. Phase Diagram 58

2.4.2. Antibacterial Ti-Cu alloys 60

2.4.3. Further Benefits of Ti-Cu 64

2.4.4. Advancing Titanium Based Alloys: Integrating Antimicrobial Properties and Enhanced Functionalities 64

2.5. Manufacturing Methods to Support Alloy Discovery 67

2.5.1. Traditional Melt 69

2.5.2. Powder Bed Fusion 71

2.5.3. Heat Treatments 75

2.5.4. Review of Literature Methods of Alloy Discovery 75

2.6. Characterisation 77

2.7. Summary and Knowledge Gap 80

3. Antimicrobial Ti-Cu Alloys: The Role of Microstructure in Arc-melted Compositions 83

3.1. Introduction 83

3.2. Methods 87

3.2.1. Sample Preparation 87

3.2.2. Microstructural Characterisation and Phase Identification 88

3.2.3. Image Analysis 89

3.2.4. Phase Analysis 91

3.2.5. Cu ion release 91

3.2.6. Contact Angle 91

3.2.7. Protein Adsorption 92

3.2.8. Microhardness 93

3.2.9. Bacterial Analysis 93

3.2.9.1. Minimum Inhibitory Concentration/ Minimum Bacterial Concentration Determination 93

3.2.9.2. Antimicrobial Analysis 93

3.2.9.3. Flow Cytometry 94

3.2.10. *In Vitro* Analysis 95

3.2.10.1. Cytotoxicity Analysis 95

3.2.10.2. Metabolic Activity Assay 95

3.3. Results 96

3.3.1. Microstructural Characterisation and Phase Identification 96

3.3.2. Cu Ion Release 101

3.3.3. Contact Angle Analysis 101

3.3.4. Microhardness 102

3.3.5. Bacterial Analysis 103

3.3.5.1. MIC and MBC Determination 103

3.3.5.2. Antimicrobial Analysis 103

3.3.5.3. Flow Cytometry 105

3.3.6. Compositional Analysis 106

3.3.7. Bacterial Imaging on the Ti-Cu Surfaces 110

3.3.8. Protein Adsorption 111

3.3.9. Cytotoxicity 112

3.4. Discussion 115

3.5. Conclusion 124

4. Effect of Manufacturing Method on the Antimicrobial Efficacy of Titanium-Copper Alloys 126

4.1. Introduction 126

4.2. Methods 129

4.2.1. Powder Characterisation 129

4.2.2. Sample Manufacture 129

4.2.2.1. Ball milling and Pressing 130

4.2.2.2. Additive Manufacture 130

4.2.2.3. Parametric Study 131

4.2.2.4. Archimedes Density 133

4.2.2.5. Optimised Builds 133

4.2.3. Samples Preparation 134

4.2.4. Microstructural Characterisation and Phase Identification 135

4.2.5. Cu ion release 135

4.2.6. Contact Angle Analysis 135

4.2.7. Protein Adsorption 136

4.2.8. Microhardness 136

4.2.9. Antimicrobial Analysis 137

4.2.10. *In Vitro* Analysis 138

4.2.10.1. Cytotoxicity Analysis 138

4.2.10.2. Cell Viability Assay 138

4.3. Results 139

4.3.1. Powder Characterisation 139

4.3.2. Ball Milling 140

4.3.3. Pressed 142

4.3.4. Additive Manufacturing 143

4.3.4.1. Parametric Builds 143

4.3.4.2. Archimedes Density 144

4.3.4.3. Parametric Build Characterisation 146

4.3.5. Microstructural Characterisation and Phase Identification 152

4.3.6. Cu Ion Release 153

4.3.7. Contact Angle Analysis 153

4.3.8. Microhardness 154

4.3.9. Antimicrobial Analysis 155

4.3.10. Protein Adsorption 156

4.3.11. Cytotoxicity 157

4.4. Discussion 160

4.5. Conclusion 165

5. The Effect of Molybdenum Addition on Mechanical and Antimicrobial Properties of Additively Manufactured Ti-Cu Alloys 167

5.1. Introduction 167

5.2. Methods 174

5.2.1. Preliminary Study: Processing window for Ti-Mo via PBF-LB 174

5.2.2. Sample Compositions 174

5.2.3. Powder Characterisation 175

5.2.4. Additive Manufacture 175

5.2.4.1. Parametric Study 176

5.2.4.2. Archimedes Density 178

5.2.4.3. Optimised Builds 178

5.2.5. Heat Treatment 179

5.2.6. Samples Preparation 179

5.2.7. Microstructural Characterisation and Phase Identification 180

5.2.8. Image Analysis 181

5.2.9. Microhardness 181

5.2.10. Antimicrobial Analysis 181

5.3. Results 182

5.3.1. Powder Characterisation 182

5.3.2. Additive Manufacturing 183

5.3.2.1. Parametric Builds 183

5.3.2.2. Archimedes Density 184

5.3.2.3. Parametric Build Characterisation 185

5.3.3. Microstructural Characterisation and Phase Identification 191

5.3.3.1. As built 191

5.3.4. Post-heat treatment 192

5.3.5. Microhardness 197

5.3.6. Antimicrobial Analysis 198

5.4. Discussion 200

5.5. Conclusion 203

6. Conclusions and Future Work 206

6.1. Overall Conclusions 206

6.2. Proposed Areas of Future Work 207

6.3. Final Remarks 210

7. List of References 211

Appendix A : Image Analysis 245

A.1. MATLAB Code: Precipitate Size 245

A.2. MATLAB Code: Hu Moments 247

A.3. Hu Moments 249

Appendix B: Protein Analysis 250

List of Figures

Figure 1.1: (a) Predicted total annual counts for primary THA/TKA use from 2020-2040 in the United States (in thousands). (b) Projected annual use of primary total knee arthroplasty (TKA) in the United States by age. (c) Projected annual use of primary total hip arthroplasty (THA) in the United States by age. Data extracted from Singh et al. [6]. 29

Figure 2.1: Ti-based alloys according to their adoption date and form (α/α-β and β-Ti), as well as their usage [36-47]. 35

Figure 2.2: (a) Alpha and (b) beta crystal structures of titanium. Adapted from Banerjee et al.[53]. 36

Figure 2.3: Different categories of titanium phase diagrams depending on the alloying elements. 37

Figure 2.4: Mechanisms of implant failure. Adapted from Li et al. [4]. 40

Figure 2.5: Stages of biofilm formation. 44

Figure 2.6: Algorithm to determine surgical approach to PJIs. Criteria include time from surgery, type of infection, condition of the implant and soft tissue, as well as the comorbidity. Figure adapted from Zimmerli et al. [9]. 47

Figure 2.7: Strategies for combating the issues relating to AMR via biomaterials. Adapted from figure from Hall et al., 2020 [89]. 48

Figure 2.8: Depiction of ROS production in cells through addition of metal ions (e.g., Ag+ or Cu2+). Adapted from Domb et al., 2019 [142]. 53

Figure 2.9: Representation of how microorganisms adapt to metals. Adapted from Lemire et al., 2013 [117]. 55

Figure 2.10: Mechanisms of cell death from copper containing alloys extracellularly and effect of Cu ions intracellularly. 57

Figure 2.11: Ti-Cu binary phase diagram produced using ThermoCalc 2023a with the TCTI2 database. 60

Figure 2.12:Ti-Mo binary phase diagram. Adapted from Zhang et al. [206]. 66

Figure 2.13: Isothermal ternary phase diagram at 950 °C for Ti-Mo-Cu alloy, created using ThermoCalc 2023a with TCTI2 database. 67

Figure 2.14: Schematic of traditional melt, additive manufacturing, powder metallurgy methods and thin film methods to facilitate alloy discovery. 69

Figure 2.15: Representation of the principles of laser powder bed fusion (PBF-LB) additive manufacturing, showing the typical physical layout of PBF-LB apparatus. Powder from the feedstock is spread across the build plate via the recoater, and thermally fused by a laser. The build plate lowers, a new powder layer is spread, and fuses with the previous layer. On the right, a cross-section of the build region is displayed. Support structures are often required for overhangs, but unmelted powder can act as some degree of support. 72

Figure 2.16: SEM microstructure of the cp–Ti samples produced by (a) Selective Laser Melting (SLM) and (b) casting. Reproduced from Mohammed et al., 2019 [237]. 74

Figure 2.17: XRD patterns for Ti_2Cu and Ti_3Cu phases [161, 253]. 79

Figure 3.1: Binary Ti-Cu phase diagram, produced using ThermoCalc 2023a with the TCTI2 database. The blue and red dots indicate the compositions and heat treatments analysed within this research. 84

Figure 3.2: Low and high magnification BSE SEM images of Ti-11.5Cu (a) as cast, (b) homogenised, (c) homogenised and aged 760°C and (d) homogenised and aged 820°C and Ti-33Cu (e) as cast and (f) homogenised. 97

Figure 3.3: BSE SEM micrographs at 1000x, 2000x and 5000x magnification of (a) 11 ac, (b) 11 hom, (c) 11 AT760, (d) 11 AT820, (e) 33 ac and (f) 33 hom. 98

Figure 3.4: XRD spectra of Ti-Cu cast, and heat treated alloys, showing the presence of α-Ti and Ti_2Cu in all alloys. 99

Figure 3.5: TEM high-angle annular dark-field (HAADF) images and EDX line scans of (a) 11 ac, (b-c) 11 AT820, (d) 33 ac and (e) 33 hom. 100

Figure 3.6: Contact angle data for Ti-64 and Ti-Cu alloys (n=3). 102

Figure 3.7: Microhardness(HV0.1) data for all arc melted Ti-Cu samples. The dashed line represents the microhardness of Ti-6Al-4V (n = 5). 103

Figure 3.8: Antimicrobial analysis of Ti-Cu alloys relating to (a) S. aureus, (b) P. aeruginosa and (c) E. coli. * represents values where $p \leq 0.05$ (n=3). 104

Figure 3.9: Analysis of antimicrobial efficacy of Ti-Cu alloys against P. aeruginosa using flow cytometry (n=3). 105

Figure 3.10: Correlation between Colony Forming Units of S. aureus and the predicted amount of the antimicrobial Ti_2Cu phase through ThermoCalc 2024a with TCTI3 database using the Scheil Predictor (as cast samples) and the Lever Rule (homogenised and heat treated samples). 108

Figure 3.11: (a–b) Confocal live/dead images showing the viability of S. aureus on the surface of (a) 11 AT820 and (b) 33 ac. (c–e) SE SEM micrographs depicting S. aureus on the surfaces of (c) Ti-6Al-4V, (d) 11 AT820, and (e) 33 ac. Arrows point to the bacteria within the images. (f) High magnification SEM image showing the small proteins adhered to the surface of the 11 AT820 sample. 111

Figure 3.12: Measured protein concentration on Ti64, a blank/empty well, and 11 AT820 and 33 ac Ti-Cu alloys for (a) cell culture and (b) bacterial media (n=3). The calibration curves used to calculate the protein concentrations can be found in the Appendix. 112

Figure 3.13: Influence of alloy composition and heat treatment protocol on murine pre-osteoblast cells over seven days through fluorescent images, of live (green) and dead (red) cells. 113

Figure 3.14: Influence of alloy composition and heat treatment protocol on murine pre-osteoblast cells over seven days. (a) quantification of cell viability, (b) metabolic activity assessed via Alamar Blue assay. (n=3) 114

Figure 3.15: Image analysis of Ti-Cu alloys using MATLAB comparing the colony forming units (against S. aureus) to (a) the area covered by the Cu rich phase, (b) mean area of precipitates, (c) perimeter of precipitates, (d) major axis of precipitates, (e) minor axis of precipitates and (f) Euclidean distance of Hu moments and CFU. 116

Figure 3.16: Correlation between Colony Forming Units (CFU/mm²) against S. aureus and microstructural features of precipitates in Ti-Cu alloys with (a) the area fraction covered by the Ti_2Cu phase, (b) area of individual precipitates, (c) the perimeter of precipitates, (d) the major axis of precipitates and (e) the minor axis of precipitates. Different magnifications are represented as follows: 1000x (red triangles), 2000x (blue squares), and 5000x (black circles). 117

Figure 3.17: Contact angle data plotted in comparison to antimicrobial data against S. aureus. 119

Figure 4.1: Binary Ti-Cu phase diagram, created using ThermoCalc 2023a with TCTI2 database. Red and blue lines depict the compositions analysed in this research. 128

Figure 4.2: (a) Particle size analysis of cp-Ti and Cu powders and (b) Ti-3Cu, (c) Ti-11.5Cu and (d) Ti-33Cu powder blend SEM micrographs. Particle size analysis of cp-Ti shows a greater particle size and wider range than the Cu powder. Cu powder in images (b-d) appear brighter than Ti powder. 140

Figure 4.3:BSE SEM micrographs and EDX scans for (a) before and, (b) after ball milling Ti-11.5Cu powder and (c) before and (d) after ball milling Ti-33Cu powder. Ball milling alters the powder morphology becoming more plate-like and irregular, greater dispersion of both elements also occurs. 141

Figure 4.4: Backscatter (BSE) and Secondary electron (SE) SEM micrographs respectively of (a) and (b) Ti-11.5Cu and (c) and (d) Ti-33Cu pressed samples. SE images show the irregularity of the surface topography. 142

Figure 4.5: Build plate pictures of (a) Ti-3Cu, (b) Ti-11.5Cu, (c) and (d) Ti-33Cu. Ti-33Cu build showed large amount of defects with 6 of the 15 cubes having to be supressed due to recoater interference. 144

Figure 4.6: (a) Archimedes Density measurements of cp-Ti, Ti-3Cu and Ti-11.5Cu alloys over varying laser energy densities. Contour plots identifying how the Archimedes density varies with laser power and scan speed for (b) cp-Ti,(c) Ti-3Cu and (d) Ti-11.5Cu. 145

Figure 4.7:Backscatter SEM micrographs of additively manufactured cp-Ti. Each sample is labelled with laser energy density. Keyhole defects were present in all samples with laser energy densities above 333Jm^{-1}. 147

Figure 4.8: Backscatter SEM micrographs of additively manufactured Ti-3Cu. Each sample is labelled with laser energy density. Keyhole defects were present in all samples with laser energy densities above 375 Jm^{-1}. Some heterogeneity and Cu rich areas are present in the lowest laser energy density parameters. 149

Figure 4.9: Backscatter SEM micrographs of additively manufactured Ti-11.5Cu. Each sample is labelled with laser energy density. High amounts of keyholing and cracking were present across the parameter range. 151

Figure 4.10: Low and high magnification BSE SEM images of (a) Ti-3Cu and (b) Ti-11.5Cu. (c) XRD patterns for Ti-3Cu and Ti-11.5Cu. 152

Figure 4.11: ICP-OES results for Ti-Cu additively manufactured samples in 0.9 % NaCl solution for up to seven days (n=3). No ion release was detected for Ti-3Cu alloys, but a constant rate of release was detected for Ti-11.5Cu over the 7 day time period. 153

Figure 4.12: Images of water droplets on (a) Ti64,(b) Ti-3Cu and (c) Ti-11.5Cu surfaces. (d) the contact angle measured on each surface. 154

Figure 4.13: Microhardness(HV0.1) data after loading with a 100g force for both additively manufactured Ti-Cu samples (n = 5). The dashed line represents the microhardness of Ti-6Al-4V. 155

Figure 4.14: Antimicrobial analysis of Ti-Cu alloys relating to a) S. aureus and b) E. coli (n=3). * represents values where $p \leq 0.05$. 156

Figure 4.15: Protein adsorption on different metal AM alloys and an empty well (blank) with (a) cell media and (b) bacterial media. 157

Figure 4.16: Fluorescent images of live (green) and dead (red) cells, demonstrating the influence of alloy composition and heat treatment protocol on murine pre-osteoblast cells over seven days. 158

Figure 4.17: (a) Quantification of cell viability from images in Figure 4.16 and (b) metabolic activity assessed via Alamar Blue assay.(n=3) 159

Figure 5.1: Ti-Mo binary phase diagram. The red line depicts the Ti-Mo composition studied in this chapter, due to the lower beta-transus temperature. Adapted from Zhang et al. [206]. ... 170

Figure 5.2: Melting and boiling point ranges of metal elements, showing the lack of overlap between elements, such as Mo and Cu, highlighting potential processing issues[314-320].. 171

Figure 5.3: Isothermal Ti-Mo-Cu phase diagram at 950 °C, created using ThermoCalc 2023a with TCTI2 database. The blue marks represent the Ti-Mo-3Cu phase composition, whereas the purple mark identifies the Ti-Mo-11.5Cu composition. 172

Figure 5.4: BSE SEM micrographs of Ti-Mo powder. Red arrows indicate the titanium powder, whereas blue arrows show the fine cuboidal Mo powder. 183

Figure 5.5: Build process images of (a) Ti-21.5Mo and (b) Ti-Mo-3Cu, illustrating short-spreading issues due to the poor spreadability of Mo in the powder blend. 184

Figure 5.6: Archimedes density graphs. (a) Archimedes density against laser energy density. (b-d) Contour plots depicting density by scan speed and laser power of (b) Ti-21.5Mo, (c) Ti-Mo-3Cu and (d) Ti-Mo-11.5Cu. The white region in (d) is due to the removal of cube 12 data due to short spreading skewing results. 185

Figure 5.7: Backscatter SEM micrographs of additively manufactured Ti-21.5Mo. Each sample is labelled with laser energy density. A large number of defects are present across all specimens with low laser energies resulting in lack of fusion defects, and the high laser energy densities causing keyhole defects. Excessive short spreading defects are seen in the specimen manufactured at 200 W and 2000 mms^{-1}. 186

Figure 5.8: Backscatter SEM micrographs of additively manufactured Ti-Mo-3Cu. Each sample is labelled with laser energy density. Mo particles have been trapped in the Ti matrix with minimal diffusion across all parameters. Keyhole defects are present at 400 Jm^{-1}. 188

Figure 5.9: Backscatter SEM micrographs of additively manufactured Ti-Mo-11.5Cu. Each sample is labelled with laser energy density. Keyhole defects are present at the highest laser energy density, with large levels of cracking within 5 of the cubes. Short spreading is present in the 200 W and 2000 mms^{-1} specimen, caused by poor powder flowability. 190

Figure 5.10: SEM micrograph at x1000 magnification of Ti-21.5Mo. Ti matrix and entrapped partially melted Mo powder particles can be observed. 191

Figure 5.11: SEM micrographs of (a) Ti-Mo-3Cu and (b) Ti-Mo-11.5Cu. Large amounts of heterogeneity is present across both samples, particularly with increase of Cu content. 192

Figure 5.12: BSE SEM and EDX maps at x1000 magnification at Ti-21.5Mo specimens as built and after 2,4 and 6 hours heat treatment. The progression of Mo diffusion can be clearly seen with increase of time as the Mo particles become less defined, and more dispersed in the Ti-matrix. 193

Figure 5.13: (a) Particles per unit area and (b) Mean particle size for each time step of heat treatment of the Ti-21.5Mo specimens. A clear reduction in number of particles and a minor reduction in particle size is apparent with increase in time. 194

Figure 5.14: SEM micrographs of Ti-Cu and Ti-Mo-Cu specimens at x1000 magnification showing the impact of heat treatment at 950°C for 6 and 24 hours. Ti-3Cu specimens see the segregation of Cu to grain boundaries, whilst Ti-11.5Cu specimens see an increase in homogeneity with formation of Cu-rich phase precipitates, similar to those seen in the cast samples. Ti-Mo-Cu alloys see homogenisation of the Ti-matrix with indication of Mo diffusion, but Ti-Mo-11.5Cu shows signs of formation of a liquidous phase during heat treatment. 196

Figure 5.15: Microhardness (HV0.1) data after loading with a 100g force, for both binary Ti-Cu and ternary Ti-Mo-Cu samples, as built and heat treated (n = 5). The dashed line represents the microhardness of Ti-6Al-4V. Heat treatment led to a decrease in hardness for all alloy compositions except Ti-Mo-11.5Cu. 198

Figure 5.16: Antimicrobial data for Ti-Cu and Ti-Mo-Cu as built and heat treated samples against S. aureus (n=3). Antimicrobial efficacy increases with increase of Cu content in the binary specimen, and 100 % efficacy achieved by all Ti-Mo-Cu samples.....199

Figure A.1: Graphs representing Hu moments (ϕ1-7) against CFU. Error bar from 11 ac shows the variation in morphology of the Ti_2Cu precipitates 249

List of Tables

Table 2.1: Classification of PJIs, relating to the route of infections and onset of symptoms [82]. 42

Table 2.2: Summary of element groups and corresponding effect on cells. 52

Table 2.3: The variations in methods and experimental conditions in analysis of Ti-Cu antimicrobial efficacy. 62

Table 2.4: Summary of Ti-Cu compositions analysed throughout literature in relation to the method of antimicrobial testing, bacteria and the method of manufacture of the samples. 76

Table 3.1: Ti-Cu alloy compositions and heat treatment protocols. 87

Table 3.2: Polishing and grinding sequences for alloy preparation with the Struers Tegramin-25. 88

Table 3.3:Microstructural features of Ti-Cu alloys, describing the area covered by Ti_2Cu phase and precipitate characteristics, extracted from BSE micrographs at x1000, x2000 and x5000 magnification. 107

Table 3.4:Average Hu moments (ϕ_{1-7}) of each Ti-Cu alloy and standard deviation, calculated from micrograph taken at x1000 magnification. 109

Table 4.1: Ti-Cu alloy compositions..... 129

Table 4.2: Set build parameters maintained across all PBF-LB builds on the RenAM 500S. 131

Table 4.3:Summary of all specimens manufactured during the parametric studies. 132

Table 4.4: Optimised processing parameters for Ti-3Cu and Ti-11.5Cu compositions..... 133

Table 4.5: Polishing and grinding sequences for alloy preparation with the Struers Tegramin-25. 134

Table 5.1: Ti-Cu and Ti-Mo-Cu alloy compositions in weight and atomic percentage, to 1 decimal place. 174

Table 5.2: Set build parameters maintained across all PBF-LB builds on the RenAM 500S. 176

Table 5.3:Summary of all specimens manufactured during the parametric studies for both Ti-Mo and Ti-Mo-Cu builds. 177

Table 5.4: Optimised processing parameters for Ti-21.5Mo, Ti-Mo-3Cu and Ti-Mo-11.5Cu compositions. 178

Table 5.5: Polishing and grinding sequences for alloy preparation with the Struers Tegramin-25. 180

List of Abbreviations

AM	Additive manufacturing
AMR	Antimicrobial Resistance
BCA	Bicinchoninic Acid
BCC	Body Centre Cubic
BSE	Backscattered Electron
CA	Contact Angle
CAD	Computer Aided Design
CALPHAD	CALculation of PHAse Diagrams
CFU	Colony Forming Units
cp-Ti	Commercially pure titanium
DED	Direct Energy Deposition
DMEM	Dulbecco's Modified Eagle Medium
DB-FIB	Dual Beam- Focussed Ion Beam
DPBS	Dulbecco's Phosphate-Buffered Saline
E. coli	*Escherichia Coli*
EBSD	Electron Backscattered Diffraction
EDM	Electro-Discharge Machining
EDX	Energy Dispersive Spectroscopy
EM	Electron Microscopy

EPS	Extracellular Polymeric Substances
FSC-A	Forward Scatter - Area
HAADF	High Angle Annular Dark Field
HCP	Hexagonal Close Packed
ICP-OES	Inductively Coupled Plasma Optical Emission Spectroscopy
MBC	Minimum Bacterial Concentration
MH	Mueller Hinton
MIC	Minimum Inhibitory Concentration
MRSA	Methicillin- resistant *Staphylococcus aureus*
MSC	Mesenchymal Stem Cells
P. aeruginosa	*Pseudomonas Aeruginosa*
PBF	Powder Bed Fusion
PBF-LB	Laser Beam Powder Bed Fusion
PI	Propidium Iodide
PJI	Prosthetic Joint Infection
PM	Powder Metallurgy
PPI	Periprosthetic Infection
QS	Quorum Sensing
RBV	Reduced Build Volume
ROS	Reactive Oxygen Species
S. aureus	*Staphylococcus Aureus*

SE	Secondary Electron
SEM	Scanning Electron Microscopy
SLM	Selective Laser Melting
SPS	Spark Plasma Sintering
SSC-A	Side Scattered - Area
STEM-XEDS	Scanning Transmission Electron Microscopy
TEM	Transmission Electron Microscopy
THA	Total Hip Arthroplasty
TJA	Total Joint Arthroplasty
TKA	Total Knee Arthroplasty
XRD	X-ray Diffraction

Chapter 1

Introduction

1. Introduction

Metallic devices are widely used to reconstruct hard tissues, equating to 70-80 % of biomedical implants globally [1-4]. Specifically, orthopaedic implants serve various purposes, including reconstructive devices, fracture stabilisation and joint replacements [5]. Total joint arthroplasties (TJA) are procedures to treat pain and limitations in joints, often associated with severe osteoarthritis [6]. A variety of joint replacements are available, including hip, knee, ankle, and shoulder arthroplasties [5].

Metal prosthetics are rapidly increasing in demand, with hip and knee replacement surgeries accounting for 117,000 surgical procedures in the UK every year [7]. A US study has also predicted that primary total knee (TKA) and hip (THA) arthroplasties will increase by 401 % and 284 % respectively by 2040, compared to 2014 figures [6]. The demand increase can be correlated to ageing populations and increases in obesity, resulting in higher demand for implants in younger age groups [7]. Figure 1.1 depicts the annual growth in the USA in THA and TKA cases and breakdown by age group in the period from 2020 to 2040 [6]. This reflects a shift towards younger, more active patients seeking a faster recovery and advanced technology [8].

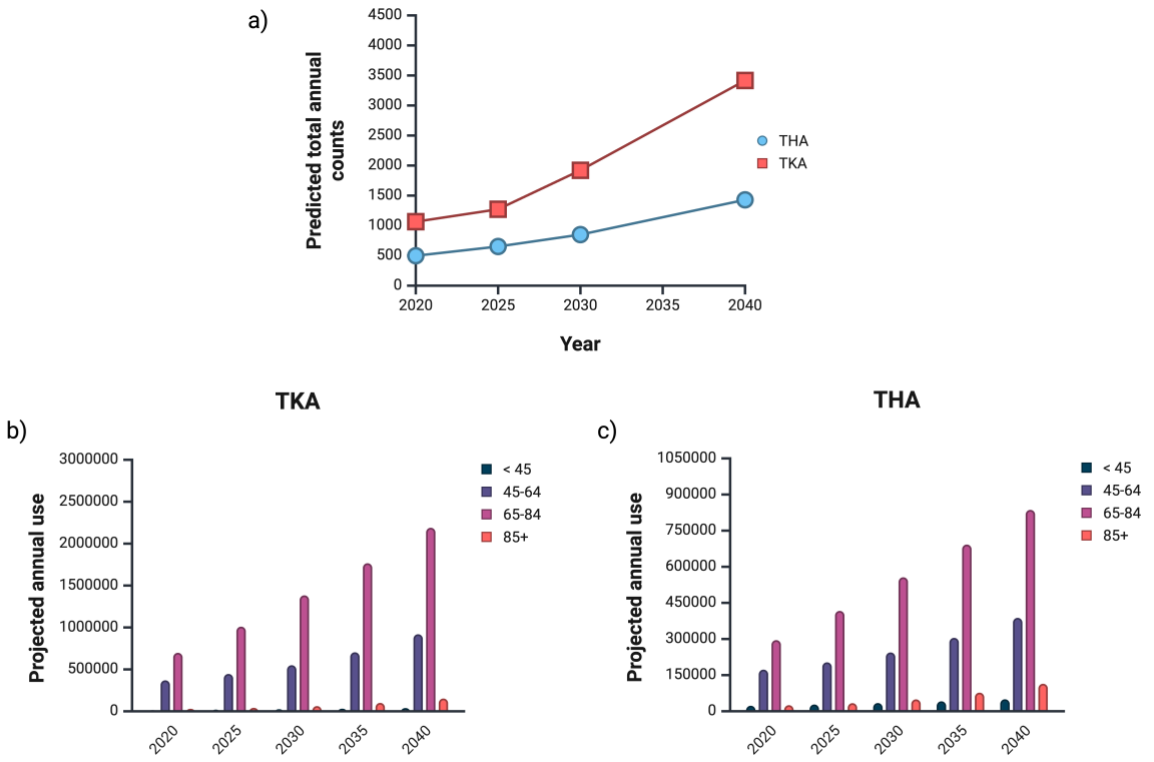

Figure 1.1: (a) Predicted total annual counts for primary THA/TKA use from 2020-2040 in the United States (in thousands). (b) Projected annual use of primary total knee arthroplasty (TKA) in the United States by age. (c) Projected annual use of primary total hip arthroplasty (THA) in the United States by age. Data extracted from Singh et al. [6].

While the complication rate of these procedures is low (5.1 % for THA and 6.9 % for TKA) several clinical challenges persist and may intensify with the growing prevalence of age- and obesity-related comorbidities [9-11]. For example, compared to 2005 figures, revision THA procedures are expected to have increased by 137 % by 2030 [12]. Furthermore, the impact of these complications has a subsequent negative effect on patient quality of life as well as high monetary cost to the health service and loss of economic contribution. Broadly there are three key clinical concerns: infection, challenges regarding osseointegration, and the mechanical incompatibility of most alloys with the surrounding bone. Beyond the initial debilitation from these associated risks, implant revision procedures are generally more expensive than the initial

surgery and further elevate the risk of infection and surgical complications. In particular, Klouche *et al.* estimate the cost of treatment for an infected hip arthroplasty is 2.6 times greater than the cost of an aseptic revision, and 3.6 times larger than a primary THA [13].

These three discussed challenges are all determined by the interaction between the implant material and native tissue. The majority of orthopaedic implants are currently fabricated from either titanium (Ti) or cobalt-chromium (Co-Cr) based alloys, as they provide durability, strength, corrosion resistance and a low immune response [14, 15]. For orthopaedic implants, osseointegration, or the integration with the surrounding bone, is crucial for load-bearing stability [16]. Clinical success of an implant depends on both initial and long-term fixation [17]. Variations in the mechanical properties between bone and the implant, particularly in load-bearing implants, can cause stress shielding and implant loosening [7, 18]. Aseptic loosening has been found to be the number one cause of failure in total hip arthroplasties (23.19 %), followed by instability (22.43 %) [12]. Materials such as stainless steel have an extremely high stiffness, approximately ten times greater than bone, and thus can cause such effects. Consequently, this is a key material characteristic that needs to be monitored during the alloy design process [19].

However, one of the biggest challenges to implants is the fine balance between encouraging cell adhesion for osseointegration, whilst reducing bacterial adhesion [7]. Infections accounted for the third highest causes of failures of THA (22.13 %) [12]. These infections are typically difficult to treat due to the formation of bacterial biofilms, which often reduce the efficacy of antibiotics through a range of mechanisms [20-22]. Though treatment of prosthetic joint infections (PJIs) is successful in the majority of cases, there is a severe negative impact on patients. The average hospital stays for infected patients requiring revisions rises from 7 to 30 days, more than quadrupling the typical length [13]. With infection rates ranging from 1 to 2

% in primary procedures and cases increasing due to the ageing population, tackling implant associated infections remains a key concern for researchers [23].

Given the significant holistic impact of implant infection, the aim of this research is to develop an inherently antimicrobial Ti-alloy through incorporation of an antimicrobial element, namely copper. Novelty and contribution to knowledge is gained through relating observed antimicrobial efficacy with specific Ti-Cu phases and microstructural features (Chapter 3). Furthermore, the opportunity to amplify these relationships through changing heat treatment protocols (Chapter 3) and switching to production via additive manufacturing (Chapter 4) were explored alongside incorporation of molybdenum to refine mechanical properties (Chapter 5).

1.1. Objectives

To achieve the overarching aim of producing an antimicrobial Ti-based alloy the following specific objectives were defined:

1. To investigate the influence of alloy microstructure on the antimicrobial performance of Ti-Cu systems.
2. To fabricate Ti–Cu alloys using various manufacturing techniques aimed at enhancing antimicrobial efficacy.
3. To elucidate the mode of antimicrobial action of Ti-Cu alloys against clinically relevant bacteria.
4. To characterise the physical, mechanical and surface properties of the Ti-Cu alloys and assess their cytocompatibility.
5. To produce a titanium-based ternary alloy with optimised properties that have refined the mechanical properties for orthopaedic implants.

1.2. Thesis Outline

Moving forward from the research overview presented in this chapter, Chapter 2 presents a comprehensive review of the relevant literature. This has been divided into six sections considering the background to metal implants, followed by a discussion of current strategies for implant associated infections. The chapter then explores the growing concern of antimicrobial resistance, which emphasises the need for alternative approaches. Ti-Cu alloys are then proposed as a promising antimicrobial material system and subsequently an examination of various manufacturing and characterisation methods to support alloy discovery are discussed.

Chapter 3 presents research demonstrating the role of microstructure in arc-melted Ti-Cu compositions on their antimicrobial efficacy. While Chapter 4 determines the impact of manufacturing method on Ti-Cu antimicrobial efficacy, focussing on the influence of additive manufacturing through rapid heating and cooling rates leading to fundamentally different microstructures compared with the equivalent cast compositions. In an effort to refine the mechanical performance for use within orthopaedic implants, Chapter 5 explores ternary alloy compositions of Ti-Mo-Cu.

CHAPTER 2

LITERATURE REVIEW

2. Literature Review

Infections are well documented problems of metal implants, which traditionally are treated by antibiotics or in worst cases result in revision surgeries. Alternative methods to prevent bacterial adhesion and infections of these implants are necessary. Herein follows a literature review of the current state of knowledge of biomedical alloys for orthopaedic implants and infection treatment methods.

2.1. Background to Metal Implants

2.1.1. Titanium Based Alloys: Current Materials and Developments

The material fabricating the orthopaedic implant is pivotal in determining their various characteristics and functionality. An ideal biomaterial for load-bearing orthopaedic implants exhibits sufficient mechanical strength, good wear resistance, modulus which matches that of the surrounding bone, and low density [24]. Crucially, above all, the material must be biocompatible, triggering no adverse tissue responses [25].

Metallic biomaterials commonly used as orthopaedic implants include stainless steels, cobalt-chromium (Co-Cr), and titanium (Ti)-based alloys [4]. Among these, Ti and its alloys are the most widely utilised for implants, owing to their biocompatibility, corrosion resistance, high wear resistance and formation of its stable oxide layer enabling it to be used as a bioinert alloying element [14, 26, 27]. Despite their critical importance and significant market size ($45.3Bn in 2021 [28]), the number of Ti alloy compositions employed remains remarkably limited. Although precise data on the alloys used by manufacturers is not available, ASTM standards for surgical implants include only seven different compositions [29-35]. From these, most Ti implants are either grade 2 commercially pure titanium (cp-Ti) or the grade 5 alloy Ti-

6Al-4V. Notably, these Ti-based biomaterials, despite their extensive use in biomedical applications, were originally developed for the aerospace industry as structural materials, rather than optimised for biological compatibility. Consequently, they may present toxic or otherwise undesirable biological effects. Figure 2.1 depicts a timeline of Ti-based alloy development and their adoption dates as well as their usages.

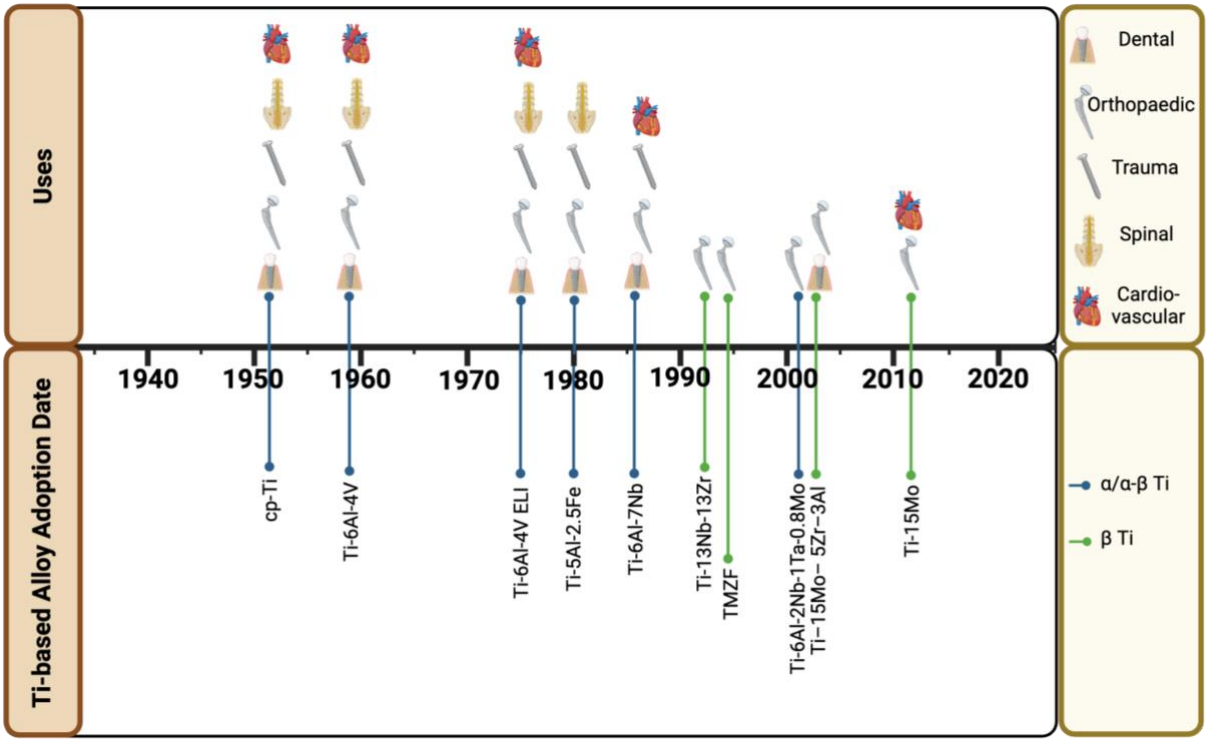

Figure 2.1: Ti-based alloys according to their adoption date and form (α/α-β and β-Ti), as well as their usage [36-47].

Ti-based alloys can be produced in three forms: alpha (α), beta (β) and alpha + beta (α+β). Figure 2.2 depicts the crystal structures of alpha and beta – titanium. Commercially pure Ti (cp-Ti) consists of the α phase, also referred to as hexagonal close packed (HCP) crystal structure, though due to its low tensile strength it is not suitable for load-bearing applications. Whereas β-Ti consists of a body centred cubic (BCC) phase. α+β alloys are more widely utilised as traumatology and load-bearing implants, with Ti-6Al-4V being the most popular of these implant materials [48, 49]. Ti-6Al-4V has high yield strength at room temperatures and

allows good osseointegration through rapid TiO_2/OH formation producing extracellular-like nanotopology on its surface, resulting in cell adhesion [49, 50]. However, there have been concerns raised over the cytotoxicity of the vanadium in Ti-6Al-4V, thus limiting the applications of the material [51]. Furthermore, the modulus of Ti-6Al-4V (approximately 110 GPa) is far greater than that of bone (around 10-40 GPa), which can trigger stress shielding effects, consequently resulting in implant failure [24]. Stress shielding occurs when the implant itself takes the load, reducing the stress on the bone. This may result in reduction of bone density around the implant, which in turn can instigate implant loosening [7, 18, 52]

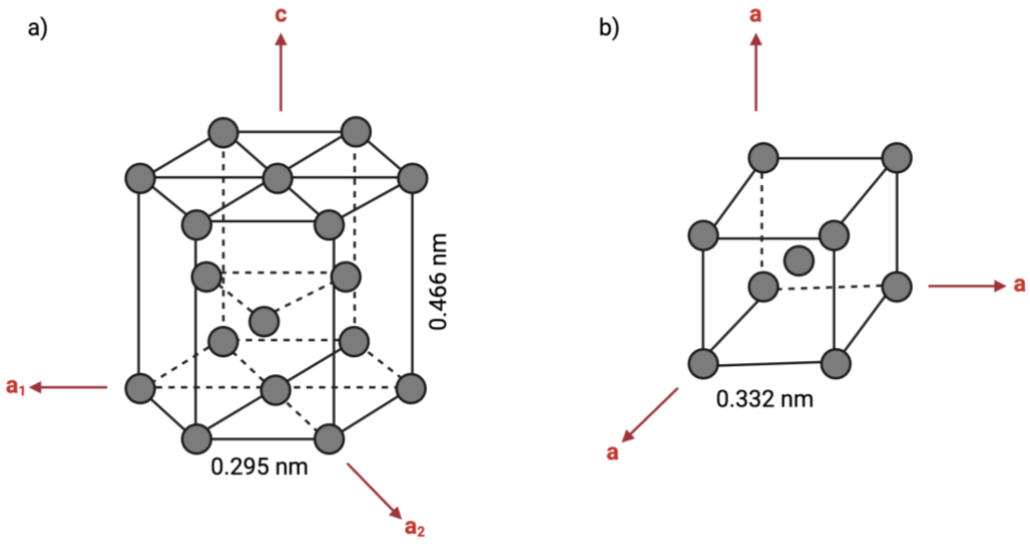

Figure 2.2: (a) Alpha and (b) beta crystal structures of titanium. Adapted from Banerjee et al.[53].

β-Ti alloys are considered the optimal materials for implant applications, due to their increased strength, ease of formability and enhanced corrosion resistance compared to α- Ti [54, 55]. Furthermore, a considerably lower elastic modulus (around 20 % reduction) is achieved by β-Ti alloys rather than the α phase, more closely matching that of bone and improving mechanical properties in comparison to Ti-6Al-4V [5, 24]. Typically, heat treatments above 883 °C are required to induce the phase transition from the α into the β phase [56]. However, the β phase can also be achieved using stabilising elements, resulting in small volumes of martensitic or

athermal phases, subject to compositions [57, 58]. Figure 2.3 shows how a titanium-based alloy phase diagram can be altered dependent on different alloying elements.

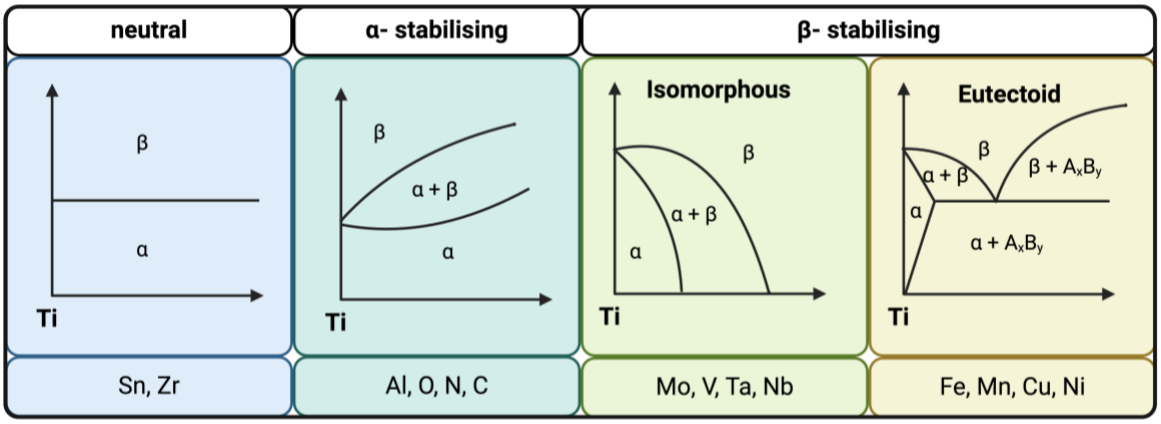

Figure 2.3: Different categories of titanium phase diagrams depending on the alloying elements.

There are two types of β stabilisers, eutectoid or isomorphous. Isomorphous stabilisers include V, Ta, Nb and Mo, and dissolve completely in the β-phase. Whereas eutectoid stabilisers include elements such as Cu, Cr, Mn and Co, which form intermetallic phases due to their limited solubility in β-Ti [59, 60]. The amount of a stabiliser dictates whether the resulting alloy will be stable or metastable. One measure of stability is molybdenum equivalency, which is used to assess the amount of a stabilising element required to prevent martensitic transformation during quenching. It is stated as a ratio of a given stabiliser in relation to the amount of molybdenum required for the same amount of stabilisation, typically around 10 % is required [60].

Whilst these traditionally utilised Ti-based materials perform well *in vivo*, there remain some concerns around their use as a biomaterial [51]. The growing uptake and increasing residency time of these implants has raised questions around the long-term impact of alloying elements within the body. It has been shown that V is released from even well-functioning Ti-6Al-4V implants and can be detected in blood, serum, and urine [61]. Likewise it is suggested that ionic

vanadium may also be released in to the body from the surface oxide layer [62] and that metal ion release similar to that from a Ti-6Al-4V implant may inhibit normal cell differentiation [63]. The precise mechanisms and severity of V toxicity, particularly in concentrations associated with Ti-6Al-4V release, remain an area of debate within literature. Nevertheless, V has been associated with a variety of toxic effects including haematological, biochemical, neurobehavioral, and reproductive [64, 65]. *In vitro* studies using rodent cells have specifically shown cytotoxic behaviour and suggest that citrate, lactate, and chloride found in blood plasma may assist the release of vanadium ions whereby it bonds with human serum albumin enabling cell uptake [62].

Concerns have also been raised regarding the release of aluminium either directly from the surface oxide layer or because of fretting [66, 67]. Elevated Al levels have been detected in patients following hip implantation [68] and shown to be released in ionic form from surface oxides when exposed to chemical species within the body [66]. Some studies have suggested that the Al is reintegrated locally into bone [69, 70], although the long-term implications of this have not been reported. Overall the impacts and concerns around V and Al highlight a need for Ti-based biomedical alloys to be designed specifically for performance within the intended biological environment [71].

Due to concerns about V and Al as stabilising elements, there has been much research conducted with the aim of developing new biomedical Ti-based alloys that maintain the α+β microstructure and mechanical properties of Ti-6Al-4V. The general approach has been to substitute the phase stabilising elements with those considered more 'biocompatible'. β stabilising elements such as niobium and tantalum [72] are typically selected to replace vanadium. Both show excellent *in vitro* performance, similar to that of titanium, for cell proliferation [73]. *In vivo* testing in a rodent model has demonstrated low inflammatory

response and undetectable dissolution of both Nb and Ta in the surrounding tissue and surprisingly a significantly greater increase in new bone formation compared with titanium [74]. Zirconium does not affect the relative stability of the α and β phases, but has been used as a substitute for aluminium to provide general solid solution strengthening of the α phase [72]. Zirconium also shows good biocompatibility [73], without the broader medical concerns of aluminium.

Most notably, this approach of element substitution resulted in the development of Ti-6Al-7Nb (ASTM F1296 [32]). Compared to Ti-6Al-4V, the two alloys perform similarly in yield strength (Ti-6Al-4V ELI: 795-875 MPa; Ti-6Al-7Nb: 880-950 MPa), ductility (Ti-6Al-4V ELI: 10-15 %; Ti-6Al-7Nb: 8.1-15 %), and elastic modulus (Ti-6Al-4V ELI: 101-110 GPa; Ti-6Al-7Nb: 114 GPa) [75]. Both also show similar corrosion [76] and metal release profiles in relevant media [77], however Ti-6Al-7Nb exhibits reduced toxicity demonstrated by cell attachment, proliferation, and viability [78]. A number of alloys with composition of Ti-15Zr-4Nb-4Ta or similar have also been investigated and show comparable mechanical properties (Ti-15Zr-4Nb-4Ta-0.2Pd) [75], low metal release [77], marginally reduced cytotoxicity, and improved *in vivo* tissue growth [79] compared with Ti-6Al-4V. However, Ti-6Al-4V currently remains the gold standard for implant materials due to its proven clinical track record, good mechanical properties and ease of manufacturing. Nevertheless, much research focusses on the further development of Ti-based alloys to combat the clinical challenges faced.

2.1.2. Clinical Challenges

Implants often fail due to a combination of mechanisms and effects (Figure 2.4), often determined by their design and means of fixation. Implant wear can cause debris to be released into the body, causing implant instability and potential systemic effects. Though these particles typically remain in the surrounding tissues, they have been located in the serum and urine of

patients suffering from implant failure. TJA can also cause differences in the load transmission within a joint, potentially causing stress shielding and hence failure of the implant. This stress shielding is often exacerbated by the differences in mechanical properties of the implant in relation to bone. Furthermore, repetitive loading can also cause the implant to become damaged and eventually fatigue, resulting in a poor bond between the implant and bone [17]. Fibrous encapsulation is another concern due to excessive micromovement of the implant at the bone interface due to poor bonding [4].

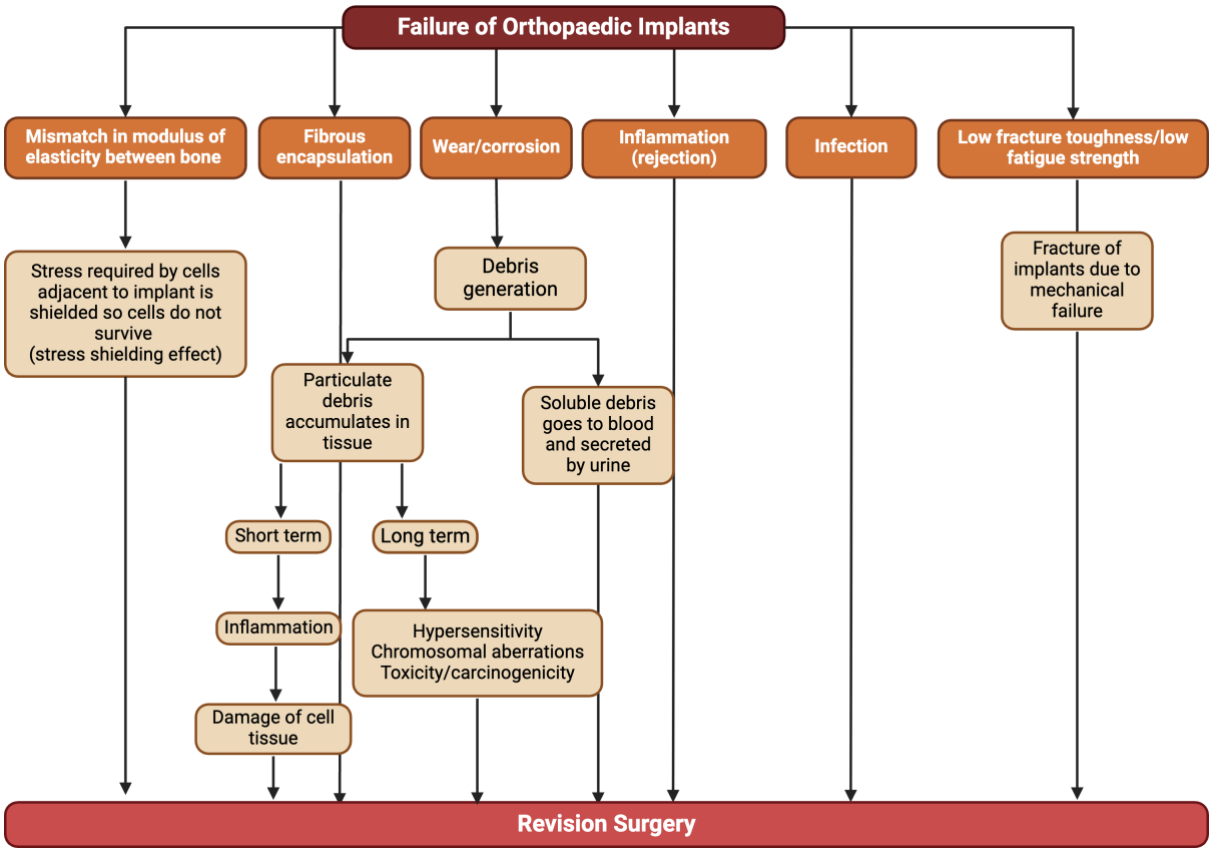

Figure 2.4: Mechanisms of implant failure. Adapted from Li et al. [4].

Infections are the third biggest cause of failure in implants [12]. With increasing global prevalence of patients with comorbidities such as diabetes, that make them especially vulnerable, management of orthopaedic implant infection is critical [17]. Most common bone tissue infections resulting from orthopaedic surgeries include osteomyelitis (infection of the

bone marrow), septic arthritis and prosthetic joint infections (PJIs). The incidence of PJIs ranges from between 1 and 2 % in primary procedures [23]. Though rates increase by 2.6 times in patients with rheumatoid arthritis, compared to osteoarthritic patients, and increased to 7 % in diabetic patients [80]. There are three routes of these infections, hematogenous (resulting from bacteria present in the blood), contiguous (transmission from local tissue) or direct (stemming from permeation of bone, either from injury, surgery or implantation). Though PJI occur in less than 1 % of hip and shoulder protheses, they are prevalent in up to 9 % of patients with elbow protheses [81]. Whilst PJIs occur less frequently than aseptic failures, they do represent one of the most devastating complications [82]. Furthermore, rates of PJIs increased by 53.4 % between 2006 and 2014 in primary total knee arthroplasties, requiring revision surgeries. These rates are expected to climb by a further 170 % by 2030 [83]. Therapies are complicated, therefore increasing hospitalisations, morbidity and mortality [82].

Typical rates of PJIs such as total hip or knee arthroplasties occur in 1.5-2.5 % of primary cases, whereas revision surgeries carry increased risks of 3.2- 5.6 %. Furthermore, these infection rates increase further for other orthopaedic devices such as elbow protheses, with rates rising to around 9 % within the first two years post-surgery. However, infection rates are substantially increased further in surgical revisions, by up to 40 % prevalence [82]. The incidence of prosthetic joint infections still lies at about 1 % of total joint replacements, though periprosthetic infections (PPI) correspond to 22 % of revision surgeries for orthopaedics and approximately 30 % of craniomaxillofacial revisions [7, 84]. Furthermore, PPI is one of the leading causes of morbidity in relation to TJA, with approximations of the mortality rate lying between 2.7 and 18 % [85]. Much progress has occurred in the eradication of implant-associated infections; with the infection rate continuously decreasing over the past 50 years [82]. Nevertheless, due to the ageing population, increasing trauma rates and increased use of

protheses and bone fixation devices, the prevalence of bone and joint infections are increasing [9, 82, 86].

Classification of the infection is summarised in Table 2.1, relating to the route of infection and the onset of symptoms.

Table 2.1: Classification of PJIs, relating to the route of infections and onset of symptoms [82].

	Classification	Characteristic
Route of infection	Perioperative	Inoculation during the surgery or immediately afterwards
	Hematogenous	Through the blood or lymph spread
	Contiguous	From an adjacent focus of infection
Relating to the inception of symptoms	Early (<3 months)	Acquired during the surgery or in the following 2-4 days (caused by very virulent organisms)
	Delayed/low-grade (3-24 months)	Obtained during the surgery and caused by less virulent organisms
	Late (>24 months)	Caused by hematogenous seeding from remote infections

2.1.3. Fundamentals of Bacterial Colonisation and Biofilm Formation

Once a medical device has been implanted, an active competition between native tissue and pathogens to integrate on the surface takes place. If host cells establish on the surface first, any potential microorganism will find a cell layer with a functional immune system that can counteract bacterial adhesion and proliferation [87, 88]. In contrast, once bacteria attach to a surface they develop a highly complex community, resulting in a three-dimensional aggregation of cells surrounded by a protective layer of extracellular polymeric substances

(EPS). This biofilm raises the ability of microorganisms to tolerate antimicrobial substances a hundred fold, complicating their treatment and resulting in a positive vector for antimicrobial resistance (AMR) development [89]. When considering strategies to prevent implant infection, understanding these early stages of bacterial mass transfer, attachment, proliferation, and biofilm formation are key. A prospective novel antimicrobial alloy should therefore be capable of modulating and preventing these fundamental bacterial interactions.

After the microorganisms have adhered to the surface, the bacterial cells will proliferate in an accumulation phase, firstly by the creation of microcolonies that will expand to form macrocolonies enclosed in a rich EPS matrix (Figure 2.5). This layer is composed of polysaccharides, nucleic acids, proteins and lipids, and acts as a protective barrier while facilitating nutrient capture and dissemination [90-92]. More relevant is the coordinated effort to regulate self-organisation and the overall behaviour of these cell aggregations. This mechanism is referred to as quorum sensing (QS) and is based on self-induction where an increase in population will lead to a rise in bacteria dependent molecules that, in turn, will promote changes in gene expression [93, 94]. By the effective use of QS these communities can regulate sporulation, biofilm production, conjugation, motility and virulence factors, resulting in a competitive advantage over planktonic cells [95]. These benefits continue to promote bacterial growth and biofilm maturation, however, as the population becomes larger, available nutrients and oxygen became scarce while metabolic by-products and toxic waste increases. This triggers a new QS response and secretion of molecules that reduce the structural integrity of the EPS matrix, followed by cell detachment both in the form of planktonic cells and micro-/macrocolonies [94, 96]. Thus, the matured biofilm becomes a new vector for infection of the medical device and host tissue. This is compounded by microbial cells retaining their highly resistant and adherent biofilm phenotype or, in the case of starved bacteria,

"persistent cells" that can lay dormant during prophylactic treatment, resurfacing as new pathogens once antibiotic therapy halts [97, 98].

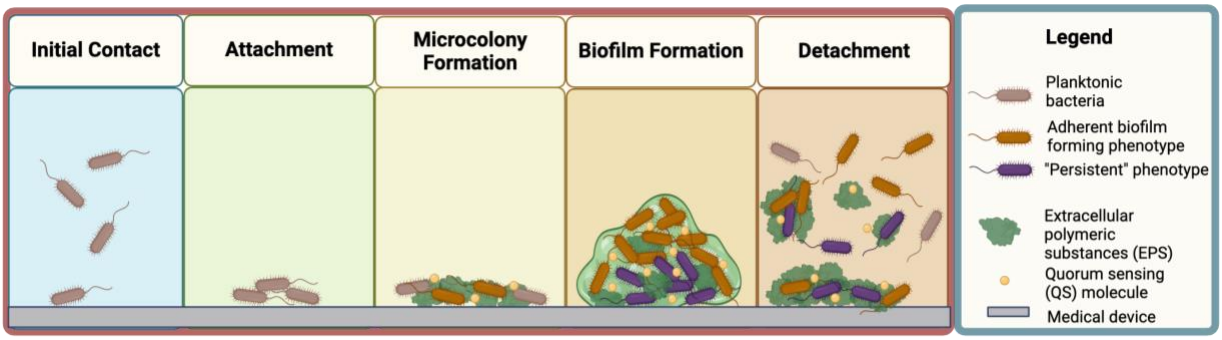

Figure 2.5: Stages of biofilm formation.

2.1.4. ***Staphylococci* Infections**

Staphylococci species are the main contributor to implant-related infections, equating to approximately 80 % of all infections. *Staphylococcus aureus* and *Staphylococcus epidermis* are the main causative agents for orthopaedic implant-based infections; accounting for two thirds of all isolated cases. Sources of bacteria are present in many places throughout the surgical procedure including within the operating room, on clothing worn by medical staff and bacteria already present on the patient's skin. More specifically, *S. aureus* is a commensal part of the flora present on human skin, however, when the cutaneous and mucous barriers are breached, severe infections can develop. Furthermore, upon adhesion to the implant surface and formation of a biofilm, a chronic infection can occur. Biofilms are formed after microbial attachment to a surface, during which an extracellular substance encapsulates the bacteria to form an extremely stable entity. Antibiotic treatments are often less efficacious towards biofilms, and so preventing their formation and reducing bacterial adhesion is critical [99].

Typically, two major infections are caused by *Staphylococcus* strains, either septic arthritis or osteomyelitis. Emergence of antimicrobial resistance (AMR) to antibiotics, such as methicillin-resistant *S. aureus* (MRSA), has resulted in increased complexity of treatments with severe

cases resulting in mortality and amputation. However, *S. epidermis* has been determined as often having more antibiotic resistance. The most common route of these bacteria are intravascular catheters [82].

2.2. Current Strategies for Managing Implant Associated Infections

There are many strategies aimed at reducing the prevalence of infections at the surgical sites, resulting in implant associated infections. The use of preventative antibiotics, both intraoperatively and postoperatively, are widely accepted as gold standard in orthopaedics. Though, duration of this prophylaxis treatment can vary between guidelines, from up to 24 or 36 hours [100]. However, scrutiny over the rise of AMR has led to WHO recommending against the practice of continuing antibiotic prophylaxis postoperatively [101].

Nevertheless, in the event that an implant associated infection occurs a range of revision surgeries are possible. These include debridement, one or two stage reimplantation or Girdlestone (total removal of prosthesis) arthroplasties, dependent on the surgery [9, 102, 103]. There are no standardised criteria to opt between one of the four options, but the type of infection, condition of the bone and soft tissue, the virulence and surgeon experience should be factors [9]. The algorithm to determine the appropriate surgical approach is depicted in Figure 2.6. A debridement approach should only be reserved for patients with stable implants and acute onset of symptoms not lasting for more than several weeks (as depicted by the red path) [9]. However, the rate of debridement success has seen to decrease linearly with time between the primary arthroplasty and PJI diagnosis [104, 105]. Thus, for those with delayed manifestation, such as 3 months after implantation, the implant should be removed even in cases with bony ingrowth. One stage revision surgeries are only appropriate for patients with minimal soft tissue damage, with failure rates between 0 and 16 % [9, 106-108]. Furthermore, if the infection was caused by a microorganism not able to be treated by a readily available oral antibiotic, one

stage revision should not be selected. This would therefore make a two stage revision surgery a more conventional option. During the first operation, device explantation occurs and a space-holder or external fixation device implanted. The duration of antimicrobial therapy is dependent on the microorganism, but typically ranges between 2 to 6 weeks, but can occasionally continue for up to 6 months. The choice of revision implant has to satisfy the demand of the patient, in terms of stability and amount of damaged bone [9]. These two-stage surgeries typically have success rates of over 90 %, typically making it the gold standard treatment for PJIs [109, 110]. In the worst case, Girdlestone procedures can occur. A Girdlestone procedure is defined by total removal of the implant in the case of hip arthroplasties, including removal of the head and neck of the femur without replacements [111]. These can be indicated due to the presence of multiple antibiotic resistant bacteria, refusal by the patient to have another operation, patients in poor health, or with inadequate bone stock [103].

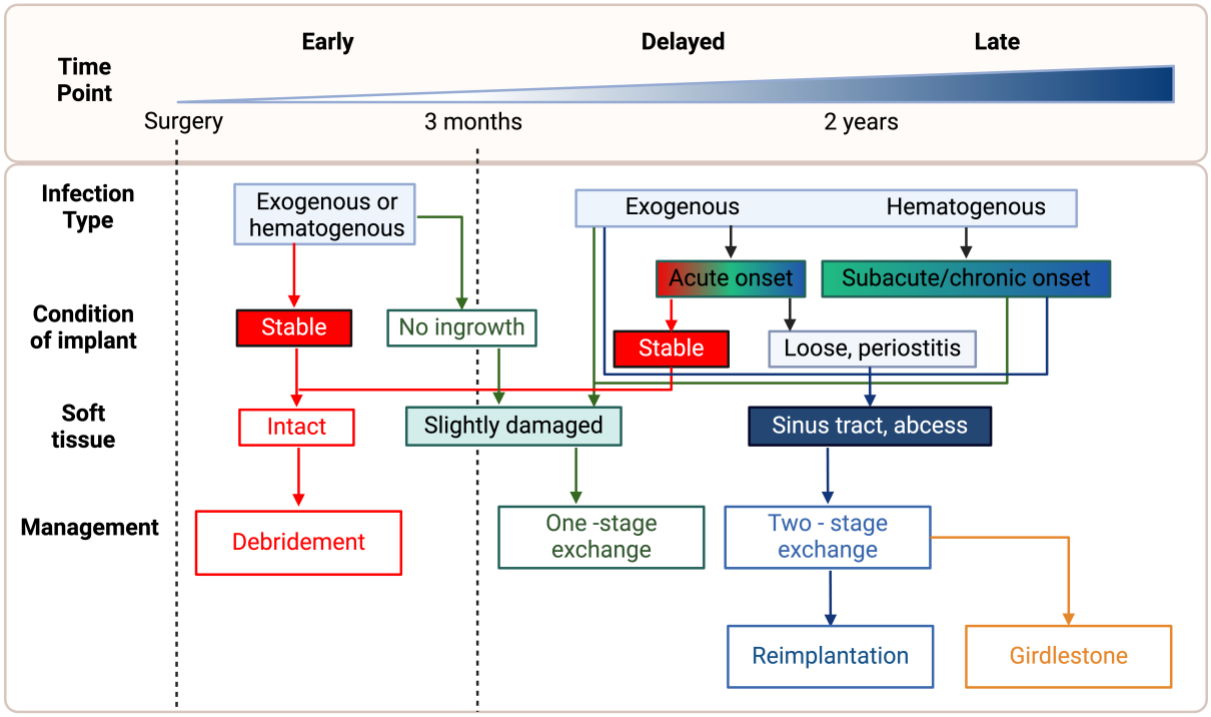

Figure 2.6: Algorithm to determine surgical approach to PJIs. Criteria include time from surgery, type of infection, condition of the implant and soft tissue, as well as the comorbidity. Figure adapted from Zimmerli et al. [9].

Although most PJIs are treatable, they significantly impact patients; extending hospital stays from 7 to 30 days and tripling revision surgery costs compared to aseptic cases[13, 112]. The increased surgery time, healthcare burden, and reduced quality of life provide grim prospects for patients, healthcare providers and implant manufacturers. This is of further concern in relation to the rise in antimicrobial resistance.

2.3. Antimicrobial Resistance

The success of current infection management options relies heavily on antibiotics. Given there is a significant rise in AMR, other methods of treatment must be discussed [113]. It is already supposed that by 2008, 50 % of deaths in Europe associated with infection were correlated to resistant bacteria, with this figure continuing to rise. It is estimated that AMR will have a

socioeconomic impact approximating to $100 trillion and 10 million people will die due to AMR annually by 2050 [89]. The WHO Global Strategy for Containment of Antimicrobial Resistance (2001) outlines the first real requirements to combat the global struggle [114]. Due to the ever-increasing problem relating to implant associated infection and antibiotic-resistant bacteria, new antimicrobial strategies must be found [89].

Bacteria possess the ability to rapidly evolve, therefore causing bacterial resistance to a vast array of pharmacological products of which new strategies cannot be produced fast enough [89]. This is not helped by a major discovery void of major classes of antibiotics between 1962 and 2000, with no successful discoveries of new generation antibiotics since 1987 [115, 116]. Figure 2.7 outlines several antimicrobial methods relating to biomaterials.

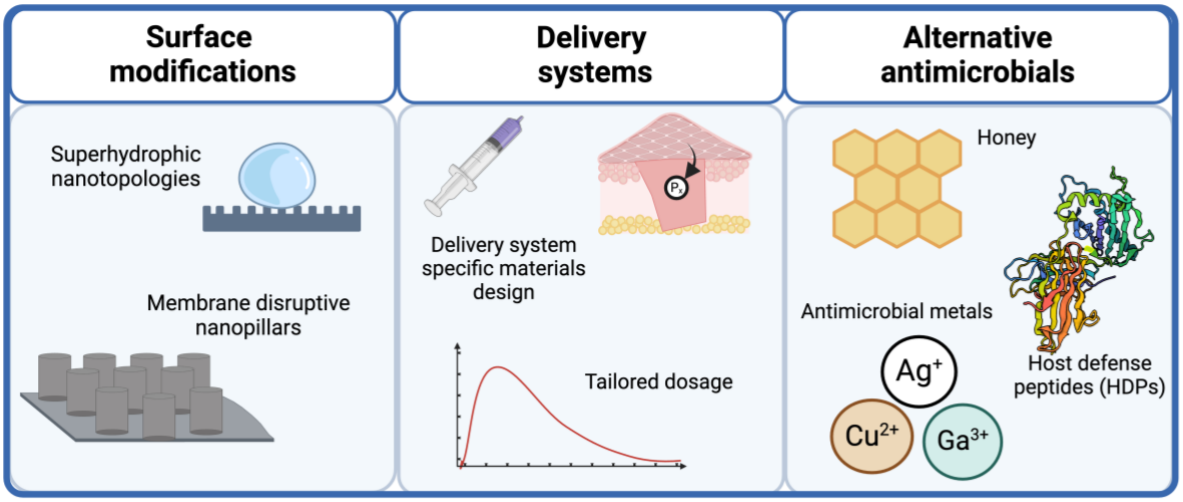

Figure 2.7: Strategies for combating the issues relating to AMR via biomaterials. Adapted from figure from Hall et al., 2020 [89].

Though there are many strategies of combatting AMR and infections, it is key to build up methods in which resistance could less likely build up. For example, conventional antibiotics work through specific modes of actions, which easily enables build-up of resistance, thus by targeting multiple cellular processes this may be circumvented. Another way to combat this is

by ensuring the antimicrobial agent is only in contact with the localised area, subsequently reducing the exposure of the rest of the microbiome [89].

2.3.1. Antimicrobial metals

Antimicrobial agents come in many forms, but the use of metal compounds as antimicrobials goes back thousands of years [113]. The first documentation dates back to 1500 BC where copper salts were used as an astringent in ancient Egypt. Though, upon discovery of antibiotics by Alexander Fleming in the 1920s, the use of metals as antimicrobials promptly declined [117]. However, with the slowing of antibiotic discovery and problems relating to AMR, the use of metals as antimicrobial agents is becoming progressively popular again [113, 117]. Many metals are known to be harmful to bacteria, for example, most commonly: Ag, Cu and Pb [118].

2.3.1.1. Mode of Action of Antimicrobial Metals

Based on the catastrophic consequences that biofilm formation can have on the medical device industry and the patient, it is paramount to develop and implement techniques that address its prevention from bacterial adhesion to biofilm maturation and cell detachment. Metallic ions possess numerous antimicrobial mechanisms specific to each element, making them effective alternatives to treat infection. Active transition metals such as As, Fe, Cu, Cr, Co, V, Te or Ni can catalyse electron transfer with metabolic by-products (e.g. H_2O_2 and O_2^-) to increase the presence of Reactive Oxygen Species (ROS) through Fenton chemistry [119, 120]. Other groups have showcased the ability of metallic ions to disrupt or destroy [4Fe-4S] protein ligands with subsequent active iron release and ROS formation [121, 122]. Moreover, ROS can arise from thiol-mediated reduction of metallic ions stemming from their affinity with sulphur

which, in turn, can result in thiol reserve depletion [123]. In contrast to ROS production, protein dysfunction can lead to cell toxicity with metallic elements reported to interact with Fe-binding sites, destroy Fe–S clusters or influence other catalytic and structural metals, e.g. Pb(II), Ni(II) or Ag(I) [124]. Other ions have showcased an ability to interfere with cell membrane structure and functions with Ag compromising the outer membrane and disrupting the electron transport chain [125, 126], or Cu and Cd affecting the integrity of cell envelopes through lipid peroxidation [127]. Cr and Ga have been linked with cell starvation due to their ability to prevent S and Fe uptake, respectively, while Mn, Cr, Co, Cd, Mo, Sb and As have been shown to promote DNA damage [124]. All these mechanisms result in a highly effective mode of action that has led to a rise in interest of harnessing metallic elements to tackle AMR through surface treatments of the base device material [128-132]. Besides the already mentioned elements, the need for greater diversity of antimicrobials and the increased risk of AMR is rapidly expanding metals explored as antimicrobial candidates, including Al, Au, Bi, Ce, Ga, Mo, Pd, Pb, Sn, Te, Tl, Zn or Zr [133-136]. Elements with established use and comparatively low toxicity, such as Ag and Cu, have become prevalent in the biomedical field, whilst those with well-established bioaccumulative toxicity such as mercury, arsenic and antimony, historically used in agriculture and medicine, have become less prevalent [124].

When metallic elements are considered from a biological perspective, they can be either fundamental to various biochemical processes or non-essential metals. Electron transfer, catalysis, cell membrane and DNA structures are only a few of the organic processes where metals are indispensable and potentially lethal to all cells in increased doses [124, 137]. On the other hand, silver (Ag), mercury (Hg) or tellurium (Te) are a few of non-indispensable metals that are extremely poisonous to a broad spectrum of organisms at relatively low concentrations [124, 138]. The ability of these elements to interfere with biological processes stems from three main properties: donor atom selectivity, reduction potential, and speciation. The ability of metal

ligands to selectively interact with specific biomolecules is conferred by a preference for donor ligands following the Irving–Williams series (Mn(II) < Fe(II) < Co(II) < Ni(II) < Cu(II) > Zn(II)) [133, 137, 139]. However, when homeostasis is altered, metals at the high end of the scale can bind to ligands requiring less competitive metals, altering protein structure and function [124]. Similarly, soft acids (e.g. Hg(II), Cu(I), Ag(I) and Cd(II)) and borderline acids (Co(II), Ni(II), Cu(II) and Zn(II)) tend to strongly interact with soft bases in the form of protein sulphhydryl (R-SH) groups, with their toxicity towards planktonic cells relating to their affinity with sulphur [140, 141]. On the other hand, a lack of selectivity can lead to "ion mimicry" where cellular dysfunction is developed over the incorrect binding of an ion metal with similar structure to the required protein cofactor [124]. Besides these interactions, metallic elements are characterised by their ability to acquire electrons. This tendency, thermodynamically defined by their reduction potential, reflects the reactivity of such species with biological molecules and roughly correlates with antimicrobial efficacy [138, 140]. Altogether, these three parameters govern reactivity of metallic species which can be potentially used to guide the development of novel alloys for antimicrobial applications. Each metal typically has specific mechanisms through which toxic effects can be caused; commonly relating to its speciation, some of which are summarised in Table 2.2.

Table 2.2: Summary of element groups and corresponding effect on cells.

Element Groups	Example Metal Elements/Ions	Method of Antimicrobial Action	Effect on Cells
Elements high in Irving-Williams series	Mn(II), Fe(II), Co(II)	Displacement of essential ligands	Alters protein structure and function
Soft and borderline acids	Hg(II), Cu(I), Ag(I), Cd(II), Co(II), Ni(II), Cu(II), Zn(II)	Interaction with Sulphhydryl (R-SH) Groups	Strong binding to protein thiol groups, leading to toxicity in planktonic cells.
Active transition metals	As, Fe, Cu, Cr, Co, V, Te, Ni	Catalyse electron transfer	Increase ROS
Catalytic or structural metals	Pb (II), Ni (II) or Ag (I)	Protein dysfunction	Interaction with Fe-binding sites, destruct Fe-S clusters
Metals with High Reduction Potential	Ag, Cu	Electron Transfer	Increased reactivity with biological molecules, correlating with antimicrobial efficacy.

However, metal ions usually have the benefit that they can target multiple components of bacterial cells, including their proteins, membranes, DNA and metabolic pathways. The most common method appears to be related to the binding affinity of the metal ions to various biological components within the cells. This is based around ligand field theory and the ability for DNA, metabolites and membrane lipids to partake in metal coordination. Metals with a strong affinity for these biomolecules can displace the essential metals usually bound, thereby disrupting their usual functions. Other mechanisms of toxicity involve the production of ROS. This is typically achieved through the binding to cysteine residues within Fe-S clusters, causing the release of free iron (either Fe^{2+} or Fe^{3+}), thus causing ROS production. This is depicted in Figure 2.8. The ROS are then able to cause cell wide damage through protein damage and dysfunction. Both Ag^{+} and Cu^{2+} have shown potential to disturb the membrane and cause lysis[142].

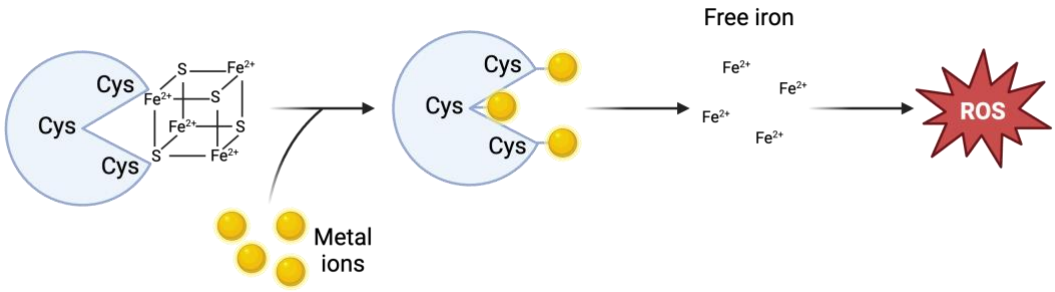

Figure 2.8: Depiction of ROS production in cells through addition of metal ions (e.g., Ag+ or Cu2+). Adapted from Domb et al., 2019 [142].

2.3.1.2. Physiological and Biochemical Responses to Metal Stress in Bacteria

There are many physiological and biochemical approaches which bacteria utilise to tolerate the presence of toxic metals, outlined in Figure 2.9. It is important to note that no single method

can be used against all metals. Bacteria have methods in which they can control the action of membrane transporters, and consequently they are able to regulate and reduce the metal uptake into the cell (Figure 2.9a) [117]. The efflux mechanism (Figure 2.9b) involves simply removing the toxic ions and metals that enter the cells through the transport system, however, this is a common mechanism of resistance to metal ions [143]. Additionally, some microorganisms can produce extracellular polymers or siderophores which can coordinate to the metal ions (Figure 2.9c). This allows them to trap, or precipitate, metal ions extracellularly. Soluble siderophores which are bound to the metal ions can help to reduce uptake or increase efflux of toxic metals. Similarly, intracellular sequestration (Figure 2.9d) involves the precipitation of the metals as metal oxides, sulphides or protein aggregates, which causes them to sequester in the periplasm, or cytoplasm. Alternatively, the metals can undergo redox and covalent reactions within the cells, which alter the species into other forms such as metal crystal precipitates or organometallic compounds [117]. This chemical modification (Figure 2.9e) can be beneficial due to the conversion of the metals into less toxic forms, or less available metal-ion species [144]. Cells can also withstand toxicity by evading metabolic pathways by producing proteins which do not bind to the metals and forcing metabolites into alternative routes (Figure 2.9f). Furthermore, molecules which are reactive towards metals, typically through oxidation, or their by-products, such as reactive oxygen species, can be repaired by enzymes or antioxidants present within the cells (Figure 2.9g) [117].

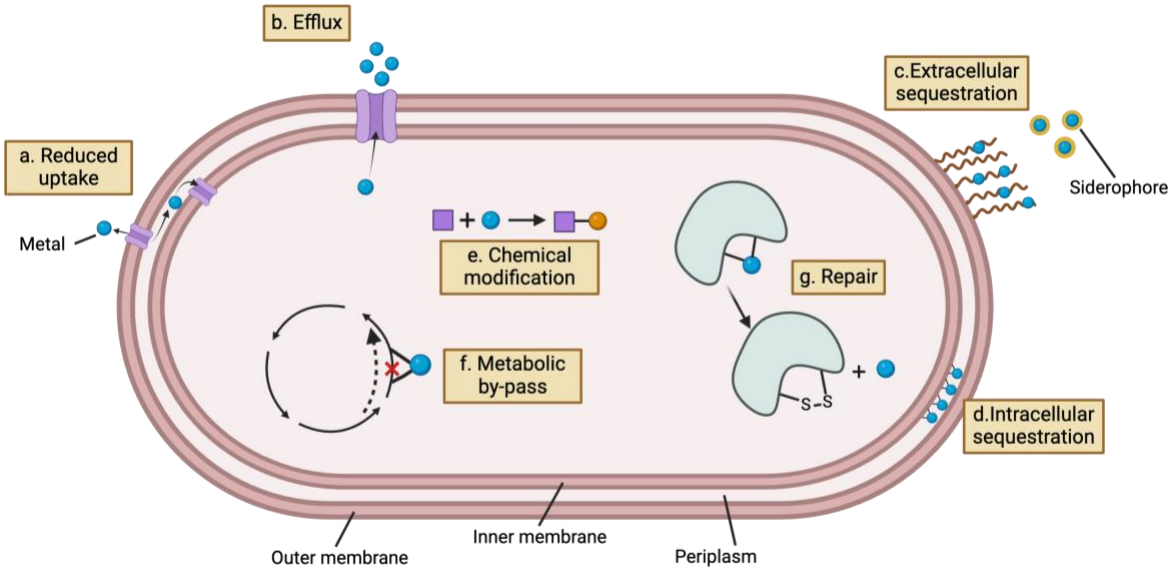

Figure 2.9: Representation of how microorganisms adapt to metals. Adapted from Lemire et al., 2013 [117].

2.3.1.3. Common Examples of Metallic Antimicrobial Elements

Two of the most widely explored metallic antimicrobial elements are silver and copper. However, the widespread use of silver as an antimicrobial agent, as well as its common misuse, has resulted in an increase in silver-resistant bacteria. Silver can be found in dressings to aid with infection management, as well as in components of dental and medical devices, such as catheters [145]. Nonetheless, misuse in areas such as in textiles for odour control has contributed to the growing resistance [146]. The first case of silver resistance was noted in 1975 after an outbreak at a burns ward, resulting in 3 deaths, however current figures for resistance are widely unknown [147]. Nevertheless, resistance to silver can both be endogenous or exogenous. However, it mainly occurs due to the restriction of the build-up of silver intracellularly, through porin loss and increased silver efflux [145].

On the other hand, Copper (Cu) and Cu alloys have been historically used for thousands of years for antimicrobial purposes, and few cases of bacterial resistance has been detected [148]. Cu is an essential trace element for humans, amongst other living organism. Cu is present within over 30 proteins, including lysyl oxidase, dopamine β-hydroxylase, cytochrome *c* oxidase and superoxide dismutase. In these proteins, copper is an electron donor/acceptor, switching between redox states Cu (I) and Cu (II). Though, in other proteins, e.g., plastocyanin, Cu acts as electron carriers [148]. However, despite these redox properties having essential properties, they can also cause cellular damage, through interactions with electronegative groups (e.g., thiol or carboxyl groups) on the bacterial cell membrane [148, 149]. Nevertheless, the mechanism of action of Cu is much debated, but is believed to be multifaceted. Many modes of action are believed to have an effect, including formation of ROS, cell membrane permeabilisation, protein alteration and denaturation of DNA [150]. Figure 2.10 highlights some mechanisms of cell apoptosis from Cu ions, on both an extracellular and intracellular level. Bacteria have developed many mechanisms to protect themselves from excess Cu. Efflux and active extrusion of Cu from the cell seems to be the key mechanism by which both Gram-negative and -positive bacteria tolerate Cu. Although, research suggests that these mechanisms, whilst they do offer some protection from copper, only delay cell death. Complete bacterial resistance to copper appears dubious for a range of reasons. Firstly, the plasmid DNA is entirely destroyed in the process, inhibiting resistance to be transferred. Similarly, contact killing on pure Cu surfaces is a very rapid process, therefore cell division does not occur, and so resistance is impeded. In cases where resistance has been noted, prolonged (1-3 days) survival on dry surfaces were only documented, with no exceptional copper resistance measured in culture [151].

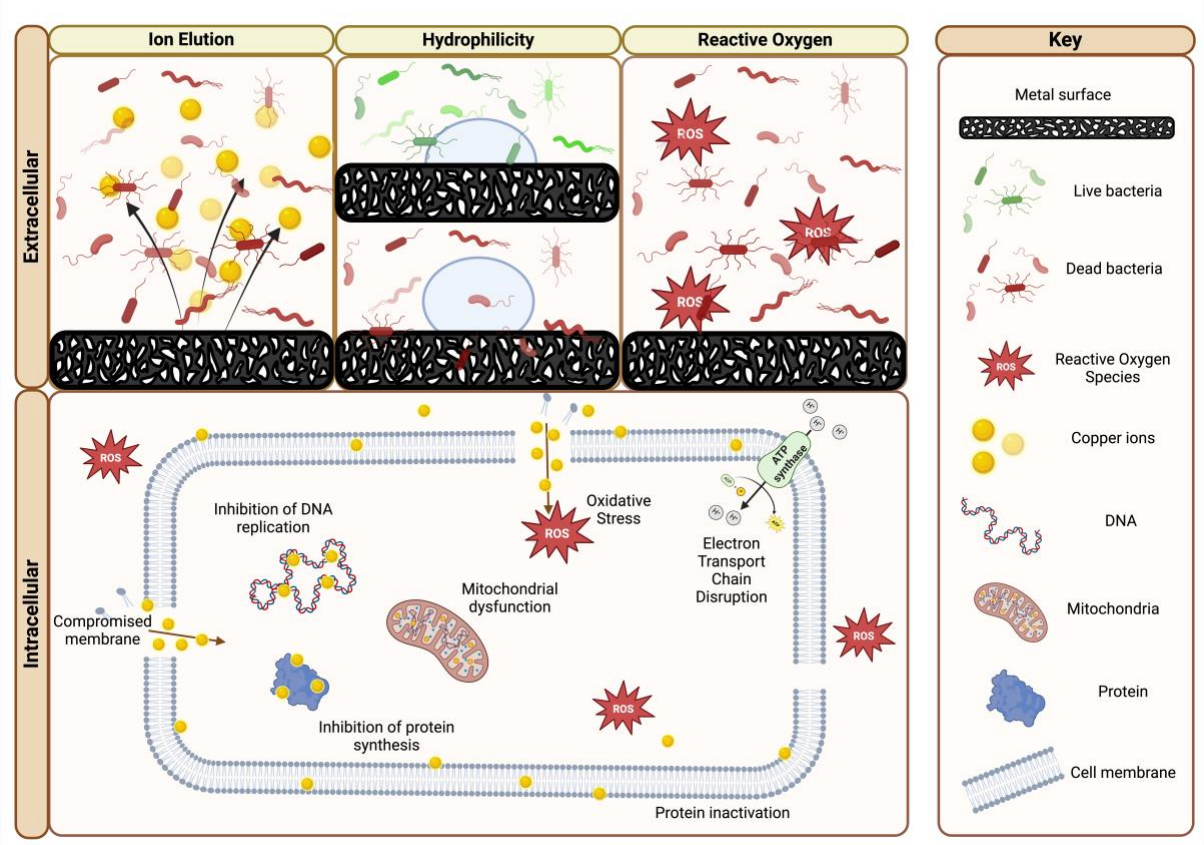

Figure 2.10: Mechanisms of cell death from copper containing alloys extracellularly and effect of Cu ions intracellularly.

Despite the previously discussed benefits of Ti-based implants, they are vulnerable to bacterial adhesion leading to biofilm formation and potentially implant failure. One of the most advantageous methods to prevent this biofilm formation is to provide an antimicrobial surface to hinder this bacterial colonisation. By introducing an antimicrobial element into the Ti-alloy system, the biofilm formation can be inhibited. Many antimicrobial elements have been researched throughout literature, including Zn, Ag and Cu. In particular, Ti-Ag based systems have been widely investigated. However, there are major drawbacks to the use of Ag, as previously discussed. Furthermore, Ti-Ag implants can lead to the formation of Ag salts which can be absorbed into the circulatory system, causing many medical problems. Silver's antimicrobial activity is also vastly pH and temperature dependent, unlike copper, which may

impede its functions [152]. As such the prevalence of Ti-Cu alloys has vastly increased amongst researchers.

2.4. Ti-Cu Alloys

Copper has been noted to bestow similar antimicrobial properties to silver, approximately five- to ten-fold compared to other elements against *S. aureus* and *E. coli* [153]. Copper has also been noted to promote bone regeneration, through proliferation of mesenchymal stem cells (MSCs) resulting in osteogenic differentiation, facilitating angiogenesis and collagen deposition [154, 155]. Furthermore, copper is an essential trace element within the body [156, 157]. However, the optimum amount should be considered within implants, as excess concentrations may trigger cytotoxic effects. Therefore, it is crucial that the development of Ti-Cu alloys is well balanced between the necessary amounts for antimicrobial properties and cytotoxicity.

2.4.1. Phase Diagram

The Ti-Cu binary alloy system has been extensively researched, with early studies dating back to 1912 [158]. Over the decades, researchers have examined various Cu compositions, identifying several intermetallic compounds including Ti_2Cu, TiCu, Ti_2Cu_3, and $TiCu_4$[159]. However, discrepancies emerged particularly regarding the Ti-rich region. The existence of the Ti_3Cu phase, reported by some researchers, was challenged by others who favoured Ti_2Cu as the stable phase [160-162]. Grdina *et al.* reported Ti_3Cu formation through a peritectic reaction, but their findings lacked reproducibility [160]. Subsequent studies using thermal analysis, X-ray diffraction, and microstructural evaluation yielded conflicting conclusions about Ti_3Cu's stability [160, 161, 163].

More recent thermodynamic evaluations, particularly those using CALPHAD (CALculation of PHAse Diagrams) and first-principles calculations, consistently support Ti_2Cu as the most stable Ti-rich intermetallic compound [158]. Figure 2.11 depicts the most commonly agreed phase diagram for the Ti-Cu system. Thus, the primary intermetallic phase formed is Ti_2Cu, although Canale *et al.* reported the formation of Ti_3Cu during cooling from high temperatures (>790 °C) [164]. Yet, subsequent studies suggest Ti_3Cu is metastable and was previously misinterpreted [162, 165, 166]. Differentiating between Ti_2Cu and Ti_3Cu is challenging due to very similar crystallographic spectra [162]. Nevertheless, understanding the distinction between these phases is crucial, as Ti_2Cu has attracted significant interest due to its reported antimicrobial properties [73, 167]. Current consensus supports the exclusion of Ti_3Cu from the equilibrium phase diagram of Ti-Cu alloys, reinforcing the role of Ti_2Cu as the dominant Ti-rich intermetallic phase under equilibrium conditions [158]. The ability to manipulate these Ti-Cu phases through precise heat treatments, precipitation and alloy composition adjustments offers a potential pathway to fine-tune the microstructure, physical properties and to tie this to the antimicrobial properties of Ti-Cu alloys.

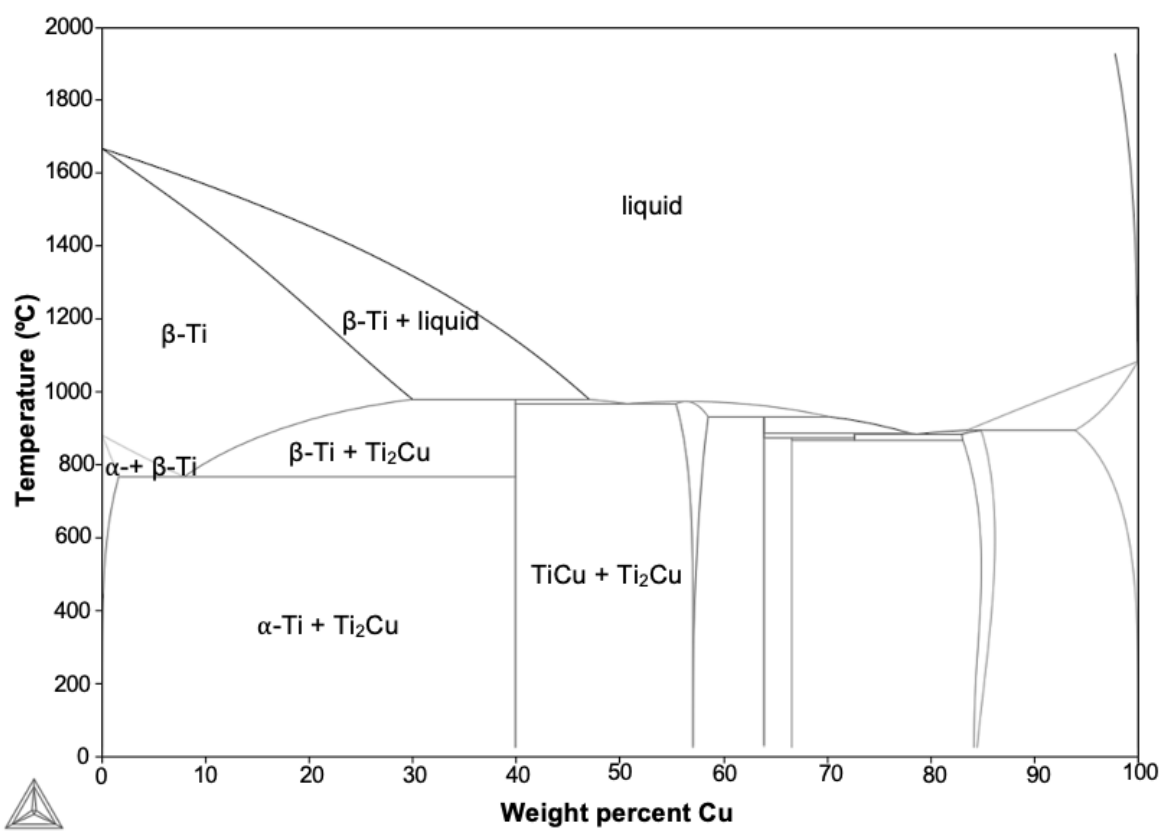

Figure 2.11: Ti-Cu binary phase diagram produced using ThermoCalc 2023a with the TCTI2 database.

2.4.2. Antibacterial Ti-Cu alloys

The antibacterial properties of Ti-Cu implants were first reported in 2009, by Shirai *et al.* [168]. Samples of Ti-1 (wt.%) Cu and Ti-5 (wt.%) Cu, henceforward denoted as Ti-1Cu and Ti-5Cu, were studied. All copper-based alloys were determined to be 'antibacterial', with materials possessing antibacterial efficacy of greater than 90 % enabling this classification as per GB4789.2-2010 Food Safety Standard [169]. This research became a critical point within antimicrobial Ti-Cu alloy research and highlighted a great potential of these materials for antibacterial implants. Subsequently, many investigations have been carried out to further improve the antibacterial activity, cell biocompatibility and mechanical properties of the alloy system.

Further work has been carried out widely on alloy systems up to 10 wt.% Cu [167, 170-176]. In particular, Zhang *et al.,* through repetition of polishing methods and the plate counting method, noted that the antimicrobial properties within the Ti-Cu alloys exist within the entire material and not just the bulk or surface. [176]. Whereas. Liu *et al*. proved that an increase in Cu concentration improves the antimicrobial efficacy of the alloys, however for an adequate antibacterial performance (greater than 90 %) at least 5 wt.% Cu is required [170]. Nevertheless, there are significant discrepancies across literature regarding the minimum Cu concentration required for antibacterial efficacy, which could be in correlation to the variation in experimental conditions seen in Table 2.3.

Table 2.3: The variations in methods and experimental conditions in analysis of Ti-Cu antimicrobial efficacy.

Alloy (wt. %)	Method	Bacteria	Conditions	Reference
Ti-0.5Cu Ti-1Cu Ti-2Cu Ti-3Cu Ti-4Cu Ti-8Cu Ti-10Cu	Killing activity test with variation of contact time	*S. aureus*	Incubated for 18-24 hours	[177]
Ti-5Cu	Quantitative antibacterial test (ISO 10993-5: 2009)	*S. aureus* *E. coli*	Incubated at 37 °C at 90 % relative humidity for 24 hours	[173]
Ti-5Cu Ti-10Cu	Plate count method BHI-S blood agar diffusion assay	*P. gingivalis*	Incubated in anaerobic conditions	[178]
Ti-1Cu Ti-2.5Cu Ti-3Cu Ti-10Cu	Bacteria direct contact test	*S. epidermis*	6 h direct contact, 24 h for growing bacteria followed by direct contact, incubation at 37°C	[179]
Ti-10Cu	Agar diffusion assay Plate count method	*S. aureus* *E. coli*	Incubated at 37 °C at 90 % relative humidity for 24 hours	[176]
Ti-5Cu	Biofilm based gene expression	*S. mutans* *P. gingivalis*	Incubated for 24 hours	[175]

It is necessary to consider the approaches used to investigate the antimicrobial performance of Ti-Cu and the impact that this may have on reported efficacy. For example, Zhang *et al.* considered the efficacy of Ti-10Cu through two different methodologies: plate counting method and an agar diffusion assay with both *S. aureus* and *E. coli* [176]. The agar diffusion test presented with no antimicrobial efficacy for the alloy, whereas the plate count method resulted in more than 99 % of the colonies being removed [176]. Furthermore, the plate count method reported in Bai *et al.* resulted in only 68 % efficacy for Ti- 10Cu [178]. This highlights that beyond the assay and methodology, the various experimental parameters may also impact the results, i.e., incubation conditions, temperature, size of the alloy and the type of bacteria.

To address this issue, it is crucial to establish standardised methodologies for testing the antimicrobial activity of Ti–Cu implants. These protocols should accurately replicate the physiological and practical conditions under which the implants function in the human body. A consistent and universally adopted testing framework would not only facilitate reliable comparisons between different Ti–Cu alloys but also enhance our understanding of the underlying antibacterial mechanisms. Ultimately, this would contribute to the development of more effective and clinically relevant Ti–Cu biomedical materials.

Furthermore, the mode of action of these alloys are still widely debated, however it is clear that the action is multifaceted in nature. Some research equates much of the antimicrobial performance to elution of copper ions [177, 180, 181], whereas others equates the antibacterial performance of Ti-Cu alloys to a contact mechanism [152, 182, 183]. Further mechanisms have been attributed to the micro galvanic cells produced due to a potential difference between the Ti matrix and the Cu-rich phase (i.e. Ti_2Cu). This is noted to be the key mechanism of action in Ti-Cu alloys with Cu concentration less than 40 wt.% [152]. In Mahmoudi *et al*. it is

discussed that by fabricating a Ti-Cu alloy which consists of a microstructure composed of intermetallic compound phases, the mechanism can be better distinguished [152].

2.4.3. Further Benefits of Ti-Cu

It is believed that a fully intermetallic microstructure also reduces the risk of cytotoxicity to native cells, as shown by Akbarpour *et al.* [180]. In addition to the antimicrobial benefits of Cu ions, there is also evidence that they may aid bone regeneration. Liu *et al.* highlighted the potential of Ti-5Cu alloys for multi-functional implants, noting their promotion of osteogenic differentiation and upregulation of osteogenesis-related gene expression [184]. Studies have also suggested that copper-containing alloys may improve angiogenesis, linking to Cu ion elution [185]. Therefore, optimising the amount of Cu released presents an opportunity not only to elicit an antimicrobial effect but it is also critical to find a balance with effects against native cells to minimise any cytotoxic effects and possibly enhance pro-regenerative factors [186]. Despite these findings, these biological functions have not been widely assessed on different cell types and overall few alloy systems have been investigated, especially above 10 wt.% Cu [175, 184-191].

2.4.4. Advancing Titanium Based Alloys: Integrating Antimicrobial Properties and Enhanced Functionalities

Beyond initial developments, few realistic Ti alloy systems have been explored that integrate the antimicrobial properties of Ti-Cu alloys with the enhanced functionalities of additional elements. While some studies have used Ti-6Al-4V as a base alloy to improve mechanical performance, concerns regarding its alloying elements highlight the need to develop new compositions starting from the Ti-Cu alloy [192-196]. Research has discussed Ti-5Al-2.5Fe-Cu and Ti-Mn-Cu alloys, however very little has been studied regarding the cytotoxicity or antimicrobial mechanism of action of these alloys [169, 197].

To advance the development of next generation biomedical Ti alloys, future research should focus on incorporating further elements known for their biological functionalities, or for improving physical and mechanical properties. Systematic studies on their synergistic effects with Cu in antimicrobial performance and biological response are essential to develop next-generation biomedical Ti alloys.

The Ti-Cu phase diagram suggests that heat treatment and rapid quenching may allow for retention of β- phase in these alloys. However, in many experimental cases, no evidence of β-stabilisation was found [198, 199]. Since β- Ti alloys are supposed to have superior corrosion resistance, higher strength and better biocompatibility (than α- Ti alloys), they are preferred for biomedical implants [200]. Molybdenum is a key β- stabilising element and due to its hardening effect, is more effective at strengthening Ti- alloys than other elements such as V and Nb [201], though care must be taken to avoid metastable omega phase formation [202]. Mo is also regarded the most suitable as it is able to stabilise the β-phase with a low solute concentration [203]. Figure 2.12 shows the binary Ti-Mo phase diagram. Binary Ti-Mo alloys with up to 20 wt.% Mo exhibit desirable properties such as a low elastic modulus and flexural strength, good corrosion resistance, predominance of the β-phase, whilst mitigating cytotoxicity and risks of allergy [203, 204]. Consequently, these alloys are considered suitable as orthopaedic implants as standardised by ASTM [203]. Additionally, it has been found that each wt.% increase in Mo lowers the β-transus by approximately 9-10 °C, which is significant when considering post-production heat treatments [205].

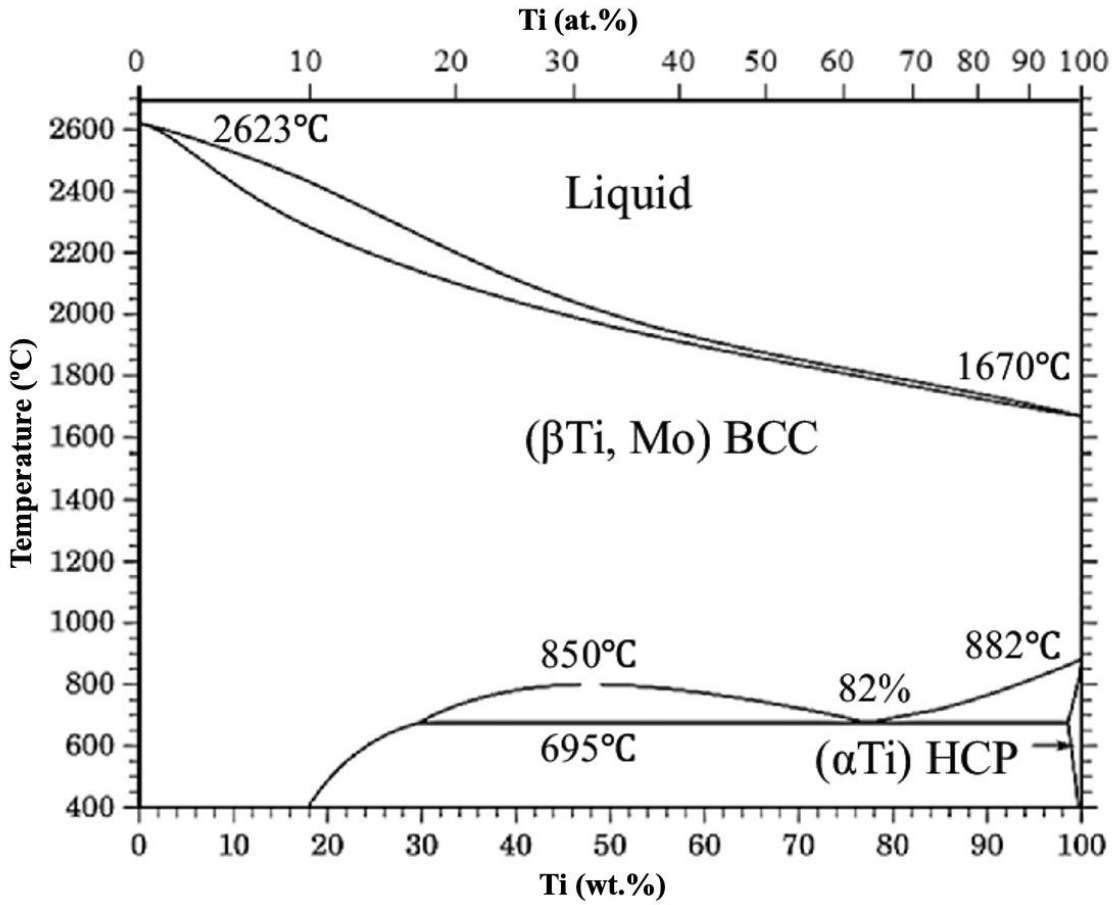

Figure 2.12:Ti-Mo binary phase diagram. Adapted from Zhang et al. [206].

In response to this, researchers have begun exploring multi-element systems, such as Ti-Mo-Cu alloys. Figure 2.13 shows an example isothermal Ti-Mo-Cu phase diagram at 950 °C. Particular interest was derived due to established use of Ti-15Mo in orthopaedic applications [29, 207, 208]. Ti-15Mo exhibits good mechanical properties and low elastic modulus, however, naturally does not have antimicrobial properties. Studies have shown that alloys with greater than 11 wt.% Cu show antimicrobial rates of greater than 90 % [207, 208]. Nevertheless, as with Ti-Cu alloys, limited work has been done to explore the underlying mechanisms by which these alloys exert antimicrobial efficacy and due to lack of standardisation of antimicrobial testing protocols, comparison across studies is difficult. Furthermore, links to microstructural properties have not been explored through differing heat treatments for microstructure tuning combined with antimicrobial efficacy.

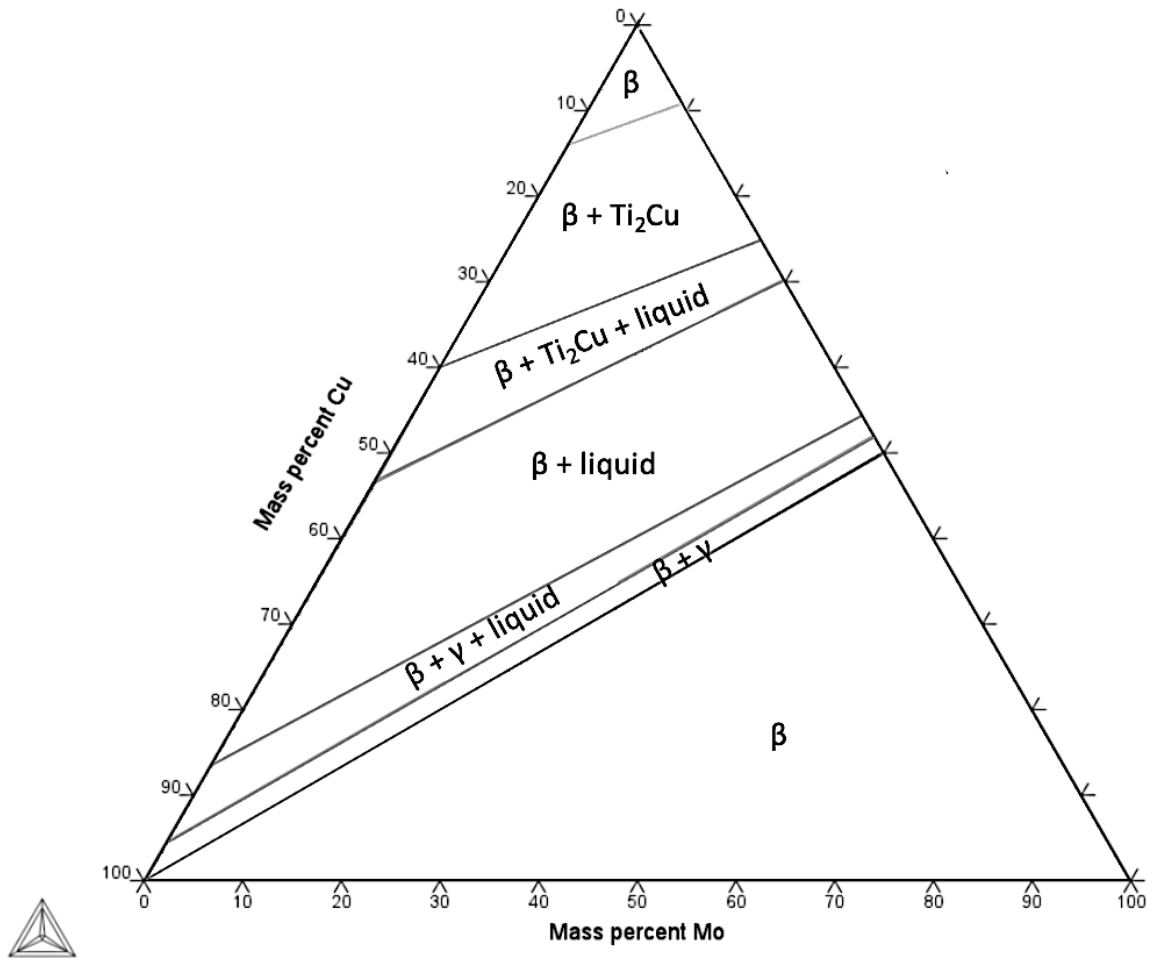

Figure 2.13: Isothermal ternary phase diagram at 950 ℃ for Ti-Mo-Cu alloy, created using ThermoCalc 2023a with TCTI2 database.

2.5. Manufacturing Methods to Support Alloy Discovery

When considering the design space of potential novel bioactive titanium alloys, there exist a plethora of metalloids, nonmetals, transition metals, rare/alkali earths and other metals of interest. There are between 30-40 candidate elements within the periodic table that may be of interest to incorporate for tuning microstructure and biological functionality resulting in ternary, Ti-Nb-Fe, to quinary, Ti-Nb-Mo-Zr-Sn, or even more complex multi-element systems, Ti-Nb-Ta-Zr-Fe-O-Si [209-211]. This leads to an upper bound of ~$7.6*10^5$ prospective

multicomponent systems that require compositional optimisation and lengthy microstructural tunning to achieve target requirements. With potentially ten to hundreds of compositional and thermomechanical combinations per system, exploring such a large design space in a reasonable timeframe while reducing research and development costs becomes a daunting process.

High-throughput combinatorial techniques that can rapidly synthesise different alloy compositions, structures, and phase distributions, are essential. Such techniques must be able to produce specimens adequate for biological testing at a rate high enough to allow for several element combinations to be tested in a short timeframe. Traditional melt and powder metallurgy methods are potential options, alongside thin-film deposition and in-situ alloying by additive manufacturing (AM) (Figure 2.14). Each method has its own benefits and limitations highlighting the need for a variety of practical tools. Such combinatorial techniques have been previously applied to other industries, for example the pharmaceutical industry often employ modelling software to produce compound libraries, to improve the research's discovery phase. Similar methods are becoming increasingly utilised in the discovery of novel inorganic materials. Though the aim is to combine the rapid approaches seen in the pharmaceutical industry with the screening techniques used in materials discovery [212]. Increasing the rate of discovery whilst reducing costs is a key focus within materials development. In particular, alloys tend to have diverse and often complicated composition-microstructure interlinks and so manufacture and characterisation of novel alloys is often an expensive and lengthy process [213]. This is especially true when, in addition to considering key physical properties, one must also consider the critical biological responses.

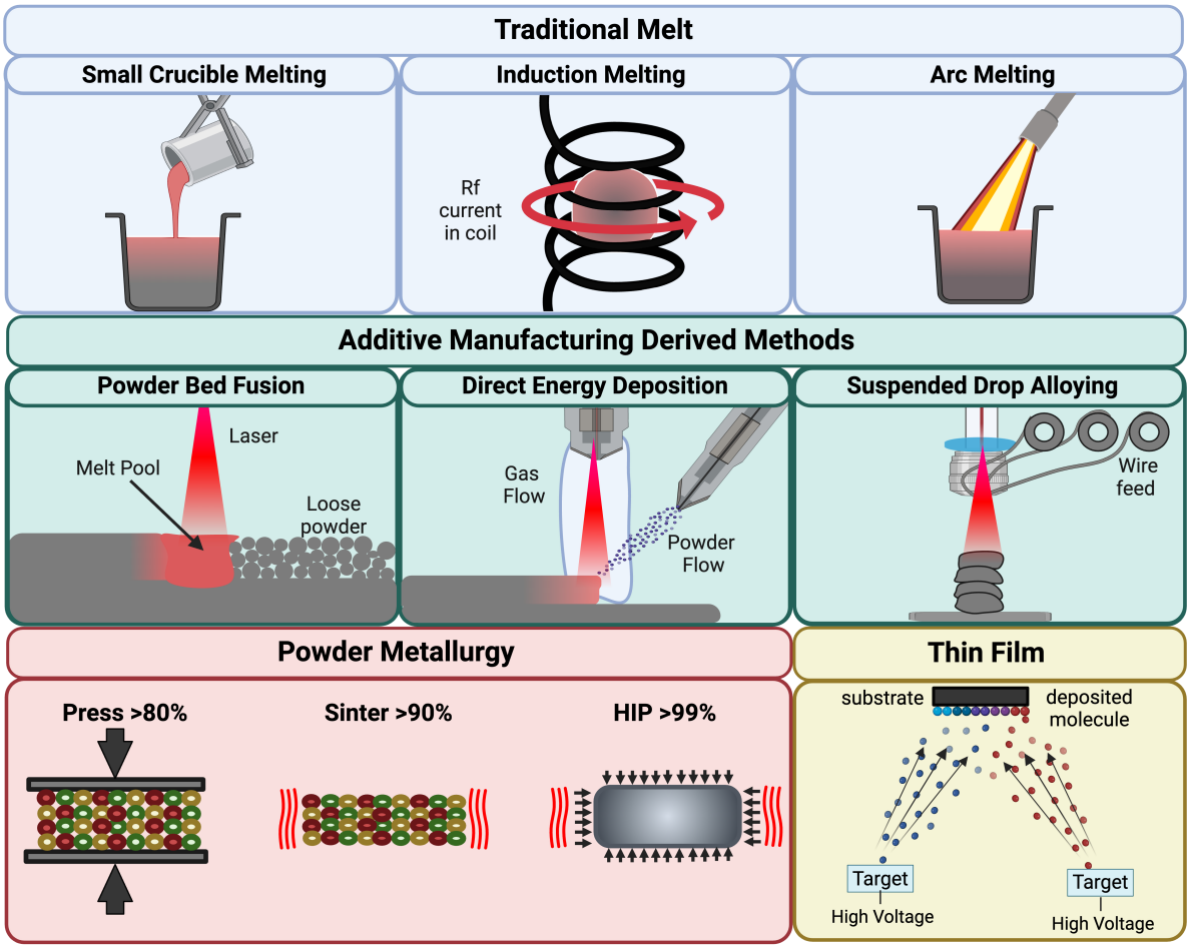

Figure 2.14: Schematic of traditional melt, additive manufacturing, powder metallurgy methods and thin film methods to facilitate alloy discovery.

2.5.1. Traditional Melt

The main objective of composition design is to select and control the microstructure and phases manifested by a metal component at the microscale knowing the process by which it will be manufactured. This includes control of grain size and morphology, as well as distribution of these phases [214]. Aside from the field of high entropy alloys, conventional alloys are typically underpinned by a binary or ternary system with minor additions of elements to refine the microstructure or enhance certain properties. Nickel superalloys used for aerospace applications are largely based on binary systems (namely Ni-Al), despite having several other elements listed in their compositions. These minor alloying elements allow precise control of the microstructure, conferring additional corrosion resistance and strength through mechanisms

such as solid solution strengthening and precipitation hardening [215]. The addition of minor alloying elements to improve material properties has been a successful strategy in the development and refinement of metallic materials such as steels, Mg-based alloys, Al-based alloys and binary intermetallic compounds [216]. However, this strategy has not been as widely adopted in developing new biomedical alloys.

Among the most highly engineered alloys, most tend to include 5-10 alloying elements, which makes it challenging to isolate the contribution of individual or combinations of elements to microstructural and phase stability. Traditionally alloy development relied on an iterative "one discrete composition or batch at a time" approach. After an initial composition, or batch, is selected, manufactured, and analysed, the composition is tweaked as deemed appropriate and the process repeated. This iterative strategy is costly and time consuming, even when using research-scale, small volume manufacturing methods. As the properties of an alloy are determined by its chemistry and microstructure, comprehensive characterisation of a new compositions should include numerous samples processed in a range of conditions (e.g. processing parameters, heat treatments cycle, surface treatments) and geometries (e.g. tensile, fatigue, creep). The numbers of samples required for characterisation also tend to rapidly increase with the complexity of the alloy and the number of alloying elements it includes. Considering basic characterisation of a binary composition following this traditional approach can take months, developing novel alloys with more than 5 alloying elements can take several years.

Some small-scale ingot production technologies exist that lend themselves favourably to a research-focus framework, such as vacuum arc melting and induction melting, which can produce small metal ingots in the range 3 to 500 g, at a rate of 1-10 ingots per day. These 'melt' methods are reliable but can be slow, with ingots often needing several remelts to achieve

compositional homogeneity [217, 218]. Methods using a crucible also open the risk of contamination and interactions with crucible materials.

Alternatively, powder metallurgy (PM) processing is recognised as a route for small pellet alloy production through either cold press + sinter, or cold press + sinter + hot isostatic press (CHIP) methods [219]. With the right workflow, these may provide a higher throughput than the melt methods as the small particle size and correctly selected sinter conditions limit the possibility of large segregation whilst enabling alloying through solid state diffusion. Likewise, the lack of a liquid stage eliminates crucible interactions.

2.5.2. Powder Bed Fusion

AM systems can be classified by how feedstock is supplied: powder bed systems, powder feed systems, and wire feed systems (Figure 2.14) [220]. Each of these relies on an energy source, often a laser, locally melting feedstock material in either powder or wire form. Given the local melting, mixing, and solidification during the fabrication process, these technologies not only enable netshape fabrication, but also the potential for in-situ alloying by using multiple feedstock materials at once. Composition changes are achieved relatively simply by varying material ratios; in the case of wires by adjusting the feed rate, and for powders by adjusting the blended ratio of elements.

Powder bed fusion (PBF) is the most utilised AM technology for the manufacturing of metal components. Both laser and electron beam can be used as the melting energy source, but for alloy development, laser is typically preferable. The high-powered laser is used to melt and fuse the metal powders, in a layer-by-layer approach, according to computer aided design (CAD) programming as represented in Figure 2.15 [221]. Electron beam processes require a vacuum atmosphere which can result in preferential volatilisation of higher vapour pressure elements during melting and alteration of the final material composition [222], whereas the

inert gas atmosphere used in PBF-LB (laser beam powder bed fusion) helps supress evaporation.

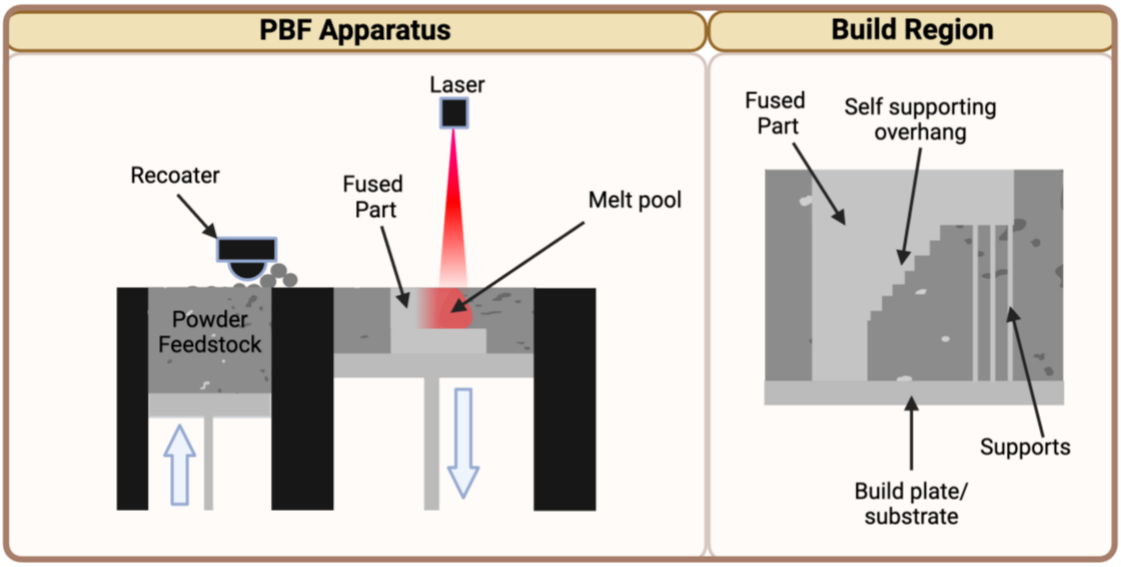

Figure 2.15: Representation of the principles of laser powder bed fusion (PBF-LB) additive manufacturing, showing the typical physical layout of PBF-LB apparatus. Powder from the feedstock is spread across the build plate via the recoater, and thermally fused by a laser. The build plate lowers, a new powder layer is spread, and fuses with the previous layer. On the right, a cross-section of the build region is displayed. Support structures are often required for overhangs, but unmelted powder can act as some degree of support.

Whereas traditional AM via PBF-LB uses pre-alloyed power feedstock, in-situ alloying typically uses mixed/blended, or mechanically alloyed powder. This allows for relatively low-effort investigation of a new alloy system by preparing different blends, using powders of the constituent elemental powders rather than dedicated atomisation of pre-alloyed material, which is a costly endeavour. Simple mixing is a low-cost and pragmatic process for blended powders, however, it has been associated with local chemical inhomogeneity where the degree of mixing is not comparable to the melt-pool size (~100 µm typically)[223]. Likewise, it is generally advised that powders have a similar particle size distribution, as broad distributions that include fine particles are known to flow and spread poorly during PBF-LB [224]. A recent variation,

satellite mixing, however, involves intentionally decorating the surface of a base spherical elemental powder with very fine alloying elements. This has been shown to improve chemical homogeneity in the alloyed material, although flowability of the satellite mixed powder was poorer than the carrier powder [223]. Mechanical milling without alloying presents another way to reduce chemical inhomogeneity by increasing powder contact area although changes to the powder morphology, away from the ideal 'spherical', presents potential flowability difficulties [224].

During processing, key variables such as power, speed, hatch spacing, and layer thickness govern many aspects of the as-built material microstructure and properties [225]. Inhomogeneity and segregation may be reduced by increasing energy input and thus the melt pool temperature and size [226]. Likewise, materials with different melting points, heat capacity, enthalpy of fusion, and reflectivity require that energy input is high enough to melt the least favourable of the blended elements to avoid unmelted particles trapped in the microstructure. This energy increase can lead to the "unmelted particle-keyhole" dilemma whereby energies required for complete melting can lead to keyhole pore formation [224, 227, 228]. It is also likely that parametric studies will be necessary for significant changes in the laser/powder interactions that accompany compositional blend changes. Depending on the system, there may be no appropriate parameter window giving a fully dense material without segregation. Laser rescanning each layer has proven effective at reducing segregation in certain cases [229]. Using a post-processing heat treatment to homogenise material through diffusion has also been demonstrated as effective [230, 231].

Despite these technical challenges, the use of in-situ alloying via PBF-LB has been widely demonstrated for Ti alloys [231-236]. The simplicity of feedstock preparation and the flexibility of final specimen geometry make it an attractive tool for investigating alloy systems.

However, it also has the benefit of differing microstructure when compared to samples manufactured through casting, resulting in different properties (Figure 2.16). Mohammed *et al.* demonstrated that cp-Ti, as one example, through fabrication by selective laser melting (SLM) consists of fine acicular martensitic grains, whereas when produced using casting methods contains plate-like grains. This leads to improved wear resistance in AM parts, when compared to their cast counterparts [237].

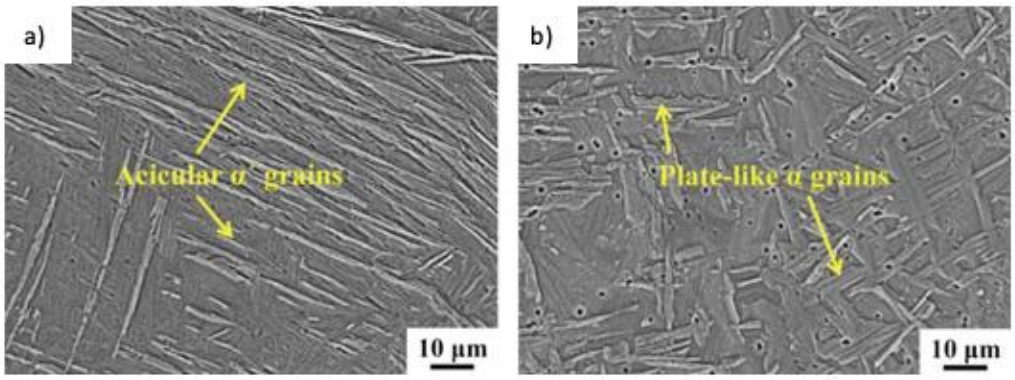

Figure 2.16: SEM microstructure of the cp–Ti samples produced by (a) Selective Laser Melting (SLM) and (b) casting. Reproduced from Mohammed et al., 2019 [237].

AM methods (particularly PBF-LB) are characterised by extremely high thermal gradients, both temporally and spatially, leading to cooling rates that are orders of magnitude higher [238, 239]. These rapid solidification conditions play a crucial role in controlling microstructural features such as grain size, orientation, and phase formation [238-240]. The localised heating and cooling cycles enable the refinement of microstructures, the formation of metastable phases, and potential suppression of coarse grain growth, which are difficult to achieve through conventional processing [238]. However, the process can also introduce challenges such as residual stresses and compositional segregation, necessitating post-processing treatments to optimise microstructure and often mechanical properties [238]. Despite these challenges, the

ability to manipulate microstructural characteristics through PBF-LB presents a significant advantage for designing biomedical titanium alloys.

2.5.3. Heat Treatments

Whilst the manufacturing method in many ways can impact the microstructure and properties of an alloy, often further processing such as heat treatments are required. Heat treatments play a critical role in controlling microstructures (e.g. phase evolution, precipitation, recrystallisation, grain growth), relieving internal stresses, enhancing mechanical performance, and tailoring functional properties for specific applications [198, 241]. This is especially important in cast and additively manufactured (AM) components, where the inherent characteristics of each process can introduce microstructural heterogeneities, residual stresses, or undesirable phases.

Heat treatments such as homogenisation, annealing, solution treatment, and ageing can be used to alter the microstructure thereby improving mechanical and biological properties. AM alloys, such as those produced by PBF-LB, may exhibit defects due to improper scanning parameters or inadequate powder melting. This can lead to issues compromising mechanical properties, as well as homogeneity of samples particularly in cases of specimen manufactured with blended powder. These issues can include undesired microstructures, porosity, high residual stresses, and anisotropy due to rapid cooling rates and directional solidification [242]. Thus, carefully designed heat treatment protocols are indispensable for both cast and AM alloys to ensure consistency, reliability, and performance in demanding environments.

2.5.4. Review of Literature Methods of Alloy Discovery

Table 2.4 summarises various studies from the literature, highlighting differences in alloy composition, manufacturing methods, heat treatment conditions, and bacterial assays. The wide variation in these parameters makes it challenging to pinpoint the key factors influencing

antimicrobial efficacy and mode of action. As expected, Cu content plays a critical role, with an increase in concentration studied, generally resulting in greater bacterial inhibition, primarily through Cu ion release, reactive oxygen species (ROS) production, and nano-scale galvanic effects. Though, manufacturing techniques such as spark plasma sintering (SPS), laser powder bed fusion (PBF-LB), and direct energy deposition (DED) may have an impact on antimicrobial efficacy, differences in bacterial strain and exposure time could contribute to the observed variations in efficacy, preventing results from different sources being reliably compared.

Table 2.4: Summary of Ti-Cu compositions analysed throughout literature in relation to the method of antimicrobial testing, bacteria and the method of manufacture of the samples.

Alloy (Ti-(wt.%)Cu)	**Manufacture Method**	**Heat Treatment Conditions**	**Bacteria and Contact Time**	**Antimicrobial Efficacy**	**Reference**
Ti-5Cu	Ball mill + hot pressure sintered	Hot pressure sintered under vacuum conditions at 30MPa and 1050 °C	*P. gingivalis* for 18 and 24 hrs	36% and 54%	[243]
Ti-10Cu				69% and 75%	
Ti-1Cu	arc melted + HT	900 °C for 18 hrs, then 798 °C for 24hrs, salt-brine water quench	*S. epidermis* for 6 hours	4%	[179]
Ti-2.5Cu				13%	
Ti-3Cu				16%	
Ti-10Cu				27%	

Ti-2Cu	Ball mill + hot pressure sintered	5-35 MPa pressure at 850-1080 °C for 30-60 mins	*S. aureus* for 24 hrs	79%	[170]
Ti-5Cu				99%	
Ti-10Cu				99.99%	
Ti-25Cu				99.99%	
Ti-2Cu			*E. coli* for 24 hrs	57%	
Ti-5Cu				99.20%	
Ti-10Cu				99.99%	
Ti-25Cu				99.99%	
Ti-3Cu	SPS	SPS at 1050 and 1200 °C	*P. gingivalis* for 72 hrs	57%	[244]
Ti-5Cu				70%	
Ti-3Cu			*S. mutans for* 72 hrs	63%	
Ti-5Cu				78%	
Ti-3.5Cu	DED	n/a	*S. algae* for 24 hrs	40%	[245]
Ti-6.5Cu				70%	
Ti-8.5Cu				99.20%	
Ti-2Cu	PBF-LB	n/a	*S. aureus* for 24 hrs	99.75%	[246]
Ti-5Cu				99.99%	
Ti-8Cu				100%	

2.6.Characterisation

Characterisation of metal alloys is crucial to understand the phases and microstructures present. Typically, techniques such as Scanning Electron Microscopy (SEM) and Transmission Electron

Microscopy (TEM) have been utilised to visualise materials at high magnifications. In particular, SEM is widely used in many scientific disciplines because of its advantages such as high resolution, large depth of field, lack of restriction on the shape and thickness of samples, and as it is a non-destructive technique [247]. Whereas, due to the short wavelength of electron beam and higher electron energies, TEM enables sub-nanometre resolution and higher magnifications [248, 249]. However, TEM requires much more complex sample preparation and extensive user skill [249].

These techniques are commonly complimented with further techniques such as Energy Dispersive Spectroscopy (EDX), Electron Backscatter Diffraction (EBSD) and X-ray Diffraction (XRD) to determine the elemental phase composition of specimens and their crystallography [250, 251]. Whilst these techniques are commonly advantageous, there are some downfalls to their uses in material development. For instance, there are many versions of the Ti-Cu phase diagram, resulting in much ambiguity around the phases present in the alloy. Further, the Ti_2Cu and Ti_3Cu phases produce very similar XRD patterns, depicted in Figure 2.17, making them difficult to distinguish [162, 252].

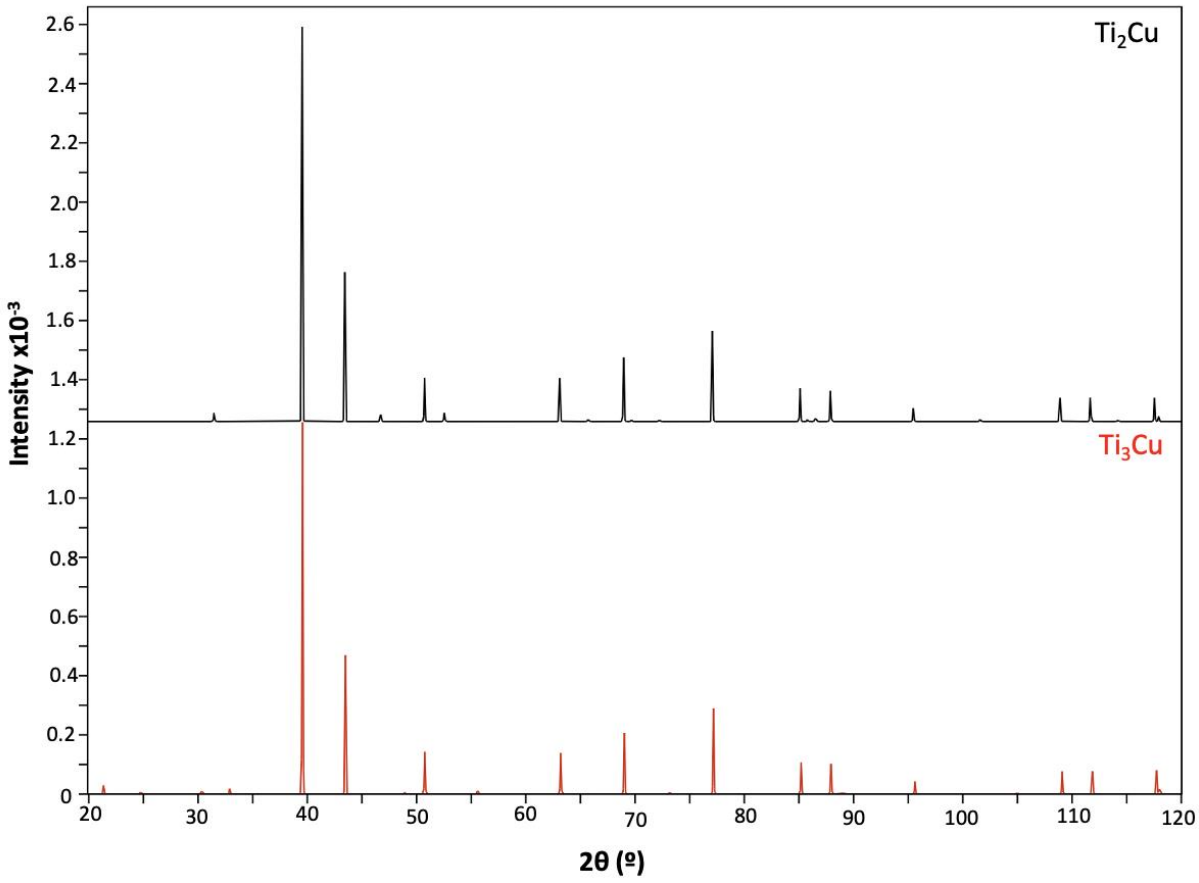

Figure 2.17: XRD patterns for Ti_2Cu and Ti_3Cu phases [161, 253].

Whilst techniques such as X-ray diffraction (XRD) and Electron Microscopy (EM) allow for an understanding of the phases present and a visual representation, this cannot always be easily quantified. Methods to describe the microstructure numerically are required to evaluate and compare different alloy systems. Shape properties, such as roundness or circularity [254], can be quantified but there is no single shape measure which works efficiently in all scenarios [255].

Shape descriptors relate to a particular shape property and have clear geometric meaning. One example is Hu moment invariants, which were introduced in 1962. Hu moments are able to quantify visual patterns and shapes independent of position, size and orientation. They are able to describe an object's shape, measuring aspects such as spread, symmetry and complexity [256]. Lower values typically indicate simple, symmetric shapes, whilst higher values reflect

asymmetry and distortion. The utilisation of Hu moments have proven to be highly effective, however, they are finite and so do not contain a complete set of image descriptors [257]. Nevertheless, there are few examples of these values being used to describe microstructural features [258, 259].

2.7.Summary and Knowledge Gap

This study focuses on developing an effective Ti-Cu antimicrobial alloy for biomedical implant applications. While previous research has explored Ti-Cu alloys, their antimicrobial mechanism remains unclear, limiting their full potential. This thesis addresses this gap by investigating the relationships between the composition, microstructure, and antimicrobial efficacy of these alloys. Additionally, further refinements have been made to optimise these effects and enhance other critical material properties.

Cast, additively manufactured and pressed Ti-Cu alloys will be manufactured to investigate the influence of manufacturing methods on the phases and microstructures of Ti-Cu alloys. Further processing conditions such as heat treatments will be applied to further differentiate the samples to establish the influences on microstructural features. The phases and microstructures of the Ti-Cu alloys will be characterised using advanced analytical techniques, such as microscopy and X-ray diffraction, to identify structural differences resulting from the manufacturing process. These will be further explored to assess the mode of action of Ti-Cu alloys, through analysis of antimicrobial properties in relation to the alloy composition, phases and microstructures. Furthermore, the study aims to differentiate between copper release and surface contact mechanisms by conducting detailed analyses on the underlying processes responsible for the intrinsic Ti-Cu antimicrobial activities.

Through additions of molybdenum, this research aims to produce a more realistic alloy closer to the desirable biological and mechanical properties. Additively manufactured Ti-Cu alloys will be optimised in terms of their biological functionality, as well as their mechanical properties through molybdenum addition. The study will also investigate the use of heat treatments, to enable Mo diffusion, whilst also aiming to further optimise these properties.

This research seeks to contribute to the understanding of the antimicrobial properties of Ti-Cu alloys, by delving into the intricate relationships between processing conditions, alloy microstructures, and phases present. The central aim for this research is the differentiation between the mode of action and copper release and surface contact mechanisms, ultimately aiming to advance the knowledge base for future development of antimicrobial Ti-Cu alloys.

Chapter 3

ANTIMICROBIAL TI-CU ALLOYS: THE ROLE OF MICROSTRUCTURE IN ARC-MELTED COMPOSITIONS

Copper-containing alloys have attracted considerable global attention in response to rising rates of orthopaedic implant infections and antimicrobial resistance. Two theories have emerged for the antimicrobial mechanisms of titanium-copper alloys: copper ion release and contact sterilisation. However, debate remains on which is the dominant mechanism and what factors drive efficacy. While previous studies have focussed on the overall effect of intermetallic Ti_2Cu phase fractions, this research digs deeper, unpicking the influence of precipitate size and morphology.

Herein we demonstrate that heat treatment (homogenisation at 950 °C and ageing at 760/820 °C) of cast Ti-11.5Cu and Ti-33Cu (wt.%) alloys may be used as a tool to tune antimicrobial potency through microstructural refinement. Specifically, it is shown that nanoscale precipitates (≈ 30 nm) of Ti_2Cu exhibited limited *in vitro* efficacy against *Staphylococcus aureus*. While larger (≈ 5 μm), rounded precipitates, exhibited superior action due to increased surface exposure contact. Contrary to previous literature, this study showed no detectable Cu^{2+} ion release in 0.9 % NaCl solution over 7 days measured by ICP-OES, suggesting that under these manufacturing conditions the antimicrobial mechanism is solely contact-dependent. *In vitro* studies indicated that while Ti_2Cu phases contribute to antimicrobial properties, a balance in Cu content and precipitate size is critical for both bacterial and native bone cell cytotoxicity. Overall, this study demonstrates a significant link between phase size, morphology and desirable antimicrobial properties of cast Ti-Cu alloys.

3. Antimicrobial Ti-Cu Alloys: The Role of Microstructure in Arc-melted Compositions

3.1. Introduction

Infection related to biomedical orthopaedic implants remains a major clinical challenge, equating to the third biggest cause of implant failure and the need for revision surgery [12]. This highlights the urgent need for antimicrobial materials that can prevent bacterial colonisation without the need for antibiotics. Titanium–copper (Ti-Cu) alloys have emerged as promising candidates, first reported in 2009 by Shirai *et al.*[168].

Several studies have been carried out on the binary Ti-Cu alloy system (Figure 3.1) up to 10 wt.% Cu [167, 170-176]. The phase diagram has guided selection of such compositions and heat treatment protocols. Notably below 40 wt.% Cu the α-Ti phase predominates below 790 °C [170]. However, above this temperature, it is possible to induce the formation of β-Ti, which has superior strength to the alpha phase [158]. The primary intermetallic phase formed is Ti_2Cu, although Canale *et al.* reported the formation of Ti_3Cu during cooling from high temperatures (>790 °C) [164]. Yet, subsequent studies suggest Ti_3Cu is metastable and was previously misinterpreted [162, 165, 166]. Differentiating between Ti_2Cu and Ti_3Cu is challenging due to very similar crystallographic spectra [162]. Nevertheless, understanding the distinction between these phases is crucial, as Ti_2Cu has attracted significant interest due to its reported antimicrobial properties [73, 167]. The ability to manipulate these Ti-Cu phases through precise heat treatments and alloy composition adjustments offers a potential pathway to fine-tune the antimicrobial properties of Ti-Cu alloys. Ethically it is critical that appropriate efficacy kinetics are developed for these advanced antimicrobial materials to ensure they effectively eradicate

species commonly associate with orthopaedic implant infections, including both gram positive and negative species.

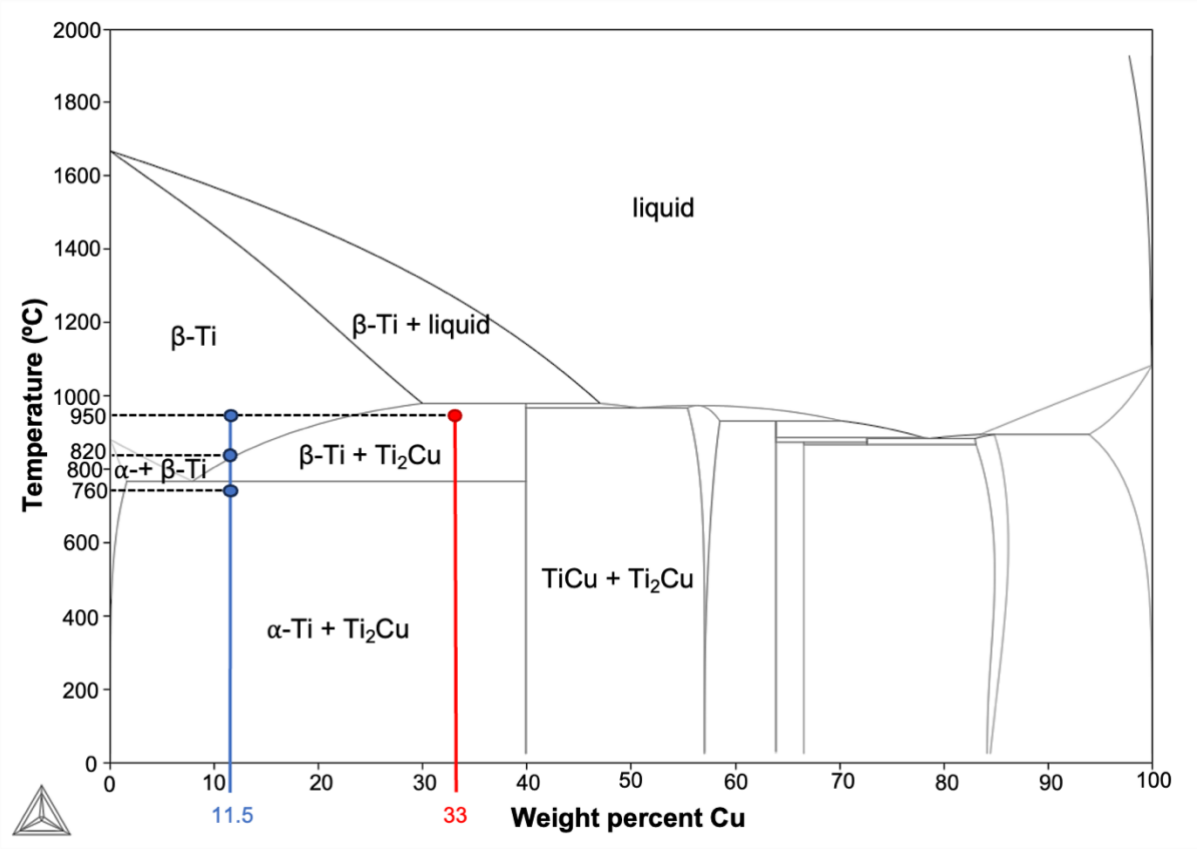

Figure 3.1: Binary Ti-Cu phase diagram, produced using ThermoCalc 2023a with the TCTI2 database. The blue and red dots indicate the compositions and heat treatments analysed within this research.

While the Ti-Cu alloy mode of action is still widely debated, it is believed to be multifaceted with contributions from both ion elution and contact mechanisms [19-21]. Regarding elution, Korda *et al.* state that the presence of Cu within the α phase plays a crucial role in the antimicrobial efficacy, as it can be easily released [177]. Liu *et al.* reported arc-melted Ti-5Cu possessed a 90 % antimicrobial rate (24 hours incubation with *S. mutans* and *P. gingivalis*) with just 0.003 µg/mL Cu elution in 0.9 % NaCl solution [175]. While Zhang *et al.* claimed a 100 % kill against *S. aureus* by releasing copper concentrations of 0.34 µg/mL from Ti-10Cu manufactured via ball milling and hot pressure sintering [176]. However, notably the minimum

inhibitory concentration (MIC) of Cu ions for *S. aureus* has been reported as 128 μg/mL [260, 261]. Given that the concentration of Cu ions released must be equal to or greater than the MIC for bacterial death to occur, it is clear that another factor is at play.

As well as ion release, several studies attribute the antibacterial performance of Ti-Cu alloys to a contact mechanism. Specifically, it has been demonstrated that the Ti_2Cu phase plays a key role and increasing Ti_2Cu content has been shown to enhance antimicrobial efficacy [171, 176]. Though the reasoning as to why Cu containing alloys instigate antimicrobial action is not well understood, it is believed that the hydrophobicity of the surface is crucial. Nan *et al.* discovered that bacteria were better adhered to Cu-containing alloys than non-Cu containing alloys, suggesting that the electrostatic forces of Cu^{2+} play a dominant role in the antimicrobial effects [182]. In particular, initial interactions between the surface and bacteria are dictated by long range Van de Waals and electrostatic forces, which depend on physicochemical properties e.g., hydrophobicity, free energy and surface energy [182, 262-266]. Furthermore, the Cu rich phase disrupts the osmotic pressure of the cell, consequently leading to cell envelope disruption [152]. Whereas, Shi *et al.* claim that the ion channels on the cell membrane are disrupted by the presence of Cu ions resulting in physiological metabolic disorders and cytoplasm leakage [183]. Further mechanisms have been attributed to micro-galvanic cells that form due to the potential difference between the Ti matrix and the Cu-rich phase (i.e., Ti_2Cu). In solution the Ti_2Cu phase acts as an anode and the Ti matrix as a cathode [190]. These micro-galvanic cells can facilitate electron transfer, which disrupts the proton motive force and inhibits the production of adenosine triphosphate (ATP), a primary source of energy for many cellular processes. This disruption accelerates the generation of intracellular reactive oxygen species (ROS), interfering with the bacterial respiratory chain and blocking electron transfer, ultimately leading to bacterial death [267]. This is noted to be the key mechanism of action in Ti-Cu alloys

with Cu concentration less than 40 wt.% [152]. A summary of these mechanisms is depicted in Figure 2.10.

Given these fundamental mechanisms of actions, the physicochemical properties, e.g. the microstructure, state of Cu and its distribution within the alloy, present an opportunity to tailor the antimicrobial efficacy of Ti-Cu alloys. Therefore, a detailed understanding of the Ti-Cu microstructure is fundamental to predict or tune the antibacterial properties. By increasing the concentration of the Ti_2Cu phase on the surface and the homogeneity of this phase, the antimicrobial activity is thought to be greatly improved. In this regard, it is beneficial to use processes such as heat treatments and ageing procedures, or surface treatments, that enhance the Ti_2Cu fraction to augment the antimicrobial and biological properties of the implant [268, 269].

Consequently, while Ti-Cu alloys present as promising alternative implant materials it is apparent that further work is essential to understand the modes of action and efficacy for these advanced engineering materials. Further focus is needed to understand the microstructural features of these materials and how they influence key biological behaviours. This research has identified that through heat treatments, the alloy microstructure can be altered, with a focus on evaluating the effects of Ti_2Cu on the antimicrobial efficacy. In addition to examining the phase itself, we will explore how its form and morphology influence both the antibacterial properties and *in vitro* functionalities of the alloys. By doing so, this research aims to provide deeper insights into the Ti-Cu alloy mode of action and the role that microstructure plays in determining *in vitro* efficacy against both gram positive and negative species.

3.2. Methods

3.2.1. Sample Preparation

Ingots of the studied alloys (Table 3.1) were made in an Arcast Arc200 arc melter (Alloyed Ltd), using pure titanium sponge and solid pure copper (grade C101). The set up included a tilt casting arrangement, with solid copper crucible and mould. Electromagnetic stirring was used to improve chemical homogeneity. The chamber was evacuated to a vacuum of approximately 10^{-2} bar before being backfilled with a partial pressure of high-purity argon for the arc melting step.

Table 3.1: Ti-Cu alloy compositions and heat treatment protocols.

	Value wt.%		**Value at%**				
	Ti	Cu	Ti	Cu	**Temperature**	**Time**	**Sample name**
Ti-11.5Cu	88.5	11.5	91.1	8.9	-	-	11 ac
					950 °C	100 hours	11 hom
					760 °C	24 hours	11 AT760
					820 °C	24 hours	11 AT820
Ti-33Cu	66.7	33.3	72.6	27.4	-	-	33 ac
					950 °C	100 hours	33 hom

Samples were enclosed in molybdenum foil and encapsulated in a quartz tube under Ar atmosphere. To enable a variety of microstructures, as cast (ac), homogenised (hom), homogenised and aged treated at 760 °C (AT760) and homogenised and aged treated at 820 °C (AT820) heat treatment conditions were assessed (Table 3.1). Heat treatments were selected to

enable different microstructures and phases to be targeted according to the phase diagram (Figure 3.1). Ageing treatments were carried out subsequent to homogenisation. All samples were water quenched immediately after furnace removal.

The alloys were then sectioned into 10x10x2 mm coupons using an Electro-discharge machine (EDM) for all characterisation and *in vitro* experiments and mechanically ground to 1200 grit then polished with diamond and OPS solution, as described in Table 3.2.

Table 3.2: Polishing and grinding sequences for alloy preparation with the Struers Tegramin-25.

Step	Grit/Polish Finish	Lubricant	Force	Rotation	Co-rotation	Time
1	MD-Piano 220	Water	20 N	300	150	Until plane
2	MD-Piano 1200	Water	20 N	300	150	Until plane
3	MD-Largo	DiaDuo 9-micron	15 N	150	150	~ 20 mins
4	MD-Allegro	DiaDuo 3-micron	15 N	150	150	~ 5 mins
5	MD-Chem	OPS	10 N	150	150	~ 30 mins

3.2.2. Microstructural Characterisation and Phase Identification

Scanning electron microscopy (SEM) imaging was completed on a ZEISS EVO10 using backscattered electron detector to reveal compositional contrast. Energy Dispersive

Spectroscopy (EDX) was carried out to produce spatially resolved elemental information at 20 keV.

X-ray diffraction (XRD) was performed using a Proto AXRD for phase identification. The system uses a copper line focus X-ray tube with a nickel k_β absorber producing K_α radiation ($K_{\alpha av}$=1.541874 Å) with a set increment size of 0.0149282° and a power setting of 30.0 kV and 20 mA.

Site-specific TEM foils were prepared from the polished samples using a FEI-Helios Nanolab 600 Dual Beam Focussed Ion Beam (DB-FIB) and the thinned foils were cleaned at 900 V using a Fishione 1040 Nanomill. STEM-EDX analyses were performed using a FEI-Titan G2 60-300 S/TEM at 300 kV equipped with a Super XG12 detector. Composition mapping was acquired using a dwell time set to 40 μs and a current ≈ 600 pA.

3.2.3. Image Analysis

BSE SEM micrographs were imported into MATLAB, converted into binary formats and the precipitates identified. Image analysis was performed to measure: total area of Cu rich areas and size of Cu rich precipitates (mean area, perimeter, major axis and minor axis). MATLAB codes can be found in the Appendix. The Hu moments (ϕ_{1-7}) were also calculated for each precipitate to give a shape descriptor, Euclidean distances then calculated between each point and plotted [270, 271]. High values of ϕ_{1-7} are typically reflected by irregular or elongated shapes, whereas low values represent a simple, symmetric and regular shape. To define the normalised scale invariants, Equation 3.1 is used:

$$\eta_{ij}=\frac{\mu_{ij}}{\mu_{00}^{\left(1+\frac{i+j}{2}\right)}}$$

[3.1]

Where η_{ij} is a scale invariant with respect to both translation and scale and μ_{ij} is a translational invariant where i+j≥2.

Based on these Hu moments ($\phi_{1\text{-}7}$) are calculated using equations 3.2-3.8.

$$\phi_1 = \eta_{20} + \eta_{02}$$

[3.2]

$$\phi_2 = (\eta_{20} + \eta_{02})^2 + 4\eta_{11}^2$$

[3.3]

$$\phi_3 = (\eta_{30} + 3\eta_{12})^2 + (3\eta_{21} - \eta_{03})^2$$

[3.4]

$$\phi_4 = (\eta_{30} + 3\eta_{12})^2 + (3\eta_{21} + \eta_{03})^2$$

[3.5]

$$\phi_5 = (\eta_{30} - 3\eta_{12})(\eta_{30} + 3\eta_{12})[(\eta_{30} + \eta_{12})^2 - 3(\eta_{21} + \eta_{03})^2] + (3\eta_{21} - \eta_{03})[3(\eta_{30} + \eta_{12})^2 - (\eta_{21} + \eta_{03})^2]$$

[3.6]

$$\phi_6 = (\eta_{20} - \eta_{02})[(\eta_{30} + \eta_{12})^2 - (\eta_{21} + \eta_{03})^2 + 4\eta_{11}(\eta_{30} + \eta_{12})(\eta_{21} + \eta_{03})]$$

[3.7]

$$\phi_7 = (3\eta_{21} - \eta_{03})(\eta_{30} + \eta_{12})[(\eta_{30} + \eta_{12})^2 - 3(\eta_{21} + \eta_{03})^2] + (\eta_{30} - 3\eta_{21})(\eta_{21} + \eta_{03})[3(\eta_{30} + \eta_{12})^2 - (\eta_{21} + \eta_{03})^2]$$

[3.8]

Euclidean distances were calculated using equation 3.9.

$$d(p,q) = \sqrt{\sum_{i=1}^{n}(p_i - q_i)^2}$$

[3.9]

3.2.4. Phase Analysis

The predicted composition of the as cast Ti-Cu alloys was determined through the use of the Scheil precipitation model on ThermoCalc 2024a using the TCTI3 database.

To calculate the predicted quantity of the phases in the homogenised and heat treated specimens, the Lever Rule was implemented.

3.2.5. Cu ion release

Following ISO 10993-12, Cu^{2+} released from Ti-Cu alloys for various periods of time was monitored in 0.9 % NaCl solution, incubated at 37 °C. The concentrations of released Cu^{2+} at 1, 3 and 7 days were determined by inductively coupled plasma optical emission spectrometry (ICP-OES), Perkin Elmer Optima 8000.

3.2.6. Contact Angle

The contact angle (CA) measurements were taken using the sessile drop technique (Attension Theta Lite Tensiometer, Biolin Scientific, USA). Five microlitres of water was deposited onto the surfaces, and after 5 seconds, images and measurements recorded. The CA was then measured using an average of three independent repeat measurements of each sample.

3.2.7. Protein Adsorption

The surface properties, and particularly hydrophobicity, can in turn have an effect on the amount of proteins adsorbed onto the alloy surface. It is important to consider the mode of binding of bacteria and other cells to determine the method through which antimicrobial properties may be imparted. As such, protein adsorption was calculated using a Pierce™ BCA Protein Assay Kit (Thermoscientific, UK), an assay based on bicinchoninic acid (BCA) for the colorimetric detection and quantification of total protein. The method uses the reduction of Cu^{2+} to Cu^{1+} by proteins in an alkaline media.

1 mL Dulbecco's Modified Eagle's Medium (DMEM) or 1 mL Mueller Hinton (MH) Broth was added to each sample condition in a 24 well-plate. DMEM was also added to an empty well to act as a blank control. All samples were then incubated at 37 °C and 5 % CO_2 for 24 hours. After 24 hours, the media was removed and samples washed.

BCA Reagent A and Reagent B were mixed in a 50:1 ratio to produce the working solution. 1 mL of the working solution was added to each sample condition and incubated at 37 °C for 30 minutes. Using a microplate reader (Spark, Tecan Trading AG, Switzerland) the absorbance of each sample was measure at 562 nm. Readings of a blank solution were then subtracted from each reading and averages calculated. A standard curve was plotted for each BCA standard against protein concentration in μg/mL, this was used to determine the protein concentration of each unknown sample. These calibration curves can be found in the Appendix (Figure A.2).

3.2.8. Microhardness

Vickers microhardness testing of mounted and polished samples was performed at 50x optical magnification and 100 g indentation force (Buehler Wilson VH1202). Five indentations were performed automatically per sample in a quincunx arrangement, with manual adjustments made when software failed to accurately locate indent corners (DiaMet, Buehler). Values were then averaged across each sample.

3.2.9. Bacterial Analysis

3.2.9.1. Minimum Inhibitory Concentration/ Minimum Bacterial Concentration Determination

To determine the minimum inhibitory concentration and minimum bacterial concentration (MIC/MBC), a bacterial culture was prepared and stock solution of $CuSO_4$ with double the expected MIC concentration was also produced. The stock solution was serially diluted in a 96-well plate, and inoculated with a standard bacterial concentration, and incubated overnight. After incubation, the MIC was identified as the first well without visible growth, and the MBC assessed by transferring 10 µL from each well to MH agar plates. Finally, after a further 24 hour incubation, the MBC was defined as the first droplet with no colonies.

3.2.9.2. Antimicrobial Analysis

Antimicrobial tests were carried out in relation to ISO 22196:2011 and JIS Z 2801 [272]. *Staphylococcus aureus* was utilised as it is a common Gram-positive bacterium often associated with implant infections, whilst *Pseudomonas aeruginosa* and *Escherichia Coli* were used as an

alternative Gram-negative bacterium. All samples were sterilised by ethanol in dark conditions for 30 minutes and left to dry for 24 hours.

Samples were then seeded with 5 μL of bacteria and a coverslip placed on top, in a petri dish with a sterile tissue wetted with 2 mL of Dulbecco's phosphate-buffered saline (DPBS). The samples were then incubated at 37 °C for 24 hours. After 24 hours, the samples were retrieved and placed in 5 mL of DPBS. Solutions containing the samples were vortexed for 2 minutes, ensuring the sample and cover slip were separated. 100 μL of the DPBS solution was extracted, placed into a 96 well plate and serially diluted in DPBS. 10 μL from each well was plated, using a spreader to ensure bacteria were well distributed and countable. Samples were cultured at 37 °C for 24 hours, before being counted.

3.2.9.3. Flow Cytometry

Samples from each condition were diluted ~1/500 for *P. aeruginosa*, in double filter sterilised DPBS. 500μL were transferred to plastic tubes and treated with 10μL of DiBAC4(3) and Propidium Iodide (PI) each following manufacturer recommendations. After 20 min of incubation at room temperature protected from light, flow cytometry was performed in a BD Accuri C6 flow cytometer (BD, Oxford, UK) using an excitation of 488nm and emission filters of 533/30 and 670 for DiBAC4(3) and PI, respectively. 25,000 events/sample were recorded at 1000-2500 events/s with all data collected and analysed using CFlow (BD, Oxford, UK). The resulting events were plotted on an FSC-A vs. SSC-A (forward scatter versus side scatter) plot and gated to remove the noise. Then, a positive, overnight culture, and negative, same culture heat treated at 80 °C for 15 min, controls were used to define areas of “Alive”, “Damaged” and “Dead” bacteria. Percentages of each gated area, resulting histograms and events corrected with

appropriate dilution factors were performed in triplicate with average and standard deviation reported.

3.2.10. *In Vitro* Analysis

Murine pre-osteoblast MC3T3 cells were inoculated in T75 flasks and incubated at 37 °C in basal media consisting of Dulbecco's Modified Eagle's Medium (DMEM) supplemented with 10 % foetal bovine serum, 12 % L-glutamine and 1 % penicillin/streptomycin. Cells were detached from the flasks, counted and diluted to seed $2x10^4$ cells per sample in a 24 well plate. After 20 minutes of contact to enable cell adhesion, 1 mL of fresh basal media was added to each well and cells incubated at 37 °C and 5 % CO_2.

3.2.10.1. Cytotoxicity Analysis

A live/dead assay was performed on three samples per condition, each stained with 200 µL of a 5mM calcein-AM and 1.5 mM propidium iodide solution and incubated for 30 minutes. Stained samples were inverted and imaged using a digital inverted microscope at x10 magnification (EVOS M5000, Invitrogen, USA). Cell viability was calculated using ImageJ (ImageJ 1.54j).

3.2.10.2. Metabolic Activity Assay

To assess metabolic activity and proliferation of cells deposited on the surface, 0.75 mL of basal DMEM containing 10 % Alamar Blue was added to the seeded samples. After 4 hours of incubation at 37 °C, a microplate reader (Spark, Tecan Trading AG, Switzerland) was utilised to carry out fluorescence measurements with excitation and emission wavelengths of 560 nm and 590 nm, respectively.

3.3. Results

3.3.1. Microstructural Characterisation and Phase Identification

Figure 3.2 illustrates the backscatter electron images of Ti-Cu alloy surfaces with 11.5 and 33 wt.% Cu, revealing their microstructure under different heat treatment conditions. As observed in Figure 3.2a, the Ti-11.5Cu as cast (11 ac) sample has a fine laminar structure, with a mixture of needle-like and rounded features (0.94 x 2.29 μm), which upon homogenisation (11 hom) becomes ultra-fine laminar. Through further ageing heat treatments, the Ti-11.5Cu 760 (11 AT760) has a more globular microstructure, consisting of a mixture of flakes and needles of a Cu-rich phase, depicted by the brighter regions. Whereas the samples aged at 820 °C (11 AT820), has a much coarser globular microstructure within an extremely fine lamellar structure, with thickness of around 80 nm. Figure 3.2e shows Ti-33Cu as cast (33 ac) possesses a dendritic microstructure with an intergranular structure that, upon homogenisation (33 hom), increase in size.

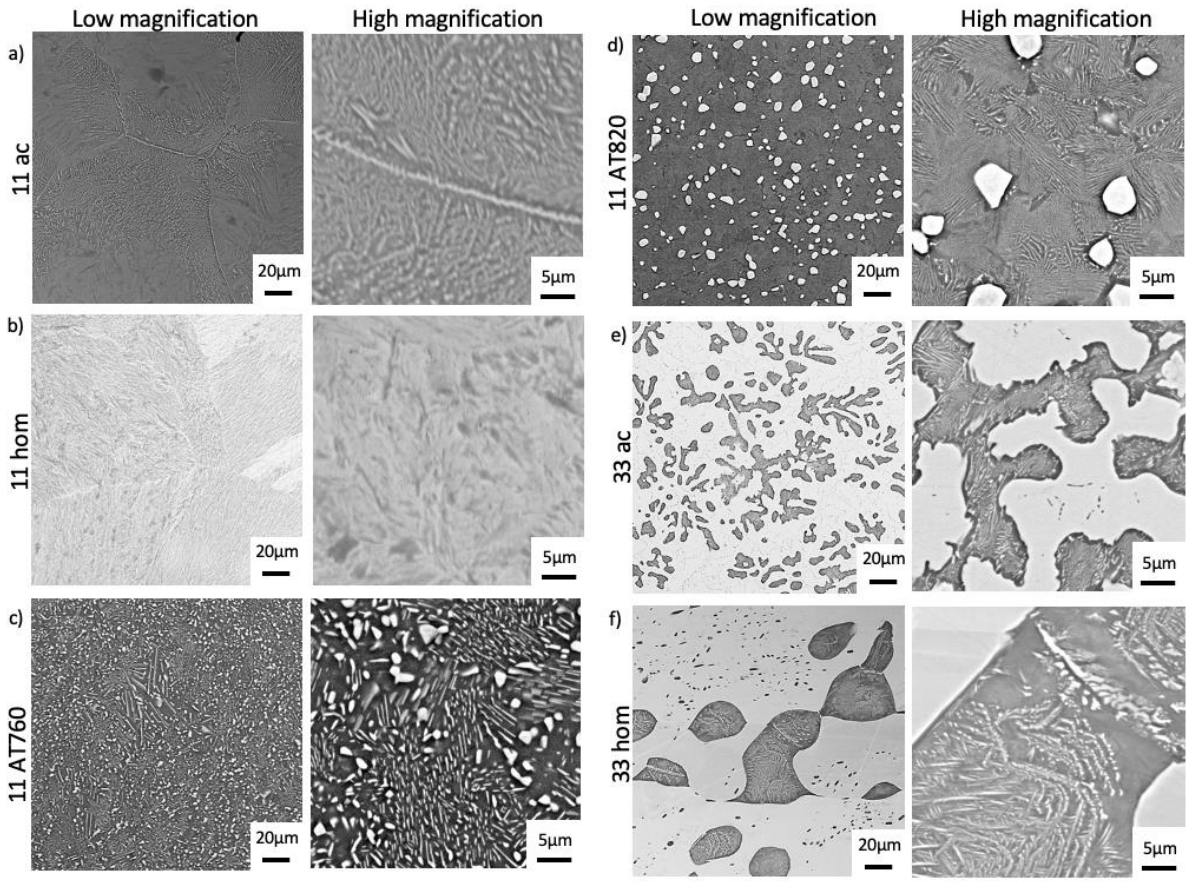

Figure 3.2: Low and high magnification BSE SEM images of Ti-11.5Cu (a) as cast, (b) homogenised, (c) homogenised and aged 760°C and (d) homogenised and aged 820°C and Ti-33Cu (e) as cast and (f) homogenised.

However, it is important to note that higher magnifications, i.e. 5000x, can result in certain microstructural features being cut off or excluded from the image field of view, which may introduce a bias in the analysis. This phenomenon is clearly demonstrated in Figure 3.3, where higher magnification micrographs show truncated features that could lead to an incomplete representation of the microstructure. Conversely, micrographs captured at lower magnifications, such as 1000x or 2000x, offer a broader field of view. At such low magnifications, nanoscale features may not be fully captured within the micrograph, potentially misleading the interpretation of precipitate size distribution, morphology, or other critical characteristics.

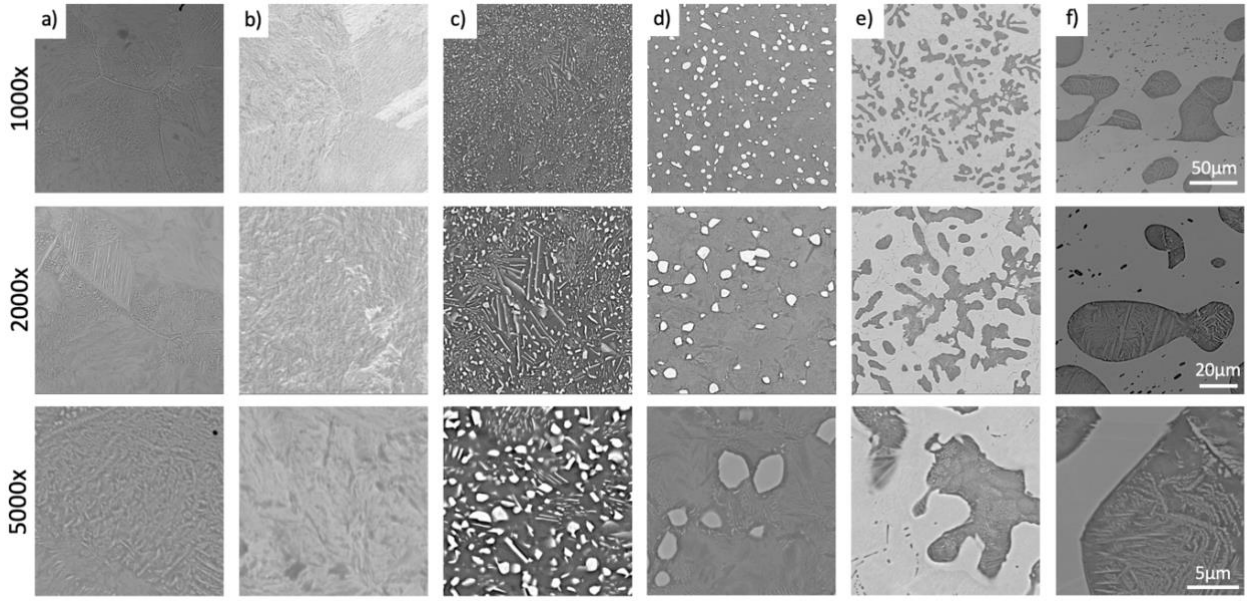

Figure 3.3: BSE SEM micrographs at 1000x, 2000x and 5000x magnification of (a) 11 ac, (b) 11 hom, (c) 11 AT760, (d) 11 AT820, (e) 33 ac and (f) 33 hom.

The XRD spectra for the cast Ti-11.5Cu and Ti-33Cu alloys, both before and after heat treatment, are presented in Figure 3.4. Diffraction peaks for Ti_2Cu and Ti_3Cu phases exhibit significant overlap, rendering this method ineffective for precise differentiation between these phases [162]. For all Ti-11.5Cu and Ti-33Cu samples, the diffraction peaks corresponding to α-Ti and Ti_2Cu were consistently observed. Notably, in the Ti-33Cu alloys, additional peaks were identified at 2θ angles of 31.5° and 47° equating to the Ti_2Cu phase.

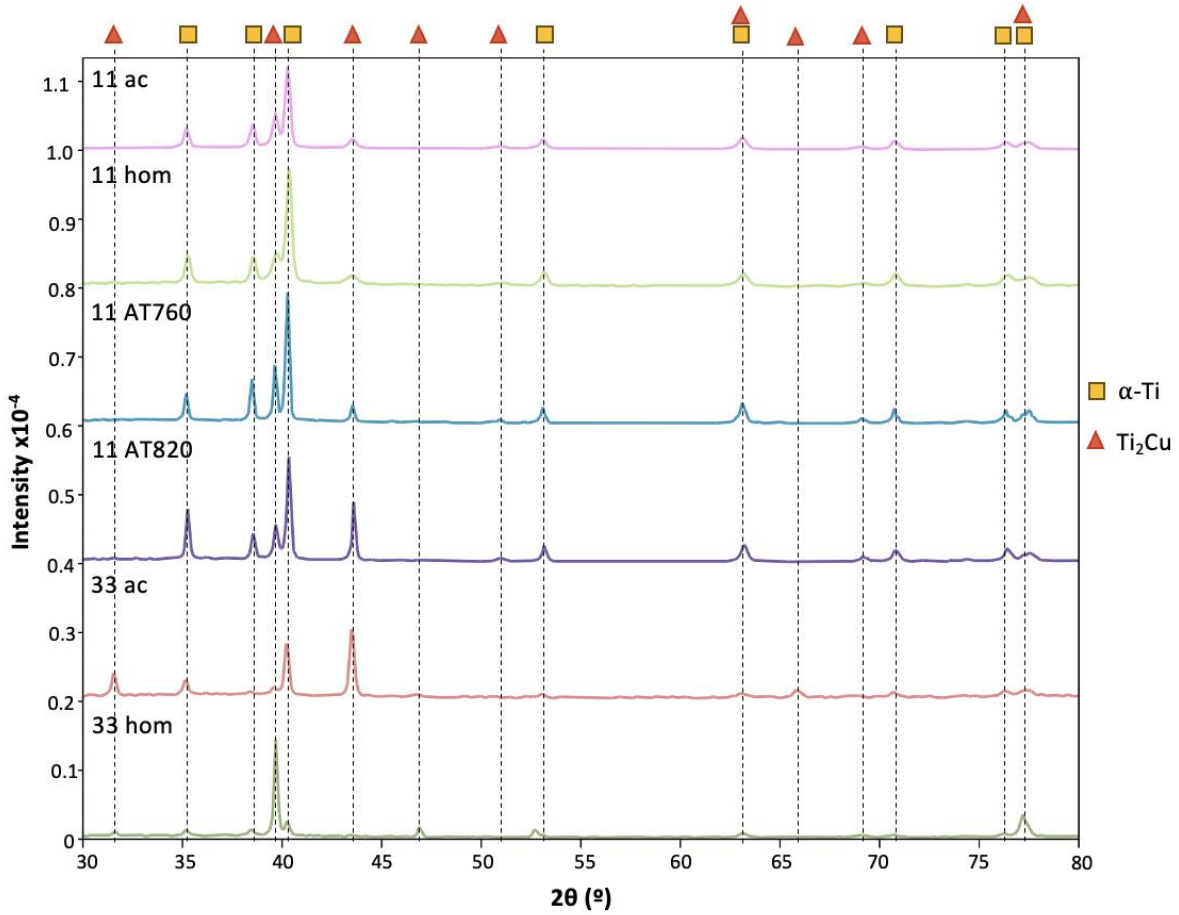

Figure 3.4: XRD spectra of Ti-Cu cast, and heat treated alloys, showing the presence of α-Ti and Ti_2Cu in all alloys.

The phase identification was refined through a combination of SEM-EDX and TEM-EDX, as shown in Figure 3.5. These analyses were conducted to ensure accurate phase determination, particularly given the peak overlap between Ti_2Cu and Ti_3Cu phases in the XRD spectra. All phases were determined to be Ti_2Cu, except for the ultrafine lamellar present in the 11 AT820 sample, which appear to be Ti_3Cu.

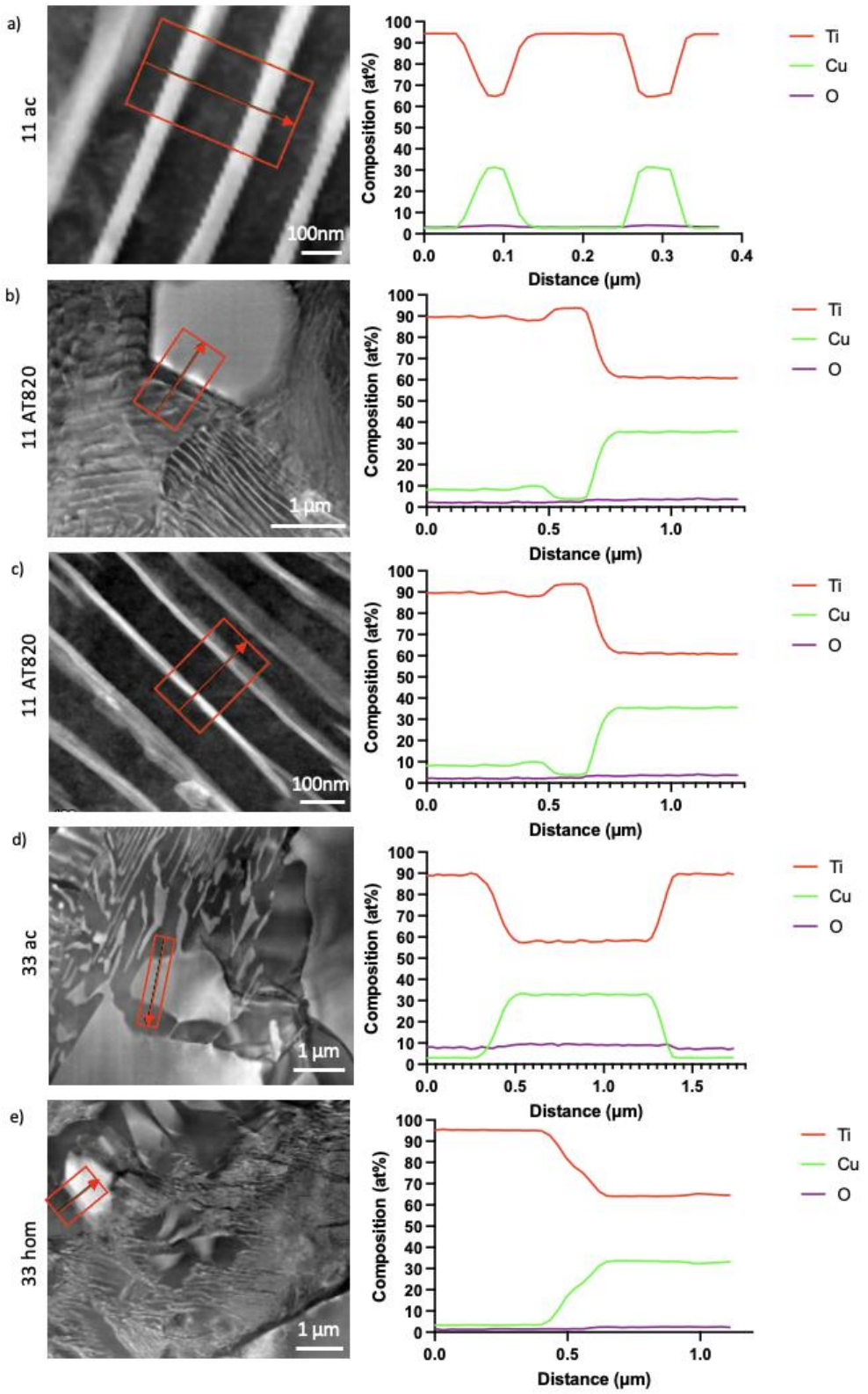

Figure 3.5: TEM high-angle annular dark-field (HAADF) images and EDX line scans of (a) 11 ac, (b-c) 11 AT820, (d) 33 ac and (e) 33 hom.

3.3.2. Cu Ion Release

ICP-OES analysis demonstrated no measurable Cu ion release from all Ti-Cu samples after 1, 3 and 7 days in 0.9 % NaCl solution stored at 37 °C. The limit of detection for this study was between 1-10 ppb of Cu.

3.3.3. Contact Angle Analysis

Figure 3.6 presents the contact angle (CA) measurements for different Ti-Cu specimen. The Ti64 alloy exhibited a contact angle of 72°, while the 11 ac sample displayed the highest hydrophilicity, as indicated by its lower CA. The 11 hom samples showed slightly lower wettability than Ti64 (7 % reduction) and , while the remainder exhibited higher CA, suggesting a more hydrophobic surface. The 33 ac and 33 hom samples, displayed the highest contact angles, indicating a shift in hydrophobicity with an increase in Cu content. Notably, the 33 ac sample demonstrated the highest contact angle among all tested materials, and is also the most antimicrobial surface. These variations in wettability are indicative of differences in composition and surface chemistry, which may influence bacterial and cell adhesion.

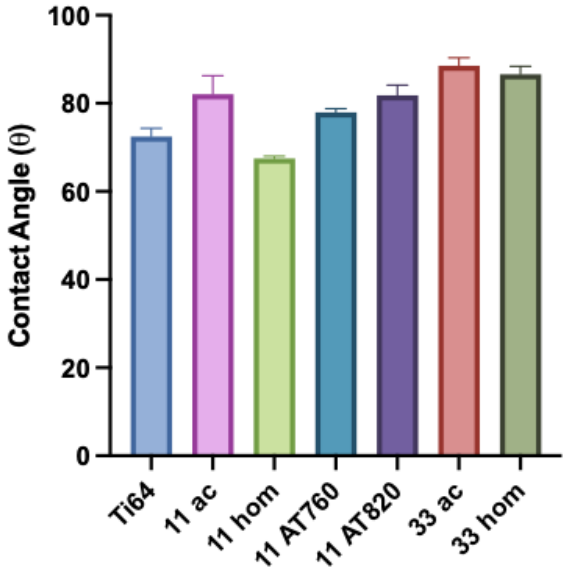

Figure 3.6: Contact angle data for Ti-64 and Ti-Cu alloys (n=3).

3.3.4. Microhardness

Figure 3.7 shows the microhardness of the arc melted Ti-Cu alloys. It can be noted that there is little variation in the microhardness of each sample condition, except for the 11 hom sample. Ti-6Al-4V, the current standard material for metallic implants, has a microhardness of approximately 350 HV (depicted on Figure 3.7 by the dashed line), whereas bone is around 21.57-51.82 HV [273]. This shows that the majority of the Ti-Cu alloys possess a slight decrease compared to Ti-6Al-4V, but further reductions are needed to more closely match that of bone. 11 ac and 11 AT820 alloys showed a 20 % decrease, whereas 11 AT760 and 33 ac showed around 30 % decrease as compared to Ti-6Al-4V. 33 hom showed a 39 % decrease and largest reduction in microhardness as compared to Ti-6Al-4V. However, 11 hom showed a 13 % increase.

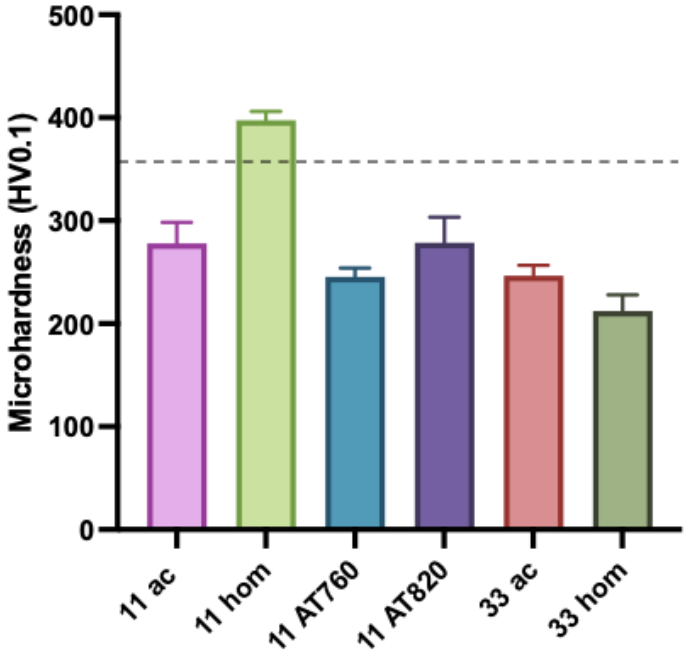

Figure 3.7: Microhardness(HV0.1) data for all arc melted Ti-Cu samples. The dashed line represents the microhardness of Ti-6Al-4V (n = 5).

3.3.5. Bacterial Analysis

3.3.5.1. MIC and MBC Determination

The MIC and MBC of $CuSO_4$ for *S. aureus* was determined to be 1024 µg/mL and for *E. coli* was 480 µg/mL. This highlights the variation in potential antimicrobial effect of Cu ions on different bacterial species.

3.3.5.2. Antimicrobial Analysis

Figure 3.8 shows the antimicrobial data for Ti-Cu alloys against negative (Ti-6Al-4V) and positive (Cu) controls for a) *S. aureus*, b) *P. aeruginosa* and c) *E. coli* after 24 hours of incubation. These results show that the antimicrobial effect is dependent on both alloy and bacterial species, with 11 AT820 and 33 ac being the best performing alloys against *S. aureus*,

however, no statistically significant efficacy was apparent from any Ti-Cu alloys against *E. coli* (Figure 3.8c). It should be noted that additions of 11.5 % Cu did not lead to a reduction in bacterial populations; in fact, some samples (11 ac and 11 hom) exhibited enhanced colony-forming units compared to Ti-6Al-4V when tested against *S. aureus*. The antimicrobial test results against *P. aeruginosa* showed no reduction in colony-forming units (CFUs) for the Ti-Cu alloys, while the Ti-6Al-4V control exhibited a decrease (Figure 3.8b).

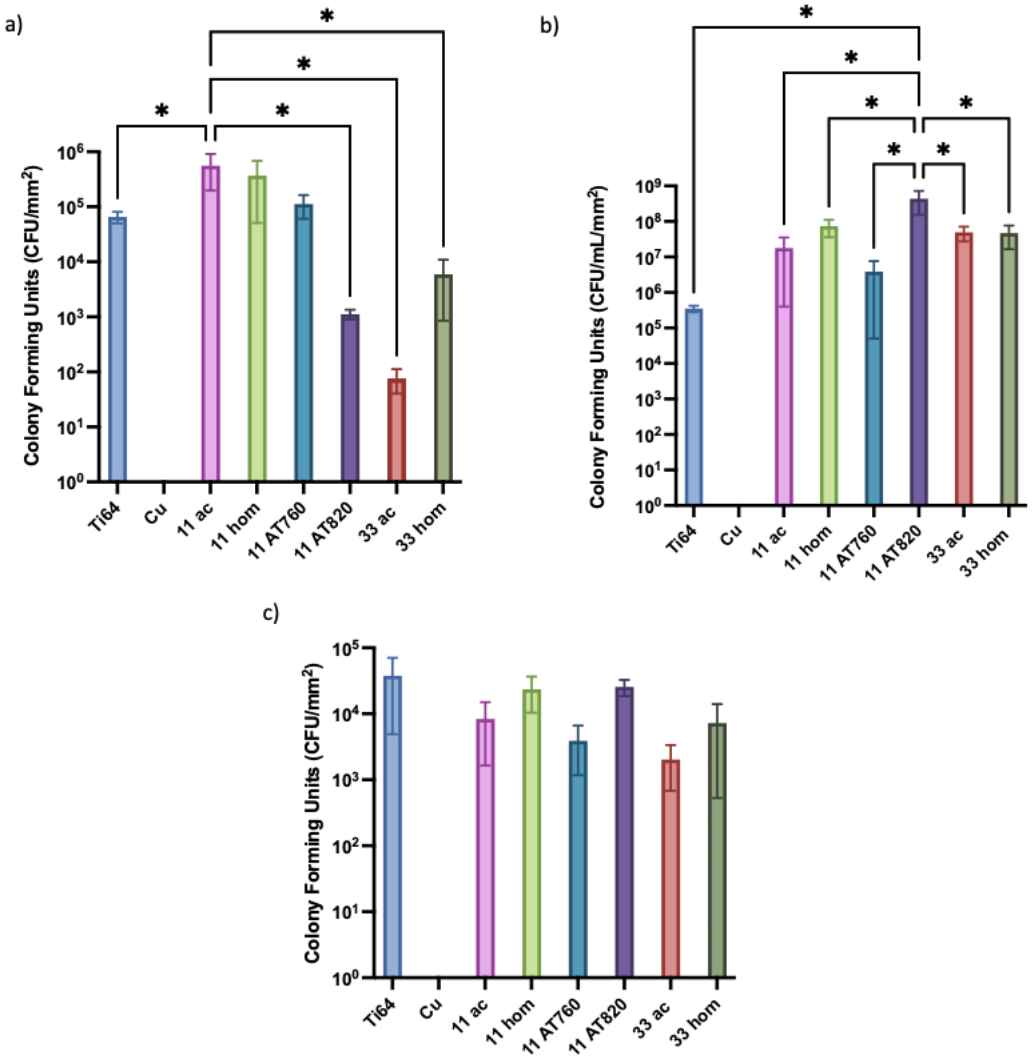

*Figure 3.8: Antimicrobial analysis of Ti-Cu alloys relating to (a) S. aureus, (b) P. aeruginosa and (c) E. coli. * represents values where $p \leq 0.05$ (n=3).*

3.3.5.3. Flow Cytometry

Flow cytometry was utilised to rapidly and accurately assess the impact of Ti-Cu alloys on bacterial viability by categorising *P. aeruginosa* cells as alive, damaged, or dead. Figure 3.9 presents the percentage distribution of cells within each category for the tested alloys. However, no clear trends could be established using this method. This limitation arises from surface oxidation occurring during antimicrobial testing, which interferes with the flow cytometer readings and subsequently distorts the results. This issue is particularly evident in the Cu sample, which appears to retain 72.6 ± 1.8 % viable bacteria, highlighting the potential inaccuracies introduced by surface oxidation.

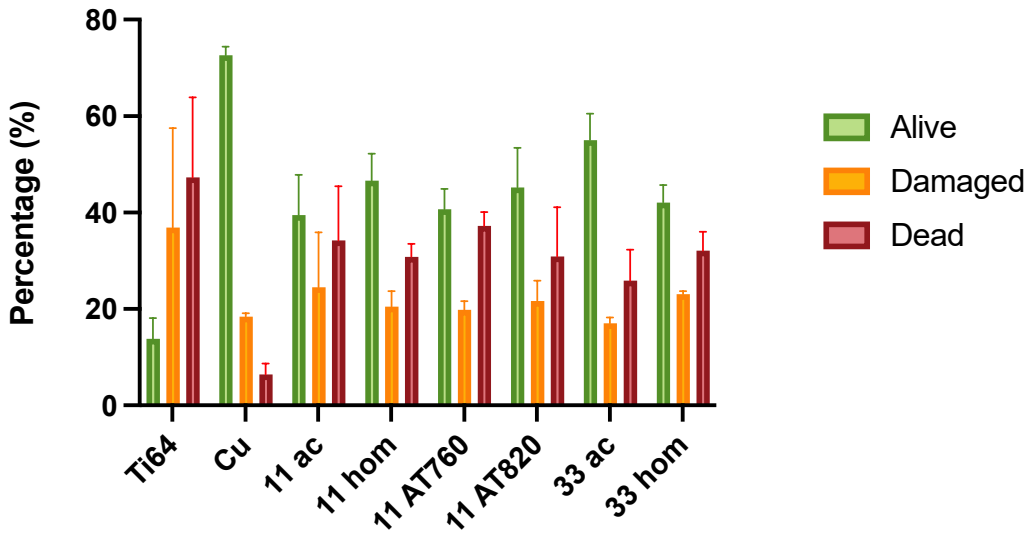

Figure 3.9: Analysis of antimicrobial efficacy of Ti-Cu alloys against P. aeruginosa using flow cytometry (n=3).

3.3.6. Compositional Analysis

To unpick whether specific microstructural features were associated with differences in antimicrobial efficacy, MATLAB was used to calculate the area covered by the Cu rich phase within the alloy and mean area of the precipitates within the samples.

As an initial study, various precipitate descriptors were identified and analysed from BSE SEM micrographs taken at magnifications of 1000x, 2000x, and 5000x (Table 3.3). The goal of this analysis was to investigate the structural characteristics and behaviour of precipitates at different magnifications, and while a spread in the data is evident, trends across the different magnification levels remain consistent, as illustrated in Table 3.3. This suggests that, despite variations in the data, certain consistent patterns or behaviours are present in the microstructure, regardless of the magnification level. Though careful consideration of magnification effects is necessary when interpreting the results.

Table 3.3:Microstructural features of Ti-Cu alloys, describing the area covered by Ti_2Cu phase and precipitate characteristics, extracted from BSE micrographs at x1000, x2000 and x5000 magnification.

	Area covered by Ti_2Cu phase (%)			**Area of precipitates (μm)**			**Perimeter of precipitates (μm)**			**Major Axis of precipitates (μm)**			**Minor Axis of precipitates (μm)**		
	1000x	**2000x**	**5000x**	**1000x**	**2000x**	**5000x**	**1000x**	**2000x**	**5000x**	**1000x**	**2000x**	**5000x**	**1000x**	**2000x**	**5000x**
11 ac	34.36	6.39	48.14	1.50	0.33	0.59	5.71	3.52	4.69	2.29	1.55	1.13	0.94	0.37	0.46
11 hom	32.12	48.63	69.27	1.23	1.72	26.06	5.45	8.85	24.84	2.12	1.98	2.55	0.91	0.96	1.57
11 AT760	23.07	24.07	25.87	1.99	1.36	0.38	5.11	4.85	2.83	2.36	2.20	1.08	1.11	0.79	0.46
11 AT820	11.23	9.90	13.76	3.84	1.48	1.06	4.47	2.89	3.17	2.12	1.36	1.21	1.18	0.65	0.63
33 ac	26.59	70.69	72.12	37.57	8.74	3.68	23.50	7.30	8.16	7.50	2.40	2.45	3.86	1.04	0.82
33 hom	19.95	77.95	47.11	11.27	9.50	140.10	7.45	7.78	63.08	2.75	2.62	14.64	1.26	1.21	8.34

Figure 3.10 illustrates the amount of Ti_2Cu phase expected in the Ti-Cu alloys through use of the Scheil predictor on ThermoCalc, in combination with the Lever Rule for the heat treated samples. This highlights that as the predicted amount of Ti_2Cu phase increases, largely there is a negative trend in the CFU count of the alloys, suggesting an increase in antimicrobial efficacy.

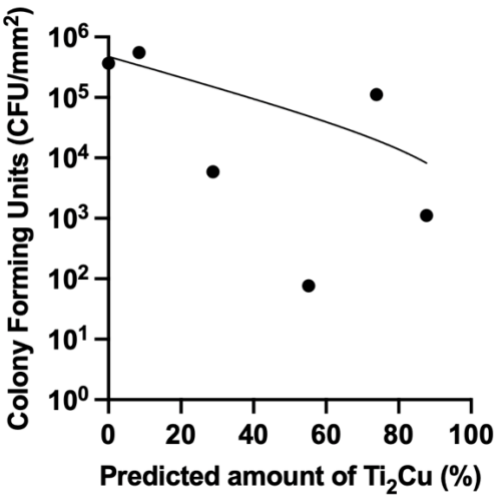

Figure 3.10: Correlation between Colony Forming Units of S. aureus and the predicted amount of the antimicrobial Ti_2Cu phase through ThermoCalc 2024a with TCTI3 database using the Scheil Predictor (as cast samples) and the Lever Rule (homogenised and heat treated samples).

Table 3.4 depicts the individual Hu moment representations. Hu moments are invariant shape descriptors that capture different aspects of an object's symmetry, spread, and complexity. Higher values indicate greater asymmetry and complexity, while lower values suggest simple, symmetric shapes like circles or regular polygons. The wide variation and high standard deviation values for some sample conditions, represents the shape differences of the precipitates. In particular, 11 ac has a wide range of both circular and rod-like precipitates, represented by both low and high values respectively.

Table 3.4:Average Hu moments (ϕ_{1-7}) of each Ti-Cu alloy and standard deviation, calculated from micrograph taken at x1000 magnification.

	ϕ_1		ϕ_2		ϕ_3		ϕ_4		ϕ_5		ϕ_6		ϕ_7	
	Average	**Std Dev**	**Average**	**Std Dev**	**Average**	**Std Dev**	**Average**	**Std Dev**	**Average**	**Std Dev**	**Average**	**Std Dev**	**Average**	**Std Dev**
11 ac	0.41	0.27	0.18	0.84	$2.84\text{x}10^{-2}$	0.40	$1.11\text{x}10^{-2}$	0.21	$6.00\text{x}10^{-2}$	3.79	$2.31\text{x}10^{-2}$	1.12	$1.28\text{x}10^{-2}$	0.83
11 hom	0.44	0.21	0.15	0.30	$2.38\text{x}10^{-2}$	0.06	$7.44\text{x}10^{-3}$	0.04	$1.58\text{x}10^{-3}$	0.05	$4.64\text{x}10^{-3}$	0.07	$-6.49\text{x}10^{-5}$	$4.68\ \text{x}10^{-3}$
11 AT760	0.28	0.16	0.06	0.21	$7.26\text{x}10^{-3}$	0.04	$3.20\text{x}10^{-3}$	0.02	$7.16\text{x}10^{-4}$	0.02	$2.34\text{x}10^{-3}$	0.04	$-1.33\text{x}10^{-5}$	$1.72\ \text{x}10^{-3}$
11 AT820	0.20	0.08	0.02	0.06	$1.42\text{x}10^{-3}$	$4.18\ \text{x}10^{-3}$	$3.85\text{x}10^{-4}$	$1.76\ \text{x}10^{-3}$	$4.32\text{x}10^{-6}$	$3.22\ \text{x}10^{-5}$	$1.17\text{x}10^{-4}$	$6.93\ \text{x}10^{-4}$	$-6.44\text{x}10^{-7}$	$8.09\ \text{x}10^{-6}$
33 ac	0.26	0.11	0.04	0.06	$4.10\text{x}10^{-3}$	$7.3\ \text{x}10^{-3}$	$8.16\text{x}10^{-4}$	$2.38\ \text{x}10^{-3}$	$8.76\text{x}10^{-6}$	$5.79\ \text{x}10^{-5}$	$2.21\text{x}10^{-4}$	$1.26\ \text{x}10^{-3}$	$-3.65\text{x}10^{-7}$	$7.15\ \text{x}10^{-6}$
33 hom	0.24	0.09	0.04	0.08	$1.10\text{x}10^{-3}$	$4.24\ \text{x}10^{-3}$	$3.30\text{x}10^{-4}$	$1.63\ \text{x}10^{-3}$	$3.37\text{x}10^{-6}$	$3.67\ \text{x}10^{-5}$	$1.11\text{x}10^{-4}$	$1.00\ \text{x}10^{-3}$	$-3.71\text{x}10^{-7}$	$4.09\ \text{x}10^{-6}$

3.3.7. Bacterial Imaging on the Ti-Cu Surfaces

Figure 3.11 presents both confocal live/dead imaging and scanning electron microscopy (SEM) micrographs to assess *S. aureus* viability and adhesion on different titanium alloy surfaces. The confocal images (Figure 3.11a–b) reveal a higher proportion of dead bacteria on 33 ac, in comparison to 11 AT820, indicating that 33 ac exhibits superior antibacterial properties.

SEM images (Figure 3.11c–e) further confirm differences in number of bacteria adhered to the alloys surfaces. On the Ti-6Al-4V surface (Figure 3.11c), large bacterial clusters, as shown by the arrows, can be observed with large numbers of nanoscale proteins also adhered. Whereas 33 ac (Figure 3.11e) exhibits fewer attached bacteria, supporting its enhanced bactericidal performance. Furthermore, Figure 3.11e shows minimal protein adsorption on the 33 ac alloy, whereas 11 AT820 surface (Figure 3.11d) shows moderate levels of bacterial adhesion, suggesting a lesser antibacterial effect. However, most significantly, it can be seen that bacterial adhesion is not dependent on the underlying microstructure, with bacteria being seen to adhere to both the Ti and Cu-rich phases. Additionally, Figure 3.11f reveals nanoscale protein adsorption on 11 AT820, highlighting potential biofilm formation mechanisms. These findings suggest that surface modifications significantly influence bacterial adhesion and viability, with 33 ac demonstrating the most promising antibacterial performance.

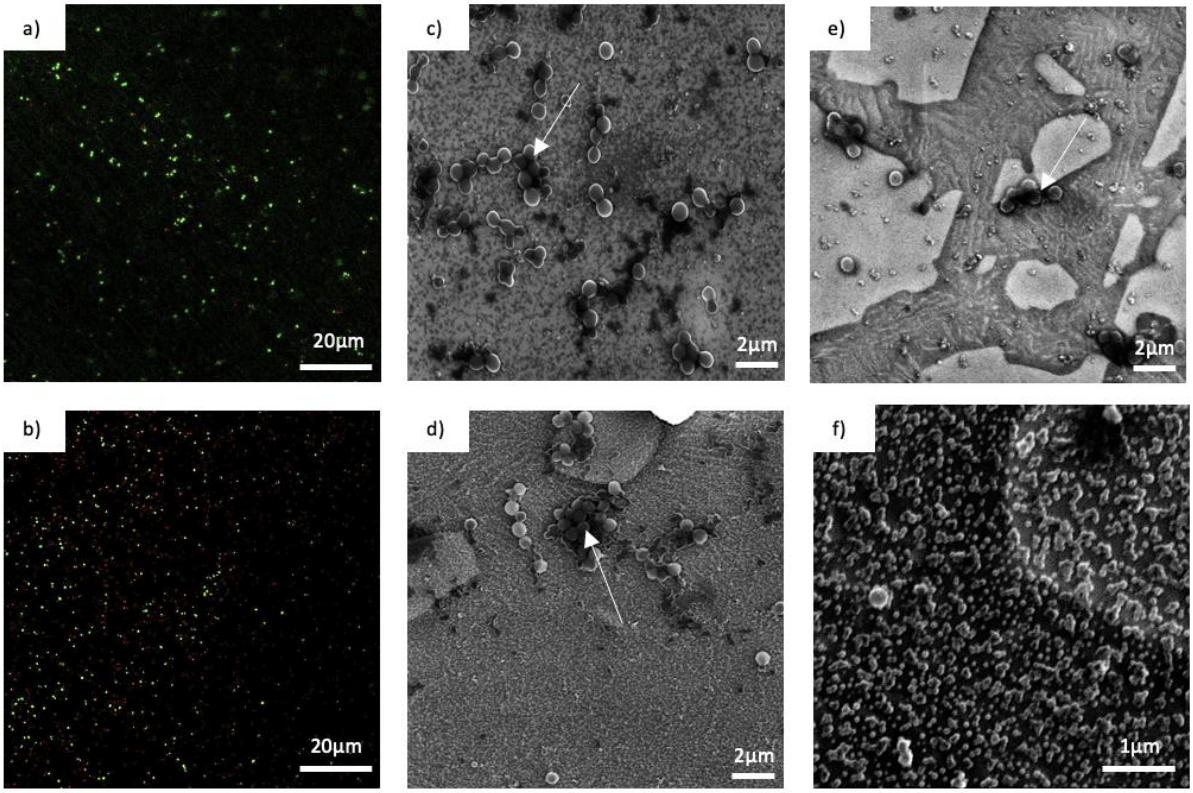

Figure 3.11: (a–b) Confocal live/dead images showing the viability of S. aureus on the surface of (a) 11 AT820 and (b) 33 ac. (c–e) SE SEM micrographs depicting S. aureus on the surfaces of (c) Ti-6Al-4V, (d) 11 AT820, and (e) 33 ac. Arrows point to the bacteria within the images. (f) High magnification SEM image showing the small proteins adhered to the surface of the 11 AT820 sample.

3.3.8. Protein Adsorption

Samples were immersed in cell culture media and bacterial media and assessed after 24 hours using a BCA Protein adsorption assay. It was showed that little to no proteins were adsorbed on the 11 AT820 and 33 ac alloys for the cell culture media, as demonstrated by Figure 3.12a. However, around 25 µg/mL were identified on the Ti64 samples. For the bacterial media, the Ti-64 sample was contaminated and so results not possible for these samples (Figure 3.12b). However, more proteins were adsorbed with the bacterial media on the 11 AT820 and 33 ac samples, than with the cell culture media. These samples were assessed due to their high antimicrobial efficacy.

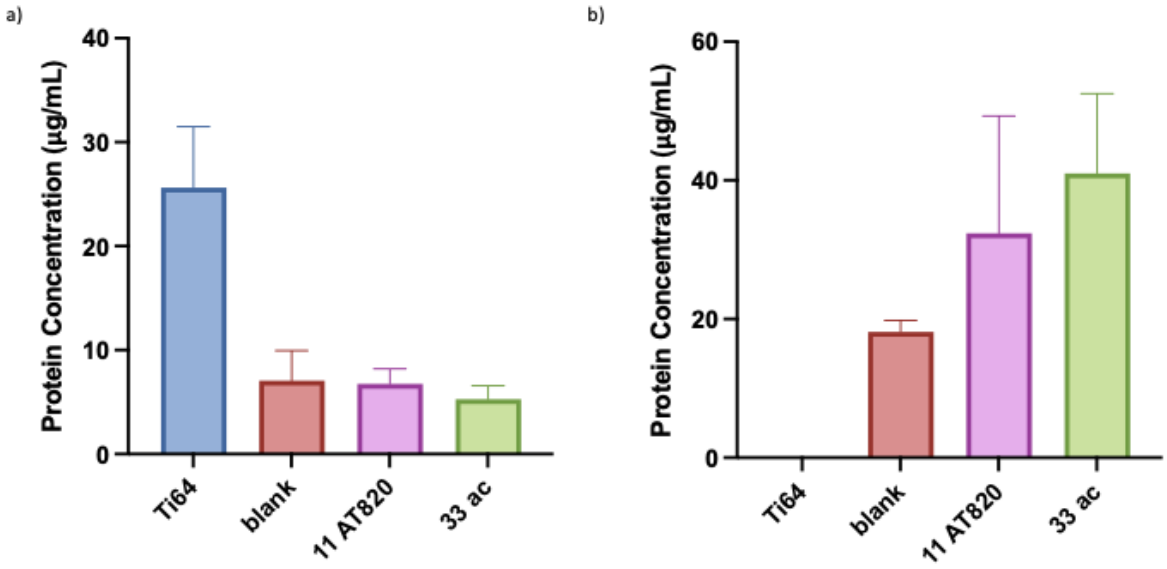

Figure 3.12: Measured protein concentration on Ti64, a blank/empty well, and 11 AT820 and 33 ac Ti-Cu alloys for (a) cell culture and (b) bacterial media (n=3). The calibration curves used to calculate the protein concentrations can be found in the Appendix.

3.3.9. Cytotoxicity

The cytotoxicity of the Ti-Cu alloys was evaluated using live/dead imaging and the metabolic activity through an Alamar Blue assay (Figure 3.13). Generally, minimal cell death is apparent after 1 day, however there is a general reduction in cell viability over time to ≈ 50 %. Except, however, results indicate that 11 ac exhibits limited cytotoxicity after 7 days with cell viability remaining at 97 % (Figure 3.13 and 3.13a). There is a marked reduction in cell viability after 7 days contact with Ti-6Al-4V, whilst surprising it is worth noting the biocompatibility concerns relating to the alloy and the limits of *in vitro* testing.

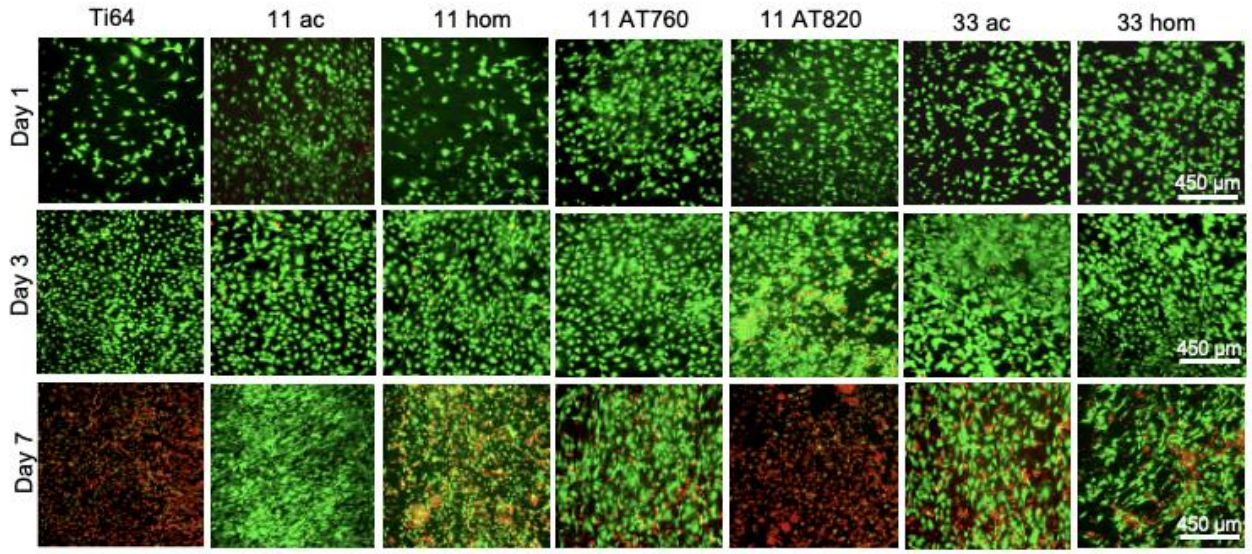

Figure 3.13: Influence of alloy composition and heat treatment protocol on murine pre-osteoblast cells over seven days through fluorescent images, of live (green) and dead (red) cells.

Notably, following heat treatments, there is a significant increase in cell death, with 11 AT820 showing the highest level of cytotoxicity and cell viability rapidly reducing after just three days to 52 %, and 29 % after seven days. In contrast the Alamar Blue assay indicates a general increase in metabolic activity of all the samples across the seven day testing period (Figure 3.14b).

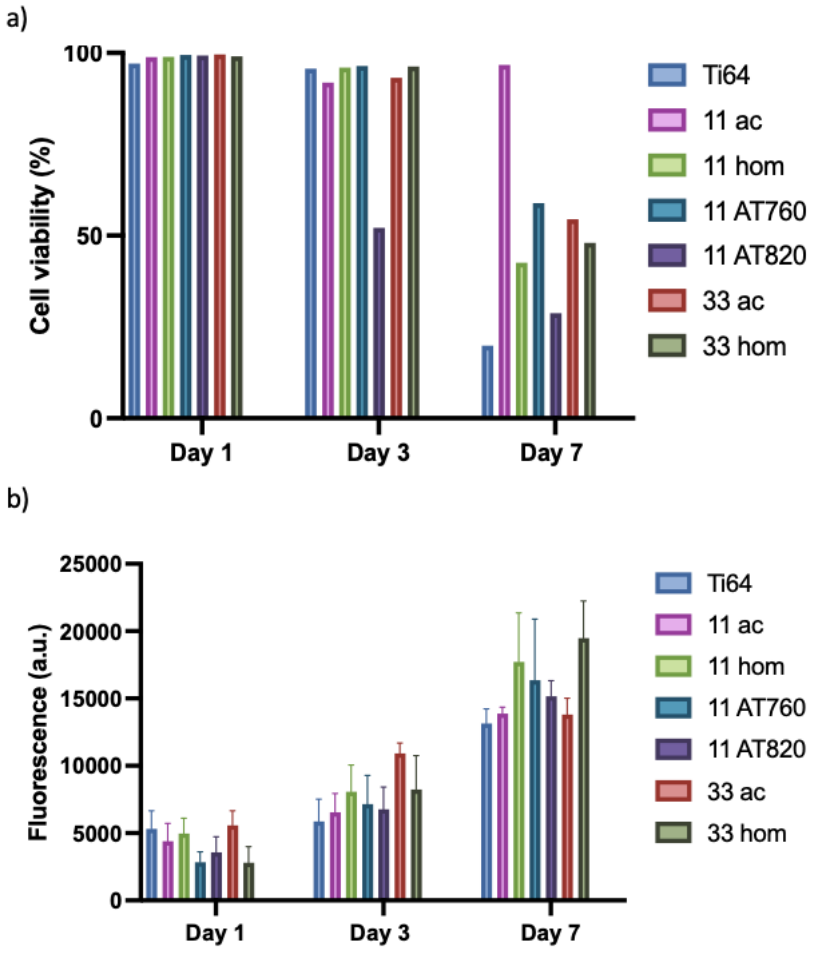

Figure 3.14: Influence of alloy composition and heat treatment protocol on murine pre-osteoblast cells over seven days. (a) quantification of cell viability, (b) metabolic activity assessed via Alamar Blue assay. (n=3)

3.4. Discussion

Within the binary Ti-Cu alloy system (Figure 3.1), Ti_2Cu is the only secondary phase expected below a 40 wt.% Cu incorporation. As such this offers an ideal opportunity to explore the impact of microstructural characteristics on desirable target biological properties for a novel orthopaedic implant alloy. In this work, focus has been on tuning antimicrobial efficacy and balancing this against minimising any cytotoxicity of Ti-Cu alloys to native bone cells.

According to current literature, contact with Ti-Cu alloys containing Ti_2Cu phase interacts with the cell wall of the bacteria, including the membrane proteins and glycoproteins [183]. Consequently, this affects cell metabolism and may cause direct damage to the cell wall and membrane, resulting in bacterial death. Through fine-tuning of the Ti_2Cu phase, the antimicrobial properties of the alloy can be optimised. Previous studies have demonstrated that an increase in Cu content can improve the antimicrobial efficacy [170, 172], however, the specific role of microstructure, precipitate size, and form have not previously been explored. This gap in knowledge underscores the importance of studying how microstructural features can be tailored to enhance antimicrobial action.

A key observation of this work is a negative correlation between the amount of Cu-rich phase and antimicrobial efficacy (Figure 3.15a – R^2 =0.9465), which contradicts previous research [171, 179, 182]. This finding challenges traditional assumptions about the relationship between copper content and antimicrobial efficacy, highlighting that the specific form and microstructural distribution of Ti_2Cu also play a crucial role. These observations also emphasise the need to focus on fine-tuning alloy composition and microstructure to optimise biological properties, such as antimicrobial efficacy. Through image analysis, it was determined that the size and shape of the precipitates has an impact on how effective they are at killing bacteria.

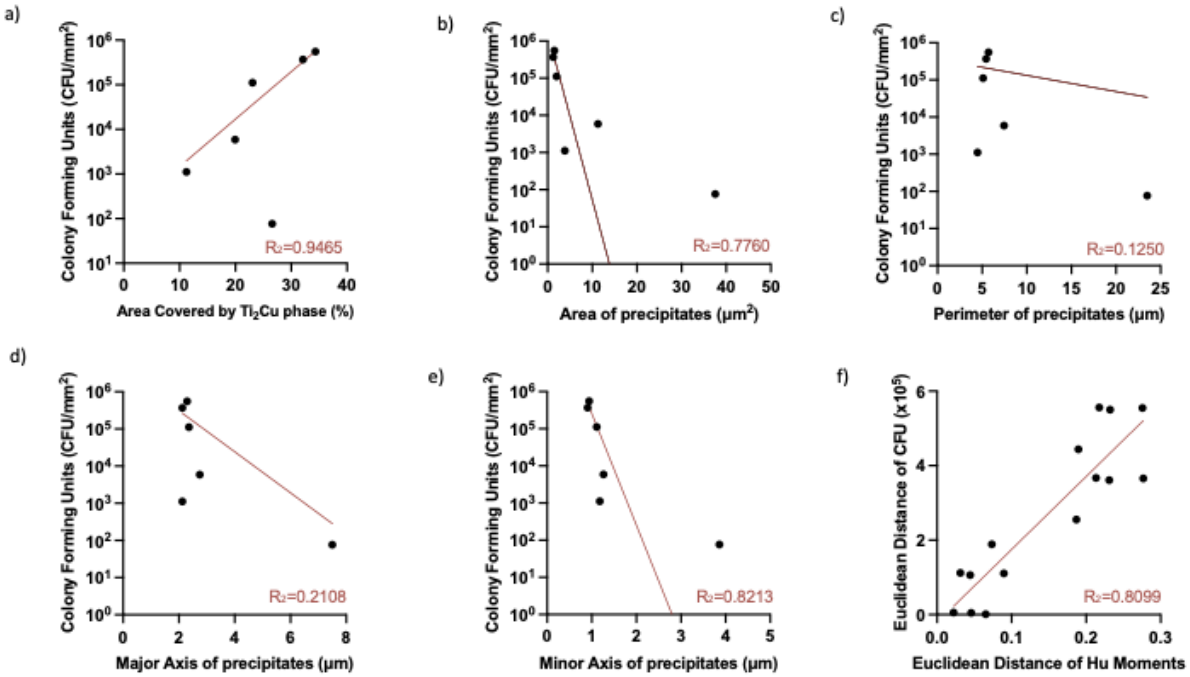

Figure 3.15: Image analysis of Ti-Cu alloys using MATLAB comparing the colony forming units (against S. aureus) to (a) the area covered by the Cu rich phase, (b) mean area of precipitates, (c) perimeter of precipitates, (d) major axis of precipitates, (e) minor axis of precipitates and (f) Euclidean distance of Hu moments and CFU.

Generally, increased area of Ti_2Cu phase was associated with higher bacterial growth (R^2= 0.9465), except for the outlier at 33 ac which was 28 % covered by Ti_2Cu phase and the most antimicrobial. Factors that appear to improve efficacy were increased precipitate area, perimeter and axis lengths. That said the high degree of variability in these quantified microstructural features is notable, particularly for samples 33 ac and 33 hom, as depicted by the high standard deviations, e.g. 261 % and 811 % compared to their averages respectively.

Although available literature suggests that it is the Ti_2Cu phase that has superior antimicrobial action, a Ti_3Cu phase has not been previously identified in these studies. In this study the contribution of these phases has not been differentiated in the image analysis performed and correlated against *in vitro* tests. Notably, in particular for the 11 AT820 sample that exhibits

Ti_3Cu microstructure in the range of 30 µm (Figures 3.2 and 3.3), we accept that at 1000x magnification these features were not easily distinguishable. That said, when the analysis was repeated at 2000x and 5000x magnification similar trends were observed (Figure 3.16). Therefore, both high and low magnification micrographs have inherent limitations that could influence the quality and accuracy of the analysis. Despite these challenges, the overall trends observed across the data suggest that the results are consistent.

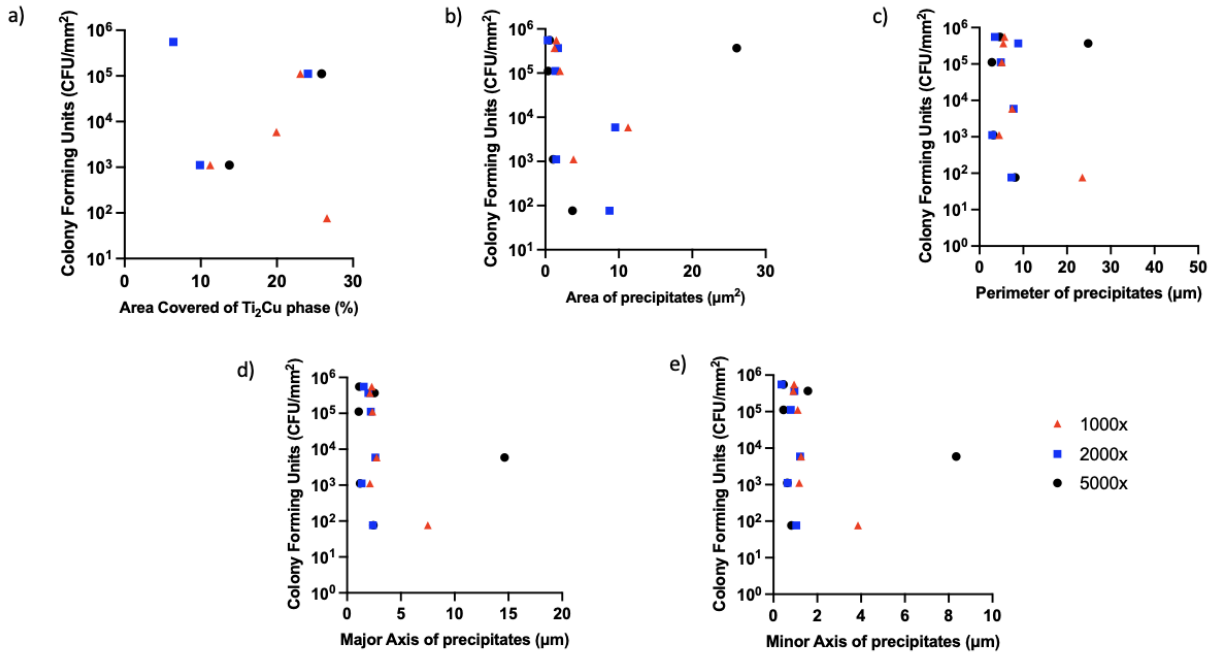

Figure 3.16: Correlation between Colony Forming Units (CFU/mm²) against S. aureus and microstructural features of precipitates in Ti-Cu alloys with (a) the area fraction covered by the Ti_2Cu phase, (b) area of individual precipitates, (c) the perimeter of precipitates, (d) the major axis of precipitates and (e) the minor axis of precipitates. Different magnifications are represented as follows: 1000x (red triangles), 2000x (blue squares), and 5000x (black circles).

Figure 3.15f shows the Euclidean distances of the calculated Hu moments against the Euclidean distances of the colony forming units. Hu moments were used to act as shape descriptors of the precipitates present in the Ti-Cu samples. Euclidean distances were then calculated as a measure

of the difference between the points, in order to equate the extent of the differences of the Hu moments and CFU. Separate graphs representing the individual Hu moments can be found in the Appendix (Figure A.1). Changes in surface morphology, as captured by Hu Moments, show a positive correlation with variations in bacterial growth (R^2=0.8099). In particular, more rounded features show a significant decrease in bacterial growth.

Interestingly, both 11 ac and 11 AT820 alloys were found to possess fine scale lamellar Ti_2Cu/Ti_3Cu structures, however, exhibit vastly different antimicrobial responses. The 11 AT820 also possesses larger round precipitates, around 5 μm diameter, which were found to produce the greater antimicrobial response. This suggests that copper precipitates, when too small, cannot penetrate the passivation film to interact with the bacteria, significantly diminishing their antimicrobial effectiveness [274]. Peng *et al.* also demonstrated that larger precipitates enhance antimicrobial performance, likely due to an increased surface contact area facilitating electron transfer [275], supporting this theory. The surface interaction between the alloy and bacterial cells is therefore a key consideration in optimising the material for biomedical use. These findings may differ from previous studies that linked the antimicrobial mechanism to increased Ti_2Cu, due to the absence of ion release in this study, unlike much of the prior research [171, 276].

The findings from Figure 3.15 suggest that both the size and shape of precipitates in an alloy can influence antimicrobial action. Rounded precipitates, as signified by a lower average Hu moment, seem to outperform irregular or elongated ones due to their broader average dimension, as determined from Figure 3.15f. It can be hypothesised that this positioning allows for electron transfer between the bacterial cells and the precipitates, potentially disrupting bacterial adhesion. Nevertheless, Figure 3.11 highlights that the bacteria adhere to both phases

present in the alloys, indicating that precipitates do not directly limit bacterial attachment. By optimising the size and shape of these precipitates, it may be possible to create a surface that prevents bacteria from bonding. Though this chapter only achieves this through alternative heat treatments, it opens up the possibility to utilise other approaches, e.g. different cooling rates [277], to optimise the microstructure for enhanced antimicrobial properties.

Surface wettability can also play a role in bacterial adhesion. Figure 3.17 illustrates the relationship between contact angle and bacterial adhesion, A weak trend of decreasing CFU counts with increasing contact angle is observed (R^2=0.1304), suggesting that more hydrophobic surfaces tend to inhibit bacterial adhesion. Specifically, alloys, with higher contact angles e.g. 11 AT820 and 33 ac, exhibit reduced bacterial adhesion due to limited surface interaction. These findings underscore the importance of surface characteristics such as surface roughness and chemical composition, beyond precipitate composition alone, in determining bacterial adhesion and thus antibacterial performance.

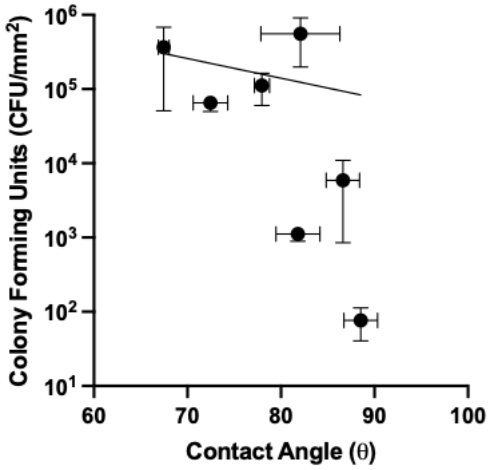

Figure 3.17: Contact angle data plotted in comparison to antimicrobial data against S. aureus.

Furthermore, the adhesion of proteins to metal alloy surfaces can significantly influence their antimicrobial efficacy by altering surface characteristics such as charge, wettability, and biofilm formation. Protein adsorption may either promote bacterial adhesion, reducing antimicrobial effectiveness, or inhibit bacterial colonisation depending on the alloy composition and surface modifications [278-281]. While proteins were identified in the bacterial SEM micrographs of these samples (shown in Figure 3.11f), Figure 3.12 shows no detectable protein adsorption in cell culture media. However, protein adsorption was shown to differ between bacterial and cell culture media, with greater protein adsorption from the bacterial media. This could be due to variations in protein composition, ionic strength and pH. These factors influence protein binding dynamics, surface interactions, and biofilm formation**,** leading to distinct adsorption behaviours on the alloy surfaces in different media and in the presence of other cells [278].

In addition to Ti_2Cu phases there is also the possibility of Cu ion release as a mechanism of action for Ti-Cu alloys. Copper ions can directly act on the surface of the bacteria, resulting in the membrane proteins failing and breaking, producing an antibacterial effect [177]. This interaction is not deemed to be solely mechanical but also biochemical; studies suggest Cu ions can alter protein structures and disrupt enzymatic functions [282, 283]. This occurs through binding to specific groups, such as sulphur or carboxylate, and generating superoxide radicals, which collectively contribute to significant bacterial damage [170]. These mechanisms highlight the multifaceted nature of Cu ions as an antimicrobial agent. Given the importance of combatting antimicrobial resistance, understanding these mechanisms may enable us to design alloys that can effectively tackle infections but also slow resistance development. In this work, however, ICP-OES analysis established the absence of detectable Cu^{2+} ion release from Ti-Cu alloys over a seven-day observation period. This finding suggests a lack of galvanic interactions between the alloy phases, indicating that no ion-mediated release mechanism is occurring.

Consequently, the observed antimicrobial activity can be attributed solely to a contact-dependent mechanism. Similar conclusions have been drawn in prior studies, where antimicrobial efficacy was associated with electron transfer rather than ion release [275, 284, 285]. This reinforces the idea that contact-based antimicrobial properties, e.g. those provided by the Cu-rich precipitates, are crucial in the antimicrobial efficacy of cast Ti-Cu alloys. The potential for ion release is however greatly influenced by the immersion environment. Given that serum proteins have been shown to enhance Cu ion elution the performance of these Ti-Cu alloys may vary in the body. As such, further investigations into how serum proteins affect ion release could provide valuable insights to support onward translation of novel biomedical alloys [286].

Nevertheless, we also see a variation in antimicrobial efficacy dependent on the bacterial species. In particular, though a change in antimicrobial efficacy for *S. aureus* dependent on microstructure is observed, this is not seen for the gram negative bacteria (*E. coli* and *P. aeruginosa*). However, the reliability of these results is uncertain due to the intrinsic genetic complexity of *P. aeruginosa*, which possesses multiple resistance mechanisms and adaptive survival strategies [287]. This opportunistic pathogen has a highly adaptable metabolism and an extensive resistance arsenal, including low outer membrane permeability, efflux pumps, and the ability to acquire resistance genes through horizontal gene transfer [287, 288]. Additionally, *P. aeruginosa* is capable of forming biofilms, which significantly enhance its resistance to antimicrobial agents and environmental stresses. The transition between planktonic and biofilm-associated states can lead to fluctuating antimicrobial susceptibility, further complicating the interpretation of test results [289]. Given these factors, the observed CFU persistence may not necessarily indicate the absence of antimicrobial activity but could instead reflect the intrinsic resistance and ability of *P. aeruginosa* to withstand adverse conditions.

Consequently, it was deemed that *P. aeruginosa* was not a suitable bacteria for further studies. Furthermore, *E. coli* has been noted to have many cellular resistance mechanisms against copper toxicity, which can cause resistance to copper-containing surfaces [290]. In particular, many genes have been identified within *E. coli* strains that have been related to copper resistance, such as copA and pcoABCD [291, 292]. Though copper resistant genes have been identified and found in natural environments, they are not as widely described [293]. Nevertheless, the MIC/MBC data predicts a higher antimicrobial efficacy of Cu to *E. coli,* suggesting that ion elution is essential for effects against *E. coli*.

Biocompatibility is a fundamental requirement for the development of any biomaterial. It is especially important for an antimicrobial alloy, to not only resist bacterial infection, but safely interact with native cells for which there are numerous types within bone tissue since it is both vascularised and infiltrated with nerves. One key aspect of evaluating cytocompatibility is through assessing metabolic activity, which provides insight into the cellular biochemical processes that reflect cell viability. However, it is important to exercise caution when interpreting metabolic activity data, as it does not directly equate to cell proliferation, growth, or apoptosis. These processes are complex and may not be fully captured by metabolic measures alone [294]. In this study, fluorescence readings over a seven-day period suggested an increase in pre-osteoblast activity. However, when compared with live/dead staining assays, significant cytotoxicity was revealed. Live/dead staining was performed on all samples across a seven-day contact period. After three days incubation, only minimal propidium iodide staining was observed across most samples, apart from the 11 AT820 sample, which showed around 50 % cell viability, indicating a marked cytotoxic response. By day seven, most samples, apart from 11 ac, exhibited substantial cytotoxicity (<60 % cell viability). These findings highlight that Cu is highly cytotoxic to native bone cells and there is also a significant microstructural impact in

this response, as demonstrated by variation in cytotoxicity between sample conditions. Thus, through compositional fine tuning this detrimental effect could be minimised.

Exhibiting a purely contact driven mechanism of action, which the absence of Cu ion release from the alloys manufactured herein present under the explored elution environment, may offer significant advantages in terms of biocompatibility. Since the antimicrobial action is primarily contact-dependent, only the bacteria that come into direct contact with the alloy surface are affected, reducing the risk of exposing surrounding tissues to potentially toxic copper ions. This localised effect also minimises the chance of bacteria being exposed to sub-lethal concentrations of Cu, which could otherwise lead to or even accelerate the development of copper resistance over time. By preventing the widespread dispersion of Cu ions, the alloy reduces the selective pressure that can drive bacterial adaptation, ultimately supporting long-term effectiveness against infections. This aspect of localised antimicrobial action also enhances the safety profile of the Ti-Cu alloys for use in clinical environments, where long-term implant biocompatibility is crucial during the lifecycle of the implant *in vivo.*

Notably this approach of microstructure tuning could be extended to screen against other beneficial target properties, such as pro-osteogenic, which would be an influential step in driving forward a new generation of implant materials that are specifically designed to address current challenges of orthopaedic devices [295].

3.5. Conclusion

Titanium-copper alloys were manufactured using arc melting and heat treated, in order to produce alloys with differing microstructure. The results from this chapter demonstrate that although Ti_2Cu does have a role in the antibacterial mechanism of Ti-Cu alloys, the size and shape of these precipitates are crucial in determining bacterial efficacy against *S. aureus*. Larger, rounded precipitates, as demonstrated by the Ti-11Cu aged 820 °C alloy, exhibited superior antimicrobial efficacy, likely due to increased surface contact with Ti_2Cu and/or Ti_3Cu and the resultant degree of electron transfer. This suggests that small precipitates may fail to penetrate the passivation layer, limiting their interaction with bacteria. Furthermore, this work systematically demonstrates that compositional and microstructural tuning are effective mechanisms to tailor antimicrobial effects and cytocompatibility of these biomaterials. Based on this work it suggests that through other methods of microstructural adaption, Ti-Cu alloys can be optimised through alternative methods.

Chapter 4

EFFECT OF MANUFACTURING METHOD ON THE ANTIMICROBIAL EFFICACY OF TITANIUM-COPPER ALLOYS

Titanium-copper alloys have become increasingly prevalent across literature, yet there is very little standardisation of manufacturing methods, heat treatment conditions, and antimicrobial assays. The wide variation in these parameters makes it challenging to pinpoint the key factors influencing antimicrobial efficacy and mode of action. Though it has been previously established that an increase in copper concentration correlates to improved antimicrobial efficacy, the influence, specifically of manufacturing method and corresponding microstructure, has not been extensively studied. Understanding how manufacturing methods and heat treatments influence microstructure is key to optimising Ti-Cu alloys for biomedical use, balancing biocompatibility and antibacterial performance. By understanding the differences between method of manufacture, through the variation in produced microstructure, the antimicrobial efficacy of the alloys can be predicted.

Throughout this chapter, pressed and additively manufactured Ti-Cu alloys were compared against cast alloys, through analysis of their microstructures and biological properties. This study demonstrates that modifying the manufacturing method of Ti-Cu alloys can enhance antimicrobial efficacy. While ball-milled and pressed samples achieved 100 % efficacy, their low densification limits their use in orthopaedic implants and this methodology is presented as an exploratory tool. Additively manufactured (AM) Ti-Cu alloys manufactured using laser powder bed fusion, however, show superior antimicrobial performance, likely due to an ionic release mechanism facilitating electrochemical interactions between α-Ti and Ti_2Cu, promoting Cu ion dissolution. Comparisons with cast and heat-treated samples confirm that AM alloys, even with reduced Cu content (3 wt.%), outperform others against *S. aureus* and *E. coli*. This improvement is attributed to the finer grain structure of PBF-LB samples, which accelerates ionic release and galvanic corrosion. Ti-11.5Cu does show improved antimicrobial efficacy compared to Ti-3Cu, however the ion release mechanism of the alloy raises concerns around cytotoxicity and contributions to antimicrobial resistance to copper. Thus, a nuanced approach to alloy design is necessary, to balance antimicrobial benefits with the long-term biological safety.

4. Effect of Manufacturing Method on the Antimicrobial Efficacy of Titanium-Copper Alloys

4.1. Introduction

Exploring additively manufactured (AM) Ti-Cu alloys presents a highly promising strategy for accelerating the discovery of antimicrobial titanium alloys. The design space for new biomedical titanium alloys spans dozens of potential elements, creating an immense number of compositional permutations [209-211]. Furthermore, alloys tend to have diverse and often complicated composition-microstructure relationship and so manufacture through traditional methods, which involves slow, iterative tuning of compositions and heat treatments, is ill-suited to efficiently navigate this vast landscape [213]. AM techniques, particularly laser powder bed fusion (PBF-LB), offers a flexible, high-throughput platform for in-situ alloying using blended elemental powders [223]. This enables rapid prototyping of novel compositions without the need for pre-alloyed feedstock, significantly reducing time and cost barriers. Furthermore, PBF-LB has already been widely demonstrated as a tool for Ti- based alloy research [231-236].

Ti-Cu alloys, in particular, have shown great potential due to copper's well-established antimicrobial properties. Studies demonstrate strong correlations between Cu content, the phases present, and antibacterial efficacy. However, comparing results across the literature is often challenging due to inconsistencies in processing routes, such as heat treatments, and biological assays.

Powder metallurgy (PM) methods, such as powder pressing, allow fabrication of parts without intermetallic phase formation. This enables the study of the effects of a pure Cu phase compared

to Ti_xCu intermetallic phases. However, the low density of these samples limits their application in orthopaedic devices. In contrast, additive manufacturing (AM) approaches offer a more consistent and controllable fabrication route. Furthermore, post-processing heat treatments to refine microstructures and enhance performance, as demonstrated in the previous chapter. Thus, AM not only supports rapid screening and compositional tuning of Ti-Cu alloys but also addresses the critical need for reproducible and scalable materials with biological functionality in orthopaedic implants.

Understanding the interplay of these factors and impact of manufacturing method and corresponding microstructure is crucial for optimising Ti-Cu alloys for biomedical applications, ensuring a balance between biocompatibility and antibacterial performance. Furthermore, through analysis of these factors, it may be possible to enable predictability of alloy properties. Figure 4.1 depicts the binary Ti-Cu phase diagram and the differences in predicted phases present at equilibrium across different compositions and temperatures.

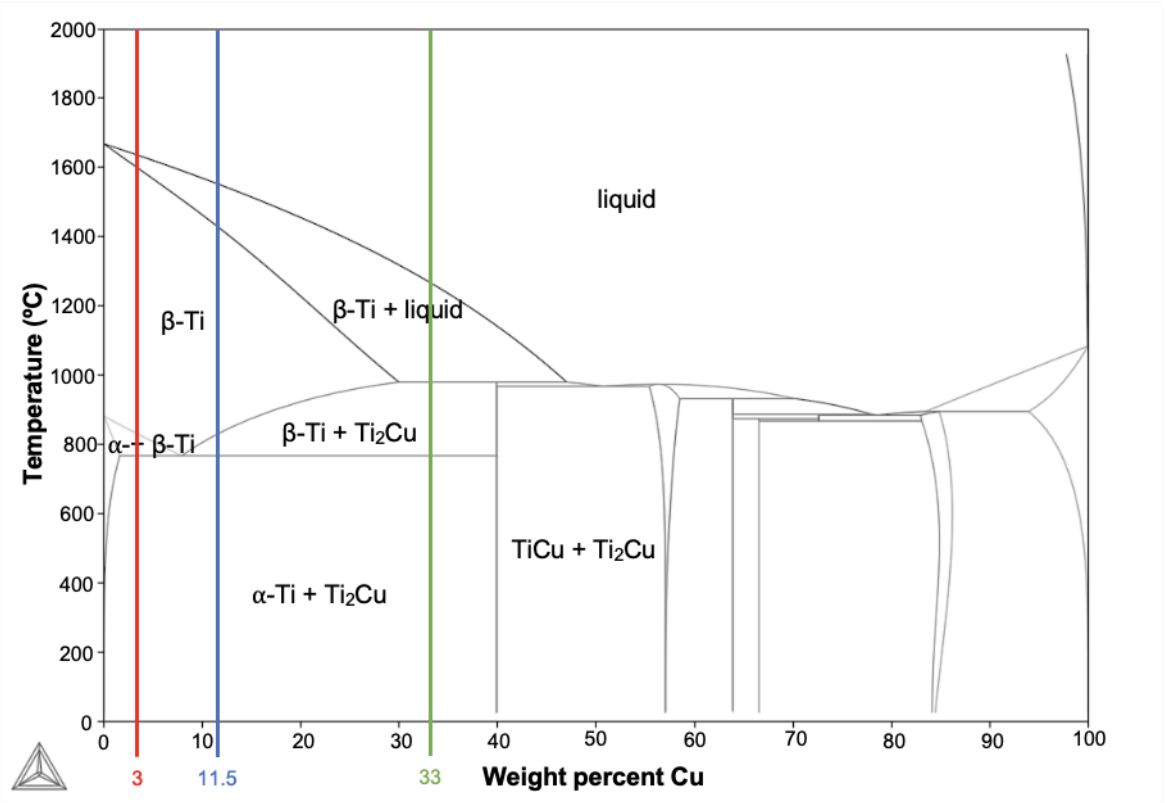

Figure 4.1: Binary Ti-Cu phase diagram, created using ThermoCalc 2023a with TCTI2 database. Red and blue lines depict the compositions analysed in this research.

Consequently, this chapter builds upon previous literature and the findings from Chapter 3 to demonstrate the antimicrobial efficacy of Ti-Cu alloys manufactured through different processing routes. Optimising these alloys for biomedical use requires a thorough examination of how manufacturing methods and heat treatments influence microstructure, balancing biocompatibility and antibacterial performance. By analysing the relationship between processing techniques and the resulting microstructure, the antimicrobial efficacy of the alloys can be predicted.

4.2. Methods

4.2.1. Powder Characterisation

The particle size was calculated using the Malvern Mastersizer 2000, using laser diffraction and water as a dispersant. Morphology was determined using backscattered electron (BSE) electron microscopy (SEM) analysis on a ZEISS EVO10. A powder sample was directly fixed to an adhesive carbon tab, and gently tapped to remove excess particles.

4.2.2. Sample Manufacture

The alloys investigated throughout this research are Ti-3Cu, Ti-11.5Cu and Ti-33Cu (weight percentage, wt. %). Table 4.1 shows these alloy compositions.

Table 4.1: Ti-Cu alloy compositions

	Value wt. %		**Value at.%**	
	Ti	Cu	Ti	Cu
Ti-3Cu	97	3	97.7	2.3
Ti-11.5Cu	88.5	11.5	91.1	8.9
Ti-33Cu	66.7	33.3	72.6	27.4

Commercially pure (grade 1) titanium, LPW Ltd, and high purity OFHC copper (Eckart) powders, 15-45 μm and 15-53 μm particle size distribution respectively, were used for blended powder processing. Ti-3Cu and Ti-11.5Cu blends were weighed under Ar atmospheres. The blends were subsequently mixed for 8 hours on a roller blender.

4.2.2.1. Ball milling and Pressing

Powder is loaded into a hardened steel container with charge in a 1:10 g ratio. The container was placed in a SPEX8000M high energy ball mill. Stearic acid was used as a process control agent and blended in the container for 5 minutes for a light coating, approximately 1% of the total powder weight. Powders were blended for five 30-minute increments, with 5 minutes rest in between to ensure the system does not overheat. Powder was then washed with ethanol and left to dry in an Argon atmosphere overnight.

Pressed samples were then produced using a Specac 15-ton hydraulic press using a 13mm Specac evacuable pellet die. 1.5 g of powder was weighed and inserted into the die, the press was manually pumped to approximately 9.5 tons and maintained for 10 minutes to ensure maximum compaction.

4.2.2.2. Additive Manufacture

The blended powder feedstock was used to produce cuboidal (10 x 10 x 10 mm) samples. All specimens were processed using a 500 W 1070 nm ytterbium fibre laser on a RenAM500S (Renishaw, UK) PBF-LB system fitted with a Reduced Build Volume (RBV) unit, allowing a maximum build volume of 64 x 80 x 80 mm. Builds were performed under an argon atmosphere, with oxygen levels maintained below 1000 ppm throughout lasing. Samples were manufactured on Ti-6Al-4V build substrates. Table 4.2 highlights the set build parameters for all builds.

Table 4.2: Set build parameters maintained across all PBF-LB builds on the RenAM 500S.

Parameter	Value
Layer thickness	30 μm
Exposure point distance	90 μm
Hatch distance	90 μm
Spot diameter	75 μm
Layer angle	67°

4.2.2.3. Parametric Study

Parametric studies were carried out to optimise laser power and scan speeds to ensure maximum densification of specimens with minimal porosity. Laser power was varied between 100 and 300 W, whilst scan speed was varied between 200 and 1000 mm/s, as depicted in Table 4.3. The Renishaw systems require a change of scan speed to be achieved through alteration of the laser dwell time, calculated using equation 4.1.

$$Dwell\ time\ (\mu s) = \frac{Point\ distance(\mu m)}{Scan\ Speed(mms^{-1})} \times 1000 \quad [4.1]$$

Energy density of the parameters can be calculated using equation 4.2.

$$Energy\ Density\ (Jm^{-1}) = \frac{Laser\ Power\ (W)}{Scan\ Speed(mms^{-1}) \times 1000} \quad [4.2]$$

Table 4.3:Summary of all specimens manufactured during the parametric studies.

Sample Number	Power (W)	Scan speed (mm/s)	Dwell time (µs)	Energy Density (J/m)
1	100	200	450	500
2	100	400	225	250
3	100	600	150	167
4	100	800	112.5	125
5	100	1000	90	100
6	200	200	450	1000
7	200	400	225	500
8	200	600	150	333
9	200	800	112.5	250
10	200	1000	90	200
11	300	200	450	1500
12	300	400	225	750
13	300	600	150	500
14	300	800	112.5	375
15	300	1000	90	300

4.2.2.4. Archimedes Density

Apparent density of samples was assessed using Archimedes measurements in pure ethanol, utilising an Adventurer Precision AX223, Ohaus. Equilibration of the ethanol was achieved by allowing the liquid to rest at room temperature prior to measurements ensuring that it did not change significantly. Three measurements were taken for each specimen and arithmetic mean and standard deviations calculated.

4.2.2.5. Optimised Builds

Builds were repeated for each Ti-Cu blend with the optimised parameters to produce specimens for characterisation and *in vitro* testing. Selected parameters for both Ti-3Cu and Ti-11.5Cu specimens are described in Table 4.4.

Table 4.4: Optimised processing parameters for Ti-3Cu and Ti-11.5Cu compositions.

Composition	Power (W)	Scan speed (mm/s)	Dwell time (µs)	Energy Density (J/m)
Ti-3Cu	100	400	225	250
Ti-11.5Cu	100	1000	90	100

4.2.3. Samples Preparation

The alloys were then vertically (X-Z plane) sectioned using an Electro-discharge machine (EDM) into 10x10x2mm coupons for all characterisation and *in vitro* experiments. Samples required for scanning electron microscopy (SEM) were then mounted in conductive Bakelite (Presidon-ML-C, Aptex Ltd). Subsequently, they were mechanically ground to 1200 grit then polished with diamond and OPS solutions, as described in Table 4.5.

Table 4.5: Polishing and grinding sequences for alloy preparation with the Struers Tegramin-25.

Step	Grit/Polish Finish	Lubricant	Force	Rotation	Co-rotation	Time
1	MD-Piano 220	Water	20 N	300	150	Until plane
2	MD-Piano 1200	Water	20 N	300	150	Until plane
3	MD-Largo	DiaDuo 9-micron	15 N	150	150	~ 20 mins
4	MD-Allegro	DiaDuo 3-micron	15 N	150	150	~ 5 mins
5	MD-Chem	OPS	10 N	150	150	~ 30 mins

4.2.4. Microstructural Characterisation and Phase Identification

Scanning electron microscopy (SEM) imaging was completed on a ZEISS EVO10 using backscattered electron (BSE) detector to reveal compositional contrast. Secondary electron (SE) SEM was utilised to visualise the surface topography of the pressed samples.

X-ray diffraction (XRD) was performed using a Proto AXRD for phase identification. The system uses a copper line focus X-ray tube with a nickel k_β absorber producing K_α radiation ($K_{\alpha av}$=1.541874 Å) with a set increment size of 0.0149282° and a power setting of 30.0 kV and 20 mA.

4.2.5. Cu ion release

According to the ISO 10993-12 standard, the Cu^{2+} released from Ti-Cu alloys for various periods of time was monitored in 0.9 % NaCl solution, incubated at 37 °C. The concentrations of released Cu^{2+} at 1, 3 and 7 days were determined by inductively coupled plasma optical emission spectrometry (ICP-OES), Perkin Elmer Optima 8000.

4.2.6. Contact Angle Analysis

The contact angle (CA) measurements were taken using the sessile drop technique (Attension Theta Lite Tensiometer, Biolin Scientific, USA). Five microlitres of water was deposited onto the surfaces, and after 5 seconds, images and measurements recorded. The CA was then measured using an average of three independent repeat measurements of each sample.

4.2.7. Protein Adsorption

Protein adsorption was calculated using a Pierce™ BCA Protein Assay Kit (Thermoscientific, UK), an assay based on bicinchoninic acid (BCA) for the colorimetric detection and quantification of total protein. The method uses the reduction of Cu^{2+} to Cu^{1+} by proteins in an alkaline media.

1 mL Dulbecco's Modified Eagle's Medium (DMEM) or 1 mL MH Broth was added to each sample condition in a 24 well-plate. DMEM was also added to an empty well to act as a blank control. All samples were then incubated at 37 °C and 5 % CO_2 for 24 hours. After 24 hours, the media was removed and samples washed.

BCA Reagent A and Reagent B were mixed in a 50:1 ratio to produce the working solution. 1 mL of the working solution was added to each sample condition and incubated at 37 °C for 30 minutes. Using a microplate reader (Spark, Tecan Trading AG, Switzerland) the absorbance of each sample was measure at 562 nm. Readings of a blank solution were then subtracted from each reading and averages calculated. A standard curve was plotted for each BSA standard against protein concentration in μg/mL, this was used to determine the protein concentration of each unknown sample.

4.2.8. Microhardness

Vickers microhardness testing of mounted and polished samples was performed at 50x optical magnification and 100 g indentation force (Buehler Wilson VH1202). Five indentations were performed automatically per sample in a quincunx arrangement, with manual adjustments made

when software failed to accurately locate indent corners (DiaMet, Buehler). Values were then averaged across each sample.

4.2.9. Antimicrobial Analysis

Antimicrobial tests were carried out in relation to ISO 22196:2011 and JIS Z 2801 [272]. *Staphylococcus aureus* was utilised as it is a common Gram-positive bacterium often associated with implant infections, whilst *Escherichia Coli* was used as an alternative Gram-negative bacterium. All samples were sterilised by ethanol in dark conditions for 30 minutes and left to dry for 24 hours.

Samples were then seeded with 5 μL of bacteria and a coverslip placed on top, in a petri dish with a sterile tissue wetted with 2 mL of Dulbecco's phosphate-buffered saline (DPBS). The samples were then incubated at 37 °C for 24 hours. After 24 hours, the samples were retrieved and placed in 5mL of DPBS. Solutions containing the AM samples were vortexed for 2 minutes, ensuring the sample and cover slip were separated. The pressed samples were lightly shaken, to minimise sample disintegration. 100 μL of the DPBS solution was extracted, placed into a 96 well plate and serially diluted in DPBS. 10 μL from each well was plated, using a spreader to ensure bacteria were well distributed and countable. Samples were cultured at 37 °C for 24 hours, before being counted.

Bacterial reduction was calculated using equation 4.3, where N_{Ti64} relates to the CFU count for the Ti64 control, whereas N_x relates to the number of bacterial colonies for each sample.

$$Bacterial\ reduction\ (\%) = \frac{N_{Ti64} - N_x}{N_{Ti64}} \times 100 \quad [4.3]$$

4.2.10. *In Vitro* Analysis

Murine pre-osteoblast MC3T3 cells were inoculated in T75 flasks and incubated at 37 °C in basal media consisting of Dulbecco's Modified Eagle's Medium (DMEM) supplemented with 10 % foetal bovine serum, 12 % L-glutamine and 1 % penicillin/streptomycin. Cells were detached from the flasks, counted and diluted to seed $2x10^4$ cells per sample in a 24 well plate. After 20 minutes of contact to enable cell adhesion, 1mL of fresh basal media was added to each well and cells incubated at 37 °C and 5 % CO_2.

4.2.10.1. Cytotoxicity Analysis

Live/dead assays were performed on three samples per condition, each stained with 200 µL of a 5 mM calcein-AM and 1.5 mM propidium iodide solution and incubated for 30 minutes. Stained samples were inverted and imaged using a digital inverted microscope at x10 magnification (EVOS M5000, Invitrogen, USA). Cell viability was calculated using ImageJ (ImageJ 1.54j).

4.2.10.2. Cell Viability Assay

To analyse metabolic activity and proliferation of cells deposited on the surface, 0.75 mL of basal DMEM containing 10 % Alamar Blue was added to the seeded samples. After 4 hours of incubation at 37 °C, a microplate reader (Spark, Tecan Trading AG, Switzerland) was utilised to carry out fluorescence measurements with excitation and emission wavelengths of 560 nm and 590 nm, respectively.

4.3. Results

4.3.1. Powder Characterisation

The particle size distribution analysis in Figure 4.2a indicates that both cp-Ti and Cu powders exhibit a similar size range. Cu possesses smaller average particle size (17.5 μm), compared to cp-Ti (35 μm). The Cu powder possesses a D10 of 7.5 μm and D90 of 27 μm, whereas cp-Ti has a D10 of 17 μm and D90 of 50 μm. This indicates that the particle size distribution of Cu powder is narrower, and more uniform compared to the broader distribution of cp-Ti. The BSE SEM micrographs in Figures 4.2b–2d illustrate the morphology of Ti-Cu powder blends with increasing Cu content. The powders exhibit a generally spherical morphology, which is characteristic of gas-atomised metal powders, with a range of particle sizes which appear to agree with the size range depicted in Figure 4.2a. In Ti-3Cu (Figure 4.2b), the particles appear relatively uniform with minimal satellite formation. As the Cu content increases to Ti-11.5Cu (Figure 4.2c) and Ti-33Cu (Figure 4.2d), the presence of finer particles and particle clustering becomes more evident, potentially indicating differences in powder flowability and distribution.

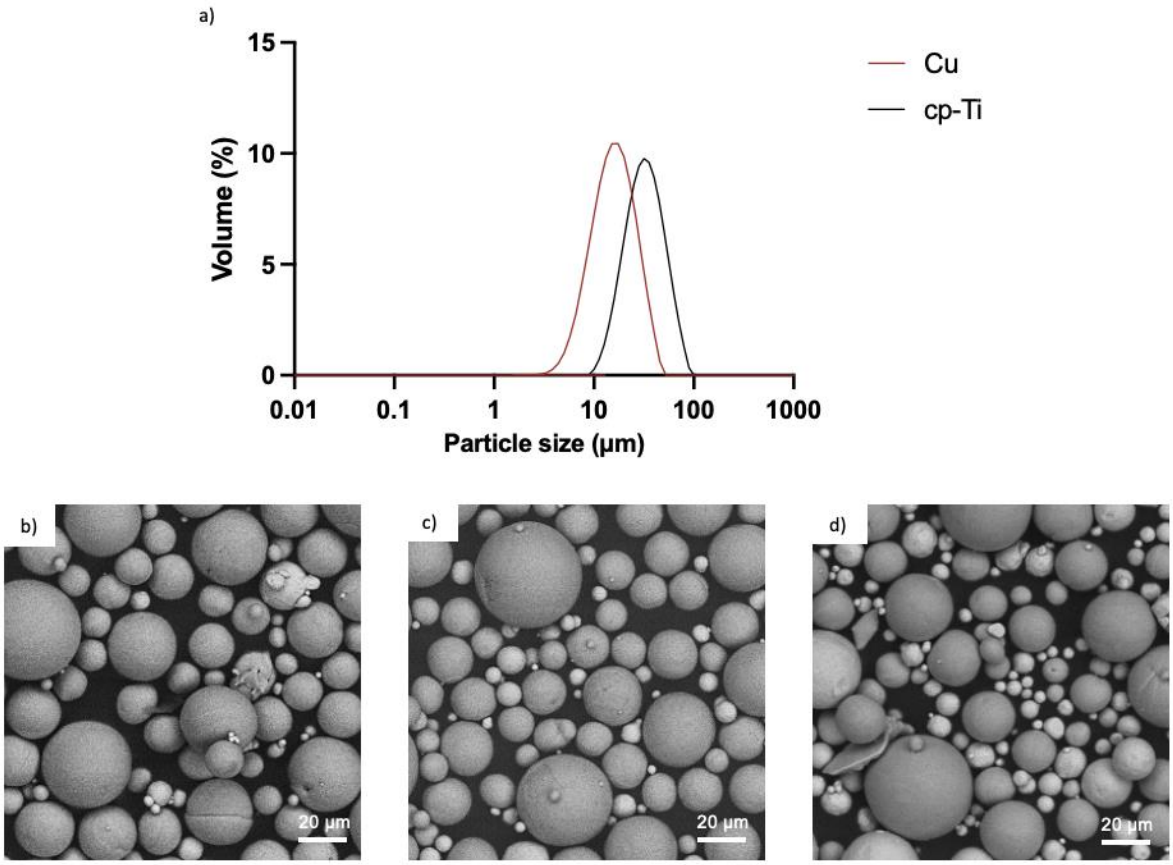

Figure 4.2: (a) Particle size analysis of cp-Ti and Cu powders and (b) Ti-3Cu, (c) Ti-11.5Cu and (d) Ti-33Cu powder blend SEM micrographs. Particle size analysis of cp-Ti shows a greater particle size and wider range than the Cu powder. Cu powder in images (b-d) appear brighter than Ti powder.

4.3.2. Ball Milling

Figure 4.3 highlights the changes in particle shape and elemental distribution after ball milling of (a–b) Ti-11.5Cu and (c–d) Ti-33Cu blends, with backscatter SEM micrographs revealing increased irregularity and plate-like morphology, thereby enhancing particle compressibility. The corresponding EDX maps show that Cu dispersion is increased through ball milling.

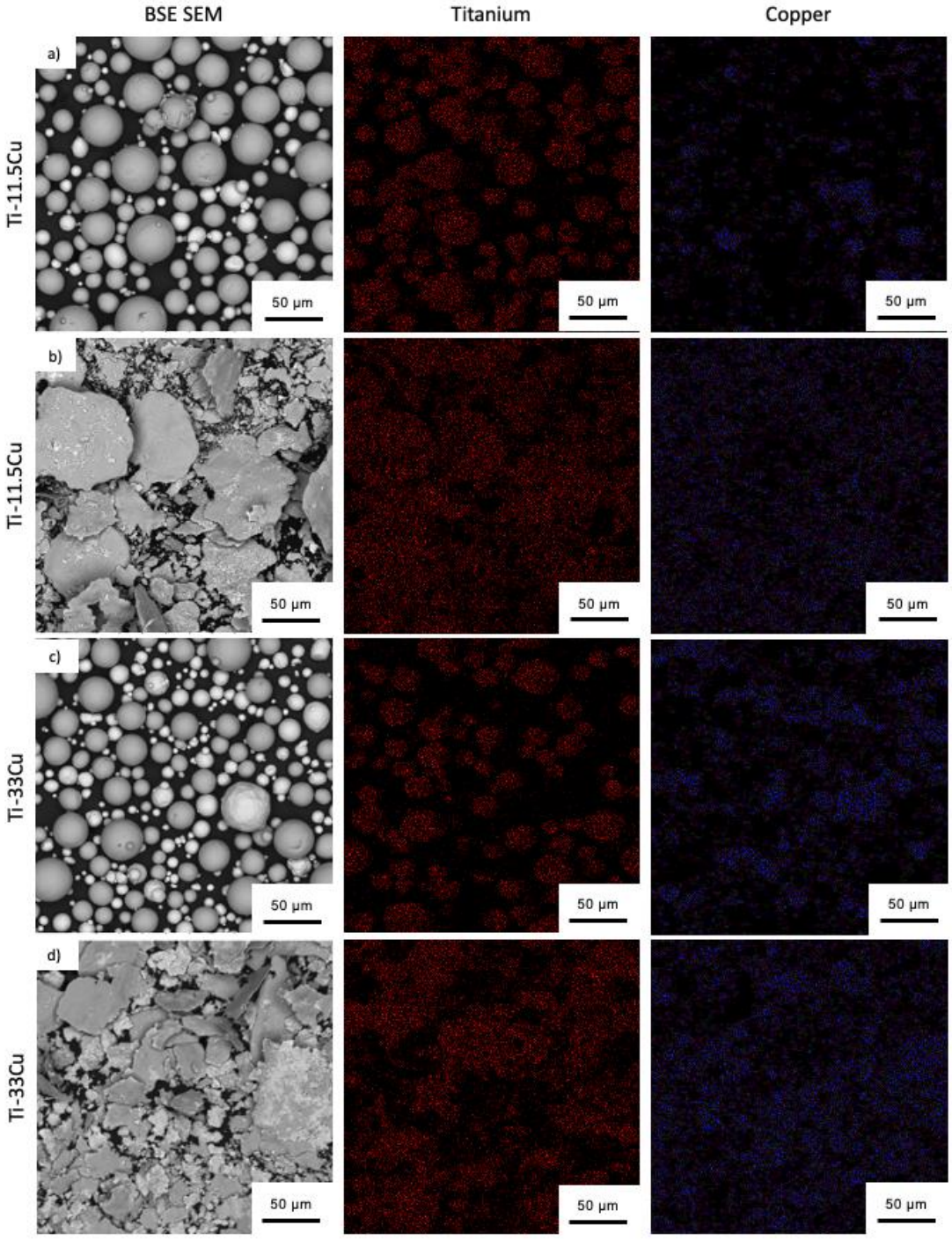

Figure 4.3:BSE SEM micrographs and EDX scans for (a) before and, (b) after ball milling Ti-11.5Cu powder and (c) before and (d) after ball milling Ti-33Cu powder. Ball milling alters the powder morphology becoming more plate-like and irregular, greater dispersion of both elements also occurs.

4.3.3. Pressed

Figure 4.4 shows the topography and elemental distribution of the pressed samples. It is apparent high levels of densification was achieved through this method; however, some powder is left uncompacted on the sample surface. Any remaining presence of stearic acid in the 'green parts' are not able to be identified through EDX analysis.

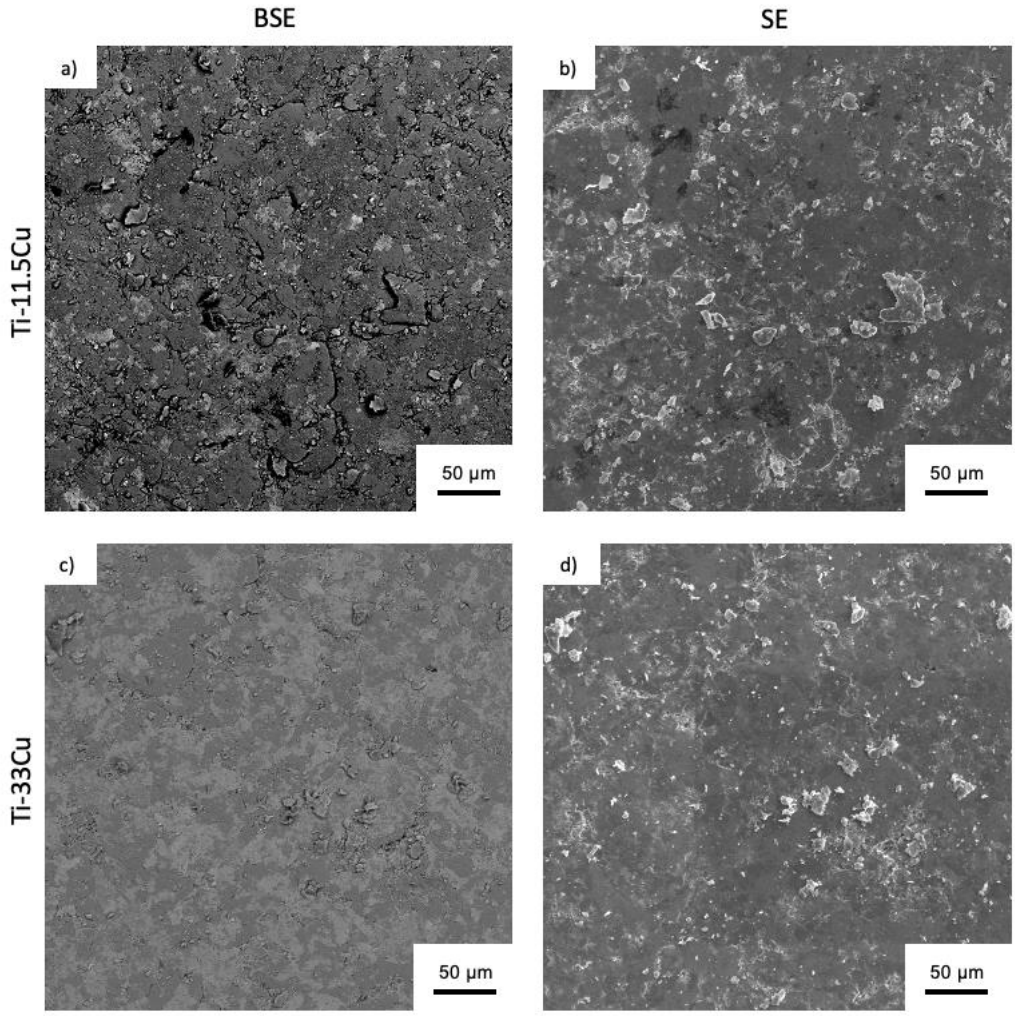

Figure 4.4: Backscatter (BSE) and Secondary electron (SE) SEM micrographs respectively of (a) and (b) Ti-11.5Cu and (c) and (d) Ti-33Cu pressed samples. SE images show the irregularity of the surface topography.

4.3.4. Additive Manufacturing

4.3.4.1. Parametric Builds

Figure 4.5 shows the build plates for each Ti-Cu composition. The Ti-3Cu and Ti-11.5Cu were generally completed successfully, though due to high laser energy for some of the cubes, some powder was remelted through the support layers, preventing easy build plate removal. Poor geometric accuracy can be observed in specimens built with high laser energy densities caused by a larger melt pool.

During the Ti-33Cu build, 6 out of 15 cubes had to be supressed due to interference with the recoater with only one cube being manufactured with no external defects. This was due to large amounts of delamination through all Ti-33Cu cubes manufactured (Figure 4.5d). Though the RenAM 500S is kept at very low oxygen levels (less than 1000 ppm) during builds, the blue colouring on the cubes indicated oxidation and metallisation has occurred. For this reason, Ti-33Cu samples were not characterised further.

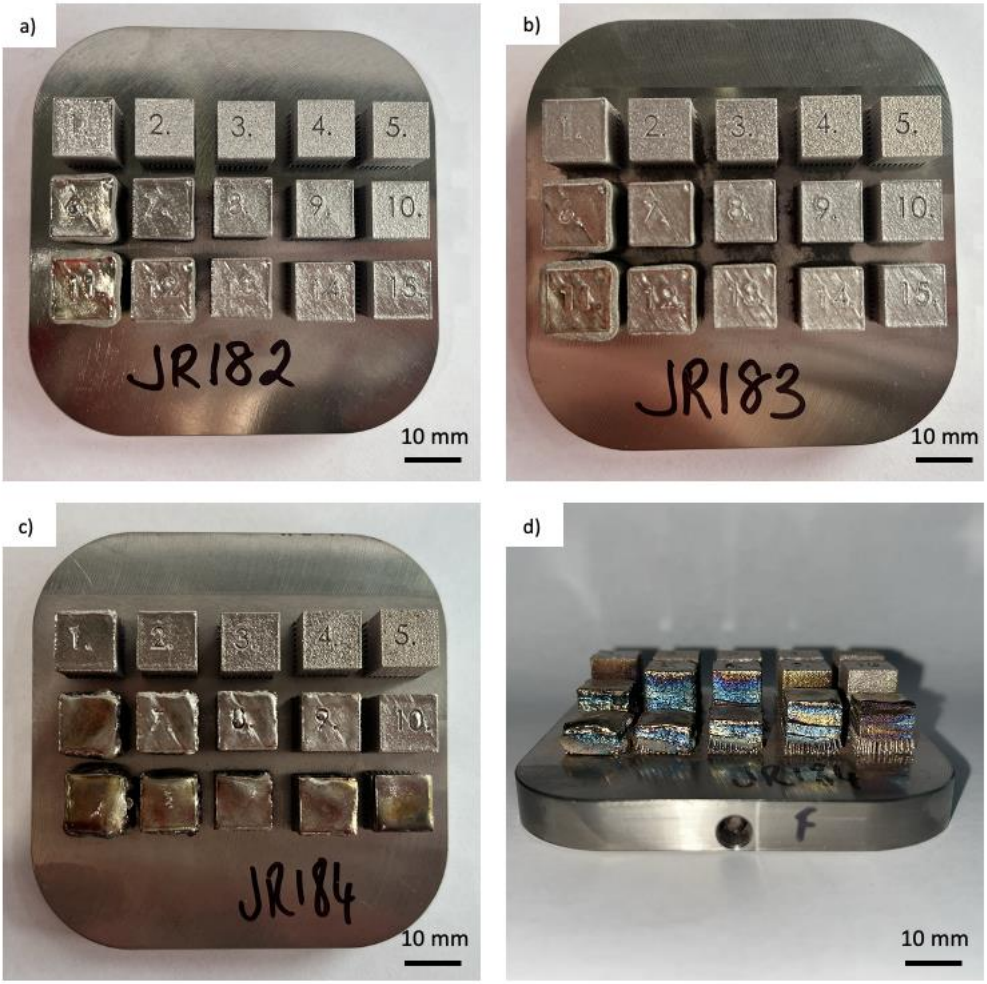

Figure 4.5: Build plate pictures of (a) Ti-3Cu, (b) Ti-11.5Cu, (c) and (d) Ti-33Cu. Ti-33Cu build showed large amount of defects with 6 of the 15 cubes having to be supressed due to recoater interference.

4.3.4.2. Archimedes Density

Figure 4.6 shows the Archimedes density results for each cp-Ti, Ti-3Cu and Ti-11.5Cu cube manufactured. The Ti-33Cu samples have not been included in this figure due to the large surface defects and pores within the samples, resulting in erroneous measurements. In general, as the laser energy density increases, the density of each composition also appears to decrease. The Ti-11.5Cu samples also have an increased density in comparison to that of the

corresponding Ti-3Cu specimens, as expected from the heightened density of Cu (8.93 gcm^{-3}) compared to Ti (4.51 gcm^{-3}) [296, 297]. Theoretical density calculations indicate that Ti-3Cu should have a density of 4.64 gcm^{-3}, with the achieved density reaching 97 % of this value. In contrast, the theoretical density of Ti-11.5Cu is 5.02 gcm^{-3}, but only 94.5 % of this value was attained.

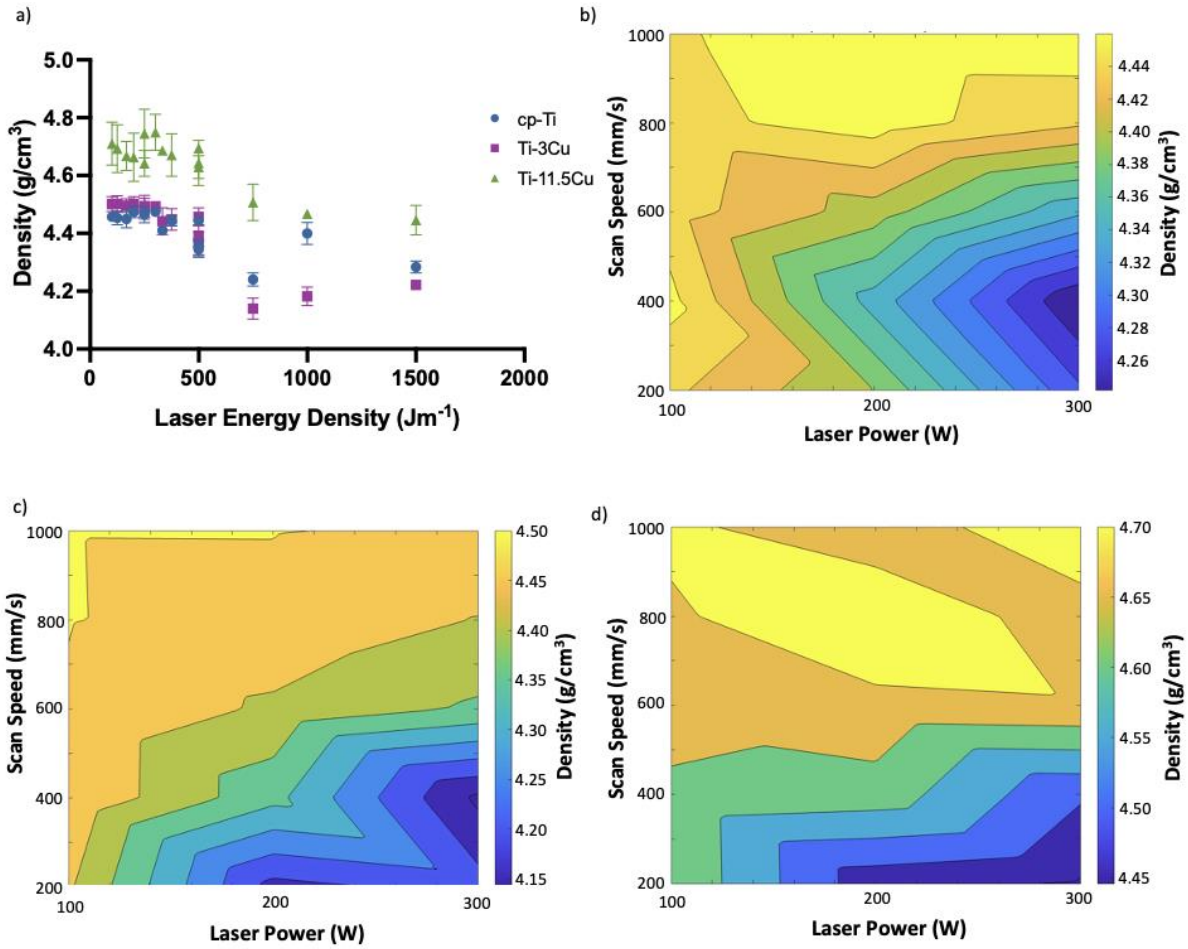

Figure 4.6: (a) Archimedes Density measurements of cp-Ti, Ti-3Cu and Ti-11.5Cu alloys over varying laser energy densities. Contour plots identifying how the Archimedes density varies with laser power and scan speed for (b) cp-Ti,(c) Ti-3Cu and (d) Ti-11.5Cu.

It is apparent that a lower laser energy density appears to produce a sample closer to full densification. Therefore, the optimal parameters are likely to have lower laser power and high

scan speeds. Though, SEM analysis was required to ensure no defects are produced within the manufactured alloys.

4.3.4.3. Parametric Build Characterisation

Figure 4.7 displays the SEM micrographs taken of each cp-Ti sample at x300 magnification. These micrographs are representative images of the microstructural features present on each sample. Notably, the samples with the highest energy densities (500-1500 Jm^{-1}) have significant porosity. Whereas the sample at 100 Jm^{-1} suffered from many lack of fusion defects, due to the low energy density. The sample with the least porosity was that at 200 W laser power and 1000 mms^{-1} scanning speed (200 Jm^{-1}), which also had the highest Archimedes density value of 4.47 gcm^{-3}. These therefore are the optimum parameters for additively manufacturing cp-Ti to achieve good densification.

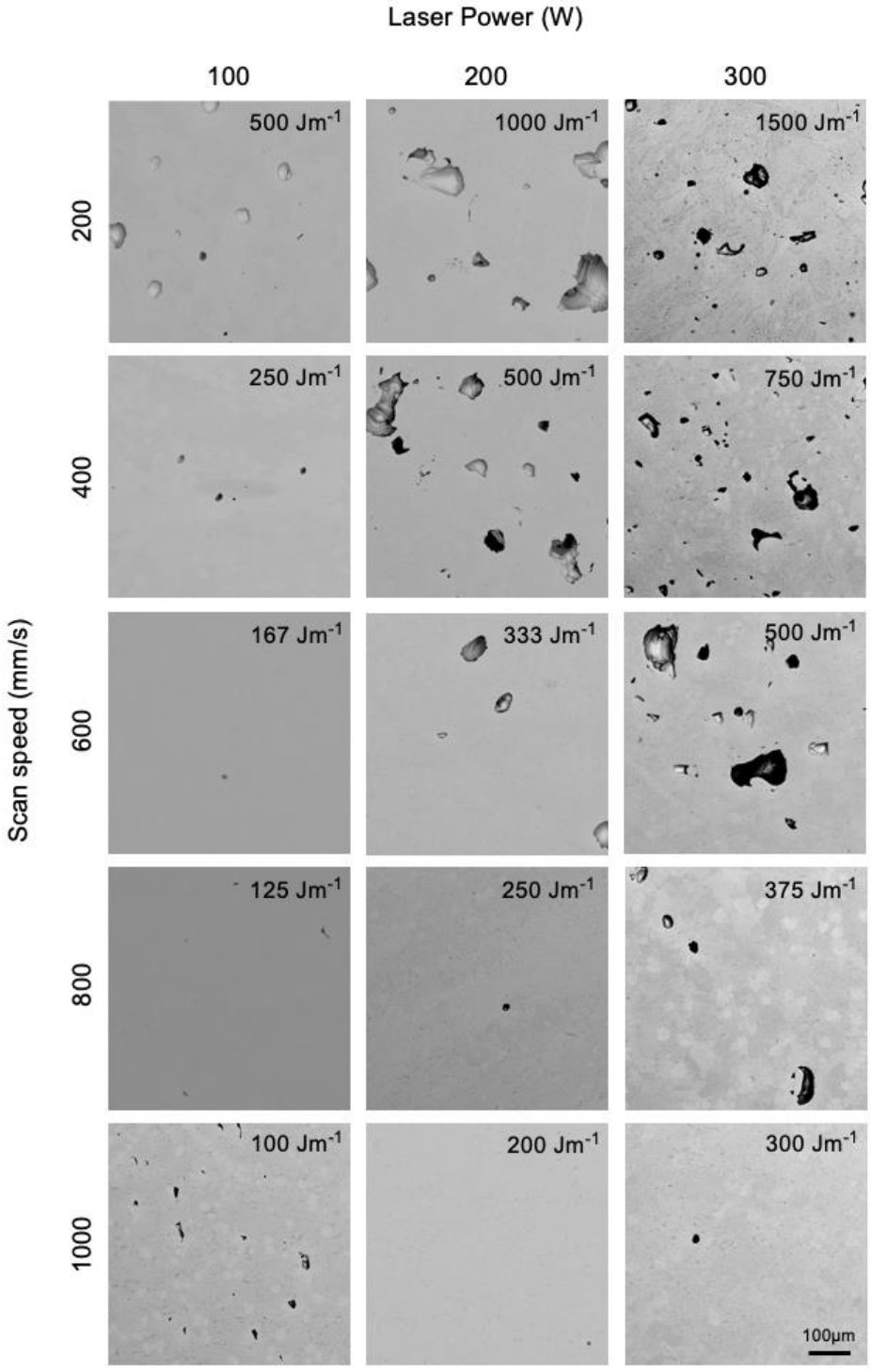

Figure 4.7:Backscatter SEM micrographs of additively manufactured cp-Ti. Each sample is labelled with laser energy density. Keyhole defects were present in all samples with laser energy densities above 333Jm^{-1}.

Figure 4.8 shows SEM micrographs of Ti-3Cu samples at x300 magnification in relation to the change in the laser power and scan speed. It can be noted that at high laser energy densities, high levels of keyholing can be detected within the samples. However, some porosity can be observed at energy densities between 200 and 500 Jm^{-1}. Low energy densities at 100 and 125 Jm^{-1}, though having full densification, appear to have some material segregation such as seen in the bright regions of the sample manufactured at 100 W and 1000 mm/s in Figure 4.8.

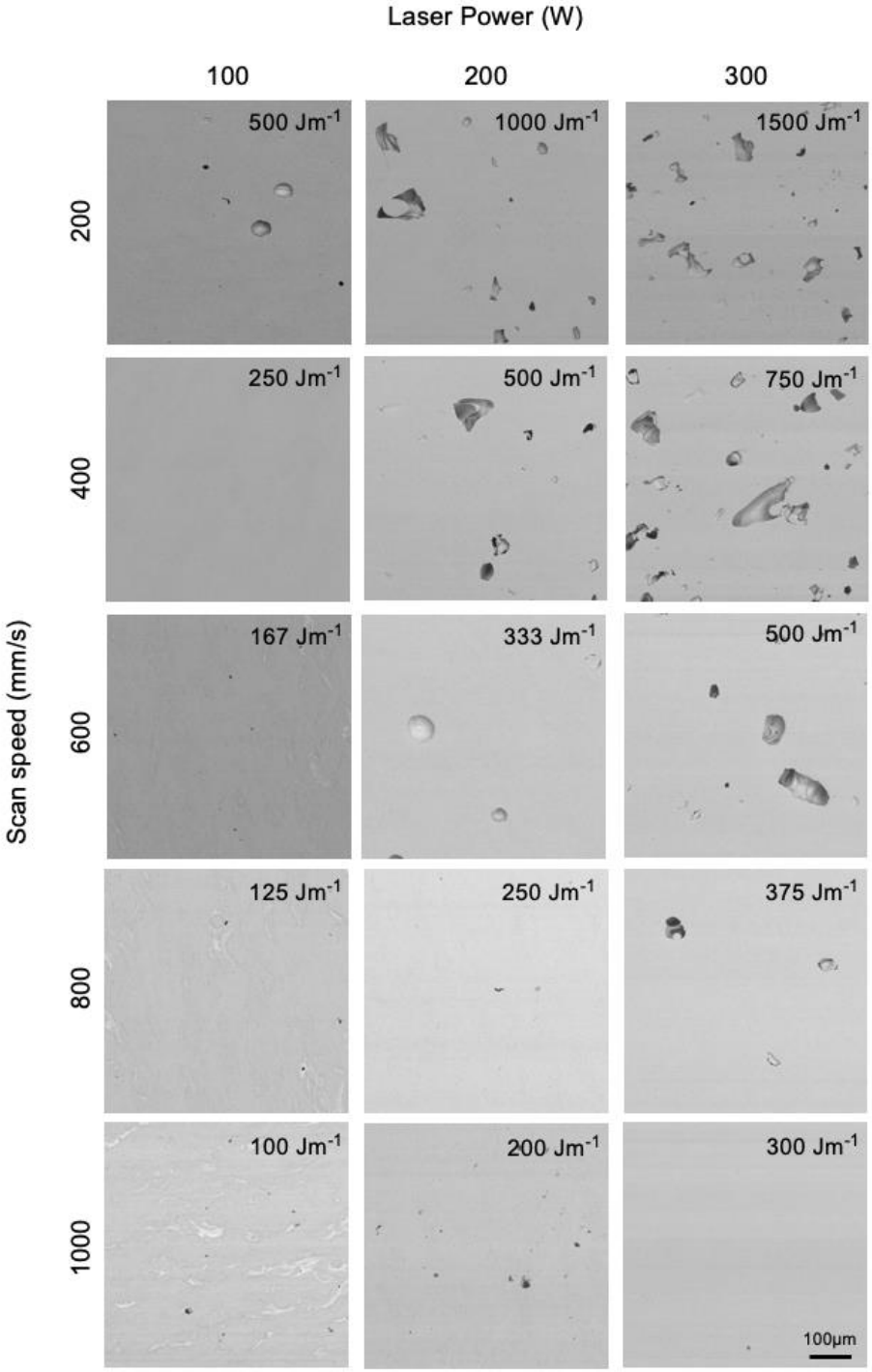

Figure 4.8: Backscatter SEM micrographs of additively manufactured Ti-3Cu. Each sample is labelled with laser energy density. Keyhole defects were present in all samples with laser energy densities above 375 Jm^{-1}. Some heterogeneity and Cu rich areas are present in the lowest laser energy density parameters.

BSE SEM micrographs of Ti-11.5Cu with varying laser parameters are shown in Figure 4.9. The increase in Cu content resulted in higher quantities of build defects within the printed samples. Similarly, to the Ti-3Cu samples, high laser energy densities caused keyholing in samples above 500 Jm^{-1}. Many samples produced at levels below 500 Jm^{-1} also exhibited cracking, typically perpendicular to build direction. Furthermore, all samples appeared to possess some porosity, indicating the difficulty in processing alloys with increasing Cu content.

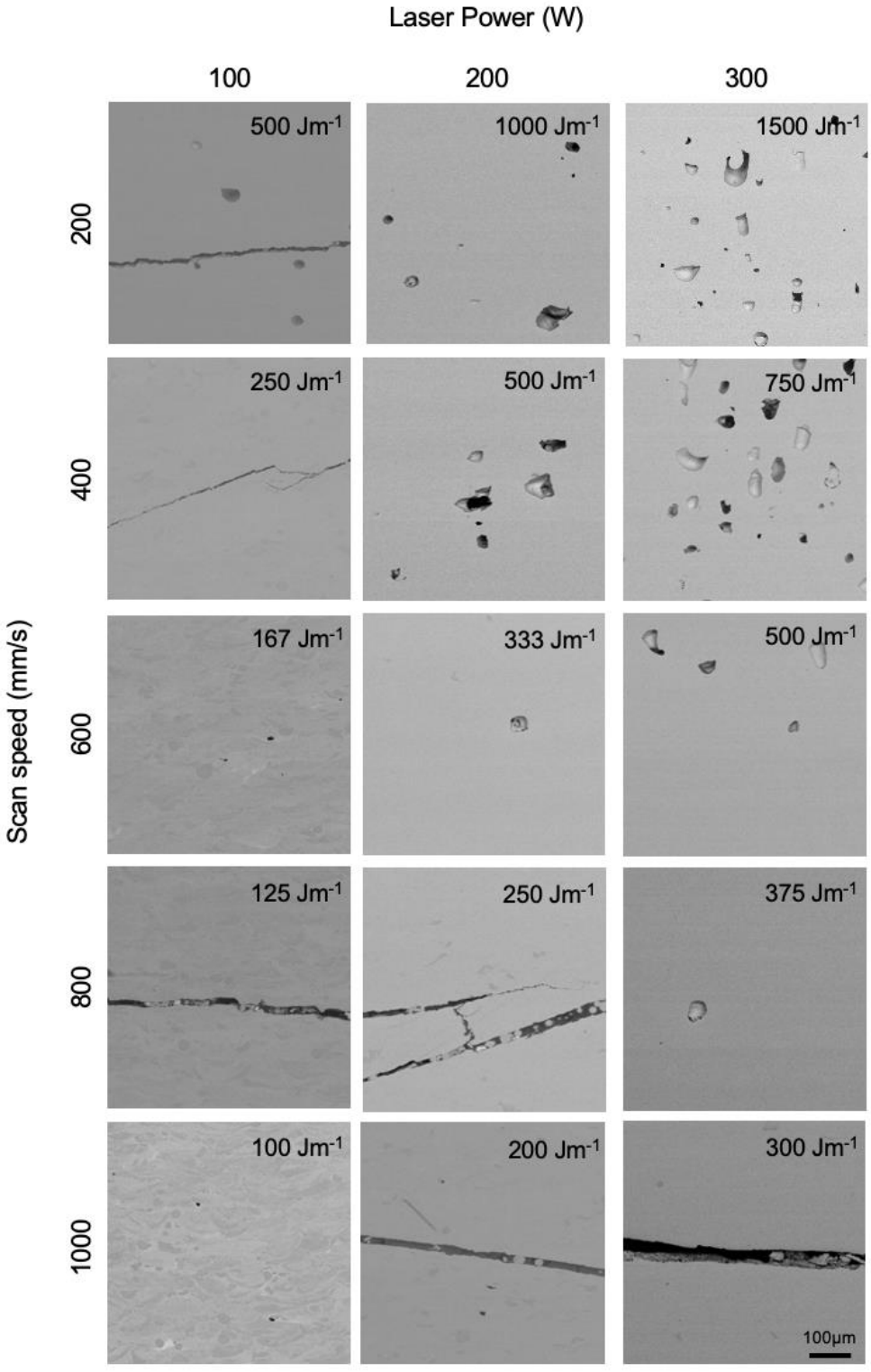

Figure 4.9: Backscatter SEM micrographs of additively manufactured Ti-11.5Cu. Each sample is labelled with laser energy density. High amounts of keyholing and cracking were present across the parameter range.

4.3.5. Microstructural Characterisation and Phase Identification

Figure 4.10 represents the backscatter electron images of the selected Ti-Cu additively manufactured samples with 3 and 11.5 wt.% Cu at low and high magnification. As observed in Figure 4.10a, the Ti-3Cu alloy possesses a relatively homogeneous structure, with some directional features along the build direction, due to the melt pool and rapid directional solidification. The high magnification image reveals a fine microstructure, likely composed of an α-Ti matrix with dispersed nanoscale precipitates. Whereas Figure 4.10b shows that the Ti-11.5Cu alloy is much more heterogeneous, indicating phase segregation and increased formation of a secondary phase. There is a lamellar-like microstructure of a Cu-rich phase. This phase is confirmed as Ti_2Cu by the XRD pattern, not present in the Ti-3Cu alloy, shown in Figure 4.10c.

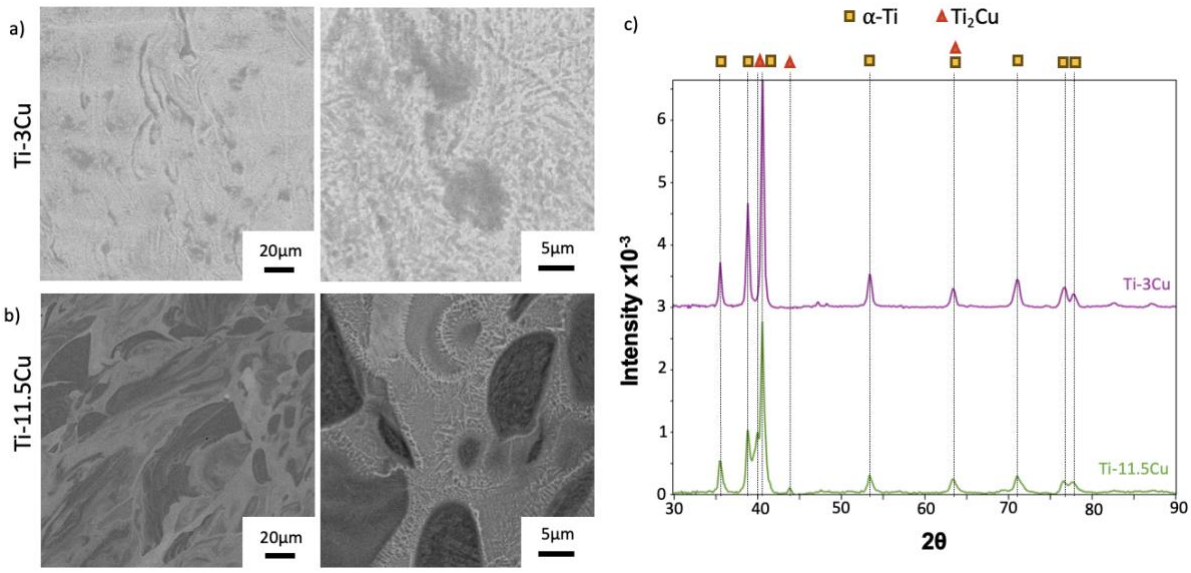

Figure 4.10: Low and high magnification BSE SEM images of (a) Ti-3Cu and (b) Ti-11.5Cu. (c) XRD patterns for Ti-3Cu and Ti-11.5Cu.

4.3.6. Cu Ion Release

To investigate the effect of Cu release on the antimicrobial efficacy of AM Ti-Cu alloys, the total cumulative release of Cu ions at 1,3 and 7 days was measured. Figure 4.11 shows the Cu ions concentration released from the Ti-3Cu and Ti-11.5Cu alloys. It can be seen that the Ti-3Cu alloy released no Cu ions over the 7 days, whereas Ti-11.5Cu released a consistent rate of Cu ions over the time period.

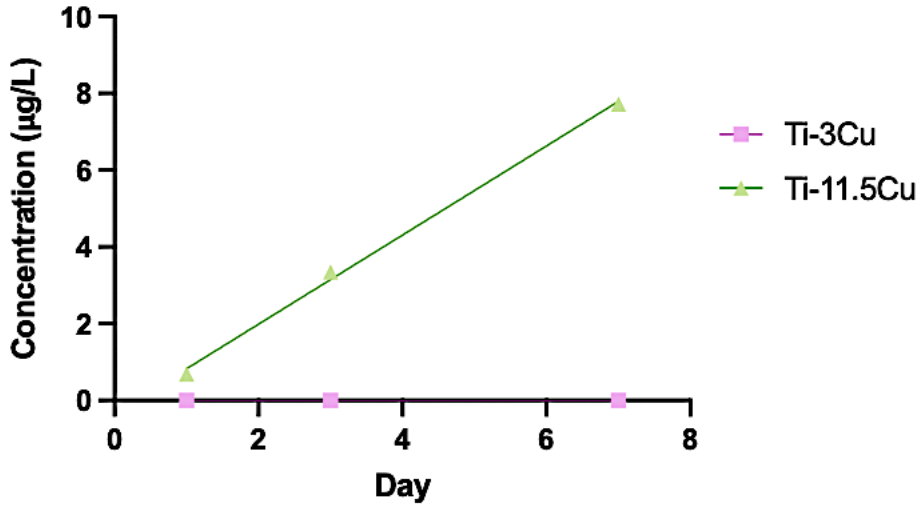

Figure 4.11: ICP-OES results for Ti-Cu additively manufactured samples in 0.9 % NaCl solution for up to seven days (n=3). No ion release was detected for Ti-3Cu alloys, but a constant rate of release was detected for Ti-11.5Cu over the 7 day time period.

4.3.7. Contact Angle Analysis

Figure 4.12 shows the measured contact angle of water on the surface of additively manufactured a) Ti64, b) Ti-3Cu and c) Ti-11.5Cu.

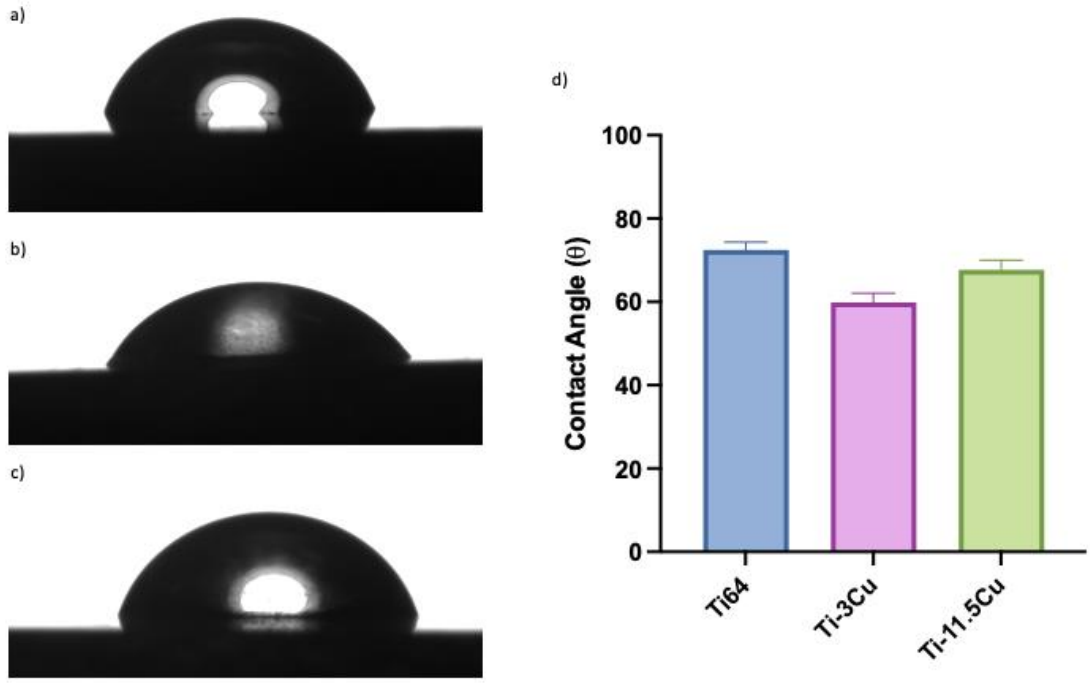

Figure 4.12: Images of water droplets on (a) Ti64,(b) Ti-3Cu and (c) Ti-11.5Cu surfaces. (d) the contact angle measured on each surface.

4.3.8. Microhardness

Figure 4.13 shows the microhardness of the additively manufactured Ti-Cu alloys, the dashed line represents the microhardness of Ti-6Al-4V, the current material standard for metallic implants, of approximately 350 HV [273]. Ti-3Cu shows an 18 % reduction in hardness in comparison to the Ti-6Al-4V control, whereas Ti-11.5Cu shows a 9 % increase.

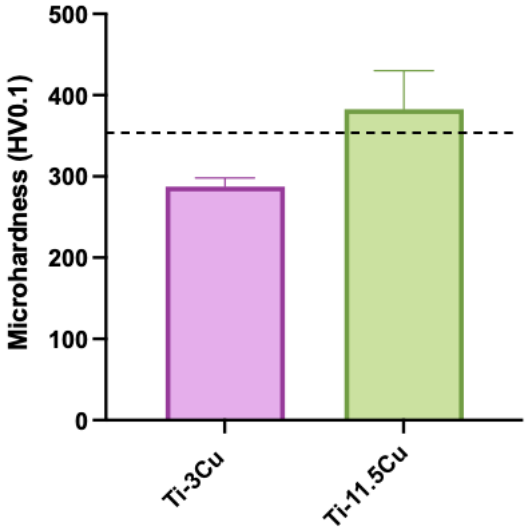

Figure 4.13: Microhardness(HV0.1) data after loading with a 100g force for both additively manufactured Ti-Cu samples (n = 5). The dashed line represents the microhardness of Ti-6Al-4V.

4.3.9. Antimicrobial Analysis

Figure 4.14 shows the antimicrobial data for the additively manufactured Ti-Cu alloys against negative (Ti-6Al-4V) and positive (Cu) controls for a) *S. aureus* and b) *E. coli* after 24 hours incubation. These results show that an increase in antimicrobial effect is correlated to an increase in Cu concentration. This effect is consistent with both bacteria. A bacterial reduction was measured compared to the Ti-64 control of 99.5% and 99.9% for additively manufactured Ti-3Cu and Ti-11.5Cu respectively, for *S. aureus*. Whereas, against *E. coli* this increased to 99.9 % and 99.99 %. Both Ti-11.5Cu and Ti-33Cu pressed specimens showed 100 % efficacy against *S. aureus* and *E. coli*.

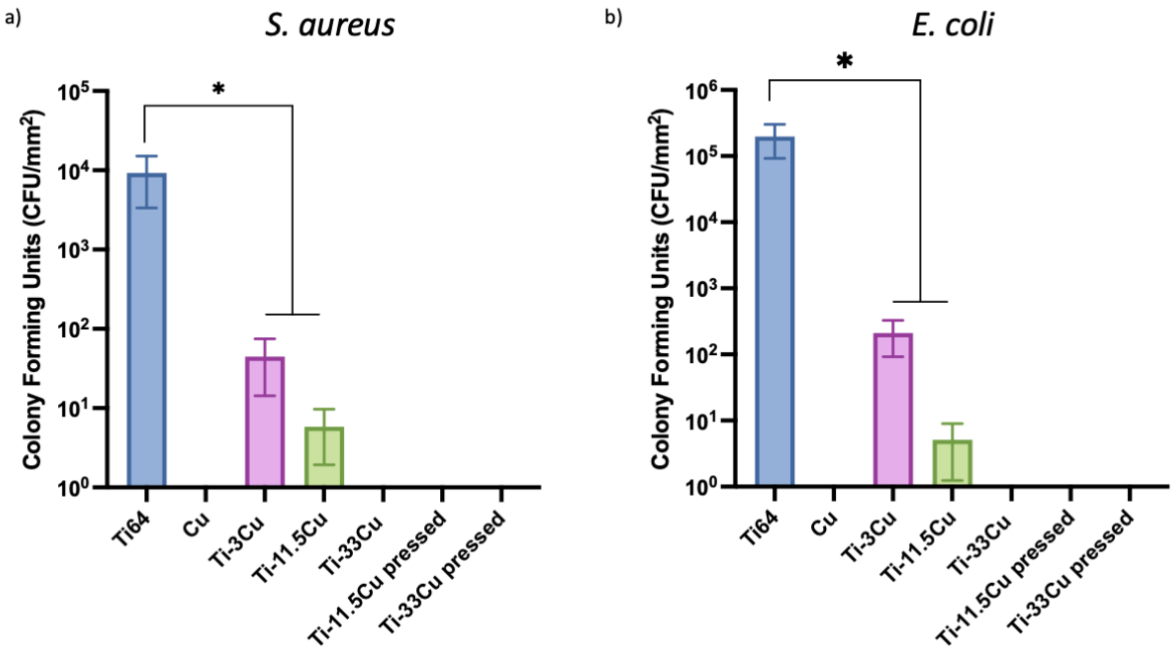

*Figure 4.14: Antimicrobial analysis of Ti-Cu alloys relating to a) S. aureus and b) E. coli (n=3). * represents values where $p \leq 0.05$.*

4.3.10. Protein Adsorption

Samples were immersed in cell culture media (Figure 4.15a) and bacterial media (Figure 4.15b) and analysed after 24 hours using a BCA protein adsorption assay. Ti64 exhibited the highest protein concentration in cell media, indicating strong surface interactions; however, contamination was observed in the bacterial media condition. As expected, the blank control showed minimal adsorption in cell media due to the absence of a metal surface, yet unexpectedly exhibited the highest protein concentration in bacterial media. The two AM Ti-Cu alloys displayed similar protein adsorption in both media types, with levels higher than the blank in cell media but not in bacterial media.

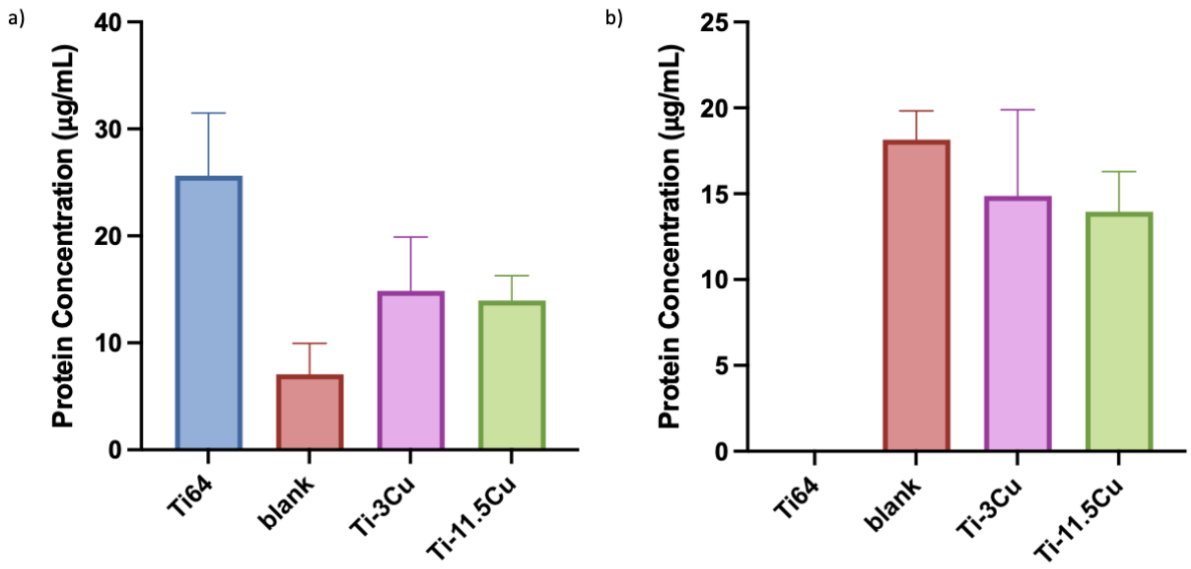

Figure 4.15: Protein adsorption on different metal AM alloys and an empty well (blank) with (a) cell media and (b) bacterial media.

4.3.11. Cytotoxicity

The cytotoxicity of the Ti-Cu alloys was evaluated using live/dead imaging and Alamar Blue assay (Figure 4.16 and 4.17). Minimal cell death is apparent after one and three days for all samples, however, after seven days a significant reduction in cell viability is visible.

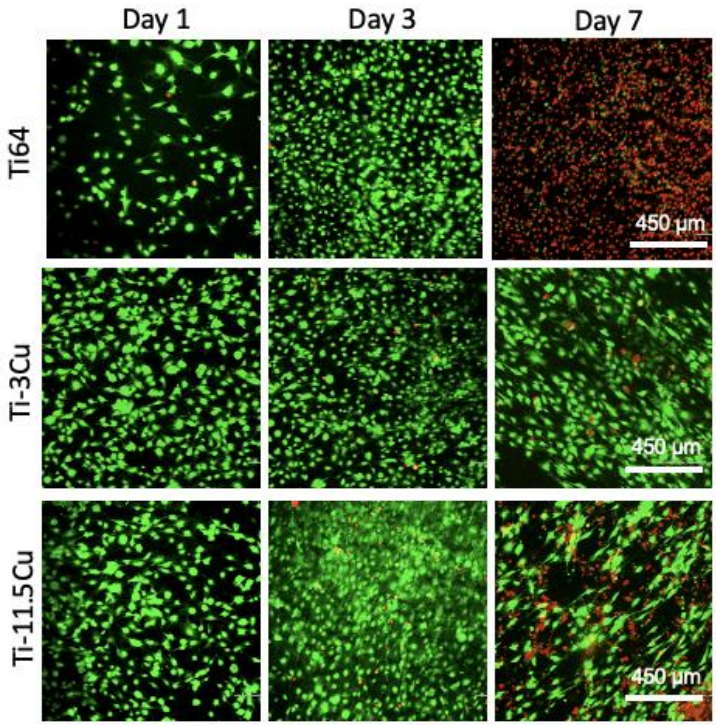

Figure 4.16: Fluorescent images of live (green) and dead (red) cells, demonstrating the influence of alloy composition and heat treatment protocol on murine pre-osteoblast cells over seven days.

Figure 4.17 shows a quantification of the images in the previous figure, and metabolic activity data through an Alamar Blue assay. Minimal reduction in cell viability had occurred after day one, however after seven days this reduced to 78 % and 51 % for Ti-3Cu and Ti-11.5Cu respectively. This suggests that there is an increase in cytotoxicity as Cu content increases. Nevertheless, this is a substantial increase in overall cell viability compared to previously studied cast samples.

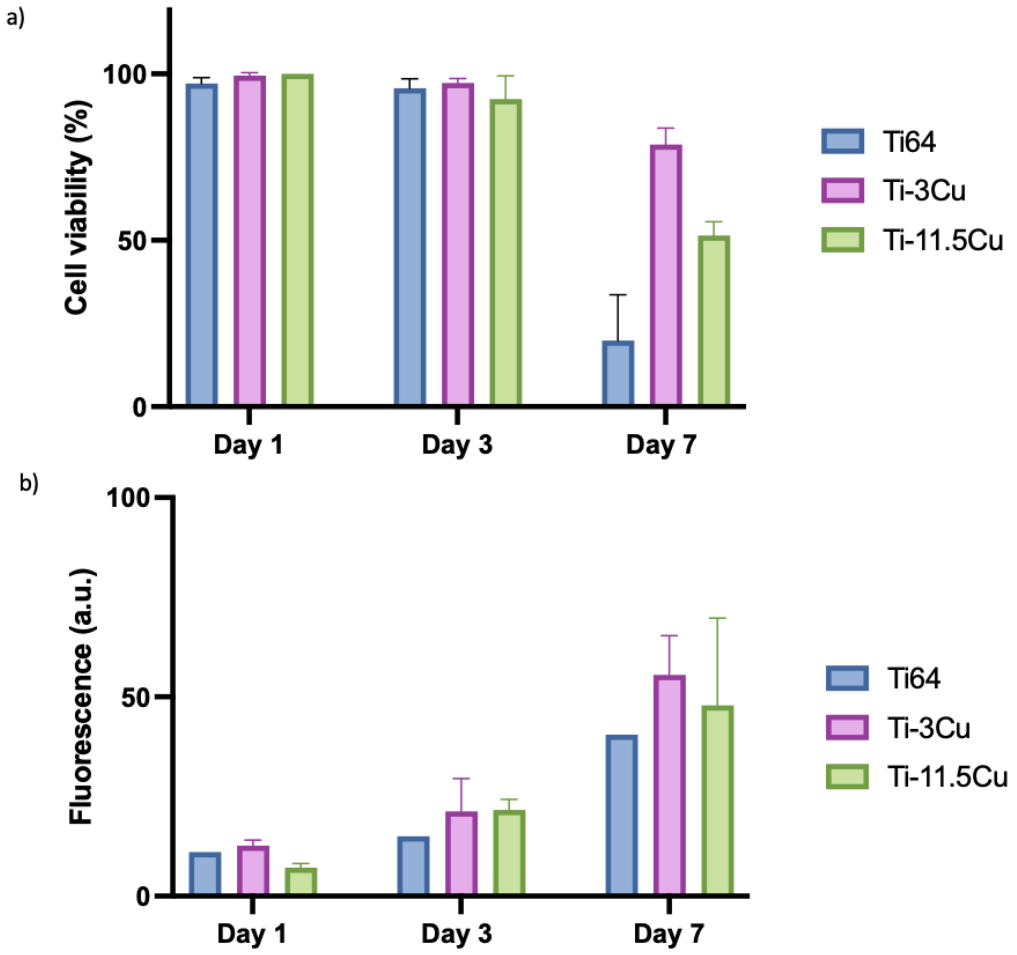

Figure 4.17: (a) Quantification of cell viability from images in Figure 4.16 and (b) metabolic activity assessed via Alamar Blue assay.(n=3)

4.4. Discussion

With very few literature studies on comparisons of manufacturing methods of Ti-Cu alloys for antimicrobial functions, combined with the lack of consistency between antimicrobial tests, comparisons across studies remain challenging. Variability in bacterial strains, inoculum concentrations, incubation times and measurement techniques can lead to discrepancies. This study examines the antimicrobial properties and cytotoxicity of Ti-Cu alloys produced using PBF-LB and powder metallurgy methods, providing valuable insights into how the manufacturing process influences these characteristics.

Many defects can often be observed in additively manufactured parts, their shape and size can often give guidance as to their origins. One example of defects commonly found is partially melted particles, this is often due to ineffective heat transfer within the material. Other defects include keyholes, which can often be denoted by having a flat surface beneath the void [298]. These are often produced by high energy outputs altering the shape of the melt pool from a shallow and semi-circular shape to a narrower deeper structure. These are problematic as they cause low fatigue strength and result in premature failure of the structures [299]. Pores which are circular in shape are commonly induced due to gas entrapped in the layers, whereas those more irregular are simply caused by poor heat transfer [298]. In order to ensure the material maintains the necessary mechanical properties, these defects must be reduced, and hence laser parameters should be optimised.

The processability of the additively manufactured Ti-Cu alloys varied significantly with copper content, as demonstrated in Figure 4.5. Ti-3Cu and Ti-11.5Cu compositions were successfully printed across a range of laser energy densities, although certain cubes experienced excessive remelting through the support structures. This occurred primarily at high laser energy inputs

resulting in poor geometric accuracy, caused by larger melt pools, complicating post-processing steps such as part removal from the build plate. Nonetheless, these two compositions generally showed acceptable processability and were suitable for further characterisation.

In contrast, the Ti-33Cu alloy demonstrated severe processability issues. 6 out of 15 cubes had to be suppressed due to recoater interference, while only one cube was successfully fabricated without visible external defects. Delamination was a pervasive issue, likely driven by the high reflectivity of copper and the resulting increase in thermal gradients and residual stresses. Additional contributing factors may include oxidation at areas of high copper concentration, which promoted the formation of porous regions. Despite maintaining oxygen levels below 1000 ppm during the build process, the observed blue discoloration on the cube surfaces suggested oxidation and potential copper metallisation had still occurred. Due to the extent of the defects and instability during printing, Ti-33Cu was deemed unsuitable for further mechanical or microstructural characterisation. Overall, the increasing Cu content significantly hindered the printability of the Ti-Cu alloys, limiting their viability for further investigations.

Previous work has determined that controlled microstructural modifications through heat treatments, can enhance both the antimicrobial performance and cytotoxicity to native bone cells. However, much of previous literature relates the antimicrobial efficacy to the presence of Ti_2Cu precipitates, which facilitate Cu ion release and contribute to bacterial inhibition [171, 176]. Nevertheless, the low laser energy density conditions utilised during the AM processing in this study minimises the diffusion of Cu into the Ti matrix. This results in reduced formation of intermetallic phases, except in the Ti-11.5Cu alloy (Figure 4.10c), where a measurable presence of intermetallic compounds, i.e. Ti_2Cu, is determined. The limited intermetallic phase formation in the lower Cu-content alloys suggests alternative mechanisms, through grain

refinement and increased surface reactivity, may play a role in antimicrobial behaviour. Furthermore, the powder metallurgy methods (ball milling and pressing) described in this chapter produces ‘green parts’, highlighting the antimicrobial efficacy of a mixture without formation of intermetallic or element diffusion.

The exploratory pressed specimens in this study were used to assess the impact of a defined amount of copper per surface area, enabling evaluation of the antimicrobial effect of pure Cu. The pressed specimens result in 100 % efficacy towards both *S. aureus* and *E. coli*, suggesting the same mechanisms as pure Cu. The antimicrobial effects of the Ti-11.5Cu AM alloy can also be attributed to the ionic release mechanism (Figure 4.11), which is likely influenced by various environmental conditions such as pH and exposure duration. Changes in pH can alter the electrochemical potential at the alloy surface, affecting the rate of Cu ion dissolution and thereby modulating its antimicrobial efficacy. Similarly, prolonged exposure to physiological fluids may lead to the formation of passivation layers, or oxides, which could either enhance or hinder Cu ion release over time [26]. Furthermore, the measured protein adsorption on the Ti-Cu AM surfaces, may impact the ion release of these alloys. Understanding these factors is crucial for predicting the long-term performance of Ti-Cu alloys *in vivo*.

The measured Ti-11.5Cu ion release in this study is potentially facilitated by localised electrochemical interactions between the α-Ti matrix and the Ti_2Cu phase. This could induce galvanic corrosion, enhancing Cu ion dissolution and further inhibit bacterial growth. Comparisons with cast and heat-treated samples, tested under identical conditions, revealed that the AM Ti-Cu alloys exhibit superior antimicrobial performance against *S. aureus* and *E. coli*, even upon reduction of Cu content to 3 wt.% . This improvement is likely linked to the finer grain structure typical of PBF-LB processed materials, due to higher cooling rates, which

enhances electron transfer, thereby accelerating ionic release and galvanic corrosion [239, 300-302].

The observed improvement in the antimicrobial properties of the alloys described in this study against *E. coli* suggests that the reduction in intermetallic phases enhances bacterial inhibition by more closely aligning with the mechanism of pure copper. Since copper exerts its antimicrobial effect primarily through the release of Cu ions, which disrupt bacterial membranes, generate reactive oxygen species (ROS), and interfere with enzymatic functions, the decrease in intermetallic phases likely increases the availability of these ions. The reduction of these phases may enhance the rate of the alloy's corrosion behaviour, promoting higher ion release and improving antibacterial properties. Nevertheless, in the case of the Ti-3Cu AM alloy, it is likely that a direct contact killing mechanism, similar to that seen in the cast samples, occurs. Membrane disruption may be possible without ion dissolution, either through generation of reactive oxygen species at the alloy surface, or through the nanoscale Ti_2Cu phase imparting electrostatic interactions to disrupt bacterial cell integrity.

In addition to antimicrobial benefits, AM Ti-Cu alloys also demonstrated improved cytocompatibility with pre-osteoblast cells compared to cast samples. This suggests that the reduction in coarse intermetallic phases, coupled with the refined grain boundaries, may contribute to enhanced cell adhesion and proliferation. The ability to tailor the microstructure and phase distribution via AM techniques presents a promising route to optimising both the antimicrobial properties and cytocompatibility of biomedical Ti-Cu alloys, further supporting their potential for biomedical implant applications.

Despite these advantages, concern regarding the long-term biocompatibility of Cu-containing Ti alloys persist. While Cu is an essential trace element in the body [148], excessive amounts of Cu can cause cytotoxicity and present with various health concerns [303]. The optimal concentration of Cu in Ti alloys remains a subject of debate, as its biocompatibility is likely linked to corrosion-induced ion release [304]. Increased ion release from Cu-containing Ti alloys may not only compromise long-term biocompatibility but also contribute to the emergence of antimicrobial resistance against copper. Although the Ti-11.5Cu alloy exhibits stronger antimicrobial properties compared to Ti-3Cu, the latter's lower Cu ion release may be advantageous in preventing cytotoxic effects and mitigating the risk of antimicrobial resistance. Furthermore, Figures 4.16 and 4.17 highlights the increase in Cu content increases the cytotoxicity of the AM alloys. This underscores the need for a nuanced approach in designing Cu-containing Ti alloys, ensuring that their antimicrobial benefits do not come at the cost of long-term safety and biological compatibility.

Potential mitigation strategies, such as surface coatings or controlled-release mechanisms, could help regulate Cu ion release, minimising cytotoxic effects while maintaining antimicrobial efficacy. Surface modifications, including oxide or polymer coatings, may serve as diffusion barriers to control ion dissolution, while engineered degradation profiles could optimise release rates to balance antibacterial performance with biocompatibility. Furthermore, by including additional alloy elements, the biocompatibility of these alloys could also be improved. Exploring such approaches will be critical in developing safe and effective Cu-containing alloys for biomedical applications.

4.5. Conclusion

Through variations in alloy manufacture, it is possible to determine the impact on microstructural differences on antimicrobial efficacy. The results from this work demonstrate that the manufacturing method, and corresponding microstructure, do play a role in the antimicrobial efficacy of Ti-Cu alloys. In a pressed form, an elemental mixture of Ti and Cu shows good efficacy, however when combined as an alloy, performance appears much more sensitive to the structure of the metal. Additive manufacturing (specifically PBF-LB) showed improved efficacy towards both *S. aureus* and *E. coli*, in comparison to samples manufactured through casting methods. This is likely due to a shift in mode of action towards ion release mechanisms, prompted by finer grain size due to high cooling rates noted in additive manufacturing.

Furthermore, this work demonstrates an improvement in cytocompatibility of AM samples compared to casting methods. Although the Ti-11.5Cu alloy showed the highest antimicrobial efficacy, the Ti-3Cu alloy presents the greatest potential for future applications. Its lack of measurable Cu ion release may help prevent cytotoxic effects while simultaneously reducing the risk of antimicrobial resistance, making it a promising alternative for biomedical use. Thus, this chapter identifies that microstructural differences related to manufacturing can be utilised to tailor antimicrobial and biological properties of Ti-Cu alloys beyond simple compositional variation.

Chapter 5

THE EFFECT OF MOLYBDENUM ADDITION ON MECHANICAL AND ANTIMICROBIAL PROPERTIES OF ADDITIVELY MANUFACTURED TI-CU ALLOYS

Whilst titanium-copper alloys are well regarded due to their intrinsic antimicrobial properties, limited research has been done to further improve their mechanical properties through strategic elemental additions. Through consideration of biocompatible β-stabilising elements, molybdenum was selected. Ti-Mo alloys are increasingly used as biomedical alloys due to their enhanced mechanical properties and corrosion resistance. For the first time, to the authors knowledge, this chapter explores the potential to process blended powder Ti-Mo-Cu compositions via PBF-LB.

Due to the fundamental differences in melting and boiling points between Cu and Mo, this study explores the use of low energy density strategies to entrap Mo within a Ti-Cu matrix, followed by post-processing heat treatment to facilitate Mo diffusion. This study demonstrates the ability to use PBF-LB through low energy densities to minimise defects and use post-processing heat treatments to enable Mo diffusion. Notably, this distinctive process approach could be leveraged generally for the processing of blended powder alloys with dissimilar processing characteristics.

Specifically, within this chapter, the viability of producing fully dense Ti-21.5Mo and Ti-Mo-Cu alloys (Ti-Mo-3Cu and Ti-Mo-11.5Cu) using low laser energy densities (100-200 W, 500-2000 mms^{-1}) via PBF-LB is confirmed. Following this initial process window identification, targeted heat treatments (950/1000 °C) were undertaken to homogenise and optimise functional performance. Despite initial challenges with powder flowability due to fine Mo particles (3-7 μm), fully dense samples were manufactured. As evidenced by changes in Mo particulate size, it was confirmed via SEM that heat treatment was capable of diffusing Mo into the surrounding Ti-matrix. Microhardness was shown to increase with Cu content, correlating with the formation of Ti_2Cu phases. Antimicrobial testing against *S. aureus* demonstrated enhanced efficacy in Ti-Mo-Cu alloys compared to their binary counterparts. This establishes the potential of Ti-Mo-Cu alloys for biomedical implant applications, balancing antimicrobial and biological properties with mechanical characteristics. Future work is necessary to further unpick microstructural features and phase composition, as well as the mechanical properties of the alloys.

5. The Effect of Molybdenum Addition on Mechanical and Antimicrobial Properties of Additively Manufactured Ti-Cu Alloys

5.1. Introduction

Although this thesis has primarily focused on enhancing the biological properties of biomedical alloys, particularly in combatting infection, it is also vital to consider the mechanical properties of these advanced Ti-based alloys. Aseptic loosening, caused by stress shielding, is the lead cause of failure in orthopaedic implants [7, 305, 306]. This effect is typically caused by a mismatch of elastic moduli between the implant and bone [5, 24]. For context, the elastic modulus of cortical human bone is 30 GPa, whereas Ti-6Al-4V is much higher at around 112 GPa [57]. It is also important to consider the impact of appropriate mechanical stabilisation on prevalence of infection, with some reports demonstrating that stable fractures are less prone to infection compared with unstable fractures. While the exact reasoning behind this remains unclear, it is suggested to be linked with improved bone regeneration under optimal stability or the detrimental effects of instability on surrounding tissues [307]. Thus, it can be considered that the mechanical properties and stability of the device have a subsequent impact on various biological properties, such as osteogenesis and even vascularisation [307, 308].

In recent years, β-Ti alloys have emerged as the most promising candidates for metallic bone implants due to their superior mechanical properties, low density and enhanced corrosion resistance compared to α-Ti alloys [54, 55, 60]. Typically, heat treatments above 883 °C are required to facilitate the transformation from the α to the β phase [56]. However, the β phase

may be stabilised at lower temperatures by incorporating particular stabilising elements into the Ti-matrix, such as molybdenum or zirconium [58]. Typically, these alloys also contain elements of a non-toxic nature and thus exhibit improved biocompatibility compared to α+β alloys [58]. A key advantage of β-Ti alloys is their considerably lower modulus (around 20 % reduction) compared to α+β alloys, which helps to mitigate stress-shielding. For example, Ti-24Nb-4Zr-8Sn has been shown to exhibit an elastic modulus of 46-55 GPa, more than a 50 % reduction compared with Ti-6Al-4V [57].

When considering elemental selection to achieve stabilisation of the beta phase, it is important to evaluate any biological implications of incorporating such elements. A key example of this is vanadium, which is known to be an effective β- stabiliser in Ti alloys giving rise to enhanced mechanical strength [60]. However, in recent years the incorporation of V in biomedical implants has raised significant concerns due to its potential cytotoxicity and systemic toxicity. Upon implantation, vanadium can be released from the alloy in the form of ions, particularly in its V^{4+} and V^{5+} oxidation states, as well as oxides such as vanadium pentoxide (V_2O_5) [58]. Furthermore, it has been shown that vanadium is released from even well-functioning Ti-6Al-4V implants and can be detected in blood, serum, and urine [61]. Likewise it is suggested that ionic vanadium may also be released in to the body from the surface oxide layer [62] and that metal ion release similar to that of a Ti-6Al-4V implant may inhibit normal cell differentiation [63]. The precise mechanisms and severity of vanadium toxicity, particularly in concentrations associated with Ti-6Al-4V release, remain an area of debate within literature. Nevertheless, vanadium has been associated with a variety of toxic effects including haematological, biochemical, neurobehavioural, and reproductive [64, 65]. *In vitro* studies using rodent cells have specifically shown cytotoxic behaviour and suggest that citrate, lactate, and chloride found in blood plasma may assist the release of vanadium ions whereby it bonds with human serum

albumin enabling cell uptake [62]. Consequently, there is motivation to consider other alternative stabilising elements as non-toxic alternatives.

With this in mind, molybdenum is being explored as an alternative β- stabiliser as it can stabilise at low solute concentrations and is deemed to be more effective at strengthening Ti-alloys than other elements, e.g., V and Nb [201, 203]. Figure 5.1 depicts the binary Ti-Mo phase diagram. Therefore, binary Ti-Mo alloys with up to 20 wt.% Mo have been widely studied and exhibit desirable properties [203, 204, 217, 309]. Consequently, these alloys are considered suitable as orthopaedic implants as standardised by ASTM [203]. In particular, Ti-15Mo has been utilised due to its excellent corrosion resistance and good mechanical properties [310]. However, a remaining challenge with incorporating Mo into Ti alloys is processability due to the high melting point of Mo and low interdiffusion rate between Mo and Ti [299, 311].

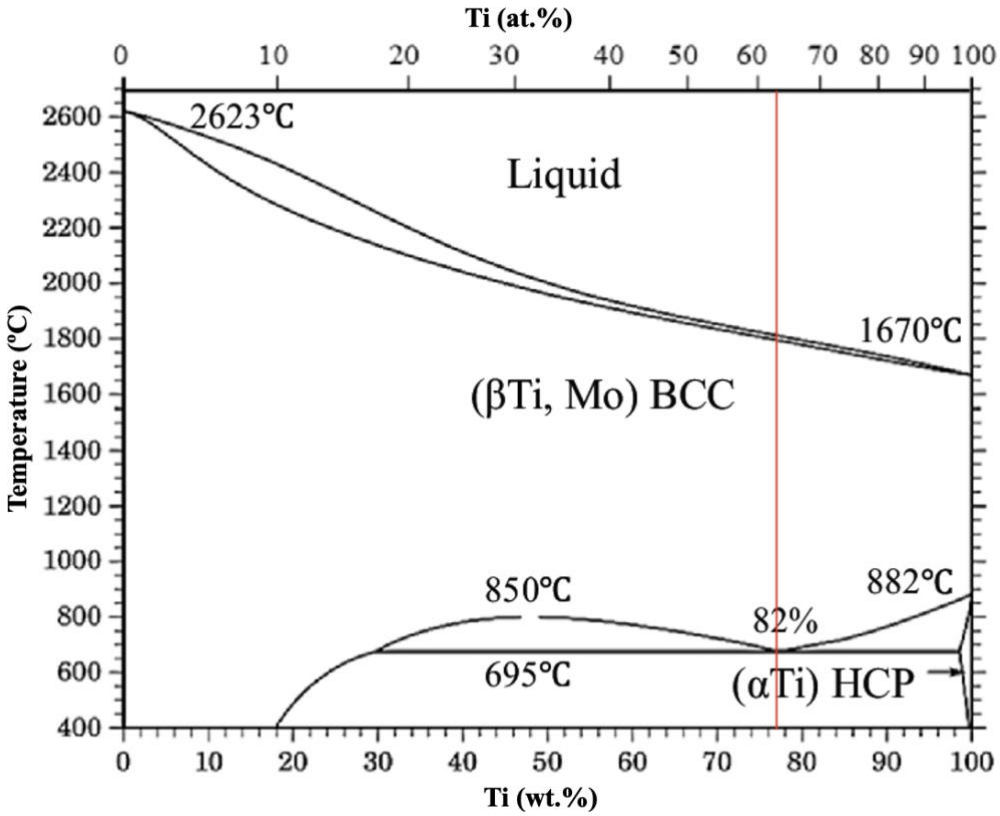

Figure 5.1: Ti-Mo binary phase diagram. The red line depicts the Ti-Mo composition studied in this chapter, due to the lower beta-transus temperature. Adapted from Zhang et al. [206].

Interestingly, PBF-LB has demonstrated high potential for manufacture of binary blended powder Ti-Mo alloys, despite the mismatch of melting points (Ti: 1668 °C and Mo: 2623 °C) and high reflectivity of Mo (Ti: 0.55 and Ti: 0.69 at a laser wavelength of 1.06 μm) [205, 236, 299, 312, 313]. While these binary studies have demonstrated the possibility to produce high density Ti-Mo PBF-LB samples, incorporation of other biologically function elements remain a challenge, especially if the boiling point lies below the melting point of Mo (2623 °C) [314]. This would be the case for Cu, which exhibits a boiling point of 2595 °C [315]. Figure 5.2 demonstrates the melting and boiling points of various potential alloying elements.

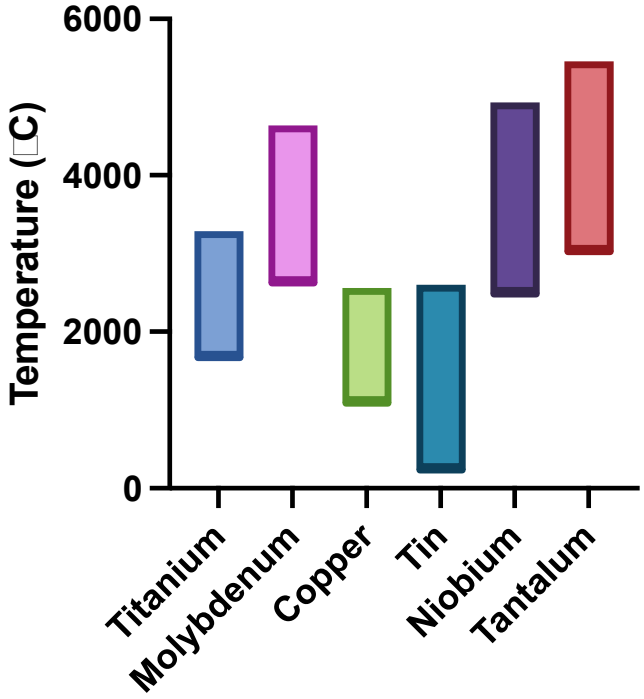

Figure 5.2: Melting and boiling point ranges of metal elements, showing the lack of overlap between elements, such as Mo and Cu, highlighting potential processing issues[314-320].

As such the production of blended powder Ti-Mo-Cu alloys via PBF-LB presents a challenge in identifying an appropriate processing window. The novel approach taken in this chapter was to identify a processing window in which to entrap the Mo within a Ti-Cu matrix and then to explore subsequent diffusion post-build via appropriate heat treatment protocols. Figure 5.3 shows an example isothermal Ti-Mo-Cu phase diagram at 950 °C.

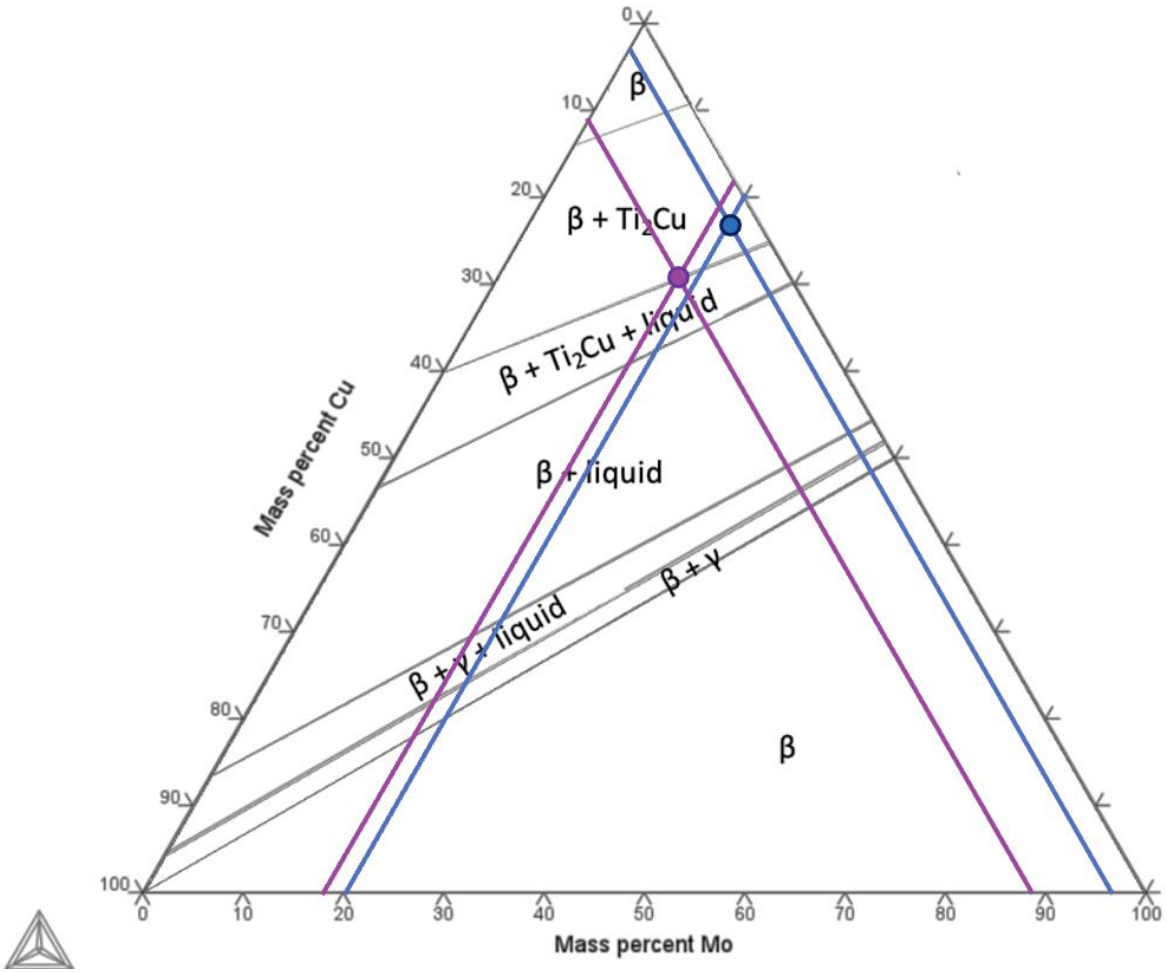

Figure 5.3: Isothermal Ti-Mo-Cu phase diagram at 950 °C, created using ThermoCalc 2023a with TCTI2 database. The blue marks represent the Ti-Mo-3Cu phase composition, whereas the purple mark identifies the Ti-Mo-11.5Cu composition.

Nevertheless, by combining the enhanced properties of a β-stabilised Ti-alloy, through Mo addition, with the antimicrobial properties of the previously discussed Ti-Cu alloys, it may be possible to develop a material that fundamentally tackles the clinical challenges of aseptic loosening and infection in tandem. Luo *et al.* demonstrated that an increase in Cu in Ti-Mo-Cu alloys resulted in a higher strength and lower elastic modulus, indicating good mechanical compatibility. However, the latter study as with much of the other literature utilised powder metallurgy (e.g. ball mill, press and sinter), limiting their direct translation into biomedical

devices [207, 321, 322]. However, Yuan *et al*. ascertained Ti-Mo-10Cu arc-melted alloys demonstrated increases yield strength and decreases elastic modulus compared to binary Ti-Cu alloys. Furthermore, Ti-Mo-10Cu alloys possessed antimicrobial rates of greater than 90 %. Though, as no range of compositions or heat treatments were demonstrated by Yuan *et al.,* it is unsure whether these systems could be further optimised [208].

Since previous findings suggest further benefits from AM methods, through this chapter we consider the ability to manufacture a Ti-Mo-Cu alloy through PBF-LB, with subsequent heat treatments to enable better diffusion.

5.2. Methods

5.2.1. Preliminary Study: Processing window for Ti-Mo via PBF-LB

A study was completed in combination with BEng student, Arya Nicum, entitled 'Blended Powder Alloying of Ti-21.5Mo via Laser Powder Bed Fusion & Heat Treatment'. This aimed to find a low-energy manufacturing method, through the use of PBF-LB, to produce a Ti-Mo alloy consisting of a Ti matrix, with Mo suspended throughout. Heat treatments were also then introduced to diffuse the Mo into the Ti matrix.

5.2.2. Sample Compositions

The alloys investigated throughout this research are Ti-3Cu, Ti-11.5Cu, Ti-21.5Mo, Ti-20Mo-3Cu and Ti-19Mo-11.5Cu (weight percentage, wt. %). Table 5.1 shows these alloy compositions.

Table 5.1: Ti-Cu and Ti-Mo-Cu alloy compositions in weight and atomic percentage, to 1 decimal place.

	Value wt. %			**Value at.%**		
	Ti	Mo	Cu	Ti	Mo	Cu
Ti-3Cu	97.0	0.0	3.0	97.7	0.0	2.3
Ti-11.5Cu	88.5	0.0	11.5	91.1	0.0	8.9
Ti-21.5Mo	78.5	21.5	0.0	88.0	12.0	0.0
Ti-20Mo-3Cu	76.1	20.9	3.0	85.7	11.7	2.5
Ti-19Mo-11.5Cu	69.5	19.0	11.5	79.3	10.8	9.9

Commercially pure (grade 1) titanium, LPW Ltd, molybdenum (Thermo Scientific) and high purity OFHC copper (Eckart) powders, 15-45 μm, 3-7 μm and 15-53 μm particle size distribution respectively, were used for blended powder processing. All powder blends were weighed under Ar atmospheres. The blends were subsequently mixed for 8 hours on a roller blender.

5.2.3. Powder Characterisation

The morphology of Ti-21.5Mo powders was determined using backscattered electron (BSE) scanning electron microscopy (SEM) analysis on a ZEISS EVO10. A powder sample was directly fixed to an adhesive carbon tab, and gently tapped to remove excess particles.

5.2.4. Additive Manufacture

The blended powder feedstock was used to produce cuboidal (10 x 10 x 10 mm) samples. All specimens were processed using a 500 W 1070 nm ytterbium fibre laser on a RenAM500S (Renishaw, UK) PBF-LB system fitted with a Reduced Build Volume (RBV) unit. Builds were performed under an argon atmosphere, with oxygen levels maintained below 1000 ppm throughout lasing. Samples were manufactured on Ti-6Al-4V build substrates. Table 5.2 highlights the set build parameters for all builds.

Table 5.2: Set build parameters maintained across all PBF-LB builds on the RenAM 500S.

Parameter	Value
Layer thickness	30 μm
Exposure point distance	90 μm
Hatch distance	90 μm
Spot diameter	75 μm
Layer angle	67°

Ti-Cu samples were manufactured according to the selected parameters in Chapter 4.

5.2.4.1. Parametric Study

Parametric studies were carried out to optimise laser power and scan speeds to ensure maximum densification of the Ti-Mo and Ti-Mo-Cu specimens with minimal porosity. Laser power was varied between 100 and 200 W, whilst scan speed was varied between 500 and 2000 mm/s, as depicted in Table 5.3. The extent of the laser power was narrowed, to reduce the extent of the energy density, in order to reduce the amount of defects in the builds, compared to those seen in the previous Ti-Cu builds. The Renishaw systems require a change of scan speed to be achieved through alteration of the laser dwell time, calculated using equation 5.1.

$$Dwell\ time\ (\mu s) = \frac{Point\ distance(\mu m)}{Scan\ Speed(mms^{-1})} \times 1000$$

[5.1]

Energy density of the parameters can be calculated using equation 5.2.

$$Energy\ Density\ (Jm^{-1}) = \frac{Laser\ Power\ (W)}{Scan\ Speed(mms^{-1}) \times 1000}$$

[5.2]

Table 5.3:Summary of all specimens manufactured during the parametric studies for both Ti-Mo and Ti-Mo-Cu builds.

Sample Number	Power (W)	Scan speed (mm/s)	Dwell time (µs)	Energy Density (J/m)
1	100	500	180	200
2	100	1000	90	100
3	100	1500	60	67
4	100	2000	45	50
5	150	500	180	300
6	150	1000	90	150
7	150	1500	60	100
8	150	2000	45	75
9	200	500	180	400
10	200	1000	90	200
11	300	1500	60	200
12	200	2000	45	100

5.2.4.2. Archimedes Density

Apparent density of samples was assessed using Archimedes measurements in pure ethanol, utilising an Adventurer Precision AX223, Ohaus. Equilibration of the ethanol was essential prior to measurements, to ensure liquid temperature did not change significantly. Three measurements were taken for each specimen and arithmetic mean and standard deviations calculated.

5.2.4.3. Optimised Builds

Builds were then repeated for each Ti-Mo and Ti-Mo-Cu blend with the optimised parameters to produce specimens for characterisation and antimicrobial testing. Selected parameters for Ti-Mo, Ti-Mo-3Cu and Ti-Mo-11.5Cu specimens are described in Table 5.4.

Table 5.4: Optimised processing parameters for Ti-21.5Mo, Ti-Mo-3Cu and Ti-Mo-11.5Cu compositions.

Composition	Power (W)	Scan speed (mm/s)	Dwell time (µs)	Energy Density (J/m)
Ti-21.5Mo	200	1500	60	133.33
Ti-Mo-3Cu	150	1500	60	100
Ti-Mo-11.5Cu	100	2000	45	50

5.2.5. Heat Treatment

As the Ti-Mo alloys were only utilised as a proof of concept, concerns about oxidation were minimal. A Carbolite Gero-30-3000 furnace was programmed to heat to 1000 °C and samples placed inside once temperature was reached. Samples were removed from the furnace at different time intervals (2, 4 and 6 hours) and allowed to air cool.

Ti-Cu and Ti-Mo-Cu samples were enclosed within a crucible and wrapped in molybdenum foil. The samples were then placed in a tube furnace (Lenton Thermal Designs) and placed under a vacuum, and backfilled with Ar. Heat treatments were carried out in order to homogenise and diffuse the molybdenum particles. The temperature of the furnace was ramped up at a rate of 10 °C/min, and then maintained at 950 °C for either 6 hours or 24 hours, in order to determine the impact of time. Samples were then vacuum cooled before removal.

Samples are identified as either as built (ab), heat treated for 6 hours (HT6), or heat treated for 24 hours (HT24).

5.2.6. Samples Preparation

The alloys were then vertically (X-Z plane) sectioned using an Electro-discharge machine (EDM) into 10x10x2mm coupons for all characterisation and *in vitro* experiments. Samples required for scanning electron microscopy (SEM) were then mounted in conductive Bakelite (Presidon-ML-C, Aptex Ltd). Subsequently, they were mechanically ground to 1200 grit then polished with diamond and OPS solutions, as described in Table 5.5.

Table 5.5: Polishing and grinding sequences for alloy preparation with the Struers Tegramin-25.

Step	Grit/Polish Finish	Lubricant	Force	Rotation	Co-rotation	Time
1	MD-Piano 220	Water	20 N	300	150	Until plane
2	MD-Piano 1200	Water	20 N	300	150	Until plane
3	MD-Largo	DiaDuo 9-micron	15 N	150	150	~ 20 mins
4	MD-Allegro	DiaDuo 3-micron	15 N	150	150	~ 5 mins
5	MD-Chem	OPS	10 N	150	150	~ 30 mins

5.2.7. Microstructural Characterisation and Phase Identification

Scanning electron microscopy (SEM) imaging was completed on a Hitachi Benchtop TM3030 or ZEISS EVO10 using backscattered electron (BSE) detector to reveal compositional contrast. EDX was also employed to determine elemental mapping.

5.2.8. Image Analysis

A series of 9 micrographs were taken from the core of each specimen at x300 magnification. ImageJ was utilised to examine and quantify the diffusion of Mo within the Ti-Mo alloys at each time step, through analysis of quantity and size of Mo particles.

5.2.9. Microhardness

Vickers microhardness testing of mounted and polished samples was performed at 50x optical magnification and 100 g indentation force (Buehler Wilson VH1202). Five indentations were performed automatically per sample in a quincunx arrangement, with manual adjustments made when software failed to accurately locate indent corners (DiaMet, Buehler). Values were then averaged across each sample.

5.2.10. Antimicrobial Analysis

Antimicrobial tests were carried out in relation to ISO 22196:2011 and JIS Z 2801 [272]. *Staphylococcus aureus* was utilised as it is a common Gram-positive bacterium often associated with implant infections. All samples were sterilised by ethanol in dark conditions for 30 minutes and left to dry for 24 hours.

Samples were then seeded with 5 μL of bacteria and a coverslip placed on top, in a petri dish with a sterile tissue wetted with 2 mL of Dulbecco's phosphate-buffered saline (DPBS). The samples were then incubated at 37 °C for 24 hours. After 24 hours, the samples were retrieved and placed in 5mL of DPBS. Solutions containing the AM samples were vortexed for 2 minutes, ensuring the sample and cover slip were separated. The pressed samples were lightly shaken, to minimise sample disintegration. 100 μL of the DPBS solution was extracted, placed into a

96 well plate and serially diluted in DPBS. 10 μL from each well was plated, using a spreader to ensure bacteria were well distributed and countable. Samples were cultured at 37 °C for 24 hours, before being counted.

Bacterial reduction was calculated using equation 5.3, where N_{Ti64} relates to the CFU count for the Ti64 control, whereas N_x relates to the number of bacterial colonies for each sample.

$$Bacterial\ reduction\ (\%) = \frac{N_{Ti64} - N_x}{N_{Ti64}} \times 100 \quad [5.3]$$

5.3. Results

5.3.1. Powder Characterisation

Figure 5.4 shows BSE SEM micrographs of a Ti-21.5Mo powder blend at low and high magnification. It can be seen the large difference in particle size between the Ti powder and Mo powder. However, it can also be seen that the Mo powder (bright white particles) also possess a more cuboidal powder. This could be determined to have a negative impact on the powder blend flowability and processibility. A wide range of particle sizes and irregular shaped particles are visible, unlike the previously discussed Ti-Cu blends.

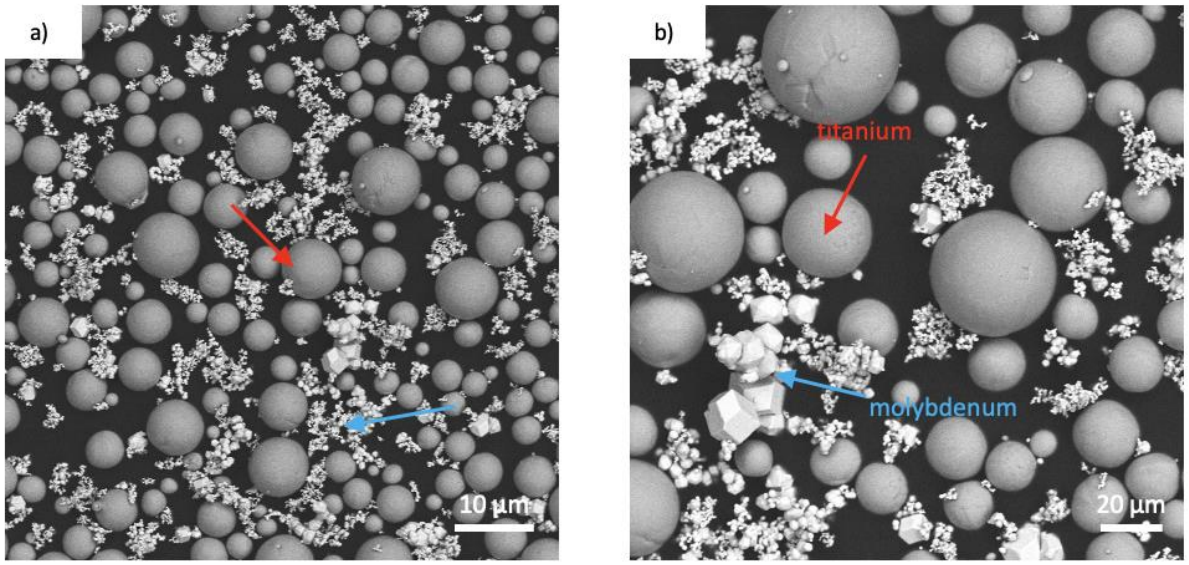

Figure 5.4: BSE SEM micrographs of Ti-Mo powder. Red arrows indicate the titanium powder, whereas blue arrows show the fine cuboidal Mo powder.

5.3.2. Additive Manufacturing

5.3.2.1. Parametric Builds

Short spreading defects were induced in the build processes due to poor powder flowability, relating to the Mo powder, as shown in Figure 5.5. Only cube 11 in the Ti-Mo-3Cu had to be suppressed, however, large defects in other samples limited successful further characterisation.

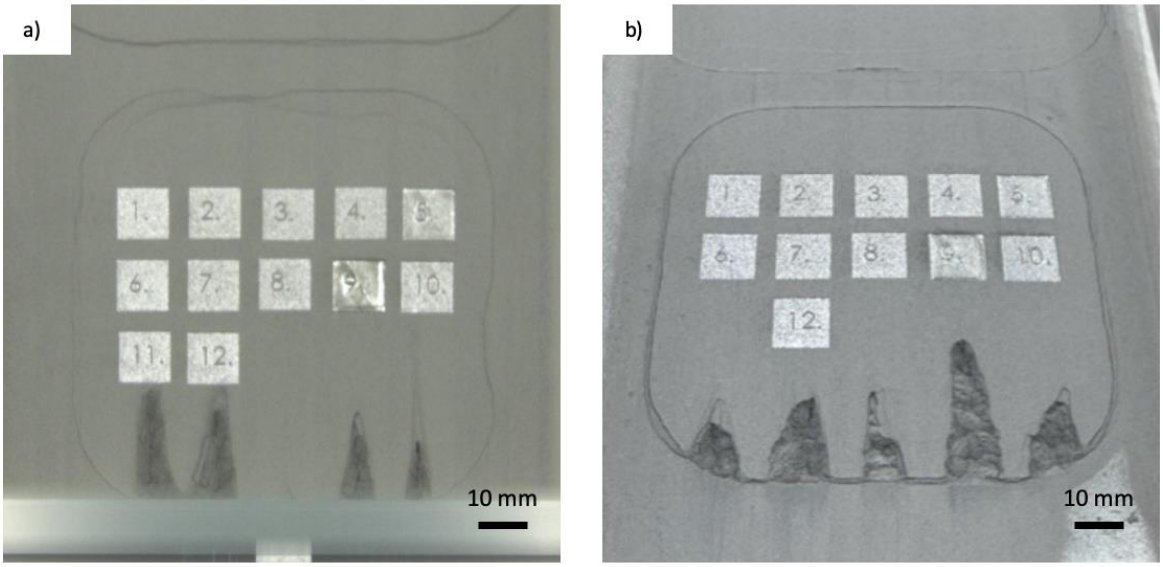

Figure 5.5: Build process images of (a) Ti-21.5Mo and (b) Ti-Mo-3Cu, illustrating short-spreading issues due to the poor spreadability of Mo in the powder blend.

5.3.2.2. Archimedes Density

Figure 5.6 shows the Archimedes density results for each Ti-21.5Mo, Ti-Mo-3Cu and Ti-Mo-11.5Cu cubes manufactured. In general, as the laser energy density increases to around 100 Jm^{-1}, the density of each composition also appears to increase, before then stabilising. Overall, the Ti-Mo-11.5Cu samples also have the highest maximum density. Short spreading affecting some cubes (e.g. cube 12 for Ti-21.5Mo, cube 11 for Ti-Mo-3Cu and cube 12 for Ti-Mo-11.5Cu) caused a reduction in density compared to predicted values.

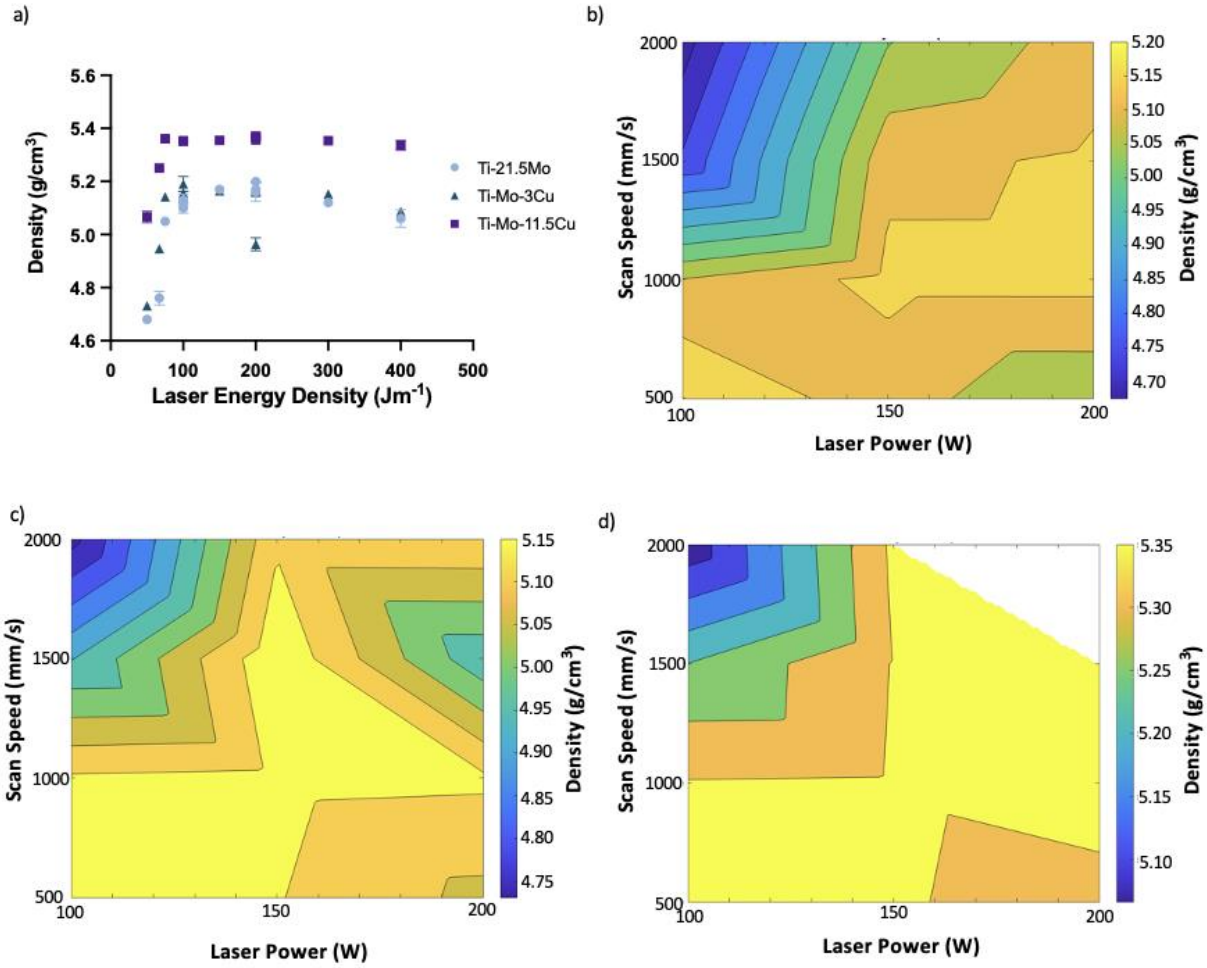

Figure 5.6: Archimedes density graphs. (a) Archimedes density against laser energy density. (b-d) Contour plots depicting density by scan speed and laser power of (b) Ti-21.5Mo, (c) Ti-Mo-3Cu and (d) Ti-Mo-11.5Cu. The white region in (d) is due to the removal of cube 12 data due to short spreading skewing results.

5.3.2.3. Parametric Build Characterisation

Figure 5.7 displays the SEM micrographs taken of each Ti-21.5Mo sample at 500x magnification. These micrographs are representative images of the microstructural features present on each sample. The large defect pictured in cube 12 (200 W, 2000 mm/s) was caused by short spreading through large amounts of the build layers. Whereas the features shown in

cubes 2,3,4,7 and 8 were likely caused by a lack of fusion. Defects seen in cubes 5 and 9, however, are likely caused by keyholing.

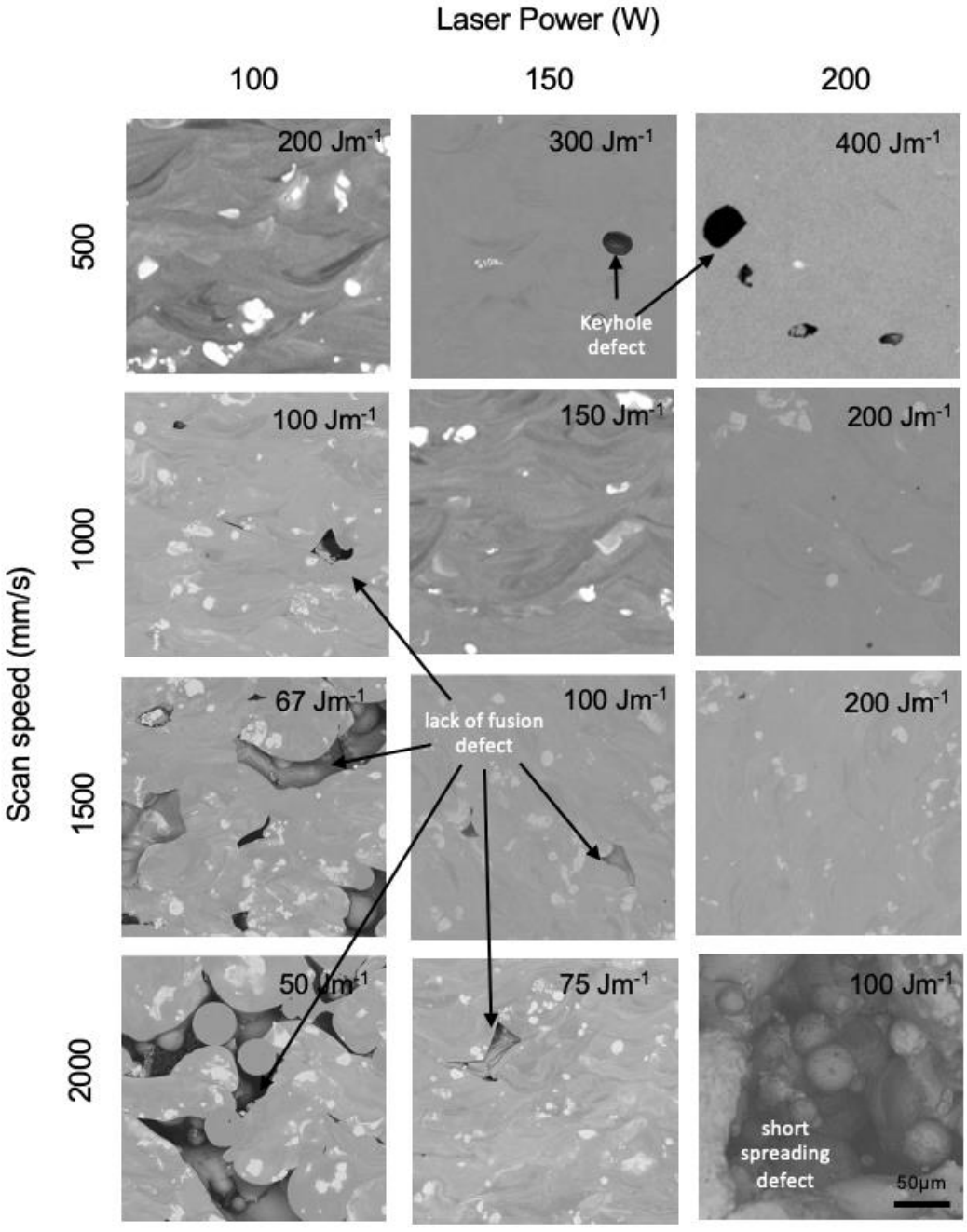

Figure 5.7: Backscatter SEM micrographs of additively manufactured Ti-21.5Mo. Each sample is labelled with laser energy density. A large number of defects are present across all specimens with low laser energies

resulting in lack of fusion defects, and the high laser energy densities causing keyhole defects. Excessive short spreading defects are seen in the specimen manufactured at 200 W and 2000 mms^{-1}.

Figure 5.8 displays the SEM micrographs taken of each Ti-Mo-3Cu sample at 300x magnification. Far fewer defects were observed compared to the Ti-21.5Mo specimens. Though short spreading was apparent in cube 11, some of the sample could be sectioned and analysed. Keyholing was apparent at 400 Jm^{-1} and lack of fusion apparent at 75 Jm^{-1} and 100 Jm^{-1}, cubes 2 and 8 respectively.

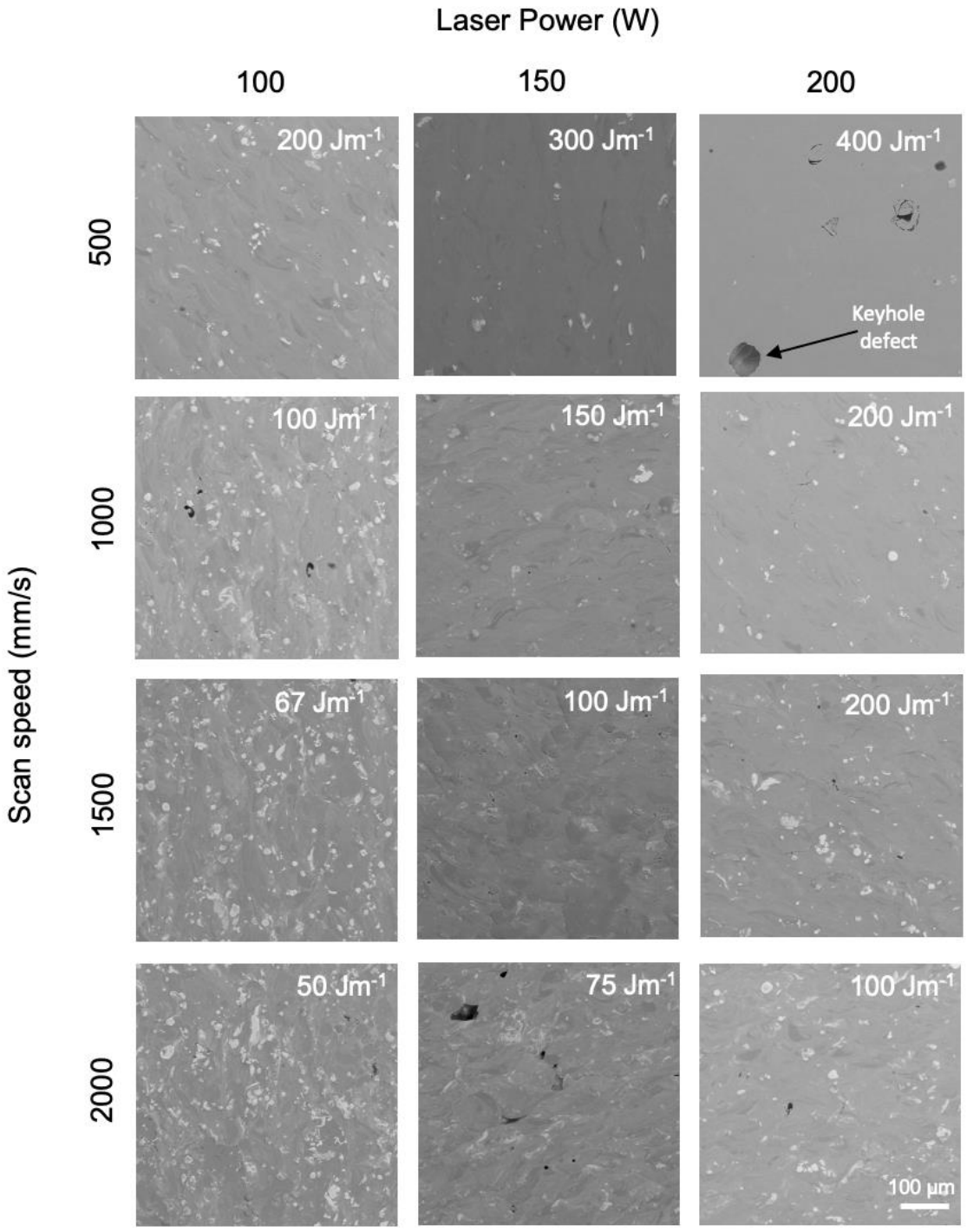

Figure 5.8: Backscatter SEM micrographs of additively manufactured Ti-Mo-3Cu. Each sample is labelled with laser energy density. Mo particles have been trapped in the Ti matrix with minimal diffusion across all parameters. Keyhole defects are present at 400 Jm^{-1}.

Figure 5.9 shows the SEM micrographs taken of each Ti-Mo-11.5Cu sample at 300 x magnification. The increase in copper within the composition appeared to have a negative impact on the processability of the powder, leading to far more defects across the specimens. Short spreading was visible in cube 12, limiting the ability to compare to other specimens. Cracking was present in cubes 2, 6,7, 10 and 11, demonstrating high residual stress.

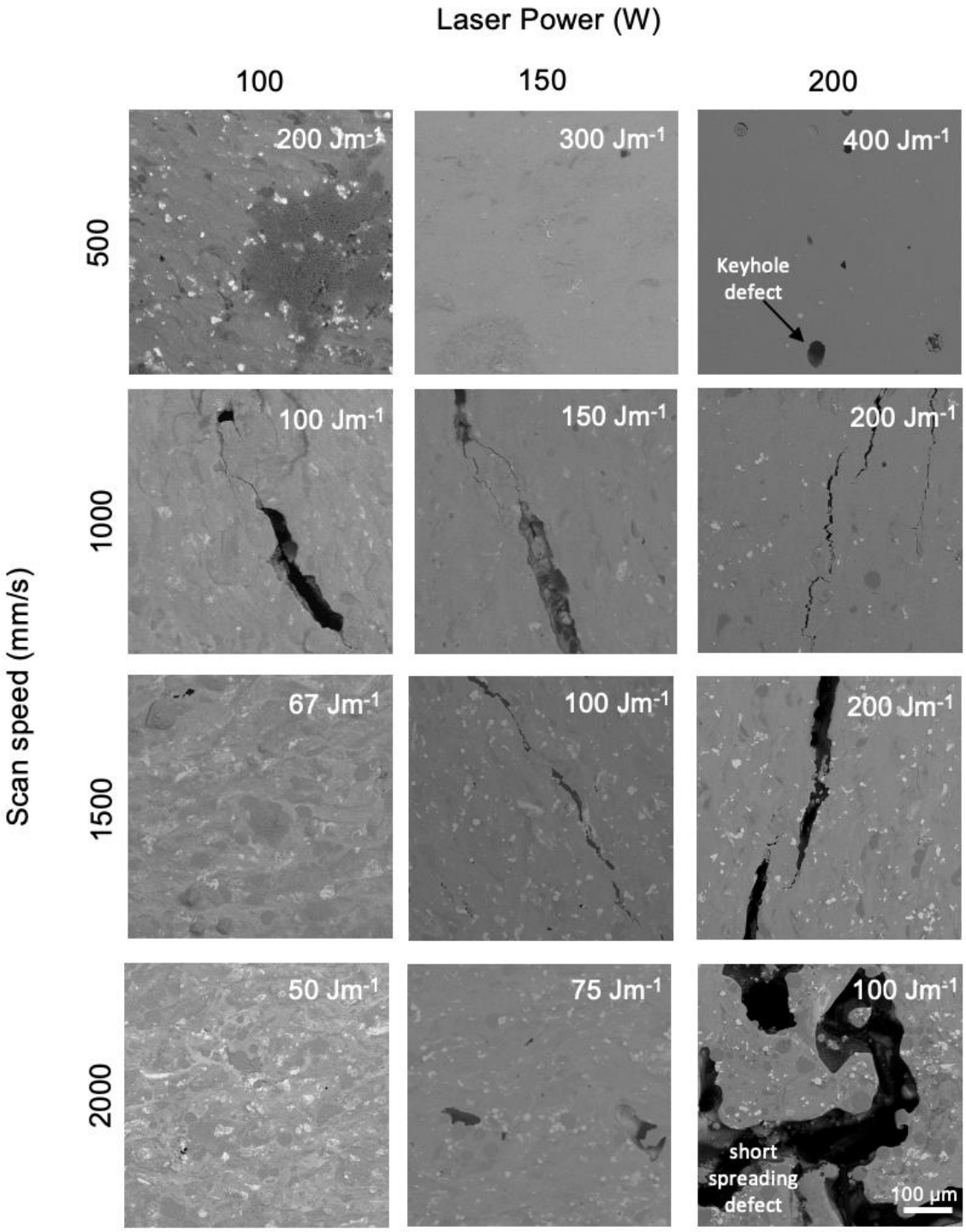

Figure 5.9: Backscatter SEM micrographs of additively manufactured Ti-Mo-11.5Cu. Each sample is labelled with laser energy density. Keyhole defects are present at the highest laser energy density, with large levels of cracking within 5 of the cubes. Short spreading is present in the 200 W and 2000 mms^{-1} specimen, caused by poor powder flowability.

5.3.3. Microstructural Characterisation and Phase Identification

5.3.3.1. As built

The microstructure of the Ti-21.5Mo specimen as built is shown in Figure 5.10. It is evident that the Mo particles have been entrapped in the Ti matrix. Furthermore, there are some signs of melting as indicated by partial dissolution of the Mo particles and diffuse boundaries.

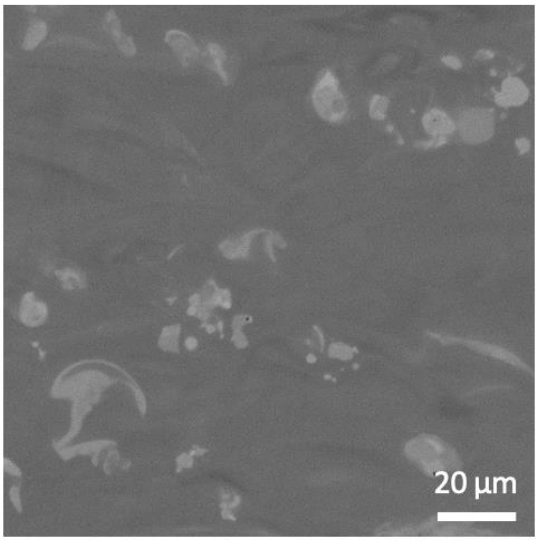

Figure 5.10: SEM micrograph at x1000 magnification of Ti-21.5Mo. Ti matrix and entrapped partially melted Mo powder particles can be observed.

Figure 5.11 shows the micrographs of the Ti-Mo-3Cu and Ti-Mo-11.5Cu as built conditions. It can be observed that there are large levels of heterogeneity across both samples. Molybdenum rich areas can be determined by the brightest regions. Ti-Mo-3Cu, Figure 5.10, shows a relatively uniform microstructure with equiaxed grain structure, with very few intermetallic phases and minimal phase segregation. However, Ti-Mo-11.5Cu, likely due to the increase in Cu content, shows a much more heterogeneous microstructure, potentially due to the increase in intermetallic phase present.

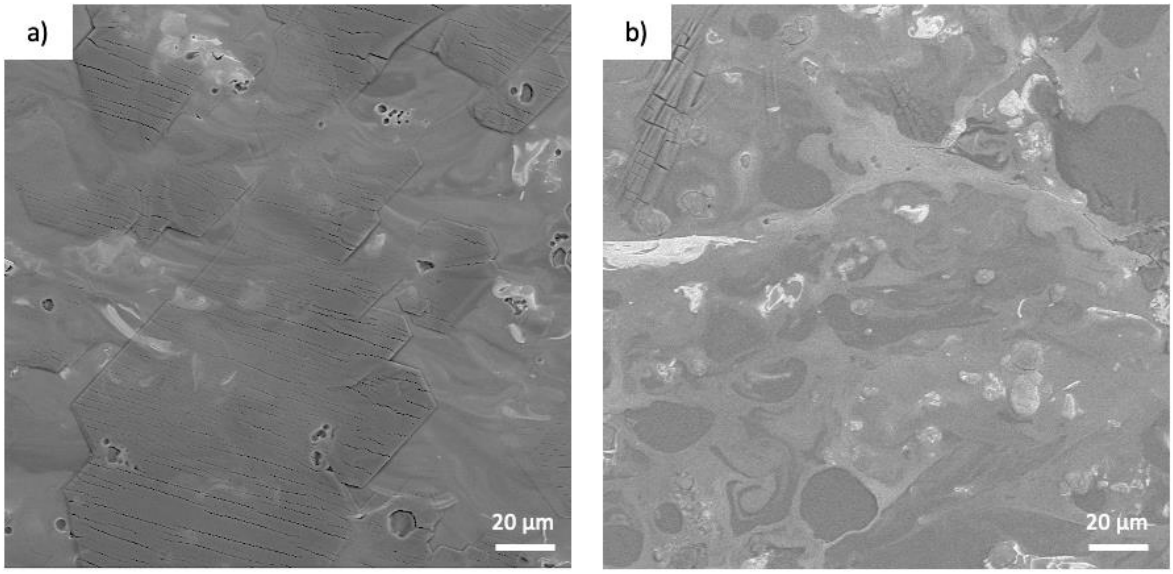

Figure 5.11: SEM micrographs of (a) Ti-Mo-3Cu and (b) Ti-Mo-11.5Cu. Large amounts of heterogeneity is present across both samples, particularly with increase of Cu content.

5.3.4. Post-heat treatment

The impact of the heat treatment was analysed on the Ti-21.5Mo specimens, to determine the progress of the Mo diffusion. Figure 5.12 was used to determine the diffusion efficacy and verified through EDX mapping.

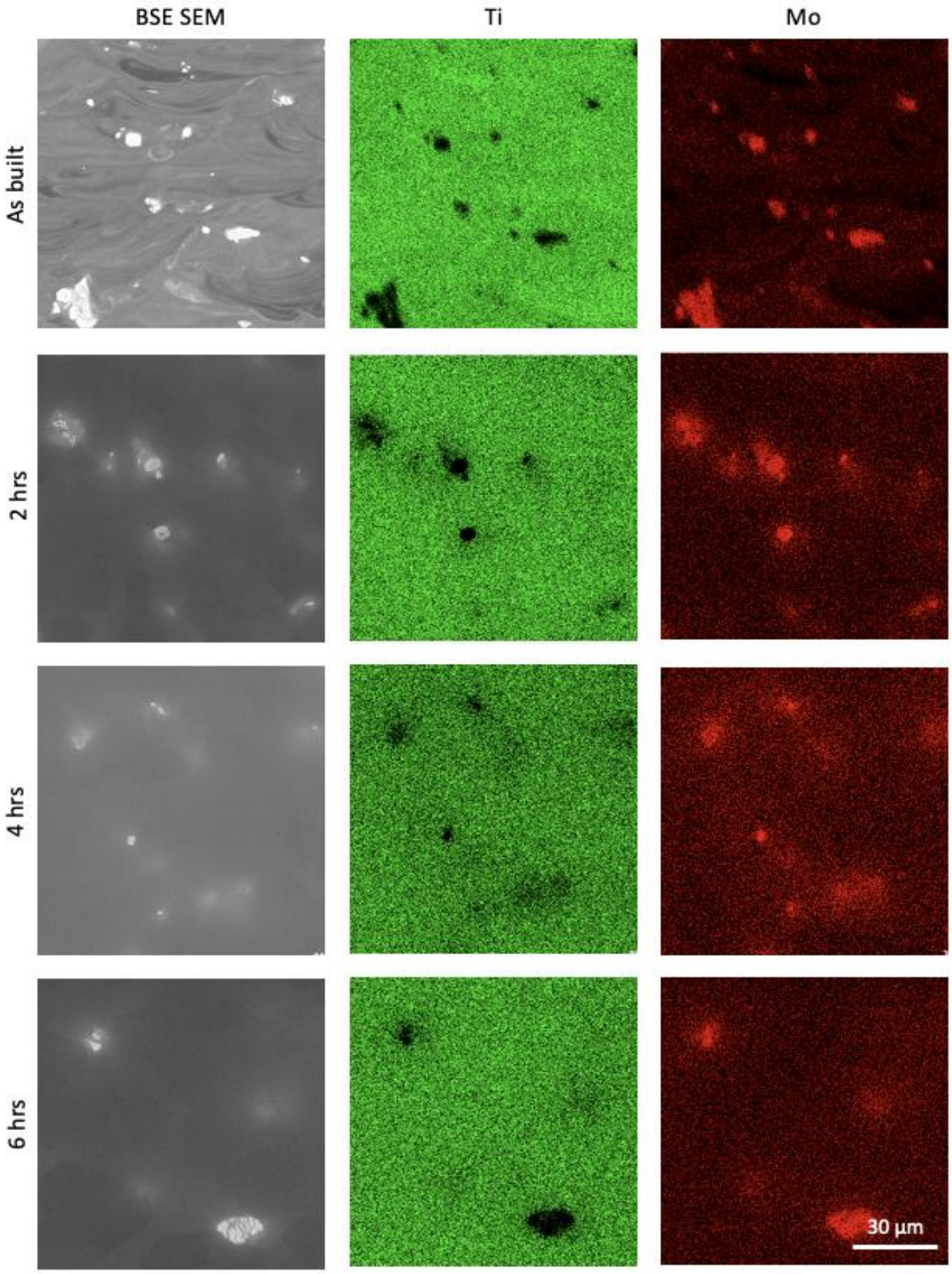

Figure 5.12: BSE SEM and EDX maps at x1000 magnification at Ti-21.5Mo specimens as built and after 2,4 and 6 hours heat treatment. The progression of Mo diffusion can be clearly seen with increase of time as the Mo particles become less defined, and more dispersed in the Ti-matrix.

The extent of the molybdenum diffusion was also analysed via ImageJ, as shown in Figure 5.13. Both Figures 5.13a and 5.13b show that the molybdenum is diffused throughout the heat treatment, reducing the quantity and size of the particles per micrograph. However, Mo particles can still be identified after 6 hours, suggesting longer heat treatments are required to completely diffuse Mo into the Ti matrix.

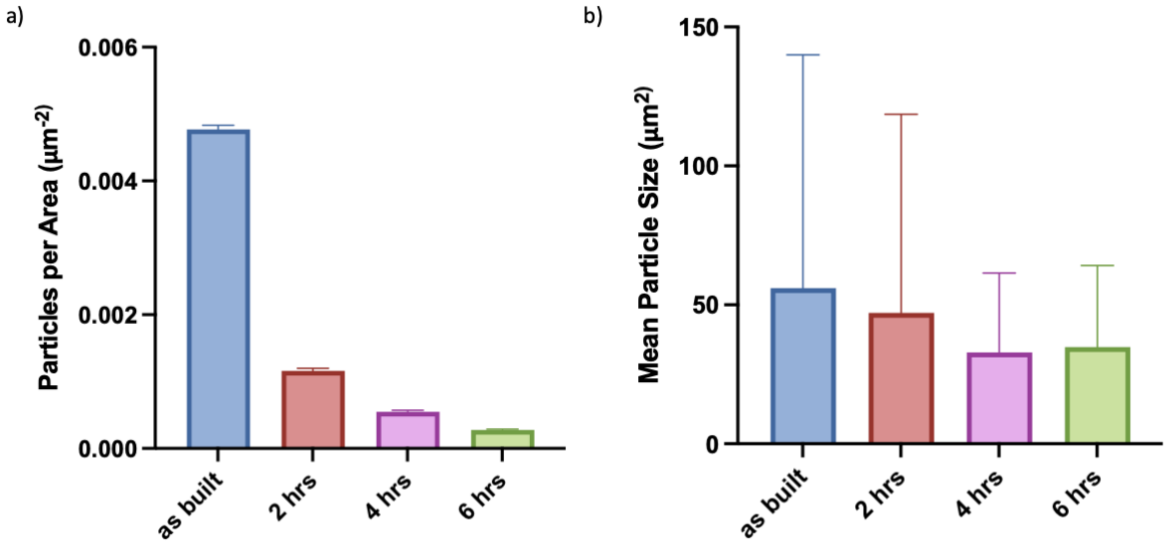

Figure 5.13: (a) Particles per unit area and (b) Mean particle size for each time step of heat treatment of the Ti-21.5Mo specimens. A clear reduction in number of particles and a minor reduction in particle size is apparent with increase in time.

Ti-Cu and Ti-Mo-Cu specimens were subsequently heat treated to determine the impact of heat treatment on mechanical and biological properties. Figure 5.14 presents SEM micrographs of Ti-3Cu, Ti-11.5Cu, Ti-Mo-3Cu and Ti-Mo-11.5Cu across three different conditions: as built, heat treated for 6 hours (HT6) and 24 hours (HT24). Following 6 and 24 hours of heat treatment, all alloys exhibit improved homogenisation. Ti-3Cu HT6 and HT24 shows accumulation of Cu around the grain boundaries. Whereas heat treatment of the Ti-11.5Cu alloy has produced an extremely fine lamellar structure of a Cu-rich phase. Ti-Mo-3Cu and Ti-Mo-11.5Cu HT6 and

HT24 shows large amount of homogenisation of the Ti-matrix, with very few features, except for some partially diffused Mo particles. Nevertheless, their distribution largely becomes more isolated with heat treatment. However, defects and potential signs of melting appear to have been bought into the Ti-Mo-11.5Cu HT6 and HT24 specimen post-heat treatment. EDX scans were intended but due to equipment availability and time constraints have been added into future works.

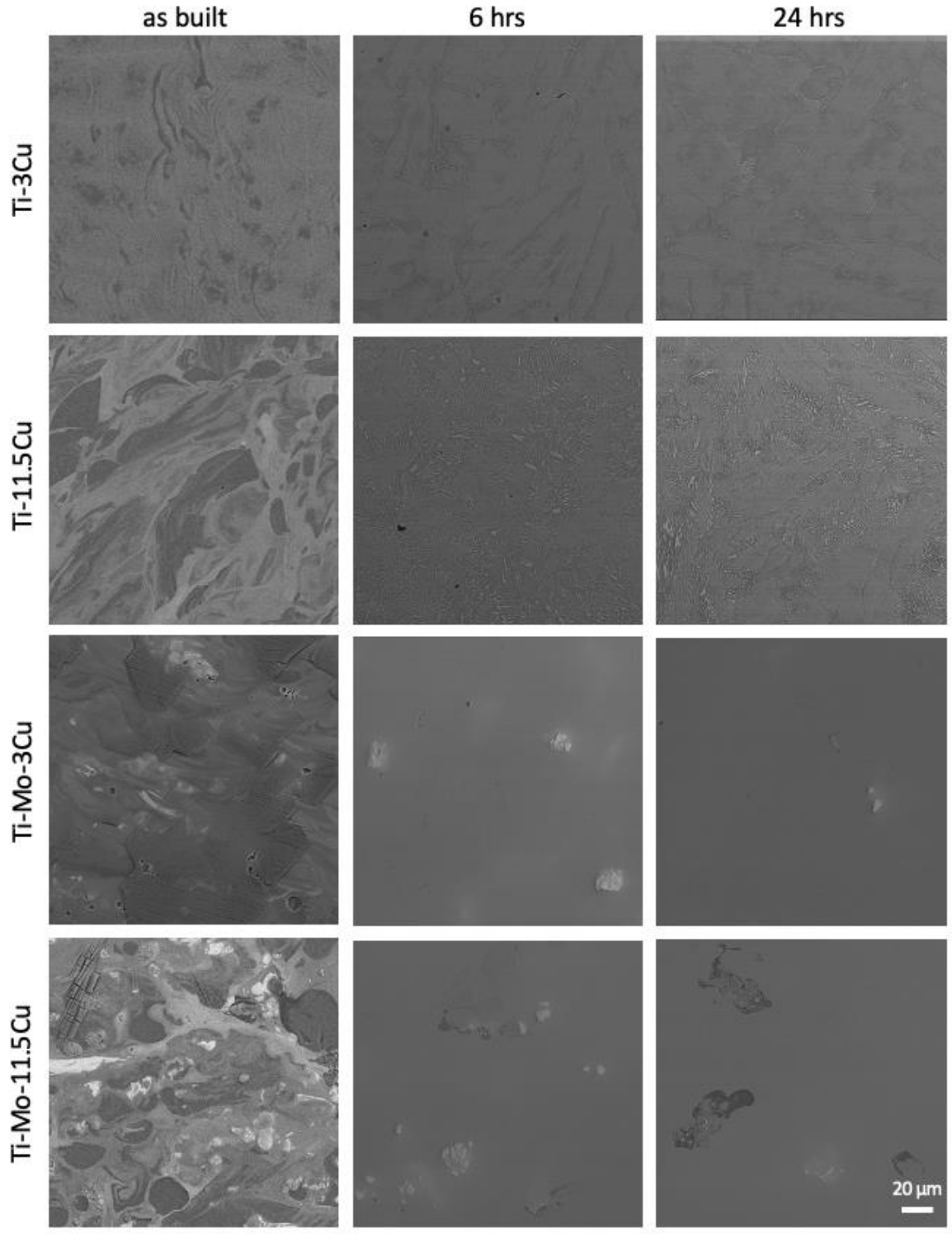

Figure 5.14: SEM micrographs of Ti-Cu and Ti-Mo-Cu specimens at x1000 magnification showing the impact of heat treatment at 950℃ for 6 and 24 hours. Ti-3Cu specimens see the segregation of Cu to grain boundaries, whilst Ti-11.5Cu specimens see an increase in homogeneity with formation of Cu-rich phase

precipitates, similar to those seen in the cast samples. Ti-Mo-Cu alloys see homogenisation of the Ti-matrix with indication of Mo diffusion, but Ti-Mo-11.5Cu shows signs of formation of a liquidous phase during heat treatment.

5.3.5. Microhardness

Figure 5.15 presents the microhardness values of Ti-Cu and Ti-Mo-Cu alloys in their as-built state and after heat treatments at 6 and 24 hours. The results demonstrate how alloy composition and thermal exposure influence mechanical properties. Ti-3Cu maintained relatively stable hardness across all conditions, showing minimal variation after heat treatment. The Ti-11.5Cu ab sample exhibited the highest microhardness among all conditions. However, a notable decrease in hardness was observed after heat treatment at both 6 and 24 hours. The Ti-Mo-3Cu ab alloy displayed moderate microhardness, which remained relatively consistent through heat treatment. However, Ti-Mo-11.5Cu showed low microhardness in the heat-treated states, particularly after 24 hours. This drop may be attributed to the formation of microcracks and more brittle morphologies during prolonged annealing, consistent with the cracking observed in SEM images. Overall, the results suggest that Cu content enhances initial hardness, but heat treatment can reduce it, especially in alloys with higher Cu- content. The inclusion of Mo appears to reduce the impact of heat treatments on the microhardness of the specimens.

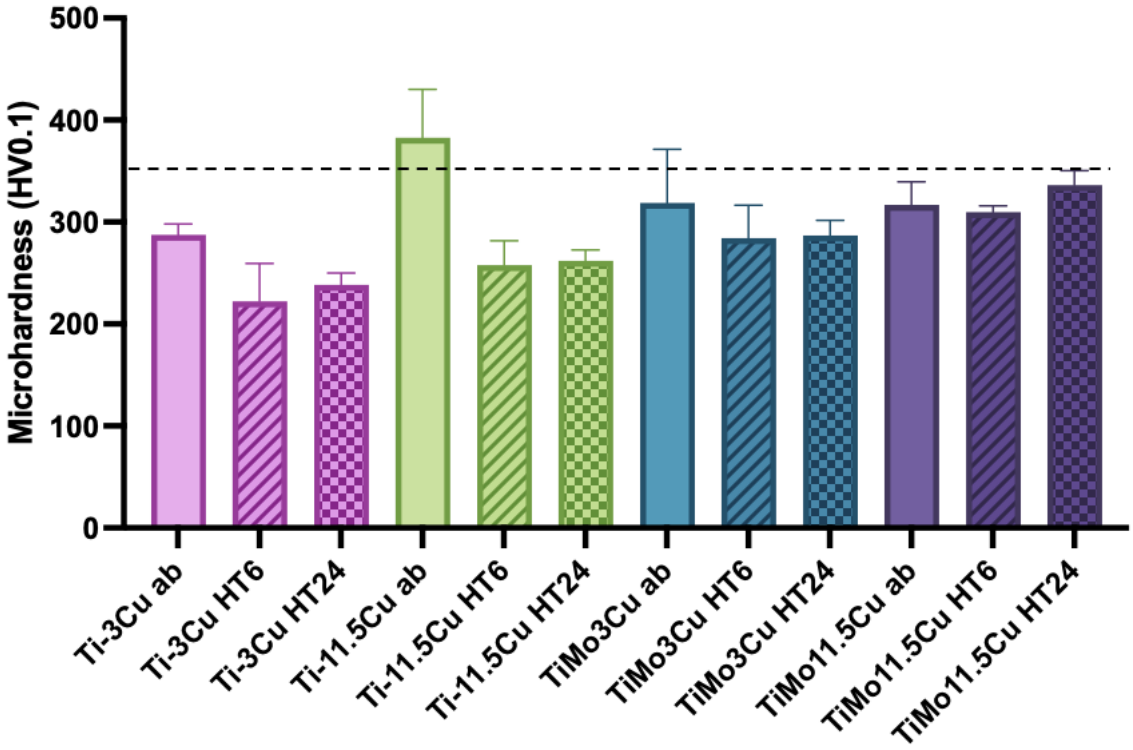

Figure 5.15: Microhardness (HV0.1) data after loading with a 100g force, for both binary Ti-Cu and ternary Ti-Mo-Cu samples, as built and heat treated (n = 5). The dashed line represents the microhardness of Ti-6Al-4V. Heat treatment led to a decrease in hardness for all alloy compositions except Ti-Mo-11.5Cu.

5.3.6. Antimicrobial Analysis

Figure 5.16 shows the antimicrobial data for Ti-Cu and Ti-Mo-Cu, both in the as built and heat treated conditions, against negative (Ti-6Al-4V) and positive (Cu) controls for *S. aureus* after 24 hours incubation. In the Ti-Cu samples as built samples, increasing Cu content corresponded to enhanced antimicrobial efficacy, consistent with Chapter 4. Specifically, Ti-3Cu ab achieved a bacterial reduction of 95.8 %, whilst Ti-11.5Cu as built exhibited a higher reduction of 99.4 %. However, heat treatments further influenced the antimicrobial efficacy, in line with observations from Chapter 3. Ti-3Cu HT6 and Ti-3Cu HT24 achieved reductions of 99.97 %

and 99.8 % respectively, whereas Ti-11.5Cu HT6 and Ti-11.5Cu HT24 demonstrated antimicrobial reductions of 99.2 % and 100 %. Notably, the Ti-Mo-Cu samples all show an increase in antimicrobial efficacy compared to the binary alloys.

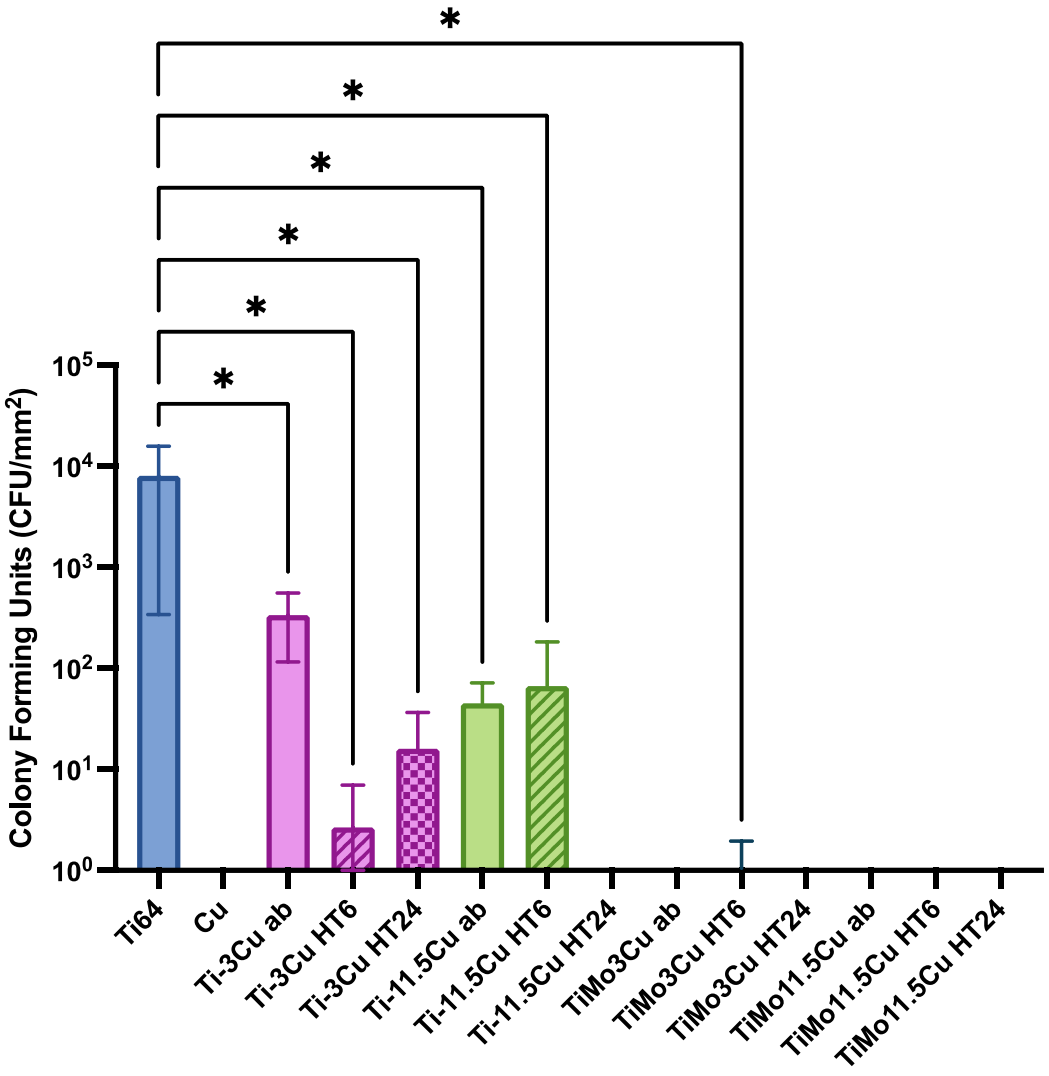

Figure 5.16: Antimicrobial data for Ti-Cu and Ti-Mo-Cu as built and heat treated samples against S. aureus (n=3). Antimicrobial efficacy increases with increase of Cu content in the binary specimen, and 100 % efficacy achieved by all Ti-Mo-Cu samples.

5.4. Discussion

The aim of the parametric studies was to achieve parameters that produced 'fully dense' specimens at the lowest energy density. Therefore, a combination of lower laser powers and higher scan speeds were used, in contrast to the parametric study in the previous chapter. Through a combination of Archimedes density and microstructural observation it was then possible to choose the lowest laser energy parameters to achieve the highest density specimen, with no defects.

In the case of the Ti-21.5Mo study, sample 11 (200 W, 1500 mms^{-1}) was selected as the optimal parameter, due to it possessing the lowest energy density within the specimens with the highest density. Other samples were also eliminated due to a range of lack of fusion or keyholing defects. Keyhole defects occur when the melt pool transforms for a shallow and semicircular shape to a narrow and deep form, typically due to high laser energy densities, causing material to vaporise and a pore to form at the bottom of the melt pool [299]. Short spreading also had negative impacts on some samples caused by poor spreadability of the Mo powder. This study highlights the sensitivity of PBF-LB parameters and the need for optimisation for each new composition and elemental addition.

The aim of the heat treatment study with the Ti-21.5Mo composition was to demonstrate effective molybdenum diffusion and ensure the impact on timesteps and temperatures. In the as built condition, as shown in Figure 5.7, defined Mo particles are present. However, upon heat treatments at 1000 °C, after 2 hours the number of particles reduced significantly. At 4 hours, the Mo particles have been largely diffused as indicated by the brighter Mo regions of the SEM images and EDX maps shown in Figure 5.12. On increase to 6 hours, the number of particles per area in the micrographs, Figure 5.13a, had decreased even further showing diffusion was

still occurring. Nevertheless, this study illustrated the feasibility of utilising low laser energy densities and subsequent heat treatments, Mo could be embedded within specimens and later diffused.

Further, the potential of using PBF-LB with low laser energy density and heat treatments, presents an option to alloy Mo with further elements with low boiling points, e.g. Cu, indicated by Figure 5.2. Thus, Ti-Mo-Cu alloys were further investigated, aiming to combine the potential for improved mechanical properties through β-stabilisation with Mo and enhanced antimicrobial properties with Cu. Though similar alloys had been previously manufactured in literature, powder metallurgy methods had been used to combat manufacturability concerns [207, 208, 321, 322].

Parametric studies of the Ti-Mo and Ti-Mo-Cu compositions highlighted issues with the flowability and spreadability of the powder blends. Due to the use of fine and cuboidal Mo powder, the flowability of the blends decreased, resulting in short spreading across all builds completed (Figure 5.5). Literature has commonly determined that cohesion between fine metal powders and satellite formation can cause powders to have reduced flowability [323-326]. Furthermore, regular spherical particles tend to flow better than irregularly shaped particles [325, 327]. Thus, for long-term development, blended powder is improbable, and atomised powders are likely to be used.

It is known that AM manufactured parts may have downfalls such as high heterogeneity and inherent residual stresses [328]. Furthermore, cracking in the Ti-Mo-11.5Cu ab parametric study specimens could be caused by introduction of Ti_2Cu phase as it is inherently brittle in nature and possesses a very high hardness value, almost 2-3 times more than high strength steels [329]. Additionally, it is possible that due to a mismatch of thermal expansion coefficients of

different phases further stress build up can occur, leading to cracking [330]. Whilst post-processing heat treatments are commonly used to mitigate intrinsic residual stress [328], heat treatments showed the ability to homogenise the microstructures for all Ti-Cu and Ti-Mo-Cu compositions, ensuring that there was larger consistency between sections. However, upon heat treatment of the Ti-Mo-11.5Cu specimens defects were formed, suggesting melting had occurred, demonstrating further processing optimisation is required.

Microhardness, as an initial rapid suggestion for mechanical properties, as shown in Figure 5.15, suggested that addition of Cu can increase the hardness of alloys. The significantly higher microhardness observed in the Ti-11.5Cu ab reflects the strong contribution of Cu-rich intermetallic phases**,** such as Ti_2Cu, which, according to the phase diagram appears to form at approximately 8-15 % at 950 °C. Whereas Mo appears to alter the impact of heat treatment and improve the thermal stability of the alloys.

The antimicrobial behaviour of the Ti-Cu and Ti-Mo-Cu specimen reveals clear trends influenced by both Cu content and heat treatment, aligning with insights established in both Chapters 3 and 4. In the Ti-Cu ab samples, an increase in Cu content directly correlates with improved antimicrobial efficacy, as previously demonstrated. However, interestingly, heat treatment further enhanced the bacterial reductions, particularly for the Ti-3Cu alloy (from 95.8 % to 99.97 % and 99.8 %). This is likely due to the microstructural alteration which appears to result in Cu accumulation at the grain boundaries, likely promoting Cu ion release from the surface. Whereas the Ti-11.5Cu alloy also results in an increase in antimicrobial efficacy after 24 hour heat treatment, probably due to an increase in Cu-rich phase.

The Ti-Mo-Cu alloys demonstrated consistently superior antimicrobial efficacy compared to the binary compositions, regardless of Cu content and heat treatment condition. Although Mo

is not inherently antimicrobial, its role as a β-phase stabiliser impacts the phase distribution that facilitates improved antimicrobial efficacy. This synergistic improvement can be explained by Mo induced microstructural changes, resulting in improvements to Cu ion release or changes in surface hydrophobicity, though further work is necessary to demonstrate the exact alterations.

These results underscore the importance of alloy composition and heat treatment understanding in designing an antimicrobial biomedical alloy. Though high Cu content yields immediate improved efficacy in binary alloys, heat treatment even in Ti-3Cu can significantly elevate performance. The enhancements seen in the Ti-Mo-Cu alloys suggests a promising strategy for developing realistic Ti-based alloys that offer both mechanical robustness and antimicrobial functionality.

5.5. Conclusion

This study demonstrated the viability of producing fully dense Ti-Mo-Cu alloys using low laser energy densities via PBF-LB, followed by targeted heat treatments to optimise microstructural uniformity and functional performance. Parametric optimisation in the Ti-21.5Mo system identified processing conditions that minimised defects such as lack of fusion and keyholing, while enabling molybdenum diffusion during post-processing heat treatments. This enabled a ternary element to be included, despite a mismatch of melting and boiling points. Consequently, Ti-Mo-Cu alloys were manufactured, combining the β-stabilising effects of Mo with the antimicrobial properties of Cu. Despite initial challenges with powder flowability due to fine Mo particles, successful fabrication and heat treatment enabled the formation of Cu-rich intermetallic phases and homogenised microstructures. Microhardness increased with Cu

content, correlating with the formation of Ti_2Cu phases. Antimicrobial testing against *S. aureus* revealed that both Cu content and heat treatment significantly influenced antimicrobial efficacy, with Ti-Mo-Cu alloys outperforming their binary counterparts. These results highlight the critical role of compositional control and heat treatments in tailoring mechanical and biological performance of titanium alloys for biomedical applications.

Chapter 6

CONCLUSIONS AND FUTURE WORK

6. Conclusions and Future Work

This chapter briefly summarises the main conclusions presented in Chapters 3, 4 and 5, including a brief evaluation of the use of Ti-Cu as an antimicrobial alloy for usage in biomedical implants. Suggestions for future research are also presented.

6.1. Overall Conclusions

The manufacture of antimicrobial Ti-Cu metal alloys through different manufacturing and processing methods shows promise as an approach for managing prosthetic joint infections. Specifically, research presented in Chapter 3 has shown the ability to alter the microstructure, and thus antimicrobial efficacy, of arc-melted Ti-Cu alloys through heat treatments (homogenisation at 950 °C and ageing at either 760 or 820 °C). Despite previous assumptions that the Ti_2Cu phase was crucial to antimicrobial efficacy, it was demonstrated that the size and morphology of the precipitates also had a key effect on efficacy against common bacterial species associated with orthopaedic implants. In particular, as cast specimens with nanoscale precipitates (≈ 30 nm) were shown to exhibit minimal antimicrobial efficacy, however, through homogenisation and ageing heat treatments, larger (≈ 5 μm) and rounded precipitates exhibited superior antimicrobial efficacy against *S. aureus*. Furthermore, it was demonstrated, that contrary to literature, the mechanism of action for these alloys was solely contact-dependent, as shown by a lack of ion release through ICP-OES analysis. *In vitro* analysis revealed that a balance of Cu content and precipitate size is also critical for native bone cell cytocompatibility.

Manufacturing methods were also shown to alter the antimicrobial efficacy of Ti-Cu alloys in Chapter 4. Through the use of additive manufacturing and powder metallurgy methods, it was

possible to alter the microstructure and further enhance the biological functionalities of these alloys. Despite previous assertations that Ti_2Cu phase was the main cause of antimicrobial effects, the lack of intermetallic phase in the pressed samples resulted in 100 % efficacy, showing the importance of the ion release mechanism. However, due to the ability of AM Ti-Cu alloys with lower Cu content (3 wt.%) to outperform the cast and heat treated samples, additive manufacturing showed high potential use for future development.

Chapter 5 highlights the ability to alloy elements with highly dissimilar melting points using blended powder additive manufacturing. Furthermore, it marks a step towards producing a more realistic alloy system, combining an antimicrobial alloy with assumed improved mechanical properties to reduce aseptic loosening effects. Additively manufactured Ti-Mo-Cu alloys showed 100 % antimicrobial efficacy, before and after heat treatment, showing a marked improvement from the works in both Chapter 3 and 4. Though further work is required to determine their composition and mechanical properties, the molybdenum addition is expected to enable formation of the superior β-phase.

6.2. Proposed Areas of Future Work

Listed below are research areas identified to develop Ti-Cu alloys as potential orthopaedic implant materials:

1) **Understanding of Ion Release Mechanism**

Whilst currently much of the antimicrobial effect of the AM Ti-Cu alloys has been equated to ion release, the mechanism is not well understood. In particular, understanding the microstructural features that enable the micro galvanic effects would provide further ability to fine-tune the microstructure and enhance the corrosion properties. Furthermore, the rate of

corrosion is also of interest. Through characterisation of the corrosion mechanism and corresponding microstructure, it may be possible to optimise these effects.

2) Impact of Ti-Cu Alloys on Alternative Biological Functionalities

Whilst cytotoxicity of implanted devices is the key concern for biological scientists, it is important to consider other biological functionalities. It is therefore vital to consider the immune system, angiogenesis and bone formation process to fully scrutinise the biological safety and efficacy of an implanted alloy. Understanding the processes following implant placement enables full comprehension of the impact and functions of alloying elements. Biologically driven criteria should encompass the influence of inflammation on wound healing, angiogenesis and osseointegration, as well as the cytotoxicity and effect on bacterial colonisation.

3) Efficacy against Biofilms

To better mimic the internal conditions of an implanted device, future studies should incorporate multispecies bacterial communities and biofilm formation in experimental setups. A large number of *in vivo* infections involve polymicrobial interactions (19 % between 1998 and 2006), where different bacterial species coexist and contribute to biofilm development [331]. The presence of multiple species can alter bacterial adhesion, biofilm architecture, and antimicrobial resistance, making it essential to study these interactions for a more clinically relevant assessment of bacterial colonisation on implant surfaces. Additionally, evaluating biofilm formation under physiological shear stress and nutrient conditions that resemble the *in vivo* environment will provide further insight into bacterial behaviour on the implant material [332]. Understanding how these treatments affect different bacterial populations will aid in the design of improved antimicrobial metal alloys with enhanced resistance to infection.

4) Contributions to Bacterial Resistance

Chapter 4 discussed the antimicrobial differences between additively manufactured Ti-3Cu and Ti-11.5Cu, potentially due to the ionic release mechanism of the Ti-11.5Cu alloy. However, it remains unclear whether bacterial resistance development differs between contact or non-contact mechanisms. Consequently, determining the mechanism for antimicrobial resistance to copper and how the mode of action of the alloys influences this process will be essential for future alloy design.

5) Optimisation of Mechanical Properties

Whilst Chapter 5 discusses the importance of the mechanical properties of metal alloys in reducing the negative effect of stress shielding, this research has not been able to investigate this fully within the given timeframe. Future work should focus on optimising the mechanical properties of these alloys and importantly ensure they align with their intended biomedical application. Further studies should explore methods to fine-tune mechanical properties such as fatigue resistance and hardness, whilst maintaining the promising biological functionalities presented in this thesis.

6) Further Investigation of Ti-Mo-Cu System

Several key challenges and properties remain to be assessed for future experimental work in the Ti-Mo-Cu systems. First, further analysis of the biological perspective is required, with both testing against bacterial species and native bone cells. In particular, analysis of the antimicrobial effects of the alloys is required for a gram negative bacteria, particularly since the cast samples showed no perceived efficacy towards *E. coli.* Additionally, the alloy mode of action should be interpreted, to determine if it is dictated by a contact mechanism or ion release.

7) Further Elemental Additions

In order to combine all the discussed target characteristics and functionalities, it may be beneficial to include further elemental additions. Through analysis of elemental effects on biological functionalities, further improved alloy properties could be achieved. For example, synergistic antimicrobial properties could be achieved through alloying with elements such as Ag and Sn, whereas improved mineralisation and osteogenesis could be enhanced by additions of Ga, Ca or Mg [134, 333, 334].

8) Microstructural and Compositional Fine Tuning

Only after fully understanding how elemental additions and the resulting microstructure influence an alloy's biological functionalities and mechanical properties can we begin fine-tuning its composition and microstructure to optimise the material. Once this has been achieved it may be possible to manufacture orthopaedic implants and devices out of the optimised alloy materials.

6.3. Final Remarks

This thesis represents an important fundamental endeavour to develop antimicrobial Ti-Cu alloys and understand their mode of action. The future work suggestions have highlighted the necessity for much further in-depth research before development into implants is viable. Taken together with the experimental contributions to knowledge in this thesis, this research highlights significant opportunities for a materials driven approach to tackle the growing demand and clinical threats to biomedical orthopaedic implants.

7. List of References

1. Raghavendra, G.M., K. Varaprasad, and T. Jayaramudu, *Biomaterials*, in *Nanotechnology Applications for Tissue Engineering*. 2015. p. 21-44.
2. Adhikari, J., P. Saha, and A. Sinha, *Surface modification of metallic bone implants—Polymer and polymer-assisted coating for bone in-growth*, in *Fundamental Biomaterials: Metals*. 2018. p. 299-321.
3. Goharian, A. and M.R. Abdullah, *Bioinert Metals (Stainless Steel, Titanium, Cobalt Chromium)*, in *Trauma Plating Systems*. 2017. p. 115-142.
4. Li, Y., C. Yang, H. Zhao, S. Qu, X. Li, and Y. Li, *New Developments of Ti-Based Alloys for Biomedical Applications.* Materials (Basel), 2014. **7**(3): p. 1709-1800.
5. Hallab, N.J. and J.J. Jacobs, *Chapter II.5.6 - Orthopedic Applications*, in *Biomaterials Science (Third Edition)*, B.D. Ratner, et al., Editors. 2013, Academic Press. p. 841-882.
6. Singh, J.A., S. Yu, L. Chen, and J.D. Cleveland, *Rates of Total Joint Replacement in the United States: Future Projections to 2020-2040 Using the National Inpatient Sample.* J Rheumatol, 2019. **46**(9): p. 1134-1140.
7. Lowther, M., S. Louth, A. Davey, A. Hussain, P. Ginestra, L. Carter, N. Eisenstein, L. Grover, and S. Cox, *Clinical, industrial, and research perspectives on powder bed fusion additively manufactured metal implants.* Additive Manufacturing, 2019. **28**: p. 565-584.
8. Mason, J.B., *The new demands by patients in the modern era of total joint arthroplasty : a point of view.* Clin Orthop Relat Res, 2008. **466**(1): p. 146-52.
9. Zimmerli, W. and P.E. Ochsner, *Management of infection associated with prosthetic joints.* Infection, 2003. **31**(2): p. 99-108.
10. Chikuda, H., H. Yasunaga, H. Horiguchi, K. Takeshita, S. Sugita, S. Taketomi, K. Fushimi, and S. Tanaka, *Impact of age and comorbidity burden on mortality and major complications in older adults undergoing orthopaedic surgery: an analysis using the Japanese diagnosis procedure combination database.* BMC Musculoskeletal Disorders, 2013. **14**(1): p. 173.

11. Curlewis, K., B. Leung, L. Sinclair, C. Thornhill, G. Chan, and D. Ricketts, *Systemic medical complications following joint replacement: a review of the evidence.* The Annals of The Royal College of Surgeons of England, 2023. **105**(3): p. 191-195.

12. Kenney, C., S. Dick, J. Lea, J. Liu, and N.A. Ebraheim, *A systematic review of the causes of failure of Revision Total Hip Arthroplasty.* Journal of Orthopaedics, 2019. **16**(5): p. 393-395.

13. Klouche, S., E. Sariali, and P. Mamoudy, *Total hip arthroplasty revision due to infection: A cost analysis approach.* Orthopaedics & Traumatology: Surgery & Research, 2010. **96**(2): p. 124-132.

14. Rack, H.J. and J.I. Qazi, *Titanium alloys for biomedical applications.* Materials Science and Engineering: C, 2006. **26**(8): p. 1269-1277.

15. Milošev, I., *The effect of biomolecules on the behaviour of CoCrMo alloy in various simulated physiological solutions.* Electrochimica Acta, 2012. **78**: p. 259-273.

16. Agarwal, R. and A.J. Garcia, *Biomaterial strategies for engineering implants for enhanced osseointegration and bone repair.* Adv Drug Deliv Rev, 2015. **94**: p. 53-62.

17. Bauer, T.W. and J. Schils, *The pathology of total joint arthroplasty.* Skeletal Radiology, 1999. **28**(9): p. 483-497.

18. van Lenthe, G.H., M.C. de Waal Malefijt, and R. Huiskes, *Stress shielding after total knee replacement may cause bone resorption in the distal femur.* The Journal of bone and joint surgery. British volume, 1997. **79**(1): p. 117-122.

19. Shayesteh Moghaddam, N., M. Taheri Andani, A. Amerinatanzi, C. Haberland, S. Huff, M. Miller, M. Elahinia, and D. Dean, *Metals for bone implants: safety, design, and efficacy.* Biomanufacturing Reviews, 2016. **1**(1).

20. Arciola, C.R., D. Campoccia, and L. Montanaro, *Implant infections: adhesion, biofilm formation and immune evasion.* Nature Reviews. Microbiology, 2018. **16**(7): p. 397-409.

21. Cerca, N., G.B. Pier, M. Vilanova, R. Oliveira, and J. Azeredo, *Quantitative analysis of adhesion and biofilm formation on hydrophilic and hydrophobic surfaces of clinical isolates of Staphylococcus epidermidis.* Res Microbiol, 2005. **156**(4): p. 506-14.

22. Stewart, P.S. and J.W. Costerton, *Antibiotic resistance of bacteria in biofilms.* Lancet, 2001. **358**(9276): p. 135-8.

23. Ahmed, S.S. and F.S. Haddad, *Prosthetic joint infection.* Bone & Joint Research, 2019. **8**(11): p. 570-572.

24. Banerjee, R., S. Nag, and H.L. Fraser, *A novel combinatorial approach to the development of beta titanium alloys for orthopaedic implants.* Materials Science and Engineering: C, 2005. **25**(3): p. 282-289.

25. Bai, Gong, Chen, Sun, Zhang, Cai, Zhu, and Xie, *Additive Manufacturing of Customized Metallic Orthopedic Implants: Materials, Structures, and Surface Modifications.* Metals, 2019. **9**(9).

26. Bocchetta, P., L.-Y. Chen, J.D.C. Tardelli, A.C.d. Reis, F. Almeraya-Calderón, and P. Leo, *Passive Layers and Corrosion Resistance of Biomedical Ti-6Al-4V and β-Ti Alloys.* Coatings, 2021. **11**(5): p. 487.

27. Grover, T., A. Pandey, S.T. Kumari, A. Awasthi, B. Singh, P. Dixit, P. Singhal, and K.K. Saxena, *Role of titanium in bio implants and additive manufacturing: An overview.* Materials Today: Proceedings, 2020. **26**: p. 3071-3080.

28. *Orthopedic Implants Market Size, Share & COVID-19 Impact Analysis, By Procedure (Joint Reconstruction Spinal Implants, Trauma Implants, Dental Implants, Ortholiologics, and Others) End-user (Hospitals, Orthopaedic Clinics, Ambulatory Surgical Centres and Others) ad Regional Forecast, 2021 - 2028*. 2022.

29. *Standard Specification for Wrought Titanium-15 Molybdenum Alloy for Surgical Implant Applications (UNS R58150)*. 2018, ASTM International.

30. *Standard Specification for Wrought Titanium-13Niobium-13Zirconium Alloy for Surgical Implant Applications (UNS R58130)*. 2021, ASTM International.

31. *Standard Specification for Wrought Titanium-12Molybdenum-6Zirconium-2Iron Alloy for Surgical Implant (UNS R58120)*. 2021, ASTM International.

32. *Standard Specification for Wrought Titanium-6Aluminum-7Niobium Alloy for Surgical Implant Applications (UNS R56700)*. 2016, ASTM International.

33. *Standard Specification for Wrought Titanium-6Aluminum-4Vanadium ELI (Extra Low Interstitial) Alloy for Surgical Implant Applications (UNS R56401)*. 2021, ASTM International.

34. *Standard Specification for Wrought Titanium-6Aluminum-4Vanadium Alloy for Surgical Implant Applications (UNS R56400)*. 2020, ASTM International.

35. *Standard Specification for Wrought Titanium-3Aluminum-2.5Vanadium Alloy for Surgical Implant Applications (UNS R56320)*. 2021, ASTM International.

36. Marin, E. and A. Lanzutti, *Biomedical Applications of Titanium Alloys: A Comprehensive Review.* Materials (Basel), 2023. **17**(1).

37. Jia, M., Y. Alshammari, F. Yang, and L. Bolzoni, *Yield of Annealing on the Properties of the Ti-5Al-2.5Fe Alloy Produced by Powder Forging.* Metals, 2023. **13**(2): p. 189.

38. van den Hout, J.A., K.L. Koenraadt, R. Wagenmakers, and S.B. Bolder, *The Accolade TMZF stem fulfils the demands of modern stem design: Minimum 5-year survival in a cohort of 937 patients.* J Orthop Surg (Hong Kong), 2018. **26**(3): p. 2309499018807747.

39. Sarraf, M., E. Rezvani Ghomi, S. Alipour, S. Ramakrishna, and N. Liana Sukiman, *A state-of-the-art review of the fabrication and characteristics of titanium and its alloys for biomedical applications.* Biodes Manuf, 2022. **5**(2): p. 371-395.

40. Yue, G.-L., T.-C. Chen, R.-K. Shiue, and L.-W. Tsay, *Phase Transformation of a Ti-15Mo-5Zr-3Al Brazed Joint Using Clad Ti-15Cu-15Ni Filler.* Metals, 2020. **10**(1): p. 83.

41. Shetty, A.A., A. Tindall, P. Ting, and F.W. Heatley, *The evolution of total knee arthroplasty. Part 1: introduction and first steps.* Current Orthopaedics, 2003. **17**(4): p. 322-325.

42. Wiles, P., *The surgery of the osteoarthritic hip.* Br J Surg, 1958. **45**(193): p. 488-97.

43. Semlitsch, M., *Titanium alloys for hip joint replacements.* Clinical Materials, 1987. **2**(1): p. 1-13.

44. Wang, K., *The use of titanium for medical applications in the USA.* Materials Science and Engineering: A, 1996. **213**(1): p. 134-137.

45. Maehara, K., K. Doi, T. Matsushita, and Y. Sasaki, *Application of Vanadium-Free Titanium Alloys to Artificial Hip Joints.* Materials Transactions - MATER TRANS, 2002. **43**: p. 2936-2942.

46. Davidson, J.A. and P. Kovacs, *Biocompatible low modulus titanium alloy for medical implants*. 1992, Google Patents.

47. Wang, K., *The characterization of Ti-12Mo-6Zr-2Fe a new biocompatible titanium alloy developed for surgical implant.* Beta Titanium Alloys in the 1990's, 1993: p. 49-60.

48. Wang, W. and C. Khoon, *Titanium Alloys in Orthopaedics*, in *Titanium Alloys - Advances in Properties Control*. 2013.

49. Aufa, A.N., M.Z. Hassan, and Z. Ismail, *Recent advances in Ti-6Al-4V additively manufactured by selective laser melting for biomedical implants: Prospect development.* Journal of Alloys and Compounds, 2022. **896**: p. 163072.

50. Shu, T., X. Wang, M. Li, S. Ma, J. Cao, G. Sun, T. Lai, S. Liu, A. Li, Z. Qu, and D. Pei, *Nanoscaled Titanium Oxide Layer Provokes Quick Osseointegration on 3D-Printed Dental Implants: A Domino Effect Induced by Hydrophilic Surface.* ACS Nano, 2024. **18**(1): p. 783-797.

51. Sidambe, A.T., *Biocompatibility of Advanced Manufactured Titanium Implants-A Review.* Materials (Basel), 2014. **7**(12): p. 8168-8188.

52. Mi, Z., S. Shuib, A. Hassan, A. Shorki, and M. Ibrahim, *Problem of stress shielding and improvement to the hip Implat designs: a review.* J. Med. Sci, 2007. **7**(3): p. 460-467.

53. Banerjee, D. and J.C. Williams, *Perspectives on Titanium Science and Technology.* Acta Materialia, 2013. **61**(3): p. 844-879.

54. Imam, M.A. and A.C. Fraker, *Titanium alloys as implant materials.* Medical applications of titanium and its alloys: The material and biological issues, 1996: p. 3-16.

55. Disegi, J.A., *Titanium alloys for fracture fixation implants.* Injury, 2000. **31**: p. D14-D17.

56. Geetha, M., A.K. Singh, R. Asokamani, and A.K. Gogia, *Ti based biomaterials, the ultimate choice for orthopaedic implants – A review.* Progress in Materials Science, 2009. **54**(3): p. 397-425.

57. Chen, L., Y.-W. Cui, and L. Zhang, *Recent Development in Beta Titanium Alloys for Biomedical Applications.* Metals, 2020. **10**: p. 1139.

58. Kolli, R.P. and A. Devaraj, *A Review of Metastable Beta Titanium Alloys.* Metals, 2018. **8**(7): p. 506.

59. Okulov, A., S. Berger, and I. Okulov, *Influence of β-Stabilizer Element on Microstructure and Mechanical Behavior of Porous Titanium Alloy Synthesized by Liquid Metal Dealloying.* Materials (Basel), 2023. **16**(16).

60. Ankem, S. and C.A. Greene, *Recent developments in microstructure/property relationships of beta titanium alloys.* Materials Science and Engineering: A, 1999. **263**(2): p. 127-131.

61. Catalani, S., S. Stea, A. Beraudi, M.E. Gilberti, B. Bordini, A. Toni, and P. Apostoli, *Vanadium release in whole blood, serum and urine of patients implanted with a titanium alloy hip prosthesis.* Clinical Toxicology, 2013. **51**(7): p. 550-556.

62. Costa, B.C., C.K. Tokuhara, L.A. Rocha, R.C. Oliveira, P.N. Lisboa-Filho, and J. Costa Pessoa, *Vanadium ionic species from degradation of Ti-6Al-4V metallic implants: In vitro cytotoxicity and speciation evaluation.* Materials Science and Engineering: C, 2019. **96**: p. 730-739.

63. Thompson, G.J. and D.A. Puleo, *Ti-6Al-4V ion solution inhibition of osteogenic cell phenotype as a function of differentiation timecourse in vitro.* Biomaterials, 1996. **17**(20): p. 1949-1954.

64. Ghosh, S.K., R. Saha, and B. Saha, *Toxicity of inorganic vanadium compounds.* Research on Chemical Intermediates, 2015. **41**(7): p. 4873-4897.

65. Goc, A., *Biological activity of vanadium compounds.* 2006. **1**(3): p. 314-332.

66. Hanawa, T., *Metal ion release from metal implants.* Materials Science and Engineering: C, 2004. **24**(6): p. 745-752.

67. Siemers, C., M. Bäker, F. Brunke, D. Wolter, and H. Sibum, *4.6 - Aluminum- and vanadium-free titanium alloys for application in medical engineering*, in *Titanium in Medical and Dental Applications*, F.H. Froes and M. Qian, Editors. 2018, Woodhead Publishing. p. 477-492.

68. Bistolfi, A., A. Cimino, G.-C. Lee, R. Ferracini, G. Maina, P. Berchialla, G. Massazza, and A. Massè, *Does metal porosity affect metal ion release in blood and urine following total hip arthroplasty? A short term study.* HIP International, 2018. **28**(5): p. 522-530.

69. Zaffe, D., C. Bertoldi, and U. Consolo, *Accumulation of aluminium in lamellar bone after implantation of titanium plates, Ti–6Al–4V screws, hydroxyapatite granules.* Biomaterials, 2004. **25**(17): p. 3837-3844.

70. Mizuno, K., F. Boschetto, K. Yamamoto, T. Honma, N. Miyamoto, T. Adachi, N. Kanamura, T. Yamamoto, Z. Wenliang, E. Marin, and G. Pezzotti, *Cytotoxicity and osteogenic effects of aluminum ions.* Journal of Inorganic Biochemistry, 2022. **234**: p. 111884.

71. Niinomi, M., *Recent research and development in titanium alloys for biomedical applications and healthcare goods.* Science and Technology of Advanced Materials, 2016. **4**(5): p. 445-454.

72. Davis, J.R., J.R. Davis, A.S.M. International, and M. American Society for, *Handbook of materials for medical devices / edited by J.R. Davis*. 2003, Materials Park, OH : ASM International: Materials Park, OH.

73. Eisenbarth, E., D. Velten, M. Müller, R. Thull, and J. Breme, *Biocompatibility of β-stabilizing elements of titanium alloys.* Biomaterials, 2004. **25**(26): p. 5705-5713.

74. Matsuno, H., A. Yokoyama, F. Watari, M. Uo, and T. Kawasaki, *Biocompatibility and osteogenesis of refractory metal implants, titanium, hafnium, niobium, tantalum and rhenium.* Biomaterials, 2001. **22**(11): p. 1253-1262.

75. Niinomi, M., *Mechanical properties of biomedical titanium alloys.* Materials Science and Engineering: A, 1998. **243**(1): p. 231-236.

76. Khan, M.A., R.L. Williams, and D.F. Williams, *The corrosion behaviour of Ti–6Al–4V, Ti–6Al–7Nb and Ti–13Nb–13Zr in protein solutions.* Biomaterials, 1999. **20**(7): p. 631-637.

77. Okazaki, Y. and E. Gotoh, *Comparison of metal release from various metallic biomaterials in vitro.* Biomaterials, 2005. **26**(1): p. 11-21.

78. Challa, V.S.A., S. Mali, and R.D.K. Misra, *Reduced toxicity and superior cellular response of preosteoblasts to Ti-6Al-7Nb alloy and comparison with Ti-6Al-4V.* Journal of Biomedical Materials Research Part A, 2013. **101A**(7): p. 2083-2089.

79. Okazaki, Y., *A New Ti–15Zr–4Nb–4Ta alloy for medical applications.* Current Opinion in Solid State and Materials Science, 2001. **5**(1): p. 45-53.

80. Hanssen, A.D. and J.A. Rand, *Evaluation and treatment of infection at the site of a total hip or knee arthroplasty.* Journal of Bone and Joint Surgery, 1998. **80**(6): p. 910.

81. Zimmerli, W., A. Trampuz, and P.E. Ochsner, *Prosthetic-Joint Infections.* New England Journal of Medicine, 2004. **351**(16): p. 1645-1654.

82. Ribeiro, M., F.J. Monteiro, and M.P. Ferraz, *Infection of orthopedic implants with emphasis on bacterial adhesion process and techniques used in studying bacterial-material interactions.* Biomatter, 2012. **2**(4): p. 176-94.

83. Schwartz, A.M., K.X. Farley, G.N. Guild, and T.L. Bradbury, Jr., *Projections and Epidemiology of Revision Hip and Knee Arthroplasty in the United States to 2030.* J Arthroplasty, 2020. **35**(6s): p. S79-s85.

84. Ferraris, S. and S. Spriano, *Antibacterial titanium surfaces for medical implants.* Mater Sci Eng C Mater Biol Appl, 2016. **61**: p. 965-78.

85. Matar, W.Y., S.M. Jafari, C. Restrepo, M. Austin, J.J. Purtill, and J. Parvizi, *Preventing infection in total joint arthroplasty.* JBJS, 2010. **92**(Supplement_2): p. 36-46.

86. Zimmerli, W., *Bone and Joint Infections: From Microbiology to Diagnostics and Treatment*. 2021: Wiley.

87. Harris, L.G. and R.G. Richards, *Staphylococci and implant surfaces: a review.* Injury, 2016. **37**(2): p. S3-S14.

88. Rochford, E.T.J., R.G. Richards, and T.F. Moriarty, *Influence of material on the development of device-associated infections.* Clinical Microbiology and Infection, 2012. **18**(12): p. 1162-1167.

89. Hall, T.J., V.M. Villapún, O. Addison, M.A. Webber, M. Lowther, S.E. Louth, S.E. Mountcastle, M.Y. Brunet, and S.C. Cox, *A call for action to the biomaterial community to tackle antimicrobial resistance.* Biomaterials Science, 2020. **8**(18): p. 4951-4974.

90. Vu, B., M. Chen, R.J. Crawford, and E.P. Ivanova, *Bacterial extracellular polysaccharides involved in biofilm formation.* Molecules, 2009. **14**(7): p. 2535–2554.

91. Cheng, G., Z. Zhang, S. Chen, J.D. Bryers, and S. Jiang, *Inhibition of bacterial adhesion and biofilm formation on zwitterionic surfaces.* Biomaterials, 2007. **28**(29): p. 4192–4199.

92. Pang, C.M., P. Hong, H. Guo, and W.T. Liu, *Biofilm formation characteristics of bacterial isolates retrieved from a reverse osmosis membrane.* Environmental science & technology, 2005. **39**(19): p. 7541-7550.

93. Vickery, K., H. Hu, A.S. Jacombs, D.A. Bradshaw, and A.K. Deva, *A review of bacterial biofilms and their role in device-associated infection.* Healthcare infection, 2013. **18**(2): p. 61-66.

94. Veerachamy, S., T. Yarlagadda, G. Manivasagam, and P.K. Yarlagadda, *Bacterial adherence and biofilm formation on medical implants: a review.* Proceedings of the Institution of Mechanical Engineers, Part H: Journal of Engineering in Medicine, 2014. **228**(10): p. 1083-1099.

95. Kreve, S. and A.C. Dos Reis, *Bacterial adhesion to biomaterials: What regulates this attachment? A review.* Japanese Dental Science Review, 2021. **57**: p. 85-96.

96. Stoica, P., M.C. Chifiriuc, M. Rapa, and V. Lazăr, *Overview of biofilm-related problems in medical devices*. Biofilms and implantable medical devices. 2017: Woodhead Publishing.

97. Khatoon, Z., C.D. McTiernan, E.J. Suuronen, T.F. Mah, and E.I. Alarcon, *Bacterial biofilm formation on implantable devices and approaches to its treatment and prevention.* Heliyon, 2018. **4**(12): p. e01067.

98. Bjarnsholt, T., *The role of bacterial biofilms in chronic infections.* Acta Pathologica, Microbiologica, et Immunologica Scandinavica, 2013. **121**: p. 1e58.

99. Gasik, M., L. Van Mellaert, D. Pierron, A. Braem, D. Hofmans, E. De Waelheyns, J. Anné, M.F. Harmand, and J. Vleugels, *Reduction of Biofilm Infection Risks and Promotion of Osteointegration for Optimized Surfaces of Titanium Implants.* Advanced Healthcare Materials, 2012. **1**(1): p. 117-127.

100. Thornley, P., N. Evaniew, M. Riediger, M. Winemaker, M. Bhandari, and M. Ghert, *Postoperative antibiotic prophylaxis in total hip and knee arthroplasty: a systematic review and meta-analysis of randomized controlled trials.* CMAJ Open, 2015. **3**(3): p. E338-43.

101. de Jonge, S.W., Q.J.J. Boldingh, J.S. Solomkin, E.P. Dellinger, M. Egger, G. Salanti, B. Allegranzi, and M.A. Boermeester, *Effect of postoperative continuation of antibiotic prophylaxis on the incidence of surgical site infection: a systematic review and meta-analysis.* The Lancet Infectious Diseases, 2020. **20**(10): p. 1182-1192.

102. Goodman, S.B. and D.J. Schurman, *Outcome of infected total hip arthroplasty. An inclusive, consecutive series.* J Arthroplasty, 1988. **3**(2): p. 97-102.

103. Sharma, H., J. De Leeuw, and D.I. Rowley, *Girdlestone resection arthroplasty following failed surgical procedures.* Int Orthop, 2005. **29**(2): p. 92-5.

104. Rahardja, R., M. Zhu, J.S. Davis, L. Manning, S. Metcalf, and S.W. Young, *Success of Debridement, Antibiotics, and Implant Retention in Prosthetic Joint Infection Following Primary Total Knee Arthroplasty: Results From a Prospective Multicenter Study of 189 Cases.* The Journal of Arthroplasty, 2023. **38**(7, Supplement 2): p. S399-S404.

105. Husted, H. and T. Toftgaard Jensen, *Clinical outcome after treatment of infected primary total knee arthroplasty.* Acta Orthop Belg, 2002. **68**(5): p. 500-7.

106. Hope, P.G., K.G. Kristinsson, P. Norman, and R.A. Elson, *Deep infection of cemented total hip arthroplasties caused by coagulase-negative staphylococci.* The Journal of Bone & Joint Surgery British Volume, 1989. **71-B**(5): p. 851-855.

107. van den Kieboom, J., V. Tirumala, H. Box, R. Oganesyan, C. Klemt, and Y.-M. Kwon, *One-stage revision is as effective as two-stage revision for chronic culture-negative periprosthetic joint infection after total hip and knee arthroplasty.* The Bone & Joint Journal, 2021. **103-B**(3): p. 515-521.

108. Peddada, K.V., B.M. Welcome, M.C. Parker, C.M. Delman, C.T. Holland, M. Giordani, J.P. Meehan, and Z.C. Lum, *Survivorship and Etiologies of Failure in Single-stage Revision Arthroplasty for Periprosthetic Joint Infection: A Meta-analysis.* JAAOS Global Research & Reviews, 2023. **7**(5): p. e22.00218.

109. Logroscino, G., V. Campana, S. Pagano, F. Taccari, M. Fantoni, and M. Saracco, *Risk factors for failure of two-stage revision arthroplasty for infected hip prosthesis: review of the literature and single centre cohort analysis.* European Review for Medical & Pharmacological Sciences, 2019. **23**.

110. Mortazavi, S.M.J., D. Vegari, A. Ho, B. Zmistowski, and J. Parvizi, *Two-stage Exchange Arthroplasty for Infected Total Knee Arthroplasty: Predictors of Failure.* Clinical Orthopaedics and Related Research®, 2011. **469**(11): p. 3049-3054.

111. Vincenten, C.M., T. Gosens, J.C. van Susante, and M.P. Somford, *The Girdlestone situation: a historical essay.* J Bone Jt Infect, 2019. **4**(5): p. 203-208.

112. Kallala, R.F., I.S. Vanhegan, M.S. Ibrahim, S. Sarmah, and F.S. Haddad, *Financial analysis of revision knee surgery based on NHS tariffs and hospital costs.* The Bone & Joint Journal, 2015. **97-B**(2): p. 197-201.

113. Turner, R.J., *Metal-based antimicrobial strategies.* Microb Biotechnol, 2017. **10**(5): p. 1062-1065.

114. Organization, W.H., *WHO global strategy for containment of antimicrobial resistance*. 2001, World Health Organization.

115. Silver, L.L., *Challenges of antibacterial discovery.* Clin Microbiol Rev, 2011. **24**(1): p. 71-109.

116. ReAct. *Few Antibiotics Under Development*. 18 April 2022]; Available from: https://www.reactgroup.org/toolbox/understand/how-did-we-end-up-here/few-antibiotics-under-development/#zp-ID-11316-280251-CEACG876.

117. Lemire, J.A., J.J. Harrison, and R.J. Turner, *Antimicrobial activity of metals: mechanisms, molecular targets and applications.* Nat Rev Microbiol, 2013. **11**(6): p. 371-84.

118. Yasuyuki, M., K. Kunihiro, S. Kurissery, N. Kanavillil, Y. Sato, and Y. Kikuchi, *Antibacterial properties of nine pure metals: a laboratory study using Staphylococcus aureus and Escherichia coli.* Biofouling, 2010. **26**(7): p. 851-8.

119. Valko, M., H. Morris, and M.T.D. Cronin, *Metals, toxicity and oxidative stress.* Current Medicinal Chemistry, 2005. **12**: p. 1161–1208.

120. Stohs, S.J. and D. Bagchi, *Oxidative mechanisms in the toxicity of metal ions.* Free Radical Biology and Medicine, 1995. **18**: p. 321–336.

121. Middaugh, J., R. Hamel, G. Jean-Baptiste, R. Beriault, D. Chenier, and V.D. Appanna, *Aluminum triggers decreased aconitase activity via Fe-S cluster disruption and the overexpression of isocitrate dehydrogenase and isocitrate lyase: a metabolic network mediating cellular survival.* Journal of Biological Chemistry. **280**(5): p. 3159-3165.

122. Macomber, L., S.P. Elsey, and R.P. Hausinger, *Fructose-1,6-bisphosphate aldolase (class II) is the primary site of nickel toxicity in Escherichia coli.* Molecular Microbiology, 2011. **82**: p. 1291–1300.

123. Harrison, J.J., V. Tremaroli, M.A. Stan, C.S. Chan, C. Vacchi-Suzzi, B.J. Heyne, M.R. Parsek, H. Ceri, and R.J. Turner, *Chromosomal antioxidant genes have metal ion-specifc roles as determinants of bacterial metal tolerance.* Environmental microbiology, 2009. **11**(9): p. 2491-2509.

124. Lemire, J.A., J.J. Harrison, and R.J. Turner, *Antimicrobial activity of metals: mechanisms, molecular targets and applications.* Nature Reviews Microbiology, 2013. **11**(6): p. 371-384.

125. Feng, Q.L., J. Wu, G.Q. Chen, F.Z. Cui, T.N. Kim, and J.O. Kim, *A mechanistic study of the antibacterial effect of silver ions on Escherichia coli and Staphylococcus aureus.* Journal of biomedical materials research, 2000. **54**(2): p. 662-668.

126. Gordon, O., T. Vig Slenters, P.S. Brunetto, A.E. Villaruz, D.E. Sturdevant, M. Otto, R. Landmann, and K.M. Fromm, *Silver coordination polymers for prevention of implant infection: thiol interaction, impact on respiratory chain enzymes, and hydroxyl radical induction.* Antimicrobial agents and chemotherapy, 2010. **54**(10): p. 4208-4218.

127. Hong, R., T.Y. Kang, C.A. Michels, and N. Gadura, *Membrane lipid peroxidation in copper alloy-mediated contact killing of Escherichia coli.* Applied and Environmental Microbiology, 2012. **78**: p. 1776–1784.

128. Li, X., T. Huang, D.E. Heath, N.M. O'Brien-Simpson, and A.J. O'Connor, *Antimicrobial nanoparticle coatings for medical implants: Design challenges and prospects.* Biointerphases, 2020. **15**(6): p. 060801.

129. Kumaravel, V., K.M. Nair, S. Mathew, J. Bartlett, J.E. Kennedy, H.G. Manning, B.J. Whelan, N.S. Leyland, and S.C. Pillai, *Antimicrobial TiO2 nanocomposite coatings for surfaces, dental and orthopaedic implants.* Chemical Engineering Journal, 2021. **416**: p. 129071.

130. Tripathi, S., A. Raheem, M. Dash, P. Kumar, A. Elsebahy, H. Singh, G. Manivasagam, and H.S. Nanda, *Surface engineering of orthopedic implants for better clinical adoption.* Journal of Materials Chemistry B, 2024.

131. Ferraris, S. and S. Spriano, *Antibacterial titanium surfaces for medical implants.* Materials Science and Engineering: C, 2016. **61**: p. 965-978.

132. Wang, M. and T. Tang, *Surface treatment strategies to combat implant-related infection from the beginning.* Journal of Orthopaedic Translation, 2019. **17**: p. 42-54.

133. Hobman, J.L. and L.C. Crossman, *Bacterial antimicrobial metal ion resistance.* Journal of medical microbiology, 2015. **64**(5): p. 471-497.

134. Zhang, E., X. Zhao, J. Hu, R. Wang, S. Fu, and G. Qin, *Antibacterial metals and alloys for potential biomedical implants.* Bioactive materials, 2021. **6**(8): p. 2569-2612.

135. Kawakami, H., K. Yoshida, Y. Nishida, Y. Kikuchi, and Y. Sato, *Antibacterial properties of metallic elements for alloying evaluated with application of JIS Z 2801:2000.* ISIJ international, 2008. **48**(9): p. 1299-1304.

136. Miyano, Y., K. Koyama, K.R. Sreekumari, Y. Sato, and Y. Kikuchi, *Evaluation of antibacterial ability of some pure metals.* Tetsu-To-Hagane/Journal of the Iron and Steel Institute of Japan, 2007. **93**: p. 57–65.

137. Waldron, K.J. and N.J. Robinson, *How do bacterial cells ensure that metalloproteins get the correct metal?* . Nature reviews Microbiology, 2009. **7**: p. 25–35.

138. Harrison, J.J., H. Ceri, C. Stremick, and R.J. Turner, *Biofilm susceptibility to metal toxicity.* Environmental Microbiology, 2004. **6**: p. 1220–1227.

139. Irving, H. and R.J.P. Williams, *The stability of transitionmetal complexes.* Journal of the Chemical Society, 1953: p. 3192–3210.

140. Workentine, M.L., J.J. Harrison, P.U. Stenroos, H. Ceri, and R.J. Turner, *Pseudomonas fluorescens' view of the periodic table. Environ.* Environmental microbiology, 2008. **10**(1): p. 238–250.

141. Nies, D.H., *Efflux-mediated heavy metal resistance in prokaryotes.* FEMS Microbiology Reviews, 2003. **27**: p. 313–339

142. Domb, A.J., K.R. Kunduru, and S. Farah, *Antimicrobial Materials for Biomedical Applications*. 2019: Royal Society of Chemistry.

143. Silver, S., *Bacterial resistances to toxic metal ions - a review.* Gene, 1996. **179**(1): p. 9-19.

144. Silver, S. and L.T. Phung, *Bacterial heavy metal resistance: new surprises.* Annual review of microbiology, 1996. **50**(1): p. 753-789.

145. Hosny, A.E.-D.M.S., S.A. Rasmy, D.S. Aboul-Magd, M.T. Kashef, and Z.E. El-Bazza, * The increasing threat of silver-resistance in clinical isolates from wounds and burns .* Infection and Drug Resistance, 2019. **Volume 12**: p. 1985-2001.

146. Turner, R., *Is Silver the Ultimate Antimicrobial Bullet?* Antibiotics, 2018. **7**(4).

147. Randall, C.P., A. Gupta, N. Jackson, D. Busse, and A.J. O'Neill, *Silver resistance in Gram-negative bacteria: a dissection of endogenous and exogenous mechanisms.* J Antimicrob Chemother, 2015. **70**(4): p. 1037-46.

148. Grass, G., C. Rensing, and M. Solioz, *Metallic copper as an antimicrobial surface.* Appl Environ Microbiol, 2011. **77**(5): p. 1541-7.

149. Bisht, N., N. Dwivedi, P. Kumar, M. Venkatesh, A.K. Yadav, D. Mishra, P. Solanki, N.K. Verma, R. Lakshminarayanan, S. Ramakrishna, D.P. Mondal, A.K. Srivastava, and C. Dhand, *Recent advances in copper and copper-derived materials for antimicrobial resistance and infection control.* Current Opinion in Biomedical Engineering, 2022. **24**: p. 100408.

150. Arendsen, L.P., R. Thakar, and A.H. Sultan, *The Use of Copper as an Antimicrobial Agent in Health Care, Including Obstetrics and Gynecology.* Clin Microbiol Rev, 2019. **32**(4).

151. Espírito Santo, C., V. Morais Paula, and G. Grass, *Isolation and Characterization of Bacteria Resistant to Metallic Copper Surfaces.* Applied and Environmental Microbiology, 2010. **76**(5): p. 1341-1348.

152. Mahmoudi, P., M.R. Akbarpour, H.B. Lakeh, F. Jing, M.R. Hadidi, and B. Akhavan, *Antibacterial Ti–Cu implants: A critical review on mechanisms of action.* Materials Today Bio, 2022. **17**: p. 100447.

153. Kawakami, H., K. Yoshida, Y. Nishida, Y. Kikuchi, and Y. Sato, *Antibacterial properties of metallic elements for alloying evaluated with application of JIS Z 2801: 2000.* ISIJ international, 2008. **48**(9): p. 1299-1304.

154. Gérard, C., L.-J. Bordeleau, J. Barralet, and C.J. Doillon, *The stimulation of angiogenesis and collagen deposition by copper.* Biomaterials, 2010. **31**(5): p. 824-831.

155. Burghardt, I., F. Lüthen, C. Prinz, B. Kreikemeyer, C. Zietz, H.-G. Neumann, and J. Rychly, *A dual function of copper in designing regenerative implants.* Biomaterials, 2015. **44**: p. 36-44.

156. Chinn, R.Y. and L. Sehulster, *Guidelines for environmental infection control in health-care facilities: recommendations of CDC and Healthcare Infection Control Practices Advisory Committee (HICPAC).* 2003.

157. Zhang, E.-L., S. Fu, R.-X. Wang, H.-X. Li, Y. Liu, Z.-Q. Ma, G.-K. Liu, C.-S. Zhu, G.-W. Qin, and D.-F. Chen, *Role of Cu element in biomedical metal alloy design.* Rare Metals, 2019. **38**: p. 476-494.

158. Akbarpour, M.R., H.M. Mirabad, A. Hemmati, and H.S. Kim, *Processing and microstructure of Ti-Cu binary alloys: A comprehensive review.* Progress in Materials Science, 2022. **127**: p. 100933.

159. Laves, F. and H. Wallbaum, *Crystal chemistry of Titanium alloys.* Naturwissenschaften, 1939. **27**(40): p. 674-675.

160. Grdina, Y.V., L.T. Gordeeva, L.G. Timonina, and N.R. Zifferman, *Metallic compounds in the Ti−Cu system.* Metal Science and Heat Treatment, 1967. **9**(2): p. 85-86.

161. Canale, P. and C. Servant, *Thermodynamic assessment of the Cu–Ti system taking into account the new stable phase CuTi3.* International Journal of Materials Research, 2022. **93**(4): p. 273-276.

162. Dyal Ukabhai, K., U.A. Curle, N.D.E. Masia, M. Smit, I.A. Mwamba, S. Norgren, C. Öhman-Mägi, N.G. Hashe, and L.A. Cornish, *Formation of Ti2Cu in Ti-Cu Alloys.* Journal of Phase Equilibria and Diffusion, 2022. **43**(3): p. 332-344.

163. Murray, J.L., *The Cu−Ti (Copper-Titanium) system.* Bulletin of Alloy Phase Diagrams, 1983. **4**(1): p. 81-95.

164. Canale, P. and C. Servant, *Thermodynamic assessment of the Cu–Ti system taking into account the new stable phase CuTi3.* International Journal of Materials Research, 2002. **93**(4): p. 273-276.

165. Zhu, Y.D., M.F. Yan, Y.X. Zhang, and C.S. Zhang, *First-principles investigation of structural, mechanical and electronic properties for Cu–Ti intermetallics.* Computational Materials Science, 2016. **123**: p. 70-78.

166. Ansara, I., V. Ivanchenko, L. Cornish, K.D. Ukabhai, and K. Nape, *Cu-Ti Binary Phase Diagram Evaluation*, in *Binary Evaluations*, A. Watson, Editor. 2021, MSI, Materials Science International Services GmbH: Stuttgart.

167. Wang, J., S. Zhang, Z. Sun, H. Wang, L. Ren, and K. Yang, *Optimization of mechanical property, antibacterial property and corrosion resistance of Ti-Cu alloy for dental implant.* Journal of materials science & technology, 2019. **35**(10): p. 2336-2344.

168. Shirai, T., H. Tsuchiya, T. Shimizu, K. Ohtani, Y. Zen, and K. Tomita, *Prevention of pin tract infection with titanium-copper alloys.* Journal of Biomedical Materials Research Part B: Applied Biomaterials, 2009. **91**(1): p. 373-380.

169. Alqattan, M., L. Peters, Y. Alshammari, F. Yang, and L. Bolzoni, *Antibacterial Ti-Mn-Cu alloys for biomedical applications.* Regenerative biomaterials, 2021. **8**(1): p. rbaa050.

170. Liu, J., F. Li, C. Liu, H. Wang, B. Ren, K. Yang, and E. Zhang, *Effect of Cu content on the antibacterial activity of titanium–copper sintered alloys.* Materials Science and Engineering: C, 2014. **35**: p. 392-400.

171. Zhang, E., X. Wang, M. Chen, and B. Hou, *Effect of the existing form of Cu element on the mechanical properties, bio-corrosion and antibacterial properties of Ti-Cu alloys for biomedical application.* Materials Science and Engineering: C, 2016. **69**: p. 1210-1221.

172. Yi, C., Z. Ke, L. Zhang, J. Tan, Y. Jiang, and Z. He, *Antibacterial Ti-Cu alloy with enhanced mechanical properties as implant applications.* Materials Research Express, 2020. **7**(10): p. 105404.

173. Liu, R., Y. Tang, L. Zeng, Y. Zhao, Z. Ma, Z. Sun, L. Xiang, L. Ren, and K. Yang, *In vitro and in vivo studies of anti-bacterial copper-bearing titanium alloy for dental application.* Dental Materials, 2018. **34**(8): p. 1112-1126.

174. Ma, Z., M. Li, R. Liu, L. Ren, Y. Zhang, H. Pan, Y. Zhao, and K. Yang, *In vitro study on an antibacterial Ti–5Cu alloy for medical application.* Journal of Materials Science: Materials in Medicine, 2016. **27**: p. 1-12.

175. Liu, R., K. Memarzadeh, B. Chang, Y. Zhang, Z. Ma, R.P. Allaker, L. Ren, and K. Yang, *Antibacterial effect of copper-bearing titanium alloy (Ti-Cu) against Streptococcus mutans and Porphyromonas gingivalis.* Scientific reports, 2016. **6**(1): p. 29985.

176. Zhang, E., F. Li, H. Wang, J. Liu, C. Wang, M. Li, and K. Yang, *A new antibacterial titanium–copper sintered alloy: preparation and antibacterial property.* Materials Science and Engineering: C, 2013. **33**(7): p. 4280-4287.

177. Korda, A.A., S. Munawaroh, and E.A. Basuki. *The antimicrobial activity and characterization of the cast titanium copper alloys with variations of copper content*. in *IOP Conference Series: Materials Science and Engineering*. 2019. IOP Publishing.

178. Bai, B., E. Zhang, J. Liu, and J. Zhu, *The anti-bacterial activity of titanium-copper sintered alloy against Porphyromonas gingivalis in vitro.* Dental materials journal, 2016. **35**(4): p. 659-667.

179. Fowler, L., O. Janson, H. Engqvist, S. Norgren, and C. Öhman-Mägi, *Antibacterial investigation of titanium-copper alloys using luminescent Staphylococcus epidermidis in a direct contact test.* Materials Science and Engineering: C, 2019. **97**: p. 707-714.

180. Akbarpour, M. and S. Moniri Javadhesari, *Densification and mechanical and antibacterial properties of low-cost powder metallurgy TiCu intermetallic alloy as a potential biomedical material.* Jom, 2020. **72**(9): p. 3262-3268.

181. Li, Y.-H., N. Chen, H.-T. Cui, and F. Wang, *Fabrication and characterization of porous Ti–10Cu alloy for biomedical application.* Journal of Alloys and Compounds, 2017. **723**: p. 967-973.

182. Nan, L., Y. Liu, M. Lü, and K. Yang, *Study on antibacterial mechanism of copper-bearing austenitic antibacterial stainless steel by atomic force microscopy.* Journal of Materials Science: Materials in Medicine, 2008. **19**: p. 3057-3062.

183. Shi, A., C. Zhu, S. Fu, R. Wang, G. Qin, D. Chen, and E. Zhang, *What controls the antibacterial activity of Ti-Ag alloy, Ag ion or Ti2Ag particles?* Materials Science and Engineering: C, 2020. **109**: p. 110548.

184. Liu, R., Z. Ma, S. Kunle Kolawole, L. Zeng, Y. Zhao, L. Ren, and K. Yang, *In vitro study on cytocompatibility and osteogenesis ability of Ti–Cu alloy.* Journal of Materials Science: Materials in Medicine, 2019. **30**: p. 1-10.

185. Li, Y., Y. Lu, B. Qiu, Y. Ze, P. Li, Y. Du, P. Gong, J. Lin, and Y. Yao, *Copper-containing titanium alloys promote angiogenesis in irradiated bone through releasing copper ions and regulating immune microenvironment.* Biomaterials Advances, 2022. **139**: p. 213010.

186. Liu, J., X. Zhang, H. Wang, F. Li, M. Li, K. Yang, and E. Zhang, *The antibacterial properties and biocompatibility of a Ti–Cu sintered alloy for biomedical application.* Biomedical Materials, 2014. **9**(2): p. 025013.

187. Zhang, E., L. Zheng, J. Liu, B. Bai, and C. Liu, *Influence of Cu content on the cell biocompatibility of Ti-Cu sintered alloys.* Mater Sci Eng C Mater Biol Appl, 2015. **46**: p. 148-57.

188. Hu, J., H. Li, X. Wang, L. Yang, M. Chen, R. Wang, G. Qin, D.F. Chen, and E. Zhang, *Effect of ultrasonic micro-arc oxidation on the antibacterial properties and cell*

biocompatibility of Ti-Cu alloy for biomedical application. Mater Sci Eng C Mater Biol Appl, 2020. **115**: p. 110921.

189. Zhang, W., S. Zhang, H. Liu, L. Ren, Q. Wang, and Y. Zhang, *Effects of surface roughening on antibacterial and osteogenic properties of Ti-Cu alloys with different Cu contents.* Journal of Materials Science & Technology, 2021. **88**: p. 158-167.

190. Xin, C., N. Wang, Y. Chen, B. He, Q. Zhao, L. Chen, Y. Tang, B. Luo, Y. Zhao, and X. Yang, *Biological corrosion behaviour and antibacterial properties of Ti-Cu alloy with different Ti2Cu morphologies for dental applications.* Materials & Design, 2022. **215**: p. 110540.

191. Liu, R., Y. Tang, H. Liu, L. Zeng, Z. Ma, J. Li, Y. Zhao, L. Ren, and K. Yang, *Effects of combined chemical design (Cu addition) and topographical modification (SLA) of Ti-Cu/SLA for promoting osteogenic, angiogenic and antibacterial activities.* Journal of Materials Science & Technology, 2020. **47**: p. 202-215.

192. Ren, L., Z. Ma, M. Li, Y. Zhang, W. Liu, Z. Liao, and K. Yang, *Antibacterial Properties of Ti–6Al–4V–xCu Alloys.* Journal of Materials Science & Technology, 2014. **30**(7): p. 699-705.

193. Aoki, T., I.C.I. Okafor, I. Watanabe, M. Hattori, Y. Oda, and T. Okabe, *Mechanical properties of cast Ti-6Al-4V-XCu alloys.* Journal of Oral Rehabilitation, 2004. **31**(11): p. 1109-1114.

194. Guo, S., Y. Lu, S. Wu, L. Liu, M. He, C. Zhao, Y. Gan, J. Lin, J. Luo, X. Xu, and J. Lin, *Preliminary study on the corrosion resistance, antibacterial activity and cytotoxicity of selective-laser-melted Ti6Al4V-xCu alloys.* Materials Science and Engineering: C, 2017. **72**: p. 631-640.

195. Ma, Z., L. Ren, R. Liu, K. Yang, Y. Zhang, Z. Liao, W. Liu, M. Qi, and R. Misra, *Effect of heat treatment on Cu distribution, antibacterial performance and cytotoxicity of Ti–6Al–4V–5Cu alloy.* Journal of Materials Science & Technology, 2015. **31**(7): p. 723-732.

196. Gomes, C.C., L.M. Moreira, V.J. Santos, A.S. Ramos, J.P. Lyon, C.P. Soares, and F.V. Santos, *Assessment of the genetic risks of a metallic alloy used in medical implants.* Genet Mol Biol, 2011. **34**(1): p. 116-21.

197. Yamanoglu, R., E. Efendi, F. Kolayli, H. Uzuner, and I. Daoud, *Production and mechanical properties of Ti–5Al–2.5 Fe–xCu alloys for biomedical applications.* Biomedical Materials, 2018. **13**(2): p. 025013.

198. Hayama, A.O.F., P.N. Andrade, A. Cremasco, R.J. Contieri, C.R.M. Afonso, and R. Caram, *Effects of composition and heat treatment on the mechanical behavior of Ti–Cu alloys.* Materials & Design, 2014. **55**: p. 1006-1013.

199. Cardoso, F.F., A. Cremasco, R.J. Contieri, E.S.N. Lopes, C.R.M. Afonso, and R. Caram, *Hexagonal martensite decomposition and phase precipitation in Ti–Cu alloys.* Materials & Design, 2011. **32**(8): p. 4608-4613.

200. Pesode, P. and S. Barve, *A review—metastable β titanium alloy for biomedical applications.* Journal of Engineering and Applied Science, 2023. **70**(1): p. 25.

201. Rajadurai, M., A. Muthuchamy, A.R. Annamalai, D.K. Agrawal, and C.-P. Jen, *Effect of Molybdenum (Mo) Addition on Phase Composition, Microstructure, and Mechanical Properties of Pre-Alloyed Ti6Al4V Using Spark Plasma Sintering Technique.* Molecules, 2021. **26**(10): p. 2894.

202. Ballor, J., T. Li, F. Prima, C.J. Boehlert, and A. Devaraj, *A review of the metastable omega phase in beta titanium alloys: the phase transformation mechanisms and its effect on mechanical properties.* International Materials Reviews, 2023. **68**(1): p. 26-45.

203. Lourenço, M.L., G.C. Cardoso, K. Sousa, T.A.G. Donato, F.M.L. Pontes, and C.R. Grandini, *Development of novel Ti-Mo-Mn alloys for biomedical applications.* Sci Rep, 2020. **10**(1): p. 6298.

204. Ribeiro, A.M., T.H.S. Flores-Sahagun, and R.C. Paredes, *A perspective on molybdenum biocompatibility and antimicrobial activity for applications in implants.* Journal of Materials Science, 2016. **51**(6): p. 2806-2816.

205. Vrancken, B., L. Thijs, J.P. Kruth, and J. Van Humbeeck, *Microstructure and mechanical properties of a novel β titanium metallic composite by selective laser melting.* Acta Materialia, 2014. **68**: p. 150-158.

206. Zhang, L.-L., L.-J. Zhang, J. Long, J. Ning, J.-X. Zhang, and S.-J. Na, *Effects of titanium on grain boundary strength in molybdenum laser weld bead and formation and strengthening mechanisms of brazing layer.* Materials & Design, 2019. **169**: p. 107681.

207. Luo, R.D., Y.X. Yuan, J.K. Ren, F. Li, Y.J. Yang, Z.Y. He, and Y.H. Jiang, *Novel function-structure-integrated Ti-Mo-Cu alloy combined with excellent antibacterial properties and mechanical compatibility as implant application.* Journal of Alloys and Compounds, 2023. **945**: p. 169323.

208. Yuan, Y., R. Luo, J. Ren, L. Zhang, Y. Jiang, and Z. He, *Design of a new Ti-Mo-Cu alloy with excellent mechanical and antibacterial properties as implant materials.* Materials Letters, 2022. **306**: p. 130875.

209. Zhang, L.-C. and L.-Y. Chen, *A Review on Biomedical Titanium Alloys: Recent Progress and Prospect.* Advanced Engineering Materials, 2019. **21**(4): p. 1801215.

210. Wu, C.-T., P.-H. Lin, S.-Y. Huang, Y.-J. Tseng, H.-T. Chang, S.-Y. Li, and H.-W. Yen, *Revisiting alloy design of low-modulus biomedical β-Ti alloys using an artificial neural network.* Materialia, 2022. **21**: p. 101313.

211. Stráský, J., P. Harcuba, K. Václavová, K. Horváth, M. Landa, O. Srba, and M. Janeček, *Increasing strength of a biomedical Ti-Nb-Ta-Zr alloy by alloying with Fe, Si and O.* Journal of the mechanical behavior of biomedical materials, 2017. **71**: p. 329-336.

212. Barber, Z.H. and M.G. Blamire, *High throughput thin film materials science.* Materials Science and Technology, 2013. **24**(7): p. 757-770.

213. Qiao, L., L. Y., and J. Zhu, *A focused review on machine learning aided high-throughput methods in high entropy alloy.* Journal of Alloys and Compounds, 2021. **877**: p. 160295.

214. Zhao, J.-C., *The diffusion-multiple approach to designing alloys.* Annual Review of Materials Research, 2005. **35**: p. 51-73.

215. Reed, R.C., *The superalloys : fundamentals and applications / Roger C. Reed*. 2006: Cambridge, UK

New York : Cambridge University Press, 2006.

216. Borkar, T., B. Gwalani, D. Choudhuri, C.V. Mikler, C.J. Yannetta, X. Chen, R.V. Ramanujan, M.J. Styles, M.A. Gibson, and R. Banerjee, *A combinatorial assessment of AlxCrCuFeNi2 (0 < x < 1.5) complex concentrated alloys: Microstructure, microhardness, and magnetic properties.* Acta Materialia, 2016. **116**: p. 63-76.

217. Oliveira, N.T.C., G. Aleixo, R. Caram, and A.C. Guastaldi, *Development of Ti–Mo alloys for biomedical applications: Microstructure and electrochemical characterization.* Materials Science and Engineering: A, 2007. **452-453**: p. 727-731.

218. Kuroda, P.A.B., M.A.R. Buzalaf, and C.R. Grandini, *Effect of molybdenum on structure, microstructure and mechanical properties of biomedical Ti-20Zr-Mo alloys.* Materials Science and Engineering: C, 2016. **67**: p. 511-515.

219. Froes, F., *Titanium: physical metallurgy, processing, and applications*. 2015: ASM international.

220. Frazier, W.E., *Metal Additive Manufacturing: A Review.* Journal of Materials Engineering and Performance, 2014. **23**(6): p. 1917-1928.

221. Jamshidi, P., M. Aristizabal, W. Kong, V. Villapun, S.C. Cox, L.M. Grover, and M.M. Attallah, *Selective Laser Melting of Ti-6Al-4V: The Impact of Post-processing on the Tensile, Fatigue and Biological Properties for Medical Implant Applications.* Materials, 2020. **13**(12): p. 2813.

222. Körner, C., *Additive manufacturing of metallic components by selective electron beam melting — a review.* International Materials Reviews, 2016. **61**(5): p. 361-377.

223. Simonelli, M., N.T. Aboulkhair, P. Cohen, J.W. Murray, A.T. Clare, C. Tuck, and R.J. Hague, *A comparison of Ti-6Al-4V in-situ alloying in Selective Laser Melting using simply-mixed and satellited powder blend feedstocks.* Materials Characterization, 2018. **143**: p. 118-126.

224. Mosallanejad, M.H., B. Niroumand, A. Aversa, and A. Saboori, *In-situ alloying in laser-based additive manufacturing processes: A critical review.* Journal of Alloys and Compounds, 2021. **872**: p. 159567.

225. Huang, K., C. Kain, N. Diaz-Vallejo, V. Sohn, and L. Zhou, *High throughput mechanical testing platform and application in metal additive manufacturing and process optimization.* Journal of Manufacturing Processes, 2021. **66**: p. 494-505.

226. Zhang, B., N.-E. Feninechе, L. Zhu, H. Liao, and C. Coddet, *Studies of magnetic properties of permalloy (Fe–30% Ni) prepared by SLM technology.* Journal of Magnetism and Magnetic Materials, 2012. **324**(4): p. 495-500.

227. Wang, C., X. Tan, Z. Du, S. Chandra, Z. Sun, C. Lim, S. Tor, C. Lim, and C. Wong, *Additive manufacturing of NiTi shape memory alloys using pre-mixed powders.* Journal of Materials Processing Technology, 2019. **271**: p. 152-161.

228. Huang, S., R.L. Narayan, J.H.K. Tan, S.L. Sing, and W.Y. Yeong, *Resolving the porosity-unmelted inclusion dilemma during in-situ alloying of Ti34Nb via laser powder bed fusion.* Acta Materialia, 2021. **204**: p. 116522.

229. Brodie, E., A. Medvedev, J. Frith, M. Dargusch, H. Fraser, and A. Molotnikov, *Remelt processing and microstructure of selective laser melted Ti25Ta.* Journal of Alloys and Compounds, 2020. **820**: p. 153082.

230. Wang, J., Y. Liu, P. Qin, S. Liang, T. Sercombe, and L. Zhang, *Selective laser melting of Ti–35Nb composite from elemental powder mixture: Microstructure, mechanical behavior and corrosion behavior.* Materials Science and Engineering: A, 2019. **760**: p. 214-224.

231. Grigoriev, A., I. Polozov, V. Sufiiarov, and A. Popovich, *In-situ synthesis of Ti2AlNb-based intermetallic alloy by selective laser melting.* Journal of Alloys and Compounds, 2017. **704**: p. 434-442.

232. Mosallanejad, M., B. Niroumand, A. Aversa, D. Manfredi, and A. Saboori, *Laser Powder Bed Fusion in-situ alloying of Ti-5% Cu alloy: Process-structure relationships.* Journal of Alloys and Compounds, 2021. **857**: p. 157558.

233. Soro, N., H. Attar, E. Brodie, M. Veidt, A. Molotnikov, and M.S. Dargusch, *Evaluation of the mechanical compatibility of additively manufactured porous Ti–25Ta alloy for load-bearing implant applications.* Journal of the mechanical behavior of biomedical materials, 2019. **97**: p. 149-158.

234. Fischer, M., D. Joguet, G. Robin, L. Peltier, and P. Laheurte, *In situ elaboration of a binary Ti–26Nb alloy by selective laser melting of elemental titanium and niobium mixed powders.* Materials Science and Engineering: C, 2016. **62**: p. 852-859.

235. Polozov, I., V. Sufiiarov, A. Popovich, D. Masaylo, and A. Grigoriev, *Synthesis of Ti-5Al, Ti-6Al-7Nb, and Ti-22Al-25Nb alloys from elemental powders using powder-bed fusion additive manufacturing.* Journal of Alloys and Compounds, 2018. **763**: p. 436-445.

236. Kang, N., Y. Li, X. Lin, E. Feng, and W. Huang, *Microstructure and tensile properties of Ti-Mo alloys manufactured via using laser powder bed fusion.* Journal of Alloys and Compounds, 2019. **771**: p. 877-884.

237. Mohammed, M., V.G. Smelov, and A. Sotov, *SLM-built titanium materials: great potential of developing microstructure and properties for biomedical applications: A Review.* Materials Research Express, 2019. **6**.

238. Thampy, V., A.Y. Fong, N.P. Calta, J. Wang, A.A. Martin, P.J. Depond, A.M. Kiss, G. Guss, Q. Xing, R.T. Ott, A. van Buuren, M.F. Toney, J.N. Weker, M.J. Kramer, M.J. Matthews, C.J. Tassone, and K.H. Stone, *Subsurface Cooling Rates and Microstructural Response during Laser Based Metal Additive Manufacturing.* Scientific Reports, 2020. **10**(1): p. 1981.

239. Kosiba, K., T. Gustmann, J.T. Kim, J. Seok, J. Jung, L. Beyer, S. Scudino, L. Giebeler, J. Han, and J.K. Hufenbach, *Experimental cooling rates during high-power laser powder bed fusion at varying processing conditions.* Journal of Alloys and Compounds, 2023. **967**: p. 171773.

240. Hooper, P.A., *Melt pool temperature and cooling rates in laser powder bed fusion.* Additive Manufacturing, 2018. **22**: p. 548-559.

241. Croft, D.N., *Chapter 3 - Effects of heat treatment*, in *Heat Treatment of Welded Steel Structures*, D.N. Croft, Editor. 1996, Woodhead Publishing. p. 21-47.

242. Doğu, M.N., S. Ozer, M.A. Yalçın, K. Davut, M.A. Obeidi, C. Simsir, H. Gu, C. Teng, and D. Brabazon, *A comprehensive study of the effect of scanning strategy on IN939 fabricated by powder bed fusion-laser beam.* Journal of Materials Research and Technology, 2024. **33**: p. 5457-5481.

243. Bai, B., E. Zhang, J. Liu, and J. Zhu, *The anti-bacterial activity of titanium-copper sintered alloy against Porphyromonas gingivalis in vitro.* Dent Mater J, 2016. **35**(4): p. 659-67.

244. Yang, H.-L., L. Zou, A.N. Juaim, C.-X. Ma, M.-Z. Zhu, F. Xu, X.-N. Chen, Y.-Z. Wang, and X.-W. Zhou, *Copper release and ROS in antibacterial activity of Ti-Cu alloys against implant-associated infection.* Rare Metals, 2023. **42**(6): p. 2007-2019.

245. Li, J., D. Zhang, X. Chen, D. Xu, D. Qiu, F. Wang, and M. Easton, *Laser directed energy deposited, ultrafine-grained functional titanium-copper alloys tailored for marine environments: Antibacterial and anti-microbial corrosion studies.* Journal of Materials Science & Technology, 2023. **166**: p. 21-33.

246. Liu, H., X. Zhang, L. Shi, Y. Hong, H. Yao, L. Ren, and K. Yang, *Effect of Cu content on the properties of laser powder bed fused biomedical titanium alloys.* Journal of Materials Research and Technology, 2024. **30**: p. 8992-8998.

247. Yu, T., F. Zhong, F. Zhang, C. Ying, and G. Geng. *Application of scanning electron microscopy in metal material detection*. in *Journal of Physics: Conference Series*. 2021. IOP Publishing.

248. Winey, M., J.B. Meehl, E.T. O'Toole, and T.H. Giddings, *Conventional transmission electron microscopy.* Molecular Biology of the Cell, 2014. **25**(3): p. 319-323.

249. Inkson, B.J., *2 - Scanning electron microscopy (SEM) and transmission electron microscopy (TEM) for materials characterization*, in *Materials Characterization Using Nondestructive Evaluation (NDE) Methods*, G. Hübschen, et al., Editors. 2016, Woodhead Publishing. p. 17-43.

250. Abd Mutalib, M., M.A. Rahman, M.H.D. Othman, A.F. Ismail, and J. Jaafar, *Chapter 9 - Scanning Electron Microscopy (SEM) and Energy-Dispersive X-Ray (EDX) Spectroscopy*, in *Membrane Characterization*, N. Hilal, et al., Editors. 2017, Elsevier. p. 161-179.

251. Epp, J., *4 - X-ray diffraction (XRD) techniques for materials characterization*, in *Materials Characterization Using Nondestructive Evaluation (NDE) Methods*, G. Hübschen, et al., Editors. 2016, Woodhead Publishing. p. 81-124.

252. Mueller, M.H. and H.W. Knott, *The Crystal Structures of Ti₂Cu, Ti₂Ni, Ti₄Ni₂O, and Ti₄Cu₂O.* Transactions of American Institute of Metallurgical Engineers, 1963. **Vol: 227**(ANL-FGF-396): p. Medium: ED; Size: Pages: 674-8.

253. Donthula, H., B. Vishwanadh, T. Alam, T. Borkar, R.J. Contieri, R. Caram, R. Banerjee, R. Tewari, G.K. Dey, and S. Banerjee, *Morphological evolution of transformation*

products and eutectoid transformation(s) in a hyper-eutectoid Ti-12 at% Cu alloy. Acta Materialia, 2019. **168**: p. 63-75.

254. Žunić, J., K. Hirota, and P.L. Rosin, *A Hu moment invariant as a shape circularity measure.* Pattern Recognition, 2010. **43**(1): p. 47-57.

255. Žunić, D. and J. Žunić, *Shape ellipticity based on the first Hu moment invariant.* Information Processing Letters, 2013. **113**(19): p. 807-810.

256. Hu, M.-K., *Visual pattern recognition by moment invariants.* IRE transactions on information theory, 1962. **8**(2): p. 179-187.

257. Wenwen, M., H. Zixin, L. Zha, S. Dongfeng, G. Zijun, H. Jian, B. Park, and W. Yingjian, *Image-free Hu invariant moment measurement by single-pixel detection.* Optics & Laser Technology, 2025. **181**: p. 111581.

258. Senthilnathan, A., P. Acar, and M. De Graef, *Markov Random Field based microstructure reconstruction using the principal image moments.* Materials Characterization, 2021. **178**: p. 111281.

259. Senthilnathan, A., I. Javaheri, H. Zhao, V. Sundararaghavan, M. DeGraef, and P. Acar, *Uncertainty quantification of metallic microstructures using principal image moments.* Computational Materials Science, 2022. **215**: p. 111775.

260. Kaul, L., A.I. Abdo, T. Coenye, B.P. Krom, M.A. Hoogenkamp, A.C.W. Zannettino, R. Süss, and K. Richter, *The combination of diethyldithiocarbamate and copper ions is active against Staphylococcus aureus and Staphylococcus epidermidis biofilms in vitro and in vivo.* Frontiers in Microbiology, 2022. **13**.

261. Baker, J., S. Sitthisak, M. Sengupta, M. Johnson, R.K. Jayaswal, and A. Morrissey Julie, *Copper Stress Induces a Global Stress Response in Staphylococcus aureus and Represses sae and agr Expression and Biofilm Formation.* Applied and Environmental Microbiology, 2010. **76**(1): p. 150-160.

262. Razatos, A., Y.-L. Ong, M.M. Sharma, and G. Georgiou, *Molecular determinants of bacterial adhesion monitored by atomic force microscopy.* Proceedings of the National Academy of Sciences, 1998. **95**(19): p. 11059-11064.

263. Gannon, J.T., V.B. Manilal, and M. Alexander, *Relationship between Cell Surface Properties and Transport of Bacteria through Soil.* Applied and Environmental Microbiology, 1991. **57**(1): p. 190-193.

264. Busscher, H.J., A.H. Weerkamp, H.C. van der Mei, A.W. van Pelt, H.P. de Jong, and J. Arends, *Measurement of the surface free energy of bacterial cell surfaces and its relevance for adhesion.* Applied and Environmental Microbiology, 1984. **48**(5): p. 980-983.

265. Rosenberg, M., H. Judes, and E. Weiss, *Cell surface hydrophobicity of dental plaque microorganisms in situ.* Infection and Immunity, 1983. **42**(2): p. 831-834.

266. Briandet, R., J.M. Herry, and M.N. Bellon-Fontaine, *Determination of the van der Waals, electron donor and electron acceptor surface tension components of static Gram-positive microbial biofilms.* Colloids and Surfaces B: Biointerfaces, 2001. **21**(4): p. 299-310.

267. Xu, D., T. Wang, Z. Lu, Y. Wang, B. Sun, S. Wang, Q. Fu, Z. Bi, and S. Geng, *Ti-6Al-4V-5Cu synthesized for antibacterial effect in vitro and in vivo via contact sterilization.* Journal of Materials Science & Technology, 2021. **90**: p. 133-142.

268. Ma, C., M. Zhu, J. Wang, X. Zhou, H. Xing, S. Ji, and H. Yang, *Mechanisms of improving the mechanical and antibacterial properties of Ti-3wt.% Cu alloys.* Materials Letters, 2022. **319**: p. 132263.

269. Yang, H.-L., M.-Z. Zhu, J.-Y. Wang, C.-X. Ma, X.-W. Zhou, H.-X. Xing, E.-L. Zhang, and S.-X. Ji, *Optimization of mechanical and antibacterial properties of Ti-3wt% Cu alloy through cold rolling and annealing.* Rare Metals, 2022: p. 1-11.

270. Ming-Kuei, H., *Visual pattern recognition by moment invariants.* IRE Transactions on Information Theory, 1962. **8**(2): p. 179-187.

271. Huang, Z. and J. Leng. *Analysis of Hu's moment invariants on image scaling and rotation*. in *2010 2nd international conference on computer engineering and technology*. 2010. IEEE.

272. Viroxy. *ISO 22196:2011*. 27 April 2022]; Available from: https://www.viroxylabs.com/microbiological-testing-services/disinfectant-efficacy-testing/iso-221962011/.

273. Li, S., J.Z. Wang, B. Yin, Z.S. Hu, X.J. Zhang, W. Wu, G.B. Liu, Y.K. Liu, L. Fu, and Y.Z. Zhang, *Atlas of Human Skeleton Hardness Obtained Using the Micro-indentation Technique.* Orthop Surg, 2021. **13**(4): p. 1417-1422.

274. Yin, H., Y. Wu, X. Li, G. Zhang, P. Zhang, W. Li, and A. Zhao, *Morphology and Antibacterial Properties of Copper Precipitates in Ferrite Stainless Steel.* Journal of Materials Engineering and Performance, 2021. **30**(1): p. 711-719.

275. Peng, C., S. Zhang, Z. Sun, L. Ren, and K. Yang, *Effect of annealing temperature on mechanical and antibacterial properties of Cu-bearing titanium alloy and its preliminary study of antibacterial mechanism.* Materials Science and Engineering: C, 2018. **93**: p. 495-504.

276. Wu, J.-H., K.-K. Chen, C.-Y. Chao, Y.-H. Chang, and J.-K. Du, *Effect of Ti2Cu precipitation on antibacterial property of Ti-5Cu alloy.* Materials Science and Engineering: C, 2020. **108**: p. 110433.

277. Zhao, D., Y. Chen, C. Jiang, Y. Li, Q. Zhao, Y. Xu, H. Zhan, M. Wan, and Y. Zhao, *Morphological evolution of Ti2Cu in Ti-13Cu-Al alloy after cooling from semi-solid state.* Journal of Alloys and Compounds, 2020. **848**: p. 156639.

278. Kallas, P., H. Valen, M. Hulander, N. Gadegaard, J. Stormonth-Darling, P. O'Reilly, B. Thiede, M. Andersson, and H.J. Haugen, *Protein-coated nanostructured surfaces affect the adhesion of Escherichia coli.* Nanoscale, 2022. **14**(20): p. 7736-7746.

279. Allen, L.T., M. Tosetto, I.S. Miller, D.P. O'Connor, S.C. Penney, I. Lynch, A.K. Keenan, S.R. Pennington, K.A. Dawson, and W.M. Gallagher, *Surface-induced changes in protein adsorption and implications for cellular phenotypic responses to surface interaction.* Biomaterials, 2006. **27**(16): p. 3096-3108.

280. Avila-Sierra, A., J.A. Moreno, K. Goode, T. Zhu, P.J. Fryer, A. Taylor, and Z.J. Zhang, *Effects of structural and chemical properties of surface coatings on the adsorption characteristics of proteins.* Surface and Coatings Technology, 2023. **452**: p. 129054.

281. Zhou, K., J. Chen, T. Wang, Y. Su, L. Qiao, and Y. Yan, *Effect of surface energy on protein adsorption behaviours of treated CoCrMo alloy surfaces.* Applied Surface Science, 2020. **520**: p. 146354.

282. Santo Christophe, E., W. Lam Ee, G. Elowsky Christian, D. Quaranta, W. Domaille Dylan, J. Chang Christopher, and G. Grass, *Bacterial Killing by Dry Metallic Copper Surfaces.* Applied and Environmental Microbiology, 2011. **77**(3): p. 794-802.

283. Wang, X., S. Liu, M. Li, P. Yu, X. Chu, L. Li, G. Tan, Y. Wang, X. Chen, Y. Zhang, and C. Ning, *The synergistic antibacterial activity and mechanism of multicomponent metal ions-containing aqueous solutions against Staphylococcus aureus.* Journal of Inorganic Biochemistry, 2016. **163**: p. 214-220.

284. Wang, G., W. Jin, A.M. Qasim, A. Gao, X. Peng, W. Li, H. Feng, and P.K. Chu, *Antibacterial effects of titanium embedded with silver nanoparticles based on electron-transfer-induced reactive oxygen species.* Biomaterials, 2017. **124**: p. 25-34.

285. Pal, S., Y.K. Tak, and J.M. Song, *Does the antibacterial activity of silver nanoparticles depend on the shape of the nanoparticle? A study of the gram-negative bacterium Escherichia coli.* Applied and environmental microbiology, 2007. **73**(6): p. 1712-1720.

286. Cortizo, M.C., M.F.L. De Mele, and A.M. Cortizo, *Metallic Dental Material BiocompatibilityinOsteoblastlikeCells: Correlation with Metal Ion Release.* Biological Trace Element Research, 2004. **100**(2): p. 151-168.

287. LaBauve, A.E. and M.J. Wargo, *Growth and laboratory maintenance of Pseudomonas aeruginosa.* Curr Protoc Microbiol, 2012. **Chapter 6**: p. Unit 6E.1.

288. Johnston Ella, L., L. Zavan, J. Bitto Natalie, S. Petrovski, F. Hill Andrew, and M. Kaparakis-Liaskos, *Planktonic and Biofilm-Derived Pseudomonas aeruginosa Outer Membrane Vesicles Facilitate Horizontal Gene Transfer of Plasmid DNA.* Microbiology Spectrum, 2023. **11**(2): p. e05179-22.

289. Žiemytė, M., M. Carda-Diéguez, J.C. Rodríguez-Díaz, M.P. Ventero, A. Mira, and M.D. Ferrer, *Real-time monitoring of Pseudomonas aeruginosa biofilm growth dynamics and persister cells' eradication.* Emerg Microbes Infect, 2021. **10**(1): p. 2062-2075.

290. Espírito Santo, C., N. Taudte, D.H. Nies, and G. Grass, *Contribution of copper ion resistance to survival of Escherichia coli on metallic copper surfaces.* Appl Environ Microbiol, 2008. **74**(4): p. 977-86.

291. Rensing, C., B. Fan, R. Sharma, B. Mitra, and B.P. Rosen, *CopA: An Escherichia coli Cu(I)-translocating P-type ATPase.* Proceedings of the National Academy of Sciences, 2000. **97**(2): p. 652-656.

292. Tseng, A.S., M.C. Roberts, S.J. Weissman, and P.M. Rabinowitz, *Study of heavy metal resistance genes in Escherichia coli isolates from a marine ecosystem with a history of environmental pollution (arsenic, cadmium, copper, and mercury).* PLoS One, 2023. **18**(11): p. e0294565.

293. Kaur, I., J. Purves, M. Harwood, J.M. Ketley, P.W. Andrew, K.J. Waldron, and J.A. Morrissey, *Role of horizontally transferred copper resistance genes in Staphylococcus aureus and Listeria monocytogenes.* Microbiology, 2022. **168**(4).

294. Longhin, E.M., N. El Yamani, E. Rundén-Pran, and M. Dusinska, *The alamar blue assay in the context of safety testing of nanomaterials.* Front Toxicol, 2022. **4**: p. 981701.

295. Rabbitt, D., V.M. Villapún, L.N. Carter, K. Man, M. Lowther, P. O'Kelly, A.J. Knowles, A. Mottura, Y.T. Tang, L. Luerti, R.C. Reed, and S.C. Cox, *Rethinking Biomedical Titanium Alloy Design: A Review of Challenges from Biological and Manufacturing Perspectives.* Advanced Healthcare Materials. **n/a**(n/a): p. 2403129.

296. Straumanis, M. and L. Yu, *Lattice parameters, densities, expansion coefficients and perfection of structure of Cu and of Cu–In α phase.* Acta Crystallographica Section A: Crystal Physics, Diffraction, Theoretical and General Crystallography, 1969. **25**(6): p. 676-682.

297. Attar, H., S. Ehtemam-Haghighi, D. Kent, X. Wu, and M.S. Dargusch, *Comparative study of commercially pure titanium produced by laser engineered net shaping, selective laser melting and casting processes.* Materials Science and Engineering: A, 2017. **705**: p. 385-393.

298. Iebba, M., A. Astarita, D. Mistretta, I. Colonna, M. Liberini, F. Scherillo, C. Pirozzi, R. Borrelli, S. Franchitti, and A. Squillace, *Influence of powder characteristics on formation of porosity in additive manufacturing of Ti-6Al-4V components.* Journal of Materials Engineering and Performance, 2017. **26**: p. 4138-4147.

299. Duan, R., S. Li, B. Cai, Z. Tao, W. Zhu, F. Ren, and M.M. Attallah, *In situ alloying based laser powder bed fusion processing of β Ti–Mo alloy to fabricate functionally graded composites.* Composites Part B: Engineering, 2021. **222**: p. 109059.

300. Pfaff, A., S. Schäffer, M. Jäcklein, and F. Balle, *Measuring the Cooling Behavior of Melt Pools in L-PBF by Pyrometry.* Materials (Basel), 2023. **16**(10).

301. Wenzler, D.L., K. Bergmeier, S. Baehr, J. Diller, and M.F. Zaeh, *A Novel Methodology for the Thermographic Cooling Rate Measurement during Powder Bed Fusion of Metals Using a Laser Beam.* Integrating Materials and Manufacturing Innovation, 2023. **12**(1): p. 41-51.

302. Oliveira, J.P., A.D. LaLonde, and J. Ma, *Processing parameters in laser powder bed fusion metal additive manufacturing.* Materials & Design, 2020. **193**: p. 108762.

303. Gaetke, L.M., H.S. Chow-Johnson, and C.K. Chow, *Copper: toxicological relevance and mechanisms.* Arch Toxicol, 2014. **88**(11): p. 1929-38.

304. Bandyopadhyay, A., I. Mitra, S. Ciliveri, J.D. Avila, W. Dernell, S.B. Goodman, and S. Bose, *Additively manufactured Ti–Ta–Cu alloys for the next-generation load-bearing implants.* International Journal of Extreme Manufacturing, 2024. **6**(1): p. 015503.

305. Kenney, C., S. Dick, J. Lea, J. Liu, and N.A. Ebraheim, *A systematic review of the causes of failure of Revision Total Hip Arthroplasty.* J Orthop, 2019. **16**(5): p. 393-395.

306. Van Lenthe, G.H., M.C. de Waal Malefijt, and R. Huiskes, *Stress shielding after total knee replacement may cause bone resorption in the distal femur.* J Bone Joint Surg Br, 1997. **79**(1): p. 117-22.

307. Foster, A.L., T.F. Moriarty, C. Zalavras, M. Morgenstern, A. Jaiprakash, R. Crawford, M.-A. Burch, W. Boot, K. Tetsworth, T. Miclau, P. Ochsner, M.A. Schuetz, R.G. Richards, and W.-J. Metsemakers, *The influence of biomechanical stability on bone healing and fracture-related infection: the legacy of Stephan Perren.* Injury, 2021. **52**(1): p. 43-52.

308. Schmidt, A.H. and M.F. Swiontkowski, *Pathophysiology of Infections After Internal Fixation of Fractures.* JAAOS - Journal of the American Academy of Orthopaedic Surgeons, 2000. **8**(5).

309. Ho, W.F., C.P. Ju, and J.H. Chern Lin, *Structure and properties of cast binary Ti–Mo alloys.* Biomaterials, 1999. **20**(22): p. 2115-2122.

310. Martins Júnior, J.R.S., R.A. Nogueira, R.O.d. Araújo, T.A.G. Donato, V.E. Arana-Chavez, A.P.R.A. Claro, J.C.S. Moraes, M.A.R. Buzalaf, and C.R. Grandini, *Preparation and characterization of Ti-15Mo alloy used as biomaterial.* Materials Research, 2011. **14**: p. 107-112.

311. Zhu, L., Q. Zhang, Z. Chen, C. Wei, G.-M. Cai, L. Jiang, Z. Jin, and J.-C. Zhao, *Measurement of interdiffusion and impurity diffusion coefficients in the bcc phase of the Ti–X (X= Cr, Hf, Mo, Nb, V, Zr) binary systems using diffusion multiples.* Journal of materials science, 2017. **52**: p. 3255-3268.

312. Palik, E.D., *Handbook of optical constants of solids*. Vol. 3. 1998: Academic press.

313. Peterson, J., A. Issariyapat, S. Kariya, J. Umeda, and K. Kondoh, *The mechanical and microstructural behavior of heat treated, texture-controlled Ti-10%Mo alloys manufactured by laser powder bed fusion.* Materials Science and Engineering: A, 2023. **884**: p. 145553.

314. Worthing, A.G., *The Temperature Scale and the Melting Point of Molybdenum.* Physical Review, 1925. **25**(6): p. 846-857.

315. Ellingsen, D.G., N. Horn, and J.A.N. Aaseth, *CHAPTER 26 - Copper*, in *Handbook on the Toxicology of Metals (Third Edition)*, G.F. Nordberg, et al., Editors. 2007, Academic Press: Burlington. p. 529-546.

316. Cornelius, B., S. Treivish, Y. Rosenthal, and M. Pecht, *The phenomenon of tin pest: A review.* Microelectronics Reliability, 2017. **79**: p. 175-192.

317. Cahill, J.A., G.M. Krieg, and A.V. Grosse, *Electrical conductivity of tin, lead, and bismuth near their boiling points with estimates to their critical temperatures.* Journal of Chemical & Engineering Data, 1968. **13**(4): p. 504-507.

318. Nico, C., T. Monteiro, and M.P.F. Graça, *Niobium oxides and niobates physical properties: Review and prospects.* Progress in Materials Science, 2016. **80**: p. 1-37.

319. Habashi, F., *Tantalum, Physical and Chemical Properties*, in *Encyclopedia of Metalloproteins*, R.H. Kretsinger, V.N. Uversky, and E.A. Permyakov, Editors. 2013, Springer New York: New York, NY. p. 2151-2153.

320. Liu, X., P.K. Chu, and C. Ding, *Surface modification of titanium, titanium alloys, and related materials for biomedical applications.* Materials Science and Engineering: R: Reports, 2004. **47**(3): p. 49-121.

321. Xu, W., C. Hou, Y. Mao, L. Yang, M. Tamaddon, J. Zhang, X. Qu, C. Liu, B. Su, and X. Lu, *Characteristics of novel Ti-10Mo-xCu alloy by powder metallurgy for potential biomedical implant applications.* Bioact Mater, 2020. **5**(3): p. 659-666.

322. Lu, X., D. Zhang, W. Xu, A. Yu, J. Zhang, M. Tamaddon, J. Zhang, X. Qu, C. Liu, and B. Su, *The effect of Cu content on corrosion, wear and tribocorrosion resistance of Ti-Mo-Cu alloy for load-bearing bone implants.* Corrosion Science, 2020. **177**: p. 109007.

323. Chu, F., K. Zhang, H. Shen, M. Liu, W. Huang, X. Zhang, E. Liang, Z. Zhou, L. Lei, J. Hou, and A. Huang, *Influence of satellite and agglomeration of powder on the processability of AlSi10Mg powder in Laser Powder Bed Fusion.* Journal of Materials Research and Technology, 2021. **11**: p. 2059-2073.

324. Meier, C., R. Weissbach, J. Weinberg, W.A. Wall, and A. John Hart, *Modeling and characterization of cohesion in fine metal powders with a focus on additive manufacturing process simulations.* Powder Technology, 2019. **343**: p. 855-866.

325. Zhao, Y., Y. Cui, Y. Hasebe, H. Bian, K. Yamanaka, K. Aoyagi, T. Hagisawa, and A. Chiba, *Controlling factors determining flowability of powders for additive manufacturing: A combined experimental and simulation study.* Powder Technology, 2021. **393**: p. 482-493.

326. Ma, Y., T.M. Evans, N. Philips, and N. Cunningham, *Numerical simulation of the effect of fine fraction on the flowability of powders in additive manufacturing.* Powder Technology, 2020. **360**: p. 608-621.

327. Xiu, H., F. Ma, J. Li, X. Zhao, L. Liu, P. Feng, X. Yang, X. Zhang, E. Kozliak, and Y. Ji, *Using fractal dimension and shape factors to characterize the microcrystalline cellulose (MCC) particle morphology and powder flowability.* Powder Technology, 2020. **364**: p. 241-250.

328. Ojo, O.O. and E. Taban, *Post-processing treatments–microstructure–performance interrelationship of metal additive manufactured aerospace alloys: A review.* Materials Science and Technology, 2023. **39**(1): p. 1-41.

329. Fan, Y., J. Fan, and C. Wang, *Formation of typical Cu–Ti intermetallic phases via a liquid-solid reaction approach.* Intermetallics, 2019. **113**: p. 106577.

330. Arsenault, R.J. and M. Taya, *Thermal residual stress in metal matrix composite.* Acta Metallurgica, 1987. **35**(3): p. 651-659.

331. Marculescu, C.E. and J.R. Cantey, *Polymicrobial Prosthetic Joint Infections: Risk Factors and Outcome.* Clinical Orthopaedics and Related Research, 2008. **466**(6): p. 1397-1404.

332. Gupta Tripti, T., K. Gupta Niraj, J. Pestrak Matthew, H. Dusane Devendra, M. Harro Janette, R. Horswill Alexander, and P. Stoodley, *Staphylococcus aureus Aggregates on Orthopedic Materials under Varying Levels of Shear Stress.* Applied and Environmental Microbiology, 2020. **86**(19): p. e01234-20.

333. Glenske, K., P. Donkiewicz, A. Köwitsch, N. Milosevic-Oljaca, P. Rider, S. Rofall, J. Franke, O. Jung, R. Smeets, R. Schnettler, S. Wenisch, and M. Barbeck, *Applications of Metals for Bone Regeneration.* International Journal of Molecular Sciences, 2018. **19**(3): p. 826.

334. Harrison, J.J., H. Ceri, C.A. Stremick, and R.J. Turner, *Biofilm susceptibility to metal toxicity.* Environmental Microbiology, 2004. **6**(12): p. 1220-1227.

Appendix A : Image Analysis

A.1. MATLAB Code: Precipitate Size

```
imageFile = 'Ti33CuAC.png';
img = imread(imageFile);
figure;
imshow(img);
title('Ti33CuAC');
if size(img, 3) == 3
    img_gray = rgb2gray(img);
else
    img_gray = img;
end
threshold = graythresh(img_gray);
bw = imbinarize(img_gray, threshold);
bw = ~bw;
figure;
imshow(bw);
title('Ti33Cu AC Binary Image');
referenceLengthInPixels = 72;
referenceLengthInUM = 20;
scale = referenceLengthInUM / referenceLengthInPixels;
[labeledImage, numParticles] = bwlabel(bw);
particleProps = regionprops(labeledImage, 'Area', 'Perimeter', 'MajorAxisLength', 'MinorAxisLength');
```

```
particleData = struct('ParticleNumber', {}, 'AreaUM2', {}, 'PerimeterUM', {}, 'MajorAxisLengthUM', {}, 'MinorAxisLengthUM', {});
for k = 1 : numParticles
    particleData(k).ParticleNumber = k;
    particleData(k).AreaUM2 = particleProps(k).Area * (scale^2);
    particleData(k).PerimeterUM = particleProps(k).Perimeter * scale;
    particleData(k).MajorAxisLengthUM = particleProps(k).MajorAxisLength * scale;
    particleData(k).MinorAxisLengthUM = particleProps(k).MinorAxisLength * scale;
end
particleTable = struct2table(particleData);
outputFileName = 'Ti33Cu AC particle_measurements.xlsx';
writetable(particleTable, outputFileName);
for k = 1 : numParticles
    fprintf('Particle %d:\n', k);
    fprintf('  Area: %.2f um^2\n', particleData(k).AreaUM2);
    fprintf('  Perimeter: %.2f um\n', particleData(k).PerimeterUM);
    fprintf('  Major Axis Length: %.2f um\n', particleData(k).MajorAxisLengthUM);
    fprintf('  Minor Axis Length: %.2f um\n', particleData(k).MinorAxisLengthUM);
    fprintf('\n');
end
figure;
imshow(label2rgb(labeledImage, 'jet', 'k', 'shuffle'));
title('Labelled Particles');
disp(['Particle measurements have been exported to ' outputFileName]);
```

A.2. MATLAB Code: Hu Moments

```
imageFile = 'Ti33CuAC.png';

img = imread(imageFile);

figure;

imshow(img);

title('Ti33CuAC');

if size(img, 3) == 3

    img_gray = rgb2gray(img);

else

    img_gray = img;

end

threshold = graythresh(img_gray);

bw = imbinarize(img_gray, threshold);

bw = ~bw;

figure;

imshow(bw);

title('Ti33Cu AC Binary Image');

referenceLengthInPixels = 72;

referenceLengthInUM = 20;

scale = referenceLengthInUM / referenceLengthInPixels;

[labeledImage, numParticles] = bwlabel(bw);

particleProps = regionprops(labeledImage, 'Area', 'Perimeter', 'MajorAxisLength', 'MinorAxisLength');

particleData = struct('ParticleNumber', {}, 'AreaUM2', {}, 'PerimeterUM', {}, 'MajorAxisLengthUM',
{}, 'MinorAxisLengthUM', {});

for k = 1 : numParticles
```

```
    particleData(k).ParticleNumber = k;
    particleData(k).AreaUM2 = particleProps(k).Area * (scale^2);
    particleData(k).PerimeterUM = particleProps(k).Perimeter * scale;
    particleData(k).MajorAxisLengthUM = particleProps(k).MajorAxisLength * scale;
    particleData(k).MinorAxisLengthUM = particleProps(k).MinorAxisLength * scale;
end
particleTable = struct2table(particleData);
outputFileName = 'Ti33Cu AC particle_measurements.xlsx';
writetable(particleTable, outputFileName);
for k = 1 : numParticles
    fprintf('Particle %d:\n', k);
    fprintf('  Area: %.2f um^2\n', particleData(k).AreaUM2);
    fprintf('  Perimeter: %.2f um\n', particleData(k).PerimeterUM);
    fprintf('  Major Axis Length: %.2f um\n', particleData(k).MajorAxisLengthUM);
    fprintf('  Minor Axis Length: %.2f um\n', particleData(k).MinorAxisLengthUM);
    fprintf('\n');
end
figure;
imshow(label2rgb(labeledImage, 'jet', 'k', 'shuffle'));
title('Labelled Particles');
disp(['Particle measurements have been exported to ' outputFileName]);
```

A.3. Hu Moments

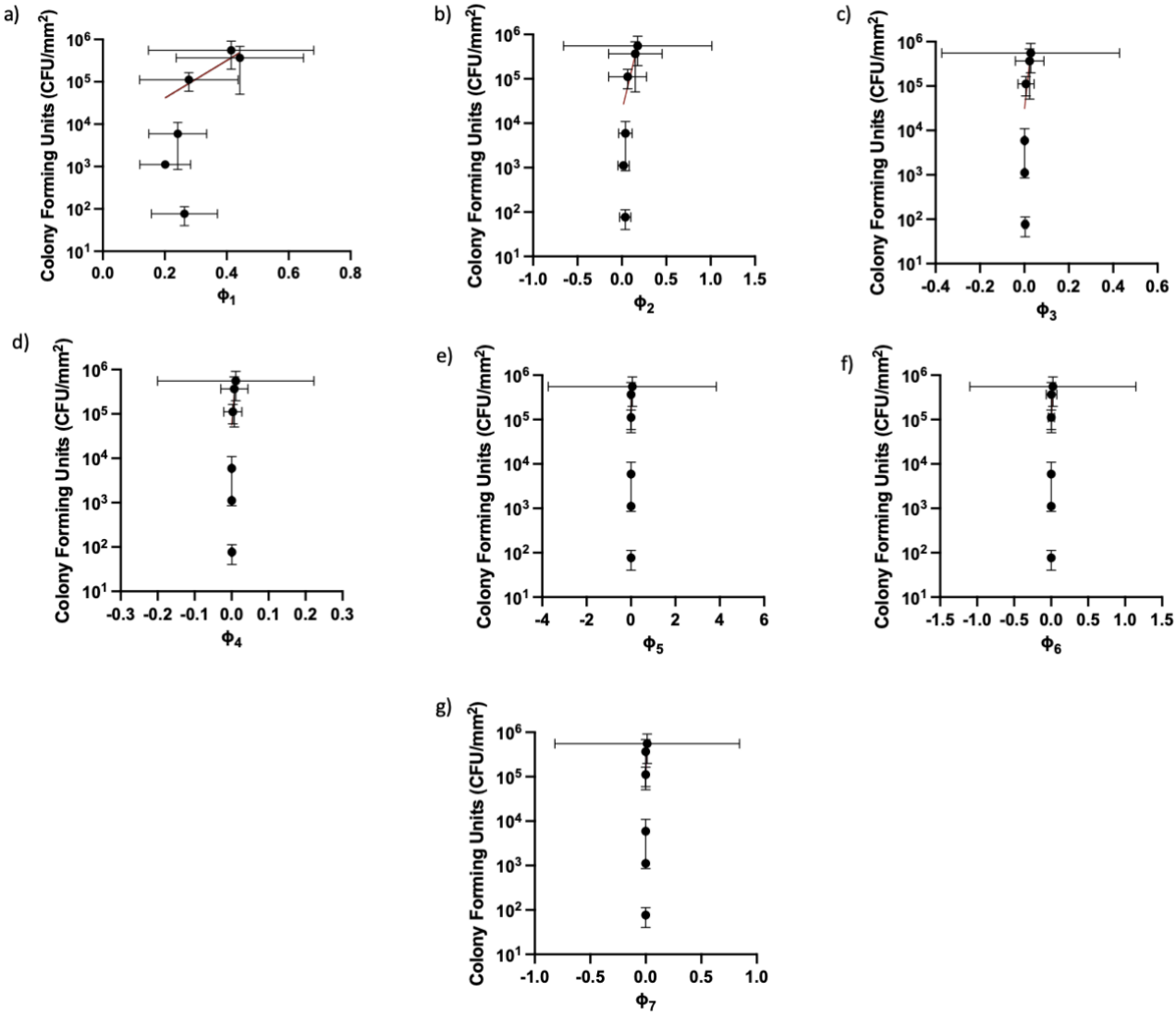

Figure A.1: Graphs representing Hu moments (ϕ1-7) against CFU. Error bar from 11 ac shows the variation in morphology of the Ti_2Cu precipitates

Appendix B: Protein Analysis.

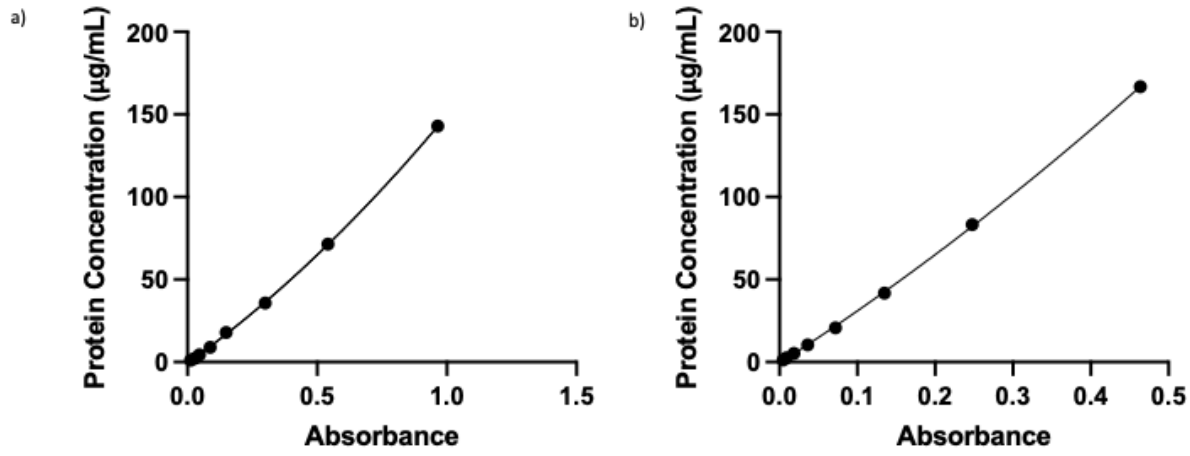

Figure A.2: Calibration curves for BCA Protein adsorption assay for (a) cell and (b) bacterial media.